UNIVERSIDAD COMPLUTENSE DE MADRID

FACULTAD DE CIENCIAS QUÍMICAS

Departamento de Química Física I

TESIS DOCTORAL

Polímeros naturales ensamblados capa a capa (layer-by-layer) para aplicaciones biomédicas

Layer-by-layer assembly of natural polymers for biomedical applications

MEMORIA PARA OPTAR AL GRADO DE DOCTOR

PRESENTADA POR

Miryam Criado González

Directoras

Rebeca Hernández Velasco
Carmen Mijangos Ugarte

Madrid, 2017

UNIVERSIDAD COMPLUTENSE DE MADRID

FACULTAD DE CIENCIAS QUÍMICAS

Departamento de Química-Física

TESIS DOCTORAL

POLÍMEROS NATURALES ENSAMBLADOS CAPA A CAPA (LAYER-BY-LAYER) PARA APLICACIONES BIOMÉDICAS

LAYER-BY-LAYER ASSEMBLY OF NATURAL POLYMERS FOR BIOMEDICAL APPLICATIONS

MEMORIA PARA OPTAR AL GRADO DE DOCTOR

PRESENTADA POR

Miryam Criado González

Directores

Rebeca Hernández Velasco

Carmen Mijangos Ugarte

CONSEJO SUPERIOR DE INVESTIGACIONES CIENTÍFICAS

Instituto de Ciencia y Tecnología de Polímeros

Madrid, 2017

TABLE OF CONTENTS

Resumen

El objetivo de esta tesis es el desarrollo de sistemas poliméricos multicapa basados en polímeros naturales mediante la técnica capa a capa (layer-by-layer, LbL) para aplicaciones en terapias de hipertermia magnética local y administración controlada de fármacos.

Los capítulos uno y dos reúnen una introducción general y objetivos junto con el estado del arte que muestra una revisión bibliográfica sobre los principales temas desarrollados durante la tesis doctoral. Del estado del arte se puede concluir que: el ensamblado LbL de polímeros naturales suscita un gran interés hoy en día debido a las potenciales aplicaciones de estos sistemas, sobre todo en el área de biomedicina. Además, la mayoría de los materiales obtenidos a partir del ensamblado de polímeros naturales se han obtenido mediante técnicas de inmersión LbL. La deposición LbL asistida por spray es una técnica rápida y sencilla para fabricar materiales nanoestructurados y ha sido menos explorada dejando un campo abierto para la investigación en esta tesis.

El tercer capítulo de la tesis se centra en la descripción de los materiales de partida utilizados así como en las técnicas de caracterización más relevantes empleadas en esta tesis. El estudio del ensamblado LbL de dos sistemas poliméricos, alginato/quitosano (Alg/Chi) y ácido hialurónico/poli(hidrocloruro de alilamina) (HA/PAH) se describe en el capítulo cuatro. Del análisis del espesor de los filmes en función del número de capas depositadas se pudo concluir que el espesor de los filmes (Alg/Chi) crecía de forma lineal mientras que el crecimiento de los filmes HA/PAH era exponencial. Además, el crecimiento de los filmes Alg/Chi fabricados mediante spray LbL era mucho mayor que el correspondiente a los filmes fabricados mediante inmersión LbL. Se ha desarrollado además un sistema nanoestratificado derivado de los filmes HA/PAH mediante la incorporación de una capa de gel formada por alginato entrecruzado con iones hierro II con potenciales aplicaciones como sistema fotosensible de liberación de fármacos que se desarrollará en el futuro.

La caracterización morfológica y mecánica de diferentes sistemas multicapa basados en alginato y chitosano se muestra en el capítulo cinco. Además, se preparó un ferrofluido acuoso a base de alginato mediante coprecipitación de sales de hierro para incorporarlo en los filmes Alg/Chi y obtener así filmes nanocompuestos. Las propiedades mecánicas de los filmes Alg/Chi, filmes Alg/Chi entrecruzados térmicamente y filmes Alg/Chi nanocompuestos se determinaron

mediante mapeo nanomecánico cuantitativo de fuerza máxima a través de microscopia de fuerzas atómicas ((PF-QNM) AFM) mostrando que el módulo elástico de los filmes Alg/Chi aumentaba con el número de bicapas depositadas y con el entrecruzamiento, mientras que los valores de deformación eran prácticamente constantes. La incorporación de nanopartículas de óxido de hierro (NPs) en los filmes Alg/Chi aumentaba su rugosidad y tenía una influencia significativa en las propiedades mecánicas aumentando el módulo elástico y la deformación, siendo este efecto más pronunciado cuando las NPs estaban presentes en la última capa. Además, se estudió la estructura interna de los filmes nanocompuestos Alg/Chi mediante dispersión de rayos X de ángulos bajos con incidencia rasante (GISAXS). Los filmes Alg/Chi nanocompuestos fabricados mediante inmersión LbL presentaban dispersión de las NPs a lo largo de toda la estructura del filme mientras que los ensamblados mediante spray LbL presentaban un cierto grado de orden de las NPs en capas.

En el capítulo seis se describe la puesta a punto de la aplicación de filmes nanocompuestos de Alg/Chi en hipertermia magnética local (MHT). Para ello, el calentamiento magnético remoto de los filmes nanocompuestos se determinó mediante aplicación de un campo magnético alternante (AMF) y los resultados mostraron un aumento lineal de temperatura desde 6 a 12 ºC con el número de capas de NPs lo que sugiere el uso de estos filmes como filmes termomagnéticos (TMFs) para la aplicación de hipertermia magnética local. Los experimentos *in vitro* llevados a cabo con células de neuroblastoma (SH-SY5Y) mostraron que los TMFs presentaban propiedades de adhesión celular y su calentamiento remoto usando un AMF proporcionaba resultados distintos dependiendo del número de ciclos de MHT y del protocolo experimental utilizado.

En el capítulo siete se muestra la aplicación de los filmes Alg/Chi como parches para liberación controlada de fármacos. El estudio de biocompatibilidad se llevó a cabo en dos tipos de células, fibroblastos dérmicos humanos (HDF) y células de adenocarcinoma de cáncer de mama (MCF-7). Se varió la química superficial de los filmes mediante deposición de una capa de ácido hialurónico (HA) al final del proceso de deposición para estudiar su influencia en la adhesión celular junto con el entrecruzamiento. Los resultados mostraron que la adhesión de las células MCF-7 aumentaba en los filmes entrecruzados químicamente cuya última capa era Alg y disminuía en los que la última capa era HA debido a un aumento del ángulo de contacto. No se observaron diferencias significativas en la adhesión de las células HDF ni con la química superficial ni con el entrecruzamiento. La aplicación final de los filmes Alg/Chi como parches para liberación de fármacos se demostró incorporando tamoxifeno, un fármaco contra el cáncer

de mama, en distintas posiciones intermedias de los filmes Alg/Chi. Los resultados mostraron una liberación más sostenida en el tiempo a medida que aumentaba el número de capas depositadas y una disminución de la viabilidad celular de las células cancerígenas MCF-7.

El capítulo ocho de la tesis constituye una extensión del procedimiento de ensamblado LbL desarrollado para la preparación de filmes a partir de polímeros naturales para el desarrollo de hidrogeles multimembrana de gelatina y sulfato de condroitina. La deposición LbL de ambos polímeros llevada a cabo sobre un núcleo de gelatina daba lugar a un aumento del módulo elástico con respecto al núcleo de gelatina sin recubrir. Los resultados obtenidos permiten anticipar el empleo de estos hidrogeles LbL como sistemas de encapsulación celular y liberación de fármacos en el futuro. El capítulo nueve recoge las conclusiones generales derivadas de este trabajo de tesis. La tesis también incluye cuatro anexos y una lista de publicaciones.

Summary

The objective of the present PhD work is the development of multilayer polymer systems based on natural polymers through layer-by-layer (LbL) assembly for applications in magnetic hyperthermia therapies and controlled drug delivery.

The first part of this thesis provides a general introduction and objectives together with a state-of-the-art which collects a literature review about the main topics related to this thesis (Chapters 1 and 2). From this state-of-the-art, it is possible to conclude that: LbL assembly of natural polymers constitutes an area of intensive research nowadays, due to the potential applications of these materials mainly on the biomedical field. In addition, most of the studies regarding LbL of natural polymers deal with dipping LbL. Spray assisted LbL is a simple and saving-time technique to fabricate nanostructured materials and it has been much less explored leaving a broad field open to research in this thesis.

The third chapter is focused on the description of materials and the most relevant characterization techniques used in this thesis. The study of the LbL assembly of two different systems based on natural polymers, alginate/chitosan (Alg/Chi) and hyaluronic acid/poly(allylamine hydrochloride) (HA/PAH) is described in the fourth chapter. From the determination of the thickness of (Alg/Chi) films as a function of the number of deposited layers, a linear growth was observed up to 5 bilayers whereas (HA/PAH) films presented an exponential growth. The growth of Alg/Chi films built up through spray LbL was much higher than that obtained when films were constructed by dipping LbL. A nanostratified system was obtained from the HA/PAH multilayer structure by incorporation of a gel-like layer formed by alginate crosslinked with iron II ions to be employed as a light-responsive drug delivery system in the future.

The morphological and mechanical characterization of different multilayer systems based on alginate and chitosan is reported in the chapter five. An alginate-based ferrofluid was synthetized by a coprecipitation method of iron salts in an alginate aqueous solution and incorporated within Alg/Chi films to obtain nanocomposite films. The mechanical properties of Alg/Chi films, thermally crosslinked Alg/Chi films and nanocomposite Alg/Chi films, built up through spray assisted LbL, were determined by PeakForce Quantitative Nanomechanical Mapping-Atomic Force Microscopy ((PF-QNM) AFM) revealing that the elastic moduli of Alg/Chi films

increased with the number of deposited bilayers and with the crosslinking, whereas deformation values were almost constant. The incorporation of iron oxide NPs within the multilayer Alg/Chi films increased the roughness of the films and greatly influenced the mechanical properties increasing the elastic moduli and the deformation values, being this effect more pronounced when NPs were on the last layer of nanocomposite films. Besides, the inner structure of nanocomposite Alg/Chi films, evaluated employing Grazing incidence small-angle X-ray scattering (GISAXS), revealed that NPs were thoroughly dispersed on nanocomposite Alg/Chi films assembled by dipping LbL, whereas spray LbL gave rise to nanocomposite films with some degree of ordering of the NPs into layers.

Chapter six describes the application of nanocomposite Alg/Chi films for local magnetic hyperthermia (MHT). To that aim, magnetic remote heating was determined by application of an alternating magnetic field (AMF) to nanocomposite Alg/Chi films with different number of NPs layers and results showed a linear temperature increase from 6 to 12 ºC with the NPs layers (from 80 to 160 layers) enabling to use these films as thermomagnetic films (TMFs) for MHT. *In vitro* experiments with neuroblastoma cells (SH-SY5Y) showed that TMFs presented cell adhesion properties and their remote heating using an AMF showed different results depending on the number of MHT cycles with a reduction in cell viability up to 67% and 20% for one and three cycles, respectively. Cell viability could decrease even more mimicking *in vivo* applications by applying the MHT on TMFs placed over neuroblastoma cells previously cultured on an Ibidi dish, giving rise to a cell viability reduction of 85% after two MHT cycles.

The application of Alg/Chi films as drug delivery patches is demonstrated in chapter seven. The biocompatibility of the films was proven employing two different kinds of cells, human dermal fibroblasts (HDF) and human caucasian breast adenocarcinoma (MCF-7) cells. The surface layer of the films was varied by spraying a layer of hyaluronic acid (HA) at the end of the deposition process in order to study their influence in the cell adhesion together with the effect of the crosslinking process. Results showed that the MCF-7 cell adhesion increased on crosslinked films with Alg-ending layer and decreased on crosslinked films ending in HA where the contact angle increased after crosslinking. There were not significant differences in HDF cell adhesion either with the surface chemistry or the crosslinking. The final application of Alg/Chi films as drug delivery patches of tamoxifen, a drug employed against breast cancer, was proven as a function of the position of TMX within the Alg/Chi films. Results showed a more sustained release over time with the number of deposited bilayers resulting in a decrease of the cell viability of MCF-7 cells.

Chapter eight constitutes an extension of the procedure developed during the thesis for the buildup of polymer films to the fabrication of multimembrane hydrogels of chondroitin sulphate and gelatin. The LbL deposition of both polymers was carried out over a gelatin gel and the mechanical properties of the resulting materials were determined through oscillatory rheological measurements. The elastic modulus increased with respect to the uncoated gelatin core without changes in their melting point, which points to a potential employment of these LbL hydrogels as cell encapsulation and drug delivery systems in the future. Chapter nine summarizes the general conclusions extracted from this thesis. The manuscript also includes four annexes and a list of publications.

CHAPTER 1

General introduction and objectives

The present PhD Thesis work ***"Layer-by-layer assembly of natural polymers for biomedical applications"***, aims to bring new insights and the establishment of a new methodology for the nanostructuration of polymer materials and the development of hydrogels obtained from natural polymers for their employment in biomedical applications.

A consolidated research line of our group at ICTP-CSIC is the study of the formation, structure, properties and applications of polymer gels. During the last years, this research has been more focused on the employment of natural polymers, specifically, those extracted from the biomass (polysaccharides such as chitosan, alginate or agarose and proteins such as gelatin) as precursors for the development of hydrogels for biomedical applications. This is motivated on the one hand, by the fact that many natural polymers are able to assemble in water in response to different stimuli (pH, temperature or ionic concentration) to give rise to hydrogels in the form of macro, micro and nanogels. On the other hand, the intrinsic characteristics of natural polymers, biocompatibility and biodegradation, make them suitable for the development of biomedical applications. Another important mode of assembly of natural polymers is the establishment of electrostatic interactions between a polycation and a polyanion. A well-known method to obtain nanostructured films taking advantage of this kind of interaction is layer-by-layer assembly (LbL), and nowadays, the growing interest on the employment of LbL with natural polymers is shown in a great number of publications dealing with the subject that employs mainly dipping techniques for the fabrication of nanostructured polymer materials. However, it is important to note that literature regarding the employment of spray assisted LbL to fabricate nanostructured systems based on natural polymers is still pretty scarce. Besides, nowadays the development of free-standing polymer films employing LbL technique constitutes an area of intensive research because it broadens the range of applications of multilayer polymer films.

In this work, spray assisted layer-by-layer has been implemented in our laboratory and employed, throughout this thesis as an easy and scalable procedure to combine polyelectrolytes into nanostructured materials. To the best of our knowledge, this technique is not settled up in any other laboratories of CSIC or Spanish Universities up to date. To this aim, a new collaboration was established with the team of Prof. F. Boulmedais (Institut Charles Sadron, CNRS, Strasbourg, France), an expert in the field of Layer-by-layer assembly and more specifically, spray assisted LbL. In these regards, this work constitute a deep study that aims to establish the best conditions for the buildup of films from natural polymers through spray assisted LbL and a comparison with the properties achieved when the fabrication is carried out through dipping assisted LbL. Very importantly, in addition to the fabrication of polymer films, a

new methodology has been implemented for the fabrication of multimembrane hydrogels based on gelatin and chondroitin sulphate that opens new perspectives within this field.

A significant effort throughout this thesis has been devoted to the determination of the structure-properties relationship through the employment of advanced characterization techniques in collaboration with the group of Prof. T. Ezquerra from the Instituto de Estructura de la Materia (CSIC). The main experimental proofs have been atomic force microscopy nanoindentation measurements and grazing incidence small angle X-ray scattering (GISAXS) carried out at the European Synchrotron Radiation Facility (ESRF), Grenoble France.

Finally, this thesis collects several exhaustive examples about the employment of the as prepared materials in biomedical applications. Specifically, the thesis collects a deep study on cell adhesion of fibroblasts and tumour cells on films made up of alginate and chitosan and the development of drug delivery patches of tamoxifen in collaboration with the group of Prof. San Roman (Instituto de Ciencia y Tecnología de Polímeros, CSIC). As a continuation of the significant efforts that we have undertaken over the last years for the development of hybrid polymer materials with iron oxide nanoparticles for magnetic hyperthermia application, the thesis includes the development of magnetic films for the application of local hyperthermia. A significant advance undertaken during this thesis is the development of a colloidal stable aqueous ferrofluid that has been the subject of a patent recently filed.

In order to get the general objective of the PhD work *"Layer-by-layer assembly of natural polymers for biomedical applications",* the manuscript is structured in nine chapters, corresponding two of them to introductory sections, one of them to Materials and Methods, four of them to main objectives of the PhD work and one to the general conclusions.

The first chapter, *General Introduction and objectives,* intends to establish the scientific framework in which the present work is carried out.

The second chapter, *State of the art,* is mainly devoted to the state of the art of LbL methodology employing natural polymers and the biomedical applications reported in literature up to date. It includes a summary of the LbL technique, the main experimental parameters that influence this process and the main experimental LbL procedures (dipping, spray and spin coating) with a comparison of their characteristics. An exhaustive table collecting relevant literature in the field of LbL with natural polymers is included at the end of the chapter.

The third chapter, entitled *Materials and methods*, is intended to describe the different materials employed throughout this thesis and the theoretical background behind the main experimental techniques employed for the characterization of the materials, among them, ellipsometry, microscopy, quartz crystal microbalance, GISAXS and atomic force microscopy nanoindentation measurements.

The fourth chapter, entitled *Layer-by-layer films from natural polymers. Study of the growth mechanism*, gives a detailed description of the fabrication of two different systems: alginate chitosan and polyallylamine/hyaluronic acid through spray and dipping procedure and the determination of their growth mechanism through a combination of experimental techniques.

The fifth chapter, *Determination of the structure-properties relationship in LbL Alg/Chi films,* aims to determine the influence of different experimental parameters such as alginate concentration, crosslinking or presence of iron oxide nanoparticles on the mechanical properties of the LbL films determined through atomic force microscopy nanoindentation measurements. Moreover, it provides results on the characterization of Alg/Chi films through GISAXS experiments aimed to elucidate differences on the inner structure of films prepared through dipping and spray techniques.

The sixth chapter, entitled *In vitro study of nanocomposite Alg/Chi films for applications in magnetic hyperthermia*, describes the cell studies carried out employing magnetic Alg/Chi films aimed to prove their application as patches for local hyperthermia employing different experimental protocols.

The seventh chapter, entitled *Study of cell adhesion and applications in drug delivery of Alg/Chi films*, provides a thorough study aimed to elucidate the influence of surface chemistry, roughness and film architecture on cell adhesion and the development of delivery patches of tamoxifen.

The eighth chapter, entitled *LbL hydrogels obtained from natural polymers*, provides a novel approach for the preparation of multimembrane hydrogels from gelatine and chondroitin sulphate employing the methodology developed throughout the thesis. It includes the morphological and rheological characterization of the resulting materials.

The ninth chapter, entitled *General conclusions and perspectives*, summarizes the most general conclusions of the work and proposes new subjects of research in this field.

CHAPTER 2

State of the art

This chapter summarizes the results found in literature about specific features related to the aims of this thesis. It includes a state-of-the-art about the layer-by-layer (LbL) assembly, the interactions driving the LbL assembly, factors influencing the LbL assembly, growth mechanisms, LbL techniques, LbL assembly of natural polymers and their biomedical applications.

2.1. LAYER-BY-LAYER ASSEMBLY

Over the last decades, the development of nanostructured polymer materials with tunable properties has gained increasing attention for application in diverse fields. In this regard, the bottom-up methodology to assemble small molecules into nanostructures has to be considered.[1] During the half first of the 20th century, the bottom-up strategies for the deposition of monolayers were based on the Langmuir-Blodgett (LB) deposition method which consist of the transfer of amphiphilic molecules from water-air interface to a solid-air interface. The necessity of very clean substrates and a dust-free atmosphere together with the low robustness of multilayers and slowness of the deposition process, hinder their widespread practical applications.[2] Time after, the layer-by-layer (LbL) assembly, based on the sequential deposition of interacting species onto a substrate, emerged as a versatile, simple, efficient, reproducible and flexible bottom-up technique[3] and it has become one of the most used techniques to coat many types of substrates, including planar surfaces,[4, 5] spherical objects,[6-8] porous matrices,[9, 10] and highly curved surfaces,[11] giving rise to nanostructured polymer materials.

LbL technique originates from works carried out by Ralph Iller[12] in 1966 when he proved the step-by-step deposition of negatively charged silica particles and positively charged Boehmite fibrils due to charge reversal after each deposition step. But it was not until 1991 that LbL buildup concept was validated[13] and the first work related to polyelectrolyte multilayer films (PEMs) dates back to 1992 when Decher et al.[14] studied the assembly of a multilayer film by alternated deposition of poly(styrene sulfonate) (PSS), used as a polyanion, and poly(allylamine hydrochloride) (PAH), used as a polycation.

The LbL assembly has advantages compared to the more conventional coating methods, including the precise control over the thickness and compositions at the nanoscale, the simplicity and versatility of the process, its suitability and flexibility to coat surfaces with irregular shapes and sizes and the possibility of scaling at industrial level.[15] These characteristics have made the LbL assembly one of the most useful techniques for building up advanced multilayer polymer

structures towards multiple applications in diverse fields such as biomedicine,[16, 17] energy,[18, 19] optics,[20, 21] coatings,[22, 23] etc.

The high impact and massive interest in the field of LbL assembly can be clearly demonstrated by a search in the SCOPUS® database using the term "layer-by-layer" as the topic keywords (Figure 2.1). As can be observed, the number of publications per year in the field of layer-by-layer (LbL) over the past decades shows an exponential growth rate giving rise to more than 1000 publications per year from 2007 and reaching 1822 publications in 2016 demonstrating the increasing interest in this technique.

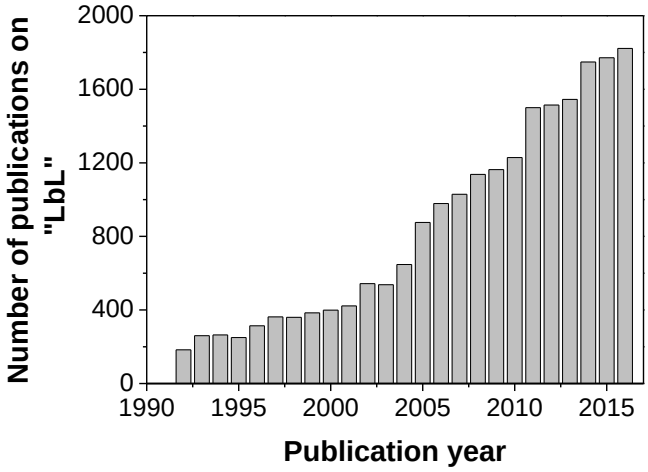

Figure 2.1. Number of publications per year with topic keywords of "layer-by-layer" since 1992. Data source: SCOPUS®.

2.1.1. Types of interactions

Multilayer assembly through the LbL technique involves different types of intermolecular interactions.

The electrostatic interaction has been the most studied driving force for the development of nanostructured multilayer films through the LbL technique.[24] It takes place between molecules and surfaces which are electrically charged. LbL assembly based on electrostatic interactions gives rise to multilayer films with well controlled structure, composition and thickness by alternate deposition of opposite charged molecules. There are multiple polymers, polycations and polyanions, that give rise to this kind of electrostatic assembly. Polycations include poly(allylamine hydrochloride) (PAH), poly(L-lysine) (PLL), poly(ethylenimine) (PEI) and chitosan (Chi), and polyanions comprise poly(styrene sulfonate) (PSS), alginate (Alg), hyaluronic acid (HA), poly(acrylic acid) (PAA), etc.

The electrostatic assembly of multilayer structures through LbL technique can be influenced by different parameters such as pH, temperature, solvent, ionic strength and type and properties of every polyelectrolyte as follows:

The properties of the PEMs depend on the pH of the polymer solutions from which the layers are adsorbed.[25] The pH controls the charge density of the adsorbing polymer layer as well as the previously adsorbed polymer layer exerting influence on LbL assembly of a polycation and a polyanion at the molecular level, that is, on the composition and structure of the multilayer system. The effect of the pH depends at a great extent on the kind of polyelectrolyte. Strong polyelectrolytes are fully charged independently of the pH; however, weak polyelectrolytes with carboxylic acid or amine functional groups are highly sensitive to the pH. It has been proved that tiny changes in the pH of weak polyelectrolyte solutions, such as polyacrylic acid (PAA), poly(allylamine) (PAH) or poly(L-lysine) (PLL), could induce pronounced changes in the growth mechanism and thickness of the LbL assembled multilayer films.[26, 27]

Regarding temperature, it has been explored that the thickness of multilayer films increases with the temperature of the polymer solutions.[28] This effect has been evaluated in different polymer systems proving that the thickness of two strong polyelectrolytes, poly(diallyldimethylammonium chloride) (PDDA) and PSS, increased in an approximately linear fashion with the increase of temperature.[29] In another example, it was demonstrated that PAH and poly(styrenesulfonate) (PSS) films fabricated at elevated temperatures were significantly thicker than similar films deposited at room temperature.[30] The structure and growth of multilayer films is also related to the solvent conditions. Decreasing the solvent quality by addition of ethanol to the aqueous polymer solutions modulates the relative strength of electrostatic and secondary intermolecular and intramolecular interactions giving rise to an increase of the multilayer film thickness and mass loading due to the reduced solvation effect of aqueous polymer solutions containing electrolyte ions.[31, 32]

The ionic strength influences the stability, permeability and thickness of multilayer films.[33] Therefore, substantial differences are observed between multilayer films assembled in solutions within or without salts,[34] with low or high salt concentration,[35] as well as with the kind of counterion.[36] Generally speaking, an increase in ionic concentration produces an increase on the film thickness. However, high salt concentrations exceeding a certain limit compensates all charge preventing multilayer adhesion of polyelectrolytes.[37] Charges on polymer repeated units can be balanced by those on oppositely charged chains or by salt ions occluded within the film.

In the case of solutions without salt, a polymer positive charge is balanced by a polymer negative charge. For solutions with salt ions, together with the polymer charge there is an extrinsic compensation balanced by salt counterions. Because of that, multilayers containing salt ions should be thicker, less interpenetrating, and individual chains would have more mobility, yielding less stable structures.[38] However, exceeding a certain threshold of salt concentration produces that the adsorbed polyelectrolytes on the substrate surface could be displaced by the salt ions.[15]

Besides the solution parameters influencing the polymer interactions, there are others related to the polymer properties such as the molecular weight, charge density and chain architectures:

The molecular weight of polymers has influence on the structure of multilayer films leading to thicker and rougher films when molecular weight increases. Generally, although the thickness and roughness of films increase with the molecular weight, the kind of growth mechanism (linear or exponential) does not depend on the polymer molecular weight.[39] Polymers with high molecular weight generally give rise to an increase of the interdiffusion in between layers because the relaxation during and after deposition, attributed to residual stresses from PEMs, increases with the molecular weight.[40]

It has been proven that the decrease of charge density of polyelectrolytes increases the thickness of multilayer films either for strong polyelectrolytes, like cellulose derivatives,[41] or weak polyelectrolytes such as PAA or PAH.[42] The chain architectures of polymers, which include chain conformation and chain interpenetration, affect the formation of multilayer films. The chain conformation dominates the growth of multilayer films at low salt concentration and the chain interpenetration has great influence at high salt concentration.[43]

Although electrostatic interactions between polycation and polyanion layers[44] are the most employed for building up multilayer polyelectrolyte films (PEMs), the following interactions can also be used to assemble LbL systems.[5] *i)* Hydrogen bonding is one of the most investigated driving forces, apart from electrostatic interactions, which allows the incorporation of uncharged materials, which can act as hydrogen bonding donors and acceptors, into the multilayer structure. The resulting materials are influenced by the temperature, pH and ionic strength being less stable than those assembled by electrostatic interactions.[45] *ii)* Covalent bonding is a chemical bond produced by shared pairs of electrons between atoms increasing the stability and strength of the multilayer structure.[24, 46] The main drawback of this kind of interaction is that some side products could be introduced into the multilayer assemblies.[1] *iii)* Charge-transfer interactions are

produced by alternate adsorption of non-ionic molecules with electron-donating and electron-accepting groups in the side chains.[47] This interaction allows to use organic solvents;[24] however, the charge-transfer complexes have low association constants limiting the achievement of well-ordered and stable multilayers.[1] *iv)* The highly selective and specific host-guest interaction is used to assembly multilayers through strong interaction between host (*e.g.*, cyclodextrins, cucurbiturils, calixarenes, pillarenes, crown ethers or porphyrins) and guest (*e.g.*, ferrocene, adamantine or azobenzece) molecules.[48, 49] *v)* The hydrophobic interaction takes place between non-polar molecules or between non-polar parts of a molecule[50] and it can be used to assemble several layers of the same polymer;[51] but they are weaker than electrostatic interactions. *vi)* Biologically specific interactions or biospecific interactions are produced by some biomaterials which are capable of interacting through different molecular interactions (*e.g.*, electrostatic, hydrophobic, etc.) with other components ensuring high specificity to the target molecules.[52] The most known are avidin-biotin, antibody-antigen and lectin-carbohydrate interactions.[24] *vii)* Coordination chemistry interactions are strong molecular interactions between a diversity of metal ions and organic ligands that enable to construct well-ordered and highly oriented and robust multilayer films.[53]

2.1.2. Mechanisms of LbL assembly

An schematic representation of LbL assembly through electrostatic interactions between a polycation and a polyanion is shown in Figure 2.2. *i)* An usually negatively charged substrate is put into contact with a solution of an oppositely charged polymer (polycation) to deposit the first monolayer, *ii)* a washing step to remove unbound material, *iii)* the positively coated substrate is put in touch with the polyanion solution to deposit a second layer and *iv*) a new washing step to remove unbound material, giving rise to the formation of a bilayer structure. This cycle can be repeated in order to obtain the desired number of bilayers to form a multilayer structure.[54, 55] During the LbL assembly, a non-stoichiometric excess of charge is absorbed after each deposition step with regards to the preceding layer. This surplus of charge provides the step-wise mechanism for the reversal of the surface charge polarity, facilitating a favorable surface for the adsorption of the subsequent layer.[15] The adsorption process is very sensitive to drying.[56]

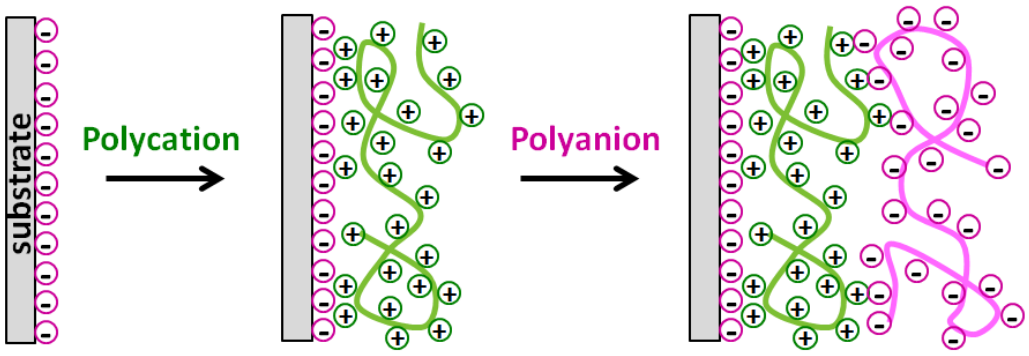

Figure 2.2. Sequential deposition of polycations and polyanions during the LbL assembly. Modified figure from Ref.[3]

Most of the substrates used for building up PEMs carry an excess of charge (*e.g.*, glass, polystyrene) which is the prerequisite for the successful adsorption of oppositely charged polymer chains. In other cases (*e.g.*, silicon, silicone rubber), it is necessary a special pretreatment such as plasma or piranha cleaning, to functionalize these substrates in order to allow the adsorption of PEMs. For a better attachment substrate-PEMs, very often the branched polyethylenimine (PEI) is used as an intermediate layer between the substrate and the first polymer layer.[57]

One of the main advantages of the LbL assembly is that the growth rate of the multilayer system can be controlled at the nanometer scale. Two types of buildup mechanisms, linear and exponential, have been reported.[39, 58]

Linear growth

The linear growth is the simplest growth mechanism in which the thickness and mass of the film increase linearly with the number of deposited bilayers.[3] At each layer deposition, the polyelectrolyte from the solution (*e.g.*, polyanion) is electrostatically attracted by the oppositely charged polyelectrolyte (*e.g.*, polycation), which forms the previously deposited layer, leaving a charge over-compensation at the interface, which gives rise to an electrostatic repulsion, restricting the polyelectrolyte adsorption to only one monolayer.[59] Every polyelectrolyte layer interpenetrates only with the adjacent ones (the previous layer and the subsequent layer).[60] A schematic representation of this kind of growth is shown in Figure 2.3a.

Exponential growth

In contrast to linear growth, in the case of exponential growth (Figure 2.3b), films grow exponentially with the number of deposited bilayers and they are characterized by high chain mobility in the direction perpendicular to the film and in the plane of the film. The origin of this exponential growth is the diffusion of at least one of the polymer constituents in and out of the film architecture.[39, 61]

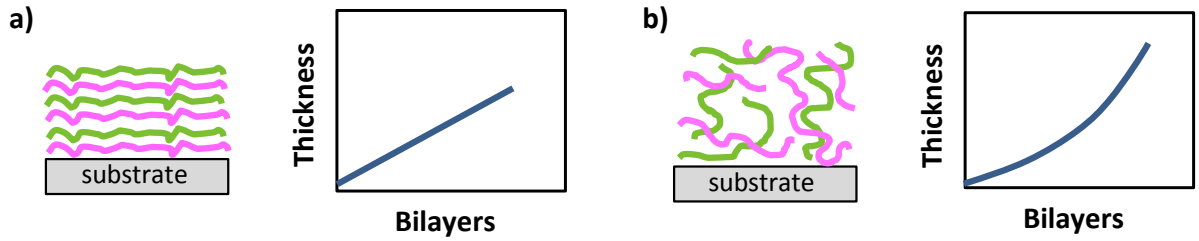

Figure 2.3. a) Linear growth with stratified layers through the multilayer structure and b) exponential growth with diffusion through the multilayer showing no clear layer structure.

Combination of both mechanisms, linear and exponential

During the LbL assembly of a polycation and a polyanion different growth mechanisms can take place as shown in Figure 2.4.[61] Considering a film with an exponential growth in which only one of the polyelectrolytes (*e.g.*, polycation, PC^+) diffuses into the whole structure and the other (polyanion, PA^-) does not diffuse, the exponential growth occurs up to a critical thickness where the growth turns again into a linear regime.[2] To explain this event, it has been considered that the structure of a multilayer film is subdivided, at least, into three zones (1, 2 and 3) during the deposition process.[59, 61, 62]

Zone 1 corresponds to the deposition of the first bilayers (at least three) which are organized in distinct and stratified layers that do not interdiffuse and grow linearly due to the influence of the substrate (Figure 2.4a).

Zone 3 is the region close to the surface and it is in contact with the polymer solution. In this zone, the deposition of a PA^- layer gives rise to a film with an outer negative excess charge. Then, this film is put into contact with the PC^+ solution and the PC^+ chains firstly interact with the outer negative charges of the PA^- layer but, immediately, they also diffuse into the film down to the substrate giving rise to a film formed by PA^- and PC^+ chains interacting strongly between them and free PC^+ chains. These free PC^+ chains diffuse into the film until its chemical potential becomes equal to that of the PC^+ chains in the solution. In addition, this diffusion could result in

a swelling of the film. When the film is then put in contact with the PA^- solution again, a negative excess charge is formed on the surface of the film and then, the remaining free PC^+ chains diffuse out of the film until reach the interface film/solution where they interact with PA^- chains from the solution creating new PA^-/PC^+ complexes that form the new outer layer of the film. The PA^- deposition process stops when all free PC^+ chains present inside the film have diffused out of it (Figure 2.4b).[35] During the exponential growth, the thickness of the zone 3 increases until this zone becomes too thick for the diffusion process and there is not transfer of material into this zone. Other parameter that hinders the diffusion and it has to be taken into account is the gradual rearrangement of the polymer chains in the film leading to make the film gradually less penetrable. At this moment, zone 2, which is the internal part of the film delimited by zones 1 and 3, appears and starts its development increasing its thickness linearly whereas the zone 3 keeps constant giving rise to the exponential to linear transition (Figure 2.4c).[61]

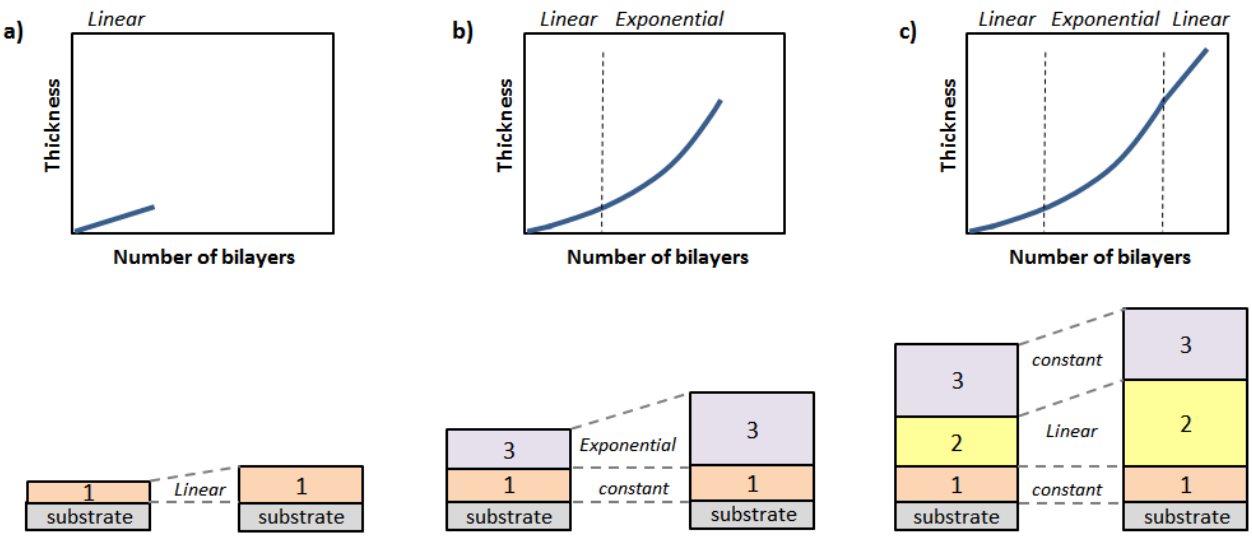

Figure 2.4. Mechanisms of growth during the LbL assembly according to the three zones model a) linear growth at the beginning of the deposition, b) exponential growth caused by the diffusion up to a critical thickness and c) the growth turns again into a linear regime. Modified figure from Ref.[61]

2.1.3. LbL techniques

The three main layer-by-layer (LbL) deposition techniques for fabrication of multilayer polymer structures are dipping, spraying and spin coating.[57, 63]

Multilayer polymer structures were built exclusively by dipping assisted LbL until 1999 when Ciba Vision[64] developed the spray assisted LBL to fabricate contact lenses and in 2001 the spin assisted LbL[65] technique appeared. Although spray LbL was discovered in 1999, the first report

about this technique data from 2000 by Schlenoff et al.[66] and the increasing attention on spray LbL began in 2005.[67] In that year a new modality of spray deposition, known as simultaneous spray coating, was developed by Porcel et al.[68] In 2009, a new LbL technique emerged by combination of spin and spray LBL and it was called spin-spray LbL[69] (Figure 2.5).

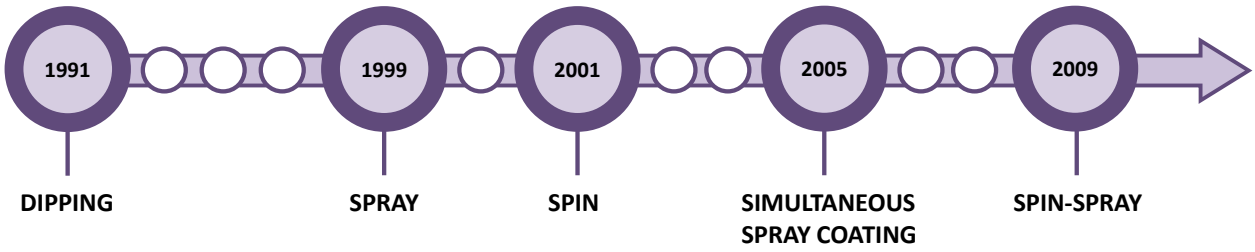

Figure 2.5. Evolution of LbL assembly since their apparition in 1991.

Dipping

Dipping LbL consists of immersing a substrate alternately into aqueous polycation and polyanion solutions with a washing step between deposited layers to remove unbound material and avoid contamination of the subsequent solution (Figure 2.6a). This cyclical process is repeated until obtain the desired number of layers.[3, 57] It is a simple technique which allows to cover substrates of almost any shape and size; however, the deposition time required for an adsorption step of polymers is around 15 – 20 minutes, making it a time-consuming process.[32] In order to scale-up this technique to industrial level, it requires a much higher volume of polymer solutions than other technologies, such as spray or spin coating, and waste can be an issue, although solutions can be reused as long as cross-contamination remains low.[1]

Spray

Spray LbL is a simple method where multilayers are assembled by sequentially spraying of polycation and polyanion solutions onto a substrate (Figure 2.6b). It allows to coat not only large and planar substrates, but also non-planar substrates. The film thickness is influenced by polymer concentrations, spray flow rate, the time of spraying (a few seconds per layer) and the waiting time whether the substrate is washed or not. Comparing with dipping LbL, the rinsing step can be suppressed giving rise to thicker films without altering their quality and decreasing the deposition time even more.[55] The film properties, such as morphology, uniformity and chemical composition, can be tailored to be similar to those prepared by dipping LbL. Spray LbL offers rapid assembly times and it is amenable to both automation and scale-up to industrial level.[67]

Spin coating

Spin LbL assembly is based on spinning a substrate to facilitate the deposition of polymers. It is performed by either casting the polycation and polyanion solutions onto a spinning substrate or casting the solution onto a stationary substrate that is then spun (Figure 2.6c).[65, 70] It is a time-saving technique with a deposition time of ~30s per layer. The thickness depends on the spin speed, with higher speeds leading to thinner films. The presence of simultaneous interactions forces, including centrifugal, viscous and air-shear forces, gives rise to low interpenetration and highly ordered films with specific layer interfaces and smoother than those obtained from dipping LbL. However, this technique has some limitations, in fact, it cannot be used to deposit uniform films on non-planar surfaces and it is not possible to coat large areas surfaces.[71] Spin LbL allows for automation, but standard spin coaters are generally designed for coating flat substrates up to 10 cm in diameter width and they are not useful for complex shapes substrates.[72]

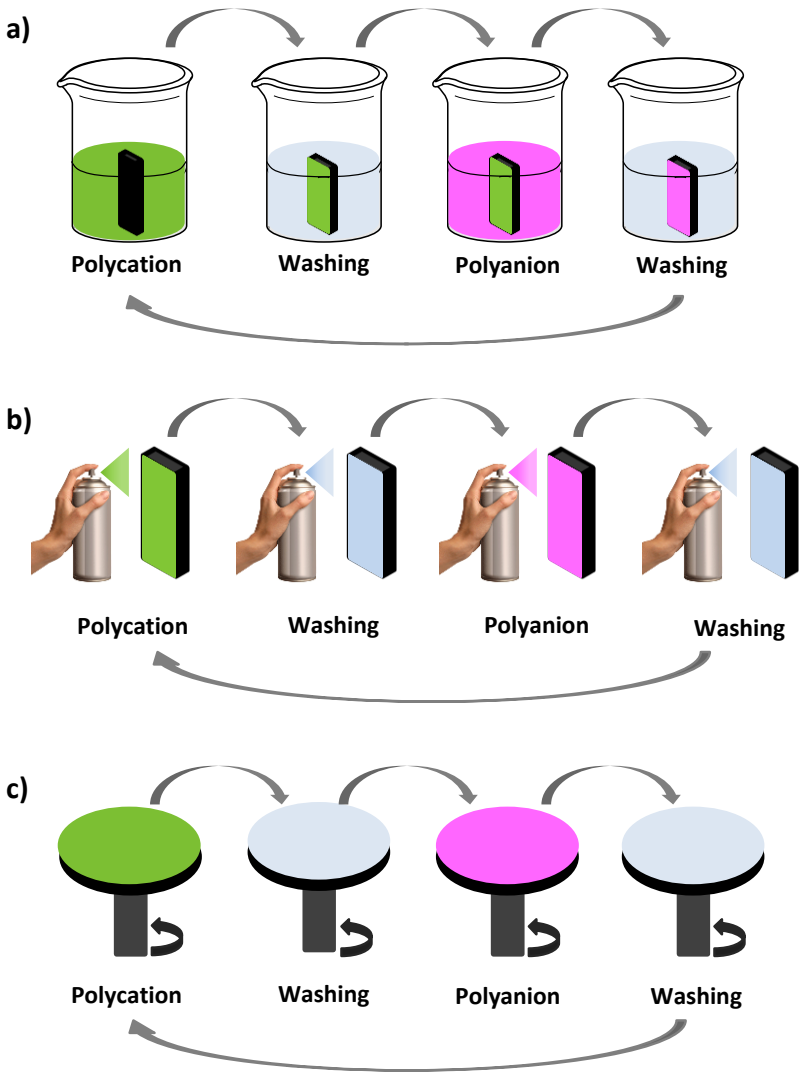

Figure 2.6. Different LbL techniques a) dipping, b) spray and c) spin coating.

The most relevant characteristic of these LbL techniques are collected in the Table 2.1 which allows to compare them easily with the aim of choosing the most suitable technique for every specific application.

Table 2.1. Characteristics of different LbL techniques and differences between them.

	Dipping	**Spray**	**Spin coating**
Deposition time	Long (minutes)	Short (seconds)	Short (seconds)
Films size	Large surfaces	Large surfaces	Up to 10cm
Deposition surface	Planar, rough, complex shape, three-dimensional	Planar, rough, complex shape	Planar
Parameters which influence the film thickness	Dipping time, solution concentration and washing time	Solution concentration, spray flux rate, spray time, evaporation time and washing time	Spin speed, solution concentrations and washing time
Automation	Yes	Yes	Yes
Visual appearance	Opaque films	Transparent films	Transparent films
Scale up	Yes	Yes	No

2.2. NATURAL POLYMERS

Natural polymers are those which are present in, or created by, living organisms. Figure 2.7 collects the different natural polymers and their classification in four groups: polysaccharides, protein origin polymers, polyesters and other polymers.[73]

Polysaccharides are polymers constituted by monosaccharide units linked by O-glycosidic bonds. They can be obtained from animal, vegetal and microbial sources. Physical properties of polysaccharides, such as solubility, gelation and surface properties, are influenced by the monosaccharide composition, chain shape and molecular weight. This group includes cellulose, chitin, chitosan, starch, alginate, hyaluronic acid, chondroitin sulphate, dextran, agarose, carrageenan, etc.[74]

Proteins can be considered as polymer structures formed by 20 different amino acids linked by amide (or peptide) bonds.[75] This group comprises collagen, gelatin, silk, fibroin, fibrin, elastin, soybean, etc. Polyamino acids are a small group of polyamides consisting of only one type of amino acid linked by amide bonds. Among them are poly(L-lysine) (PLL), poly(g-glutamic acid) (PGA), polyarginyl–polyaspartic acid, etc.[73]

Polyesters are polymers formed by a dicarboxylic acid and a diol. A special group of polyesters, polyhydroxyalkanoates, are produced by a diverse variety of microorganisms as an internal carbon and energy storage, as part of their survival mechanism. They are composed of 3-, 4-, or rarely 5-hydroxy fatty acid monomers, which form linear polyesters.[76, 77] Besides these, there are other natural polymers, such as lipids, lignin, natural rubber or shellac, which have to be considered.

Every group of natural polymers possesses its inherent properties. Generally speaking, polysaccharides function in membranes and intracellular communication, proteins function as structural materials and lipids as energy stores.[74] Amongst them, polysaccharides and proteins receive particular attention for the development of biomedical applications and they are the subject of study in this PhD work. The most important characteristics of the natural polymer employed as starting materials in this work will be described in the materials section (chapter 3).

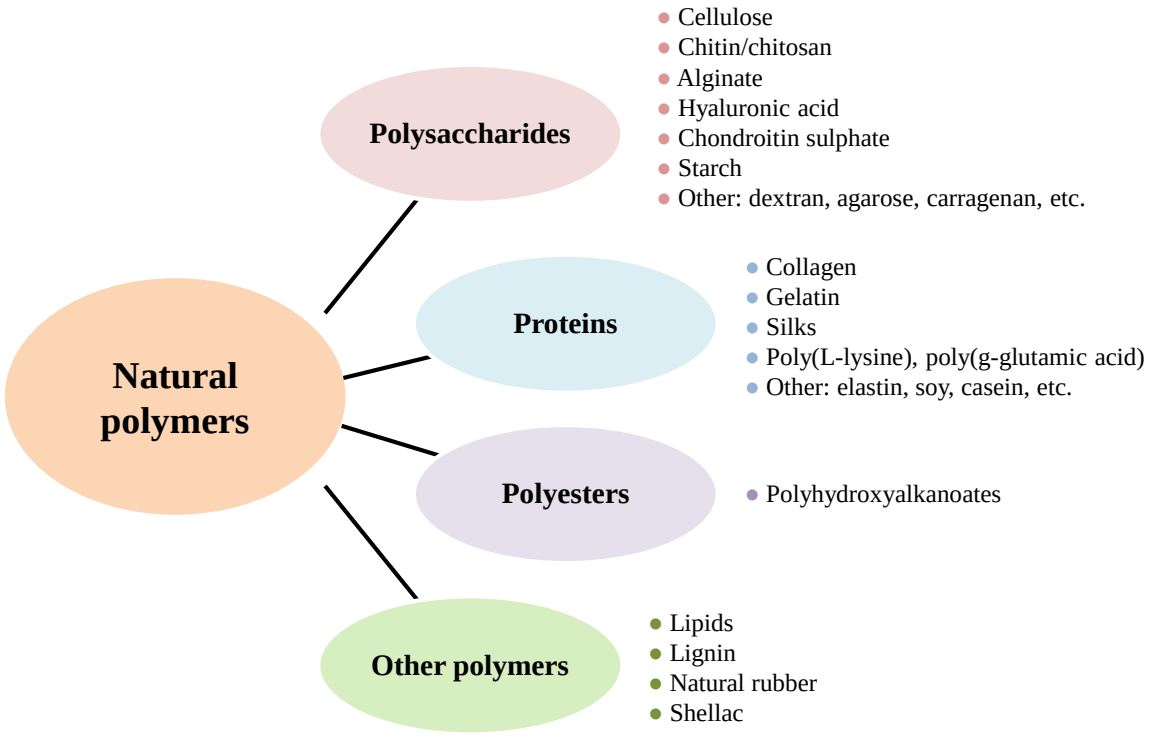

Figure 2.7. Classification of natural polymers.

2.2.1. LbL of natural polymers

Figure 2.8 illustrates a chronogram with the evolution of LbL assembly regarding natural polymers. In 1999, Elbert et al.[78] developed for first time the multilayer assembly of two natural polymers, poly(L-lysine) (PLL) and alginate (Alg), through dipping LbL. Since then, different multilayer systems based on natural polymers have been studied comprising four different polycations, PLL, Chi, collagen (COL) and gelatin (GL), and a diversity of polyanions, HA, Alg, Chondroitin sulphate (ChS), etc. In 2006, Porcel et al.[61] built up PLL/HA films by spray-assisted LbL and in 2007, Fujie et al.[79] assembled Chi/Alg films through spin-assisted LbL.

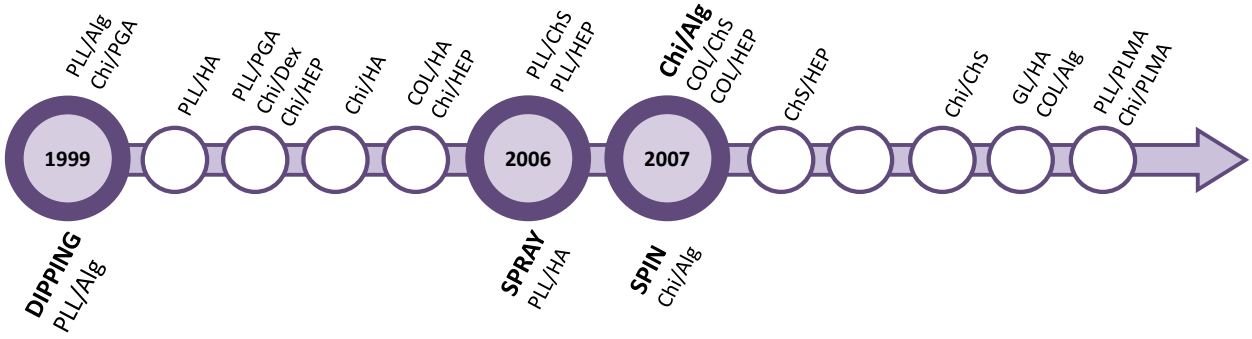

Figure 2.8. Evolution of LbL assembly related to natural polymers from 1999.

In nature, there are few examples of natural polymers acting as polycations, mainly chitosan, poly(L-lysine), collagen and gelatin.

The growth mechanism of multilayer films prepared from PLL as polycation and different polyanions such as HA, Alg, ChS, heparin (HEP) or PGA, has been reported to be exponential.[78, 80, 81] In the case of films of poly(L-lysine) (PLL) and hyaluronic acid (HA) prepared through alternate dipping LbL, the assembly process is characterized by two growth regimes. At the beginning of the deposition process, the surface of the substrate is covered by isolated islands and islets which grow by the deposition of more polymer layers on their top and by mutual coalescence until obtain a continuous film, approximately after eight deposited bilayers, showing a linear growth. At this point, the second regime starts showing an exponential growth as number of deposited bilayers increase due to the diffusion of free PLL chains 'into' whole film when the film is in contact with a PLL solution and 'out' of the film when the film is further brought in contact with a HA solution interacting with HA chains at the outer limit of the multilayer.[58, 82, 83] In the specific case of PGA, it was checked that the exponential growth was not only attributed

to the diffusion of PLL chains into the whole structure,[80] but also to the diffusion of PGA chains into the whole film.[84]

As in the case of poly(L-lysine), chitosan can be assembled with diverse polyanions, such as HA, Alg, HEP, Dex, ChS and PGA. One of the first multilayer systems comprising Chi as polycation was obtained by means of assembly with dextran sulfate (Dex) and heparin (HEP).[34] When Chi is assembled with HA, at the beginning of the Chi/HA buildup process the surface of the substrate was covered by isolated islets that grew and coalesced as the number of deposited bilayers increased until obtain a continuous film, as in the case of PLL/HA.[35] The multilayer growth process of Chi/HA, Chi/Dex and Chi/HEP was exponential, being Chi the dominating specie of the two polymers and electrostatic interactions are accompanied of other short-range interactions such as hydrogen bonding.[85] The exponential growth was due to the diffusion of Chi molecules within the film and the structure of the Chi/HEP films was highly interpenetrated without clear boundaries between each layer.[35, 86]

In contrast to the behavior observed for PLL and Chi, the assembly between COL and HA through dipping LbL exhibited a linear growth and it was proven that COL did not diffuse into the film and interacted only with its outer layer. However, the films were not constituted of homogeneously distributed polyanion/polycation complexes, but they were formed of fibers whose width increased with the number of deposition steps.[87] The fibrillary structure of the layers was also observed when COL was assembled with ChS and HEP.[88]

Experimental factors influencing the growth through LbL assembly

Even though the same general characteristics can be found regarding the growth mechanisms, the growth process is influenced by a series of parameters such as molecular weight, pH, ionic strength, solvent, method of preparation and nature of the polyanion. In this section, the experimental factors influencing the LbL growth process of PLL and Chi acting as polycations will be discussed due to the fact that they are the most studied in literature.

- *Molecular weight*

The molecular weight of PLL can influence the growth process. In the linear growth regime, the film thickness increases after each deposition step independently of the molecular weight. On the contrary, in the exponential regime it has a significant influence. Low molecular weights allowed that PLL chains diffused into the whole film during each deposition step, whereas high molecular weights restricted the PLL chains diffusion to the upper part of the film.[89]

The effect of the Chi molecular weights on the thickness and surface morphology has also been evaluated. For a constant molecular weight of the polyanion (~400000 Da) and molecular weights of chitosan of 30000 and 160000Da, at a constant pH and ionic strength, it was proven that higher molecular weights gave rise to higher thicknesses; however, the exponential growth rate was the same for high and low Chi molecular weights.[39] When molecular weight of Chi increased up to 460000 Da, it was observed that the tendency was the opposite and the exponential growth was faster for a molecular weight of chitosan of 110000 Da than for 460000 Da.[35] With regards to surface morphology, high molecular weights of Chi gave rise to a shorter island growth and coalescence stage as well as an earlier transition from islands to a vermiculate morphology than low molecular weights.[39]

- *pH, ionic strength and solvent*

The driving force of the assembly is influenced by the pH. Multilayer PLL/PGA films showed different behaviors depending on the pH of assembly. The main driving force of the assembly at pH 7.4 is electrostatic interaction, whereas hydrogen bonding and hydrophobic interaction are the dominant interactions in films built up at low pH.[90] The growth of these films was higher at acidic pH.[91] When PLL is assembled with HA, the acid-base equilibria of multilayer PLL/HA films showed that these films can be electrostatically adsorbed under highly charged "sticky" conditions but then quickly transformed into stable low-friction films simply by altering their pK_a on adsorption, at the same pH environment.[27]

The effect of the pH and ionic strength in the growth process of Chi/Dex and Chi/HEP films showed an increase in the film thickness with the increase in the NaCl concentration at a fixed pH.[34] The same effect was found for Chi/HEP films when the pH was increased at a fixed ionic strength.[85, 92] In the case of Chi/HA films, at low salt concentrations (10^{-4} M NaCl), the surface of the substrate was covered by islets up to 50 bilayers with a linear increase of the film growth. At high salt concentration (0.15 M NaCl), the formation of an uniform film took place only after a few deposition steps showing an exponential growth.[35] When Chi is assembled with Alg, the study of the buildup process at different concentrations, pH and ionic strength allowed to conclude that the fastest film growth took place for chitosan and alginate concentrations of 1.0 and 5.0 mg/mL and pH 5 and 3, respectively, conditions under which alginate is in high concentration and only partially ionized in a way that its negative charge interact weakly with the positively charged amino groups of Chi.[93, 94]

The effect of the solvent in the assembly process of Chi and PGA showed that the adsorption process from an aqueous phase was not stable; however, the use of an organic solvent as a less soluble solvent gave rise to thicker films and achieved stable deposition.[95]

- *Method of preparation*

The effect of the method of preparation in the buildup process was firstly studied by Porcel et al.[61] who built up PLL/HA films via spray assisted LbL and dipping LbL. In both cases the film growth first evolved exponentially with the number of deposited bilayers and, after a given number of deposition steps, its thickness evolution became linear again. This second transition was investigated in detail through spray LbL reaching the conclusion that this transition always took place after about 12 deposition steps independently of the parameters controlling the deposition process, time of spraying and polyelectrolyte concentrations. These changes in the growth process were explained using the model of the three zones described in the section 2.1.2. in which the exponential to linear transition is attributed to the restructuration of the film that progressively prevented the diffusion of one of the polyelectrolytes over part of the film and this "forbidden" zone then grew linearly with the number of deposition steps.

- *Nature of the charged groups of the polyanion*

The nature of the charged groups of the polyanion also influences the assembly of the multilayer films. Taking into account that electrostatic interactions as well as hydrogen bond interactions are important in the film buildup, the quantification of internal ion pairing (extrinsic versus intrinsic charges) and water content were studied for three different systems based on PLL, PLL/HA, PLL/ChS and PLL/HEP, in order to examine the influence of the COO^- and SO_3^- groups on the film growth, the water content and the ion pairing. Although these polyanions differed in their charge, the disaccharide units attracted approximately two lysine groups per monomer. The percentage of free NH_3^+ in the films decreased as the charge density of the disaccharide increased and it was related to PLL diffusion influencing directly the film growth. It was also proven that PLL/HA and PLL/ChS films were the most hydrated ones. The selective crosslinking of carboxylate and ammonium ions via carbodiimide chemistry allowed to determine the COO^-/NH_3^+ and SO_3^-/NH_3^+ ion pairing showing that 46% of NH_3^+ groups are unpaired in PLL/HA films, 21% in PLL/ChS films and none in PLL/HEP films reaching to the conclusion that this ratio was close to the stoichiometry of these groups in the dissacharide monomeric unit (2:1 for PLL/HA films and 1:1 for PLL/ChS films).[96]

Regarding the influence of the nature of the polyanion in the wettability and ion pairing, three different multilayer films with Chi as polycation, Chi/HEP, Chi/HA and Chi/ChS, were studied. The most hydrophilic films Chi/HA were formed by the assembly of a weak polycation (Chi) and a weak polyanion (HA) and the most hydrophobic ones (Chi/HEP and Chi/ChS) were formed by combination of weak (Chi) – strong (HEP or ChS) polyelectrolytes. The assembly of two weak polyelectrolytes Chi/HA reduced ion pairing and enabled the swelling of the film, whereas the combination weak – strong polyelectrolytes reduced the swelling because of an increase of ion pairing.[44]

Crosslinking of LbL films obtained from natural polymers

The crosslinking process of multilayer polymer films built up from PLL and a determined polyanion induces the following changes: *i)* the rigidity of films increases, *ii)* the diffusion of the PLL chains in the network is reduced, *iii)* the adhesion of films to the substrate increases and *iv)* the degradation decreases.[97]

The effect of the crosslinking on the mechanical properties of the resulting films has been examined by different techniques such as Atomic force microscopy (AFM) nanoindentation mesasurements and dynamic mechanical analysis (DMA).[98, 99] Crosslinking gave rise to an increase of the elastic modulus making films stiffer than native ones (Figure 2.9).[99-101]

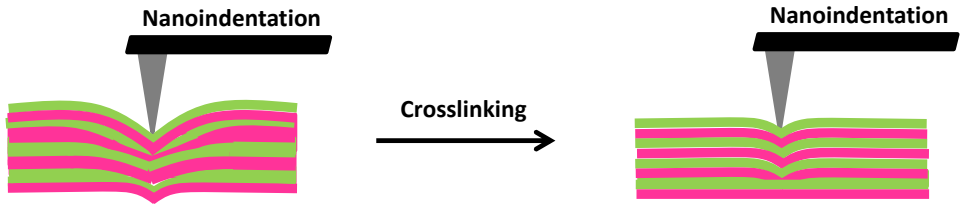

Figure 2.9. Schematic representation corresponding to the increase of the stiffness of multilayer polymer films after crosslinking.

There are different kinds of crosslinking processes. The most used are chemical crosslinking, using the carbodiimide chemistry (1-ethyl-3-(3-(dimethylamino)-propyl)carbodiimide (EDC) in combination with N-hydroxy-sulfosuccinimide (NHS)) or genipin, a natural origin polymer, and thermal crosslinking, employing high temperatures during a time interval which are different for every polymer system. Both crosslinking processes gives rise to amide bonds formation between carboxylic groups of the polyanion (PA) and amine groups of the polycation (PC), as can be observed in Figure 2.10.[4, 97] As an example, multilayer PLL/HA films were crosslinked using these two mechanisms, chemical (EDC/NHS) or thermal (90 ºC for 4h) crosslinking, and further

detached from the substrate to obtain free-standing PLL/HA films. The method employed for the detaching process influenced the final structure of the film. Films built up on glass were detached by immersing the film in a basic solution (0.1M NaOH) giving rise to non-porous and smooth membranes. On the contrary, films built up on polystyrene can be detached by dissolving the polystyrene substrate in tetrahydrofuran (THF) leading to a porous membrane with micrometric holes.[4]

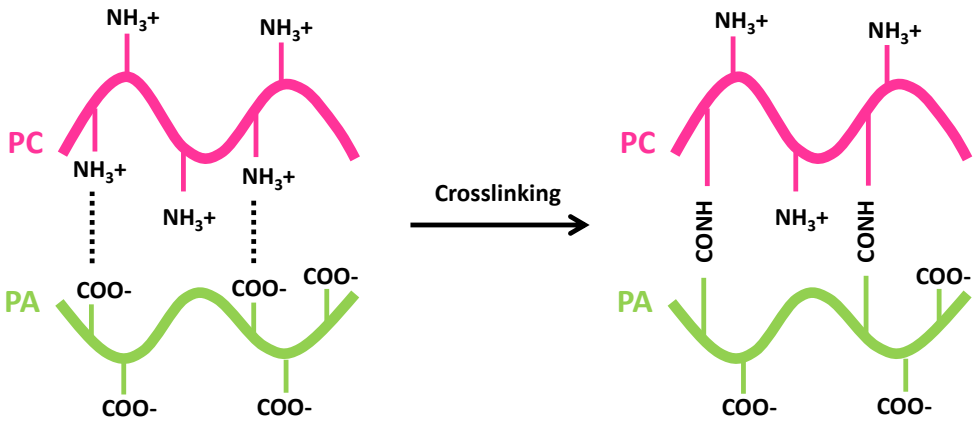

Figure 2.10. Schematic representation corresponding to the formation of amide bonds between carboxylic groups of the polyanion (PA) and amine groups of the polycation (PC) after thermal or chemical crosslinking.

Other methods of crosslinking include the combination of covalent and ionic crosslinking, using genipin and calcium chloride ($CaCl_2$), provided free-standing Chi/Alg films with enhanced mechanical properties and shape memory ability. $CaCl_2$ was used to induce ionic crosslinking due to the formation of stable complexes between the calcium ions and deprotonated carboxylic groups of the Alg into multilayer membranes with and without previous genipin crosslinking. This ionic crosslinking gave rise to free-standing membranes with improved mechanical strength, calcium-induced adhesion and shape memory ability. Precisely, the use of $CaCl_2$ allowed to reverse the crosslinking process by using a competing ligand, ethylendiaminetetraacetic acid (EDTA), which acts as a chelating agent sequestering the calcium ions. It was proved that the mechanical behavior of ionic and covalent crosslinking was different and the application of a stress to ionically crosslinked materials gave rise to a relaxation of the multilayers with water release and a plastic deformation as the crosslinking was dissociated, whereas in covalently crosslinked films leaded also to a relaxation of the multilayers with water release and an elastic deformation due to their inability to dissociate and reform bonds.[102]

The biodegradation is also influenced by the crosslinking degree. Multilayer PLL/HA films crosslinked using the carbodiimide chemistry showed a highly resistant to hyaluronidase, an enzyme that naturally degrades hyaluronan.[97] The degradation of Chi/HA films, evaluated *in vitro*, in contact with enzymes, plasma and macrophages, and *in vivo*, in mouse peritoneal cavity, can be tuned by film crosslinking. Native films showed degradation by enzymes and crosslinked films were more resistant to enzymatic degradation. Plasma also induced changes in the structure of native films but not in crosslinked films. On the contrary, cells induced degradation in both types of films. Regarding the *in vivo* degradation, native films showed an almost complete degradation, whereas crosslinked films were only partially degraded.[103] The stability of multilayer films with COL as polycation is different depending on the nature of the polyanion. COL/ChS films are stable in culture media at physiological conditions, whereas COL/HA, COL/HEP and COL/Alg films are unstable.[17, 88, 104] The dissolution and biodegradation of COL/HA and COL/Alg films at physiological pH can be avoided by chemical crosslinking of these films in order to obtain stable membranes.[17, 104]

2.2.2. Biomedical applications of LbL films from natural polymers

Natural polymers are of great interest in the biomedical field due to the fact that most of them present the following features: *i)* biodegradability, they do not show adverse effects on the environment or human being, *ii)* biocompatibility and non-toxicity, almost all of these materials are carbohydrates in nature and composed of repeating monosaccharide units, *iii)* economic, they are cheaper than synthetic polymers, *iv)* safety, they do not have side effects whereas synthetic polymers could produce side effects, *v)* availability, they are produced naturally in large quantity.[73, 105] These characteristics make natural polymers have gained increasing attention for the development of biomedical applications. With the aim of LbL systems can be employed for biomedical applications, they have to be biocompatible. At the same time, it is necessary to know their behavior at physiological conditions.

Among the different applications for LbL natural polymer films, three of the most studied are coatings for tissue engineering and platforms for cell adhesion and for drug delivery.

Coatings for tissue engineering

Most of applications found in literature regarding LbL multilayer films obtained from natural polymers are focused on their employment as coatings for tissue engineering. Some selected

examples of this application, such as coatings for knee prostheses, dermal patches, coatings for stents and dental implants, are shown in Figure 2.11.

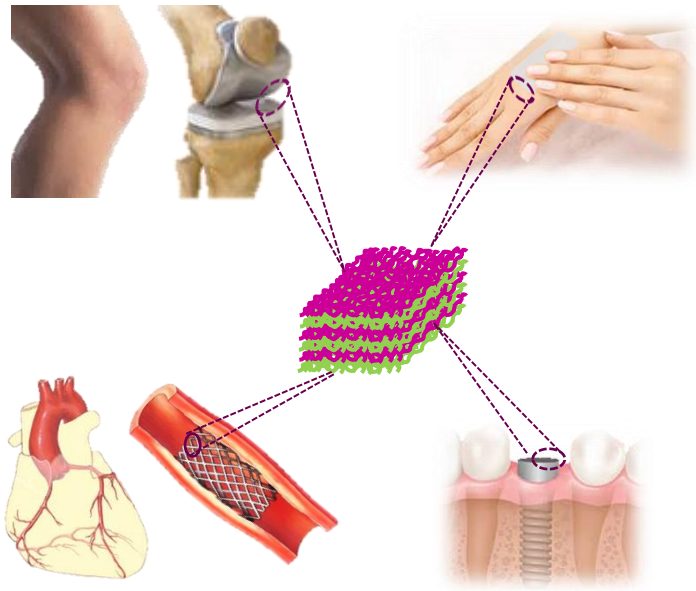

Figure 2.11. LbL coatings from natural polymers for different tissue engineering applications: knee prostheses, dermal patches, stents and dental implants.

A detailed description of the application of LbL materials from natural polymers as coatings for tissue engineering is provided below as a function of the polymer which acts as a polycation.

- *Multilayer films with PLL acting as polycation*

The ability of multilayer PLL/Alg films to generate thin coatings on tissue surfaces, the inherent biocompatibility and degradability, together with the bioinertness, allows to control the wound healing as well as the immunoisolation of the underlying surface to be used as barriers on biological surfaces.[78] In this regards, multilayer PLL/Alg films were used to coat magnesium based degradable scaffolds to improve their surface bioactivity. For that purpose, they were crosslinked using the carbodiimide chemistry and surface functionalized with fibronectin immobilization. The *in vitro* cytocompatibility studies with MC3T3-E1 osteoblast cells demonstrated that the pretreatment of the magnesium substrate greatly influenced the biocompatibility of the films proving that fluoride pretreatment is necessary for the long-term stability of PLL/Alg films and, therefore, for the slow corrosion of the magnesium substrates in order to be applied as matrices for delivery of drugs and other biomolecules for successful bone regeneration *in vivo*.[106] The spray deposition of PLL and HA layers was further employed to coat porous scaffolds of modified hyaluronic acid to give rise to a multilayer 3D structure, formed by

the multilayer PLL/HA film covering the scaffold, which promoted the adhesion and proliferation of keratinocytes creating an epidermal structure that mimicked the natural skin microenvironment for potential use in skin tissue engineering applications.[9]

The 'in' and 'out' diffusion of PLL during the exponential growth of multilayer films was explored to load and release growth factors. Besides, the pH tunable charge density within the multilayer provided the possibility to adjust the amount of growth factors embedded. Different kinds of growth factors, such as HIV-1 TAT (47-57), basic fibroblastic factor (bFGF) and alpha-melanocyte stimulating hormone (α-MSH), have been embedded into PLL/HA, PLL/ChS and PLL/PGA multilayer films. These growth factors maintained their long time activity when they were embedded into the multilayer structure and after crossing the multilayer membrane, whereas its short time activity depended on their integration depth.[81, 107, 108] Multilayer PLL/PGA films were the first example of a multilayer film whose biological activity was based on a synergy effect of two active compounds, BMP2 and TGFb1 growth factors, in order to be employed for cartilage and bone differentiation. *In vitro* studies with mesenchymal stem cells revealed that cells came into contact with the growth factors through the PLL/PGA films due to the degradation by cells and both growth factors, BMP2 and TGFb1, needed to be present simultaneously in the film to drive the embryoid bodies (EBs) to cartilage and bone formation.[108] Apart from growth factors, proteins and enzymes can also be incorporated in multilayer films with PLL as polycation and they also maintained their activity while they were encapsulated.[4, 109, 110] In the case of proteins, it has been proved that proteins interacted with cells through local degradation of the PLL/PGA film.[109, 110]

Other approach to use multilayer films in tissue engineering applications is the formation of micro-stratified structures composed of PLL-based multilayers with gel layers in between these. For that purpose, micro-stratified structures composed of PLL/HA layers with alternate alginate gel layers were built up through spray assisted LbL where Alg gel layers were obtained by crosslinking Alg with $CaCl_2$ using two different experimental methods, spraying or dipping, which led to microporous gels or homogeneous gels, respectively.[111] This micro-stratified structure was further employed to incorporate fibroblastic 3T3 cells or melanocytic B16-F1 cells into the Alg gel layers. The multilayers PLL/HA had the following functions: act as a separator between two gel layers containing different types of cells, work as reservoirs for biologically active compounds interacting with cells embedded in the adjacent gel layers due to their exponential growing and offer mechanical stability to the gel. This was also studied for other polymer system PLL/PGA acting as multilayer structure between gel layers. It was observed that

the bioactivity of the multilayer films originates mainly from the local degradation carried out by the cells and the cellular activity could be tuned as a function of the nature of polymer multilayers and the position of active molecules in the architecture.[112]

- *Multilayer films with Chi acting as polycation*

The use of Chi-based films as blood-compatibility materials depends on their thrombogenic potential and the hemocompatibility. The extent of platelet adhesion and surface-induced activation are early indicators of thrombogenic potential and the clotting time of activated partial thromboplastin time (APTT) together with the prothrombin time (PT) are indicators of the coagulation activation. The anti-vs procoagulant activity of films based on Chi was dependent on the salt concentration, the number of deposited bilayers and the nature of the polyanion. The bioactivity of Chi/HEP films was different from Chi/Dex films and the surface of the Chi/HEP assembly showed strong anticoagulant activity which is useful for coating various blood contacting biomedical materials.[34]

Multilayer Chi/HEP films have been employed to coat different materials such as stainless steel coronary stents and NiTi endovascular stents, to accelerate the re-endothelialization and healing process after coronary stent deployment. *In vitro* studies proved that these coatings decreased the platelet adhesion in comparison with uncoated NiTi stents displaying good haemocompatibility and enhanced thromboresistance. *In vivo* studies in a porcine coronary injury model and arteriovenous shunt model demonstrating that this coating promoted re-endothelialization and good haemocompatibility with improved anticoagulation properties.[16, 113] The platelet adhesion could be increased by incorporation of sodium nitroprusside (SNP) within the multilayer, as it was proved by *ex vivo* assays on the vascular wall of a porcine model. The enhanced thromboresistance of the multilayer together with the anti-inflammatory and wound healing properties of HA and Chi are expected to reduce the neointimal hyperplasia associated with stent implantation.[16]

Apart from cardiovascular coatings, Chi/HEP films can be employed to modify the surface of titanium implants improving its biocompatibility for use in dental or orthopedic implants, as it was checked *in vitro* with osteoblast cells improving their adhesion, proliferation and differentiation.[114] In this sense, basic fibroblast growth factor (FGF-2) was bound to Chi/HEP multilayers to enhance the bone marrow-derived ovine (MSCs) cell proliferation to be employed as promising surface coatings that can stabilize and potentiate the activity of growth factors for therapeutic applications.[115] Multilayer Chi/HA, Chi/Alg and Chi/HA-DN films have also been

employed as titanium coatings.[116, 117] Multilayer Chi/Alg films have been employed to load antibodies with binding activity of the antigen to the immobilized antibody which can be tuned by pH control converting these films into good candidates as sensitive immunosensors.[118]

Apart from the use of multilayer films based on Chi for coating different materials in order to improve their biocompatibility, they can be applied directly in contact with human tissues as wound healing patches. In this regards, multilayer Chi/HA films have been used to repair porcine arteries by placing them on damaged arteries. It was observed a strong adhesion of the coating on the artery when Chi was the contact surface due to the fact that it is a polycation and exhibited excellent bioadhesive properties toward negatively charged surfaces presented by damaged arteries.[119]

Chi-based films have also been employed as antibacterial coatings. Multilayer Chi/HEP films were used to coat poly(ethylene terephthalate) (PET) films in order to control the degree of interpenetration of the layers and the antibacterial properties by altering the assembly pH. The antibacterial property was proved *in vitro* with Escherichia coli (E. coli) bacteria, showing that the number of adhered bacteria decreased with a decrease in the assembly pH making these nanostructured films useful as powerful anti-infection coatings for medical devices.[120] Same results were observed when these Chi/HEP films were used to coat polystyrene films.[121] The bacterial resistant properties were also observed for the combination of Chi with other polyanions, such as HA.[35]

- *Multilayer films with COL acting as polycation*

Multilayer films based on COL, can also be employed as coatings for different materials. As in the case of Chi-based films, the use of these films as blood-compatibility materials depends on their thrombogenic potential and the hemocompatibility. In this sense, COL/HEP films has been applied to improve the blood-compatibility of titanium due to the fact that they decreased the platelet adhesion and activation, and prolonged the APTT and PT, indicating low coagulation activation. Multilayer titanium coated COL/HEP structures presented enhanced anticoagulation properties for potential applications as cardiovascular implants.[122-124] These COL/HEP multilayers have also been used to cover stainless steel coronary stents.[125] COL has also be combined with other polyanions, HA and ChS, to be employed as coatings of different materials such as, poly(L-lactic acid) (PLLA)[126, 127] and polyurethane (PU)[128] to enhanced their biocompatibility for tissue engineering applications.

Denaturalization of collagen by acid and alkaline processes gives rise to other natural polymer known as gelatin (GL). The assembly of GL and HA has been employed as a biomaterial coating, in this case for polyethylene terephthalate (PET) artificial ligament grafts. Their biocompatibility was proved either *in vitro* with human dermal fibroblast (HDF) or *in vivo* on anterior cruciate ligament reconstruction in rabbits and pigs, demonstrating that these multilayer coatings inhibited inflammatory cell infiltration and promoted new ligament tissue regeneration among the graft fibers enabling their use as coatings for ligament reconstruction applications.[129]

Although LbL films obtained from natural polymers have been mainly employed as coatings for tissue engineering, they have also been used as platforms for cell adhesion and drug delivery applications.

Platforms for studying cell adhesion

The main factors that influence cell adhesion on LbL films are crosslinking degree, pH of assembly, number of deposited layers and nature of the ending layer. Multilayer PLL/HA films crosslinked using the carbodiimide chemistry showed an improved cell adhesion, whereas the native films were highly cell antiadhesive.[97] This increase on cell adhesion is due to the increase of the film rigidity after crosslinking as has been shown for different kinds of cells.[99, 130-133] Cell adhesion is also influenced by the swelling behavior. Multilayer PLL/PGA films built up at basic pH shrank in contact with salt containing solutions were found to be highly cell adhesive, whereas those assembled at acidic pH swelled being highly cell resistant.[91] The cerebral cortical NSPCs cell adhesion on these films achieved large neural network size and a large number of functional neurons making them accurate for neural regeneration.[134] The number of deposited bilayers and the nature of the ending layer influenced the cell adhesion. Cell adhesion was more favorable on multilayer PLL/HA films than PLL/ChS films.[81] Cell adhesion can be enhanced by the presence of growth factors (bFGF) into the multilayer structure. In this regards, it was proven that the incorporation of bFGF into PLL/ChS and PLL/HA films gave rise to an increase in the number of adhered cells.[81]

As in the case of PLL-based films, the crosslinking degree influences the cell adhesion on Chi-based films. Multilayer Chi/HA and Chi/Alg films crosslinked using the carbodiimide chemistry possessed enhanced cell adhesion due to the increase of their stiffness.[98-100] The influence of the surface chemistry and the number of bilayers on cell adhesion was studied for the system Chi/Alg showing that Alg ending films were more adhesive to these ones with Chi as outermost layer and cell adhesion increased with the number of bilayers.[93, 94] The effect of the modification

of HA with dopamine (HA-DN) in the multilayer assembly with Chi has been explored and compared with Chi/HA films, showing that Chi/HA-DN films possessed enhanced cell adhesion, proliferation and viability.[116, 135]

COL/Alg films possess excellent properties for cellular adhesion and proliferation of human umbilical vein endothelial cells (HUVEC) promoting its use as cell stimulating materials to coat prostheses for *in vivo* applications such as inner lining of lumens for vascular and tracheal implants.[17] The cell adhesion is greatly influenced by the nature of the outermost layer. *In vitro* experiments with diverse kinds of cells, such as chondrocytes and chondrosarcoma cells, in different films with collagen acting as polycation, COL/HA, COL/ChS and COL/HEP, proved that films promoted excellent cell adhesion when COL was the outermost layer providing insight into the use of these multilayer films for biomedical applications.[87, 88]

A schematic representation of cell adhesion in multilayer polymer films obtained from natural polymer is illustrated in Figure 2.12.

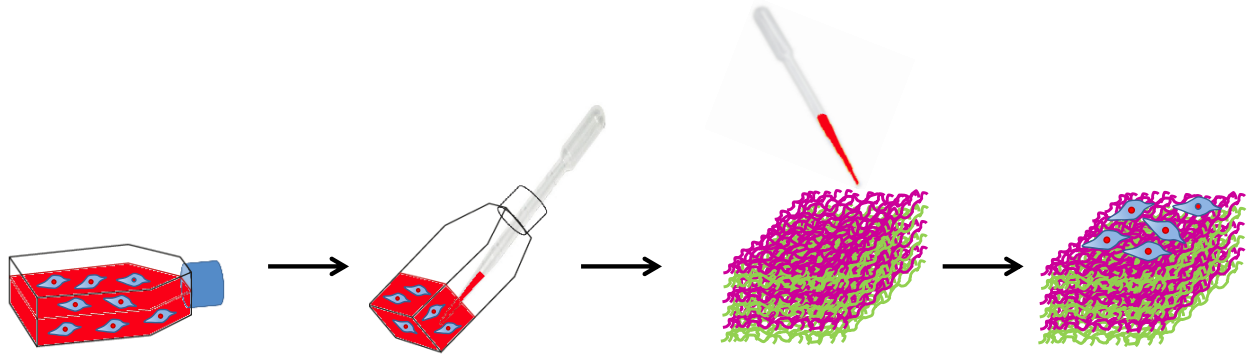

Figure 2.12. Schematic representation of cell adhesion on LbL films from natural polymers.

Materials for drug delivery

The possibility of incorporating different therapeutic agents into multilayer films is of vital importance to treat diverse diseases. In this context, these films have been employed to load antitumor therapeutic agents, such as sodium diclofenac and paclitaxel, and anti-inflammatory drugs, such as piroxicam (Px), inside films with different number of bilayers.[99, 136] Multilayer PLL/HA films loaded with antitumor drugs showed a decrease of human colonic adenocarcinoma HT29 cell viability over three days[99] and PLL/PGA films loaded with the anti-inflammatory drug showed an anti-inflammatory activity controlled over different times by adjusting the multilayer architecture.[136]

Multilayer Chi/Alg systems have also been evaluated as drug delivery patches. For that purpose, latanoprost, an antiglaucoma ophthalmic drug, was loaded into the multilayer structure to study their effect *in vitro* and *in vivo* proving that this pad reduced the intraocular pressure (IOP) in patients with glaucoma disease.[137] Other therapeutic agent, adenosine deaminase inhibitor, was loaded in an intermediate position of this multilayer film to study its release which was attributed to a diffusion controlled mechanism. This free-standing nanofilm could act as a nanopatch for targeted anti-inflammatory drug delivery to treat localized pathologies as inflammatory bowel disease.[138] Antitumor drugs, such as sodium diclofenac and paclitaxel, have also be incorporated into Chi/HA films giving rise to a reduction of human colonic adenocarcinoma HT29 cell viability over three days in contact with these loaded films.[99] Furthermore, these Chi/HA multilayers were evaluated to act as localized drug delivery systems promoting the artery healing process, incorporating L-arginine into the multilayer structure. Results showed that these films improved its protective effect against platelet adhesion, as compared to arteries protected by a film without L-arginine.[119]

There are different factors such as the number of bilayers, the pH of the drug loading solution and the ionic strength of solution, which influence the drugs load capacity into multilayer films by diffusion. Multilayer Chi/HA films were immersed in myoglobin (Mb) solution at pH 5.0 giving rise to a gradual load of Mb into the films. Thicker films could load more Mb and the incorporated Mb took longer time to reach the equilibrium. Positively charged Mb at pH 5.0 demonstrates more loading amount than negatively charged Mb at pH 9.0 and neutral Mb at pH 7.0 showing that the main driving force for the bulk loading of Mb was most probably the electrostatic interaction between oppositely charged Mb in solution and HA in the films, while other interactions such as hydrogen bonding and hydrophobic interaction may also play an important role. The ionic strength or the concentration of NaCl in the Mb loading solution also influenced the loading behavior. As the ionic strength of Mb loading solution increased, the quantity of Mb loaded increased and the corresponding loading time decreased.[139]

A brief schematic representation regarding the employment of LbL films obtained from natural polymers as platforms for drug delivery is shown in Figure 2.13.

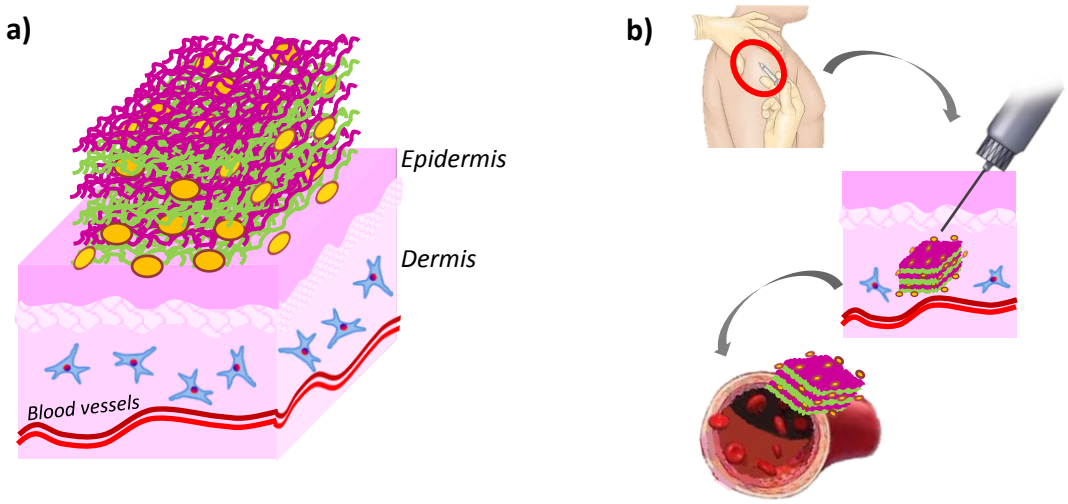

Figure 2.13. Schematic representation of multilayer films employed as patches for a) transdermal and b) injectable drug delivery applications.

2.2.3. Nanocomposite LbL systems based on natural polymers and biomedical applications

The LbL deposition method can be applied not only to polymers, but also to combinations of polymers and nanoparticles. Almost any type of charged species, including inorganic molecular clusters, nanoparticles, nanotubes and nanowires, can be successfully used as components to prepare LbL nanocomposite films.[140]

The first multilayer films with nanoparticles built up via LbL assembly was developed in 1995 by Kotov et al.[141] who fabricated ordered nanostructured films, composed of alternative layers of cationic poly(diallylmethylammonium chloride) and different negatively charged semiconductor particles, thiol and sodium hexametaphosphate-stabilized lead sulfide (PbS), titanium dioxide ($Ti0_2$), and cadmium sulfide (CdS) particles. They showed the existence of a marked dependence on the sequence in which the CdS and $Ti0_2$ particles were layered. This discovery together with an accurate selection of components has given rise to nanostructured films with the desired mechanical, optical, electrical and magnetic properties.[142, 143]

However, there are few reports regarding nanocomposite films based on natural polymers with organic and inorganic nanoparticles embedded.

Nanocomposite multilayer films of chitosan and hyaluronic acid with polyelectrolyte complex nanoparticles (PCNs) made of chitosan and heparin incorporated have been developed. The homogeneously PCNs distributed on and into multilayer films were employed to introduce

discrete nanoscale surface topographical features and varying surface chemistry into the multilayer films in a controlled way. In addition, the position of the PCNs normal to the surface can be adjusted by the number of polymer layers added on top of adsorbed PCNs.[144] Very recently, multilayer nanostructured biomimetic nanocomposite films similar to the extracellular matrix (ECM) containing the arginine-glycine-aspartate (RGD) sequence and growth factors for promoting cell adhesion and osteoinductivity have been explored. So that, RGD grafted oxidized sodium alginate (OAlg), denoted as RGD-OAlg, and chitosan (Chi) were assembled into multilayer films and chitosan-coated bovine serum albumin nanoparticles were encapsulated giving rise to biomimetic ECM coatings with enhanced osteoinductivity *in vitro* and *in vivo* for applications in bone formation.[145]

Regarding inorganic nanoparticles, silver, gold and magnetite nanoparticles have been incorporated into multilayer films based on natural polymers.[146-149]

Silver nanoparticles (Ag-NPs) have high toxicity to microorganisms and low toxicity to animal cells. This antimicrobial activity makes them promising candidates for antimicrobial coatings. The potential of multilayer films containing silver NPs to be used as antimicrobial coatings depends on the silver content in the multilayer, which in turn can be modulated via multiple depositions of silver NPs layers.[150] The hydrophilicity, antibacterial activity, hemocompatibility, and cytocompatibility of poly(L-lactic acid) (PLLA) were improved through dipping assisted LbL deposition of chitosan (Chi) and dextran sulfate-stabilized silver nanoparticles onto a PLLA membrane. The multilayer film resisted platelet adhesion and human plasma fibrinogen adsorption, while prolonging the blood coagulation time proving their hemocompatibility. It also possessed antibacterial activity and improved proliferation and viability of human endothelial cells (ECs). These characteristics turn it into a good antithrombogenic coating for hemodialysis devices.[146] Multilayer coatings for Ti surfaces, based on dipping LbL assembly of HA and chitosan-silver nanoparticles (Chi-AgNPs), have also been developed exhibiting relatively long-term antibacterial efficacy and favorable biocompatibility to prevent implant associated infection and facilitate osseointegration in the early stage of implantation. Furthermore, this multilayer coating could serve as the base layer to fabricate coatings for other medical devices such as catheters, wound dressing and bone cements.[147]

Gold nanoparticles (Au-NPs) are relatively inert in the biological environment and have diverse physical properties which make them suitable for multiple biomedical applications such as biosensors, photothermolysis of cancer cells and tumors, targeted delivery of drugs and antigens,

optical imaging of cells and tissues, immunoassays and clinical chemistry.[151, 152] In this sense, nanocomposite multilayer platforms based on the spin LbL assembly of chitosan and alginate incorporating core-shell nanoparticles of gold coated with poly(vinylpyrrolidone) (PVP) have been evaluated for photothermal ablative applications.[148]

Magnetic nanoparticles (NPs) have the ability to response to applied magnetic fields and can be used for diverse applications such as magnetic separation, therapeutic vehicles for drug delivery, heat carriers in hyperthermia treatments and visualization agents in magnetic resonance imaging.[153, 154] Recently, nanocomposite multilayered films based on alternate assembly of alginate and chitosan with magnetic nanoparticles (NPs) incorporated into the structure have been fabricated through dipping LbL giving rise to films with 500 bilayers Chi/Alg and only 5 NPs layers. The inclusion of NPs affected and enhanced L929 fibroblasts cell behavior *in vitro* and, at the same time, they provided magnetic properties to these films. These characteristics made them accurate for potential biomedical applications as contrast agents for magnetic resonance imaging, local drug delivery or hyperthermia-based therapy.[149]

The incorporation of calcium phosphate into multilayer coatings is used for bone tissue engineering to improve implant osseointegration leading to a tight and stable junction between the implant and host bone. For that purpose, calcium chloride ($CaCl_2$) and ammonium phosphate dibasic ($(NH_4)_2HPO_4$) solutions were put into contact with Chi/ChS films giving rise to the formation of calcium phosphate precipitates (CaP) into the multilayers due to the fact that multilayers could trap Ca^{2+} and PO_4^{3-} ions by ionic change giving rise to favorable nucleation sites to initiate the precipitation of CaP. Chi/ChS multilayers acted as a template for calcification to develop biomimetic structures for potential orthopedic applications.[155]

A summary about bibliography data of different multilayer systems based on natural polymers with PLL, Chi, COL and GL as polycations is shown in Table 2.2 which collects the kind of LbL assembly technique employed, studies carried out and potential biomedical applications.

Table 2.2. Studies of multilayer films based on natural polymers with PLL, Chi, COL and GL as polycations, kind of LbL assembly technique employed and potential biomedical application.

PC	PA	Study	Method	Potential application	Refs
PLL	Alg	Growth Crosslinking *In vitro* experiments	Dipping	Wound healing Barriers on biological surfaces	78, 106, 156
	HA	Growth Crosslinking Mechanical properties Free-standing *In vitro* studies	Dipping	Bioactive films Biomaterial coating for tissue engineering Reservoir for growth factors	4, 27, 58, 81-83, 96, 97, 99, 100, 107, 130-133, 157
		Growth Crosslinking Coating of scaffolds *In vitro* studies Formation of Alg gel into the multilayer structure	Spray	Coatings Scaffolds to act as reservoir	9, 111, 112
		Growth Comparison dipping vs. spray	Dipping Spray	-	61, 89
	ChS	Growth *In vitro* studies	Dipping	Reservoir for growth factors	81, 96
	HEP	Growth Dissolution, controlled HEP release	Dipping	controlled local drug delivery	96, 158
	PGA	Growth Crosslinking *In vitro* studies	Dipping	Tissue engineering Biosensors Anti-inflammatory properties	80, 84, 90, 91, 108-110, 134, 136, 159-161
			Spray		112
Chi	HA	Growth Crosslinking Mechanical properties Free-standing Vascular diffusion of HA Drug delivery Thromboresistance studies Haemocompatibility *In vitro* studies *Ex vivo* stability	Dipping	Antimicrobial coatings Tissue engineering Reduce the neointimal hyperplasia associated with stent implantation Wound healing	16, 35, 39, 44, 99, 100, 103, 116, 117, 119, 135, 139, 162
	Alg	Growth Crosslinking Mechanical properties Free-standing Drug delivery Permeability pH-responsiveness *In vitro* studies Shape memory	Dipping	Drug delivery, biosensors, diagnostics and biomimetic implantable membranes for tissue engineering	25, 93, 94, 98, 101, 102, 117, 118, 135, 163, 164

Chi		Growth Adhesive and mechanical properties Free-standing Drug delivery Skin adhesion *In vivo* studies *Ex vivo* studies	Spin	Drug delivery Antiglaucoma pads anti-inflammatory pads Tissue engineering	79, 137, 138, 165
	HEP	Growth Viscoelastic properties Coagulation assay Drug delivery *In vitro* experiments	Dipping	Anti-infection coatings, re-endothelialization and intimal healing for implants	34, 44, 85, 86, 92, 113-115, 120, 121
	Dex	Growth Coagulation assay	Dipping	Coating materials in contact with blood	34
	ChS	Growth Interactions		Bioactive patches Tissue engineering	44, 155
	PGA	Growth	Dipping	-	95, 166
COL	HA	Growth Crosslinking *In vitro* studies Coating of PLLA	Dipping	Coating prostheses Bone regeneration Artificial extracellular matrixes	87, 104, 126
	HEP	Growth Hemocompatibility *In vitro* studies Adhesion test	Dipping	In situ endothelialization of blood contacting materials Coating titanium for cardiovascular implants Tissue engineering	88, 122-125
	ChS	Growth Crosslinking *In vitro* studies Coating of PU	Dipping	Coatings Cartilage tissue engineering	88, 127, 128
	Alg	Growth Crosslinking *In vitro* studies	Dipping	Coating prostheses	17
GL	HA	Modify polyethylene terephthalate (PET) artificial ligament grafts Mechanical properties *In vitro* studies *In vivo* experiments	Dipping	Substitutes for ligament reconstruction	129

As conclusion, it is worth to mention that most multilayer systems based on natural polymers reported on literature have been assembled by dipping LbL, a time consuming technique which is not appropriate to scale at industrial level. In this regards, in this PhD work the development of different polymer systems will be carried out by spray assisted LbL, a saving-time technique, whenever possible. There are few studies regarding to the incorporation of nanoparticles into natural multilayer films and, therefore, a scarce literature concerning to the study of their nanomechanical properties and inner structure. Although there are diverse works reporting the characteristics and properties of natural multilayer systems, few of them proved the final application of the developed materials. In this sense, the incorporation of magnetic nanoparticles into Alg/Chi films will be carried out to study their nanomechanical properties and their application in magnetic hyperthermia therapies. Cell adhesion is modulated by several parameters as shown in bibliography. Considering the multiples advantages of employing natural polymers for biomedical applications, cellular adhesion of different kinds of cells will be carried out on multilayer Alg/Chi films.

2.3. REFERENCES

1. Xiao, F.-X.; Pagliaro, M.; Xu, Y.-J.; Liu, B., Layer-by-layer assembly of versatile nanoarchitectures with diverse dimensionality: a new perspective for rational construction of multilayer assemblies. *Chemical Society Reviews* **2016,** 45, (11), 3088-3121.

2. Michel, M.; Toniazzo, V.; Ruch, D.; Ball, V., Deposition mechanisms in layer-by-layer or step-by-step deposition methods: From elastic and impermeable films to soft membranes with ion exchange properties. *ISRN Materials Science* **2012,** 2012.

3. Decher, G., Fuzzy Nanoassemblies: Toward Layered Polymeric Multicomposites. *Science* **1997,** 277, (5330), 1232.

4. Lavalle, P.; Boulmedais, F.; Ball, V.; Mutterer, J.; Schaaf, P.; Voegel, J.-C., Free standing membranes made of biocompatible polyelectrolytes using the layer by layer method. *Journal of Membrane Science* **2005,** 253, (1–2), 49-56.

5. Jiang, C.; Tsukruk, V. V., Freestanding Nanostructures via Layer-by-Layer Assembly. *Advanced Materials* **2006,** 18, (7), 829-840.

6. Aharinejad, S. H.; Lametschwandtner, A., Fundamentals of Scanning Electron Microscopy. In *Microvascular Corrosion Casting in Scanning Electron Microscopy*, Springer: Wien, 1992; pp 44-51.

7. Yan, S.; Rao, S.; Zhu, J.; Wang, Z.; Zhang, Y.; Duan, Y.; Chen, X.; Yin, J., Nanoporous multilayer poly(l-glutamic acid)/chitosan microcapsules for drug delivery. *International Journal of Pharmaceutics* **2012,** 427, (2), 443-451.

8. Feng, W.; Nie, W.; He, C.; Zhou, X.; Chen, L.; Qiu, K.; Wang, W.; Yin, Z., Effect of pH-Responsive Alginate/Chitosan Multilayers Coating on Delivery Efficiency, Cellular Uptake and Biodistribution of Mesoporous Silica Nanoparticles Based Nanocarriers. *ACS Applied Materials & Interfaces* **2014,** 6, (11), 8447-8460.

9. Monteiro, I. P.; Shukla, A.; Marques, A. P.; Reis, R. L.; Hammond, P. T., Spray-assisted layer-by-layer assembly on hyaluronic acid scaffolds for skin tissue engineering. *Journal of Biomedical Materials Research Part A* **2015,** 103, (1), 330-340.

10. Zhu, Y.; Gao, C.; He, T.; Liu, X.; Shen, J., Layer-by-Layer Assembly To Modify Poly(l-lactic acid) Surface toward Improving Its Cytocompatibility to Human Endothelial Cells. *Biomacromolecules* **2003,** 4, (2), 446-452.

11. Vautier, D.; Hemmerlé, J.; Vodouhe, C.; Koenig, G.; Richert, L.; Picart, C.; Voegel, J.-C.; Debry, C.; Chluba, J.; Ogier, J., 3-D surface charges modulate protrusive and contractile contacts of chondrosarcoma cells. *Cell Motility and the Cytoskeleton* **2003,** 56, (3), 147-158.

12. Iler, R. K., Multilayers of colloidal particles. *Journal of Colloid and Interface Science* **1966,** 21, (6), 569-594.

13. Decher, G.; Hong, J.-D., Buildup of ultrathin multilayer films by a self-assembly process, 1 consecutive adsorption of anionic and cationic bipolar amphiphiles on charged surfaces. *Makromolekulare Chemie. Macromolecular Symposia* **1991,** 46, (1), 321-327.

14. Decher, G.; Hong, J. D.; Schmitt, J., Buildup of ultrathin multilayer films by a self-assembly process: III. Consecutively alternating adsorption of anionic and cationic polyelectrolytes on charged surfaces. *Thin Solid Films* **1992,** 210, 831-835.

15. de Villiers, M. M.; Otto, D. P.; Strydom, S. J.; Lvov, Y. M., Introduction to nanocoatings produced by layer-by-layer (LbL) self-assembly. *Advanced Drug Delivery Reviews* **2011,** 63, (9), 701-715.

16. Thierry, B.; Winnik, F. M.; Merhi, Y.; Silver, J.; Tabrizian, M., Bioactive Coatings of Endovascular Stents Based on Polyelectrolyte Multilayers. *Biomacromolecules* **2003,** 4, (6), 1564-1571.

17. Chaubaroux, C.; Vrana, E.; Debry, C.; Schaaf, P.; Senger, B.; Voegel, J.-C.; Haikel, Y.; Ringwald, C.; Hemmerlé, J.; Lavalle, P.; Boulmedais, F., Collagen-Based Fibrillar Multilayer Films Cross-Linked by a Natural Agent. *Biomacromolecules* **2012,** 13, (7), 2128-2135.

18. Cassagneau, T.; Fendler, J. H., High density rechargeable lithium- ion batteries self- assembled from graphite oxide nanoplatelets and polyelectrolytes. *Advanced Materials* **1998,** 10, (11), 877-881.

19. Jiang, S. P.; Liu, Z.; Tian, Z. Q., Layer-by-Layer Self-Assembly of Composite Polyelectrolyte–Nafion Membranes for Direct Methanol Fuel Cells. *Advanced Materials* **2006,** 18, (8), 1068-1072.

20. Nuraje, N.; Asmatulu, R.; Cohen, R. E.; Rubner, M. F., Durable Antifog Films from Layer-by-Layer Molecularly Blended Hydrophilic Polysaccharides. *Langmuir* **2011,** 27, (2), 782-791.

21. Kyung, K.-H.; Fujimoto, K.; Shiratori, S., Control of structure and film thickness using spray layer-by-layer method: application to double-layer anti-reflection film. *Japanese Journal of Applied Physics* **2011,** 50, (3R), 035803.

22. Pan, H.; Song, L.; Ma, L.; Pan, Y.; Liew, K. M.; Hu, Y., Layer-by-layer assembled thin films based on fully biobased polysaccharides: chitosan and phosphorylated cellulose for flame-retardant cotton fabric. *Cellulose* **2014,** 21, (4), 2995-3006.

23. Andreeva, D. V.; Fix, D.; Möhwald, H.; Shchukin, D. G., Self-Healing Anticorrosion Coatings Based on pH-Sensitive Polyelectrolyte/Inhibitor Sandwichlike Nanostructures. *Advanced Materials* **2008,** 20, (14), 2789-2794.

24. Borges, J.; Mano, J. F., Molecular Interactions Driving the Layer-by-Layer Assembly of Multilayers. *Chemical reviews* **2014,** 114, (18), 8883-8942.

25. Silva, J. M.; Caridade, S. G.; Costa, R. R.; Alves, N. M.; Groth, T.; Picart, C.; Reis, R. L.; Mano, J. F., pH Responsiveness of Multilayered Films and Membranes Made of Polysaccharides. *Langmuir* **2015,** 31, (41), 11318-11328.

26. Shiratori, S. S.; Rubner, M. F., pH-Dependent Thickness Behavior of Sequentially Adsorbed Layers of Weak Polyelectrolytes. *Macromolecules* **2000,** 33, (11), 4213-4219.

27. Burke, S. E.; Barrett, C. J., pH-Responsive Properties of Multilayered Poly(l-lysine)/Hyaluronic Acid Surfaces. *Biomacromolecules* **2003,** 4, (6), 1773-1783.

28. Lvov, Y.; Decher, G.; Moehwald, H., Assembly, structural characterization, and thermal behavior of layer-by-layer deposited ultrathin films of poly(vinyl sulfate) and poly(allylamine). *Langmuir* **1993,** 9, (2), 481-486.

29. Tan, H. L.; McMurdo, M. J.; Pan, G.; Van Patten, P. G., Temperature Dependence of Polyelectrolyte Multilayer Assembly. *Langmuir* **2003,** 19, (22), 9311-9314.

30. Büscher, K.; Graf, K.; Ahrens, H.; Helm, C. A., Influence of Adsorption Conditions on the Structure of Polyelectrolyte Multilayers. *Langmuir* **2002,** 18, (9), 3585-3591.

31. Poptoshev, E.; Schoeler, B.; Caruso, F., Influence of Solvent Quality on the Growth of Polyelectrolyte Multilayers. *Langmuir* **2004,** 20, (3), 829-834.

32. Dubas, S. T.; Schlenoff, J. B., Factors Controlling the Growth of Polyelectrolyte Multilayers. *Macromolecules* **1999,** 32, (24), 8153-8160.

33. Salomäki, M.; Laiho, T.; Kankare, J., Counteranion-Controlled Properties of Polyelectrolyte Multilayers. *Macromolecules* **2004,** 37, (25), 9585-9590.

34. Serizawa, T.; Yamaguchi, M.; Akashi, M., Alternating Bioactivity of Polymeric Layer-by-Layer Assemblies: Anticoagulation vs Procoagulation of Human Blood. *Biomacromolecules* **2002,** 3, (4), 724-731.

35. Richert, L.; Lavalle, P.; Payan, E.; Shu, X. Z.; Prestwich, G. D.; Stoltz, J.-F.; Schaaf, P.; Voegel, J.-C.; Picart, C., Layer by Layer Buildup of Polysaccharide Films: Physical Chemistry and Cellular Adhesion Aspects. *Langmuir* **2004,** 20, (2), 448-458.

36. Salomäki, M.; Tervasmäki, P.; Areva, S.; Kankare, J., The Hofmeister Anion Effect and the Growth of Polyelectrolyte Multilayers. *Langmuir* **2004,** 20, (9), 3679-3683.

37. Buron, C. C.; Filiâtre, C.; Membrey, F.; Bainier, C.; Buisson, L.; Charraut, D.; Foissy, A., Surface morphology and thickness of a multilayer film composed of strong and weak polyelectrolytes: Effect of the number of adsorbed layers, concentration and type of salts. *Thin Solid Films* **2009,** 517, (8), 2611-2617.

38. Schlenoff, J. B.; Ly, H.; Li, M., Charge and Mass Balance in Polyelectrolyte Multilayers. *Journal of the American Chemical Society* **1998,** 120, (30), 7626-7634.

39. Kujawa, P.; Moraille, P.; Sanchez, J.; Badia, A.; Winnik, F. M., Effect of Molecular Weight on the Exponential Growth and Morphology of Hyaluronan/Chitosan Multilayers: A Surface Plasmon Resonance Spectroscopy and Atomic Force Microscopy Investigation. *Journal of the American Chemical Society* **2005,** 127, (25), 9224-9234.

40. Soltwedel, O.; Nestler, P.; Neumann, H.-G.; Paßvogel, M.; Köhler, R.; Helm, C. A., Influence of Polycation (PDADMAC) Weight on Vertical Diffusion within Polyelectrolyte Multilayers during Film Formation and Postpreparation Treatment. *Macromolecules* **2012,** 45, (19), 7995-8004.

41. Koetse, M.; Laschewsky, A.; Jonas, A. M.; Wagenknecht, W., Influence of Charge Density and Distribution on the Internal Structure of Electrostatically Self-assembled Polyelectrolyte Films. *Langmuir* **2002,** 18, (5), 1655-1660.

42. Choi, J.; Rubner, M. F., Influence of the Degree of Ionization on Weak Polyelectrolyte Multilayer Assembly. *Macromolecules* **2005,** 38, (1), 116-124.

43. Liu, G.; Zou, S.; Fu, L.; Zhang, G., Roles of Chain Conformation and Interpenetration in the Growth of a Polyelectrolyte Multilayer. *The Journal of Physical Chemistry B* **2008,** 112, (14), 4167-4171.

44. Almodóvar, J.; Place, L. W.; Gogolski, J.; Erickson, K.; Kipper, M. J., Layer-by-Layer Assembly of Polysaccharide-Based Polyelectrolyte Multilayers: A Spectroscopic Study of Hydrophilicity, Composition, and Ion Pairing. *Biomacromolecules* **2011,** 12, (7), 2755-2765.

45. Stockton, W. B.; Rubner, M. F., Molecular-Level Processing of Conjugated Polymers. 4. Layer-by-Layer Manipulation of Polyaniline via Hydrogen-Bonding Interactions. *Macromolecules* **1997,** 30, (9), 2717-2725.

46. Kohli, P.; Blanchard, G. J., Applying Polymer Chemistry to Interfaces: Layer-by-Layer and Spontaneous Growth of Covalently Bound Multilayers. *Langmuir* **2000,** 16, (10), 4655-4661.

47. Shimazaki, Y.; Mitsuishi, M.; Ito, S.; Yamamoto, M., Preparation of the Layer-by-Layer Deposited Ultrathin Film Based on the Charge-Transfer Interaction. *Langmuir* **1997,** 13, (6), 1385-1387.

48. Crespo-Biel, O.; Dordi, B.; Reinhoudt, D. N.; Huskens, J., Supramolecular Layer-by-Layer Assembly: Alternating Adsorptions of Guest- and Host-Functionalized Molecules and Particles Using Multivalent Supramolecular Interactions. *Journal of the American Chemical Society* **2005,** 127, (20), 7594-7600.

49. Li, C.; Luo, G.-F.; Wang, H.-Y.; Zhang, J.; Gong, Y.-H.; Cheng, S.-X.; Zhuo, R.-X.; Zhang, X.-Z., Host–Guest Assembly of pH-Responsive Degradable Microcapsules with Controlled Drug Release Behavior. *The Journal of Physical Chemistry C* **2011,** 115, (36), 17651-17659.

50. Pace, C. N.; Fu, H.; Fryar, K. L.; Landua, J.; Trevino, S. R.; Shirley, B. A.; Hendricks, M. M.; Iimura, S.; Gajiwala, K.; Scholtz, J. M.; Grimsley, G. R., Contribution of Hydrophobic Interactions to Protein Stability. *Journal of molecular biology* **2011,** 408, (3), 514-528.

51. K, J.; Hsu, S. L.; McCarthy, T. J., Versatile Multilayer Thin Film Preparation Using Hydrophobic Interactions, Crystallization, and Chemical Modification of Poly(vinyl alcohol). *Langmuir* **2007,** 23, (6), 3260-3264.

52. Cassier, T.; Lowack, K.; Decher, G., Layer-by-layer assembled protein/polymer hybrid films: nanoconstruction via specific recognition. *Supramolecular Science* **1998,** 5, (3), 309-315.

53. Cheetham, A. K.; Rao, C. N. R.; Feller, R. K., Structural diversity and chemical trends in hybrid inorganic-organic framework materials. *Chemical Communications* **2006**, (46), 4780-4795.

54. Hoogeveen, N. G.; Cohen Stuart, M. A.; Fleer, G. J.; Böhmer, M. R., Formation and Stability of Multilayers of Polyelectrolytes. *Langmuir* **1996,** 12, (15), 3675-3681.

55. Izquierdo, A.; Ono, S. S.; Voegel, J. C.; Schaaf, P.; Decher, G., Dipping versus Spraying: Exploring the Deposition Conditions for Speeding Up Layer-by-Layer Assembly. *Langmuir* **2005,** 21, (16), 7558-7567.

56. Cochin, D.; Laschewsky, A., Layer- by- layer self- assembly of hydrophobically modified polyelectrolytes. *Macromolecular Chemistry and Physics* **1999,** 200, (3), 609-615.

57. von Klitzing, R.; Köhler, R.; Chenigny, C., Neutron Reflectometry at Polyelectrolyte Multilayers. In *Multilayer Thin Films*, Second ed.; Wiley-VCH: Germany, 2012; pp 219-268.

58. Picart, C.; Lavalle, P.; Hubert, P.; Cuisinier, F. J. G.; Decher, G.; Schaaf, P.; Voegel, J. C., Buildup Mechanism for Poly(l-lysine)/Hyaluronic Acid Films onto a Solid Surface. *Langmuir* **2001,** 17, (23), 7414-7424.

59. Ladam, G.; Schaad, P.; Voegel, J. C.; Schaaf, P.; Decher, G.; Cuisinier, F., In Situ Determination of the Structural Properties of Initially Deposited Polyelectrolyte Multilayers. *Langmuir* **2000,** 16, (3), 1249-1255.

60. Jomaa, H. W.; Schlenoff, J. B., Salt-Induced Polyelectrolyte Interdiffusion in Multilayered Films: A Neutron Reflectivity Study. *Macromolecules* **2005,** 38, (20), 8473-8480.

61. Porcel, C.; Lavalle, P.; Ball, V.; Decher, G.; Senger, B.; Voegel, J.-C.; Schaaf, P., From Exponential to Linear Growth in Polyelectrolyte Multilayers. *Langmuir* **2006,** 22, (9), 4376-4383.

62. Salomäki, M.; Vinokurov, I. A.; Kankare, J., Effect of Temperature on the Buildup of Polyelectrolyte Multilayers. *Langmuir* **2005,** 21, (24), 11232-11240.

63. Richardson, J. J.; Björnmalm, M.; Caruso, F., Technology-driven layer-by-layer assembly of nanofilms. *Science* **2015,** 348, (6233), aaa2491.

64. Winterton, J. V. L.; Lally, J.; Stockinger, F. Coating of polymers, Novartis AG. World Patent WO 9935520, **1999**.

65. Cho, J.; Char, K.; Hong, J. D.; Lee, K. B., Fabrication of Highly Ordered Multilayer Films Using a Spin Self-Assembly Method. *Advanced Materials* **2001,** 13, (14), 1076-1078.

66. Schlenoff, J. B.; Dubas, S. T.; Farhat, T., Sprayed Polyelectrolyte Multilayers. *Langmuir* **2000,** 16, (26), 9968-9969.

67. Schaaf, P.; Voegel, J.-C.; Jierry, L.; Boulmedais, F., Spray-Assisted Polyelectrolyte Multilayer Buildup: from Step-by-Step to Single-Step Polyelectrolyte Film Constructions. *Advanced Materials* **2012,** 24, (8), 1001-1016.

68. Porcel, C. H.; Izquierdo, A.; Ball, V.; Decher, G.; Voegel, J. C.; Schaaf, P., Ultrathin Coatings and (Poly(glutamic acid)/Polyallylamine) Films Deposited by Continuous and Simultaneous Spraying. *Langmuir* **2005,** 21, (2), 800-802.

69. Merrill, M.; Sun, C., Fast, simple and efficient assembly of nanolayered materials and devices. *Nanotechnology* **2009,** 20, (7), 075606.

70. Chiarelli, P. A.; Johal, M. S.; Casson, J. L.; Roberts, J. B.; Robinson, J. M.; Wang, H. L., Controlled Fabrication of Polyelectrolyte Multilayer Thin Films Using Spin-Assembly. *Advanced Materials* **2001,** 13, (15), 1167-1171.

71. Li, Y.; Wang, X.; Sun, J., Layer-by-layer assembly for rapid fabrication of thick polymeric films. *Chemical Society Reviews* **2012,** 41, (18), 5998-6009.

72. Vozar, S.; Poh, Y.-C.; Serbowicz, T.; Bachner, M.; Podsiadlo, P.; Qin, M.; Verploegen, E.; Kotov, N.; Hart, A. J., Automated spin-assisted layer-by-layer assembly of nanocomposites. *Review of Scientific Instruments* **2009,** 80, (2), 023903.

73. Kaplan, D. L., Introduction to biopolymers from renewable resources. In *Biopolymers from renewable resources*, Springer: Berlin, 1998; pp 1-29.

74. Malafaya, P. B.; Silva, G. A.; Reis, R. L., Natural–origin polymers as carriers and scaffolds for biomolecules and cell delivery in tissue engineering applications. *Advanced Drug Delivery Reviews* **2007,** 59, (4–5), 207-233.

75. Prasad, P. N., The human body. In *Introduction to nanomedicine and nanobioengineering*, John Wiley & Sons: Hoboken, 2012; Vol. 7, pp 15-50.

76. Rydz, J.; Sikorska, W.; Kyulavska, M.; Christova, D., Polyester-Based (Bio)degradable Polymers as Environmentally Friendly Materials for Sustainable Development. *International Journal of Molecular Sciences* **2015,** 16, (1), 564-596.

77. Follain, N.; Chivrac, F.; Girard, F.; Marais, S., Barrier Properties of Biodegradable Bacterial Polyester Films. In *Natural Polymers, Biopolymers, Biomaterials, and Their Composites, Blends, and IPNs*, Apple Academic Press: 2012; pp 61-78.

78. Elbert, D. L.; Herbert, C. B.; Hubbell, J. A., Thin Polymer Layers Formed by Polyelectrolyte Multilayer Techniques on Biological Surfaces. *Langmuir* **1999,** 15, (16), 5355-5362.

79. Fujie, T.; Okamura, Y.; Takeoka, S., Ubiquitous Transference of a Free-Standing Polysaccharide Nanosheet with the Development of a Nano-Adhesive Plaster. *Advanced Materials* **2007,** 19, (21), 3549-3553.

80. Lavalle, P.; Gergely, C.; Cuisinier, F. J. G.; Decher, G.; Schaaf, P.; Voegel, J. C.; Picart, C., Comparison of the Structure of Polyelectrolyte Multilayer Films Exhibiting a Linear and an Exponential Growth Regime: An in Situ Atomic Force Microscopy Study. *Macromolecules* **2002,** 35, (11), 4458-4465.

81. Tezcaner, A.; Hicks, D.; Boulmedais, F.; Sahel, J.; Schaaf, P.; Voegel, J.-C.; Lavalle, P., Polyelectrolyte Multilayer Films as Substrates for Photoreceptor Cells. *Biomacromolecules* **2006,** 7, (1), 86-94.

82. Picart, C.; Mutterer, J.; Richert, L.; Luo, Y.; Prestwich, G. D.; Schaaf, P.; Voegel, J. C.; Lavalle, P., Molecular basis for the explanation of the exponential growth of polyelectrolyte multilayers. *Proceedings of the National Academy of Sciences of the United States of America* **2002,** 99, (20), 12531-12535.

83. Picart, C.; Mutterer, J.; Arntz, Y.; Voegel, J.-C.; Schaaf, P.; Senger, B., Application of fluorescence recovery after photobleaching to diffusion of a polyelectrolyte in a multilayer film. *Microscopy Research and Technique* **2005,** 66, (1), 43-57.

84. Lavalle, P.; Vivet, V.; Jessel, N.; Decher, G.; Voegel, J.-C.; Mesini, P. J.; Schaaf, P., Direct Evidence for Vertical Diffusion and Exchange Processes of Polyanions and Polycations in Polyelectrolyte Multilayer Films. *Macromolecules* **2004,** 37, (3), 1159-1162.

85. Lundin, M.; Solaqa, F.; Thormann, E.; Macakova, L.; Blomberg, E., Layer-by-Layer Assemblies of Chitosan and Heparin: Effect of Solution Ionic Strength and pH. *Langmuir* **2011,** 27, (12), 7537-7548.

86. Lundin, M.; Blomberg, E.; Tilton, R. D., Polymer Dynamics in Layer-by-Layer Assemblies of Chitosan and Heparin. *Langmuir* **2010,** 26, (5), 3242-3251.

87. Zhang, J.; Senger, B.; Vautier, D.; Picart, C.; Schaaf, P.; Voegel, J.-C.; Lavalle, P., Natural polyelectrolyte films based on layer-by layer deposition of collagen and hyaluronic acid. *Biomaterials* **2005,** 26, (16), 3353-3361.

88. Mhanna, R. F.; Vörös, J.; Zenobi-Wong, M., Layer-by-Layer Films Made from Extracellular Matrix Macromolecules on Silicone Substrates. *Biomacromolecules* **2011,** 12, (3), 609-616.

89. Porcel, C.; Lavalle, P.; Decher, G.; Senger, B.; Voegel, J. C.; Schaaf, P., Influence of the Polyelectrolyte Molecular Weight on Exponentially Growing Multilayer Films in the Linear Regime. *Langmuir* **2007,** 23, (4), 1898-1904.

90. Zhou, J.; Wang, B.; Tong, W.; Maltseva, E.; Zhang, G.; Krastev, R.; Gao, C.; Möhwald, H.; Shen, J., Influence of assembling pH on the stability of poly(l-glutamic acid) and poly(l-lysine) multilayers against urea treatment. *Colloids and Surfaces B: Biointerfaces* **2008,** 62, (2), 250-257.

91. Richert, L.; Arntz, Y.; Schaaf, P.; Voegel, J.-C.; Picart, C., pH dependent growth of poly(L-lysine)/poly(L-glutamic) acid multilayer films and their cell adhesion properties. *Surface Science* **2004,** 570, (1–2), 13-29.

92. Boddohi, S.; Killingsworth, C. E.; Kipper, M. J., Polyelectrolyte Multilayer Assembly as a Function of pH and Ionic Strength Using the Polysaccharides Chitosan and Heparin. *Biomacromolecules* **2008,** 9, (7), 2021-2028.

93. Caridade, S. G.; Monge, C.; Gilde, F.; Boudou, T.; Mano, J. F.; Picart, C., Free-Standing Polyelectrolyte Membranes Made of Chitosan and Alginate. *Biomacromolecules* **2013,** 14, (5), 1653-1660.

94. Deng, H.; Zhou, X.; Wang, X.; Zhang, C.; Ding, B.; Zhang, Q.; Du, Y., Layer-by-layer structured polysaccharides film-coated cellulose nanofibrous mats for cell culture. *Carbohydrate polymers* **2010,** 80, (2), 474-479.

95. Serizawa, T.; Goto, H.; Kishida, A.; Endo, T.; Akashi, M., Improved alternate deposition of biodegradable naturally occurring polymers onto a quartz crystal microbalance. *Journal of Polymer Science Part A: Polymer Chemistry* **1999,** 37, (6), 801-804.

96. Crouzier, T.; Picart, C., Ion Pairing and Hydration in Polyelectrolyte Multilayer Films Containing Polysaccharides. *Biomacromolecules* **2009,** 10, (2), 433-442.

97. Richert, L.; Boulmedais, F.; Lavalle, P.; Mutterer, J.; Ferreux, E.; Decher, G.; Schaaf, P.; Voegel, J.-C.; Picart, C., Improvement of Stability and Cell Adhesion Properties of Polyelectrolyte Multilayer Films by Chemical Cross-Linking. *Biomacromolecules* **2004,** 5, (2), 284-294.

98. Silva, J. M.; Duarte, A. R. C.; Caridade, S. G.; Picart, C.; Reis, R. L.; Mano, J. F., Tailored Freestanding Multilayered Membranes Based on Chitosan and Alginate. *Biomacromolecules* **2014,** 15, (10), 3817-3826.

99. Schneider, A.; Vodouhê, C.; Richert, L.; Francius, G.; Le Guen, E.; Schaaf, P.; Voegel, J.-C.; Frisch, B.; Picart, C., Multifunctional Polyelectrolyte Multilayer Films: Combining Mechanical Resistance, Biodegradability, and Bioactivity. *Biomacromolecules* **2007,** 8, (1), 139-145.

100. Boudou, T.; Crouzier, T.; Auzély-Velty, R.; Glinel, K.; Picart, C., Internal Composition versus the Mechanical Properties of Polyelectrolyte Multilayer Films: The Influence of Chemical Cross-Linking. *Langmuir* **2009,** 25, (24), 13809-13819.

101. Martins, G. V.; Mano, J. F.; Alves, N. M., Nanostructured self-assembled films containing chitosan fabricated at neutral pH. *Carbohydrate polymers* **2010,** 80, (2), 570-573.

102. Silva, J. M.; Caridade, S. G.; Reis, R. L.; Mano, J. F., Polysaccharide-based freestanding multilayered membranes exhibiting reversible switchable properties. *Soft Matter* **2016,** 12, (4), 1200-1209.

103. Picart, C.; Schneider, A.; Etienne, O.; Mutterer, J.; Schaaf, P.; Egles, C.; Jessel, N.; Voegel, J. C., Controlled Degradability of Polysaccharide Multilayer Films In Vitro and In Vivo. *Advanced Functional Materials* **2005,** 15, (11), 1771-1780.

104. Johansson, J. Å.; Halthur, T.; Herranen, M.; Söderberg, L.; Elofsson, U.; Hilborn, J., Build-up of Collagen and Hyaluronic Acid Polyelectrolyte Multilayers. *Biomacromolecules* **2005,** 6, (3), 1353-1359.

105. Beneke, E. C.; Viljoen, M. A.; Hamman, H. J., Polymeric Plant-derived Excipients in Drug Delivery. *Molecules* **2009,** 14, (7).

106. Kunjukunju, S.; Roy, A.; Ramanathan, M.; Lee, B.; Candiello, J. E.; Kumta, P. N., A layer-by-layer approach to natural polymer-derived bioactive coatings on magnesium alloys. *Acta Biomaterialia* **2013,** 9, (10), 8690-8703.

107. Wang, X.; Ji, J., Postdiffusion of Oligo-Peptide within Exponential Growth Multilayer Films for Localized Peptide Delivery. *Langmuir* **2009,** 25, (19), 11664-11671.

108. Dierich, A.; Le Guen, E.; Messaddeq, N.; Stoltz, J. F.; Netter, P.; Schaaf, P.; Voegel, J. C.; Benkirane-Jessel, N., Bone Formation Mediated by Synergy-Acting Growth Factors Embedded in a Polyelectrolyte Multilayer Film. *Advanced Materials* **2007,** 19, (5), 693-697.

109. Jessel, N.; Atalar, F.; Lavalle, P.; Mutterer, J.; Decher, G.; Schaaf, P.; Voegel, J. C.; Ogier, J., Bioactive Coatings Based on a Polyelectrolyte Multilayer Architecture Functionalized by Embedded Proteins. *Advanced Materials* **2003,** 15, (9), 692-695.

110. Benkirane-Jessel, N.; Lavalle, P.; Meyer, F.; Audouin, F.; Frisch, B.; Schaaf, P.; Ogier, J.; Decher, G.; Voegel, J. C., Control of Monocyte Morphology on and Response to Model Surfaces for Implants Equipped with Anti-Inflammatory Agent. *Advanced Materials* **2004,** 16, (17), 1507-1511.

111. Mjahed, H.; Porcel, C.; Senger, B.; Chassepot, A.; Netter, P.; Gillet, P.; Decher, G.; Voegel, J.-C.; Schaaf, P.; Benkirane-Jessel, N.; Boulmedais, F., Micro-stratified architectures based on successive stacking of alginate gel layers and poly(l-lysine)-hyaluronic acid multilayer films aimed at tissue engineering. *Soft Matter* **2008,** 4, (7), 1422-1429.

112. Grossin, L.; Cortial, D.; Saulnier, B.; Félix, O.; Chassepot, A.; Decher, G.; Netter, P.; Schaaf, P.; Gillet, P.; Mainard, D., Step- by- Step Build- up of Biologically Active Cell- Containing Stratified Films Aimed at Tissue Engineering. *Advanced Materials* **2009,** 21, (6), 650-655.

113. Meng, S.; Liu, Z.; Shen, L.; Guo, Z.; Chou, L. L.; Zhong, W.; Du, Q.; Ge, J., The effect of a layer-by-layer chitosan–heparin coating on the endothelialization and coagulation properties of a coronary stent system. *Biomaterials* **2009,** 30, (12), 2276-2283.

114. Shu, Y.; Ou, G.; Wang, L.; Zou, J.; Li, Q., Surface modification of titanium with heparin-chitosan multilayers via layer-by-layer self-assembly technique. *Journal of Nanomaterials* **2011,** 2011, 2.

115. Almodóvar, J.; Bacon, S.; Gogolski, J.; Kisiday, J. D.; Kipper, M. J., Polysaccharide-Based Polyelectrolyte Multilayer Surface Coatings can Enhance Mesenchymal Stem Cell Response to Adsorbed Growth Factors. *Biomacromolecules* **2010,** 11, (10), 2629-2639.

116. Zhang, X.; Li, Z.; Yuan, X.; Cui, Z.; Yang, X., Fabrication of dopamine-modified hyaluronic acid/chitosan multilayers on titanium alloy by layer-by-layer self-assembly for promoting osteoblast growth. *Applied Surface Science* **2013,** 284, 732-737.

117. Neto, A. I.; Vasconcelos, N. L.; Oliveira, S. M.; Ruiz-Molina, D.; Mano, J. F., High-Throughput Topographic, Mechanical, and Biological Screening of Multilayer Films Containing Mussel-Inspired Biopolymers. *Advanced Functional Materials* **2016,** 26, (16), 2745-2755.

118. Yuan, W.; Dong, H.; Li, C. M.; Cui, X.; Yu, L.; Lu, Z.; Zhou, Q., pH-Controlled Construction of Chitosan/Alginate Multilayer Film: Characterization and Application for Antibody Immobilization. *Langmuir* **2007,** 23, (26), 13046-13052.

119. Thierry, B.; Winnik, F. M.; Merhi, Y.; Tabrizian, M., Nanocoatings onto Arteries via Layer-by-Layer Deposition: Toward the in Vivo Repair of Damaged Blood Vessels. *Journal of the American Chemical Society* **2003,** 125, (25), 7494-7495.

120. Fu, J.; Ji, J.; Yuan, W.; Shen, J., Construction of anti-adhesive and antibacterial multilayer films via layer-by-layer assembly of heparin and chitosan. *Biomaterials* **2005,** 26, (33), 6684-6692.

121. Follmann, H. D. M.; Martins, A. F.; Gerola, A. P.; Burgo, T. A. L.; Nakamura, C. V.; Rubira, A. F.; Muniz, E. C., Antiadhesive and Antibacterial Multilayer Films via Layer-by-Layer Assembly of TMC/Heparin Complexes. *Biomacromolecules* **2012,** 13, (11), 3711-3722.

122. Chen, J. L.; Li, Q. L.; Chen, J. Y.; Chen, C.; Huang, N., Improving blood-compatibility of titanium by coating collagen–heparin multilayers. *Applied Surface Science* **2009,** 255, (15), 6894-6900.

123. Chen, J.; Chen, C.; Chen, Z.; Chen, J.; Li, Q.; Huang, N., Collagen/heparin coating on titanium surface improves the biocompatibility of titanium applied as a blood-contacting biomaterial. *Journal of Biomedical Materials Research Part A* **2010,** 95A, (2), 341-349.

124. Chou, C.-C.; Zeng, H.-J.; Yeh, C.-H., Blood compatibility and adhesion of collagen/heparin multilayers coated on two titanium surfaces by a layer-by-layer technique. *Thin Solid Films* **2013,** 549, 117-122.

125. Lin, Q.; Yan, J.; Qiu, F.; Song, X.; Fu, G.; Ji, J., Heparin/collagen multilayer as a thromboresistant and endothelial favorable coating for intravascular stent. *Journal of Biomedical Materials Research Part A* **2011,** 96A, (1), 132-141.

126. Zhao, M.; Li, L.; Li, B.; Zhou, C., LBL coating of type I collagen and hyaluronic acid on aminolyzed PLLA to enhance the cell-material interaction. *Express Polymer Letters* **2014,** 8, (5).

127. Gong, Y.; Zhu, Y.; Liu, Y.; Ma, Z.; Gao, C.; Shen, J., Layer-by-layer assembly of chondroitin sulfate and collagen on aminolyzed poly(l-lactic acid) porous scaffolds to enhance their chondrogenesis. *Acta Biomaterialia* **2007,** 3, (5), 677-685.

128. He, X.; Wang, Y.; Wu, G., Layer-by-layer assembly of type I collagen and chondroitin sulfate on aminolyzed PU for potential cartilage tissue engineering application. *Applied Surface Science* **2012,** 258, (24), 9918-9925.

129. Li, H.; Chen, C.; Zhang, S.; Jiang, J.; Tao, H.; Xu, J.; Sun, J.; Zhong, W.; Chen, S., The use of layer by layer self-assembled coatings of hyaluronic acid and cationized gelatin to improve the biocompatibility of poly(ethylene terephthalate) artificial ligaments for reconstruction of the anterior cruciate ligament. *Acta Biomaterialia* **2012,** 8, (11), 4007-4019.

130. Schneider, A.; Francius, G.; Obeid, R.; Schwinté, P.; Hemmerlé, J.; Frisch, B.; Schaaf, P.; Voegel, J.-C.; Senger, B.; Picart, C., Polyelectrolyte Multilayers with a Tunable Young's Modulus: Influence of Film Stiffness on Cell Adhesion. *Langmuir* **2006,** 22, (3), 1193-1200.

131. Ren, K.; Crouzier, T.; Roy, C.; Picart, C., Polyelectrolyte multilayer films of controlled stiffness modulate myoblast cells differentiation. *Advanced Functional Materials* **2008,** 18, (9), 1378-1389.

132. Richert, L.; Schneider, A.; Vautier, D.; Vodouhe, C.; Jessel, N.; Payan, E.; Schaaf, P.; Voegel, J.-C.; Picart, C., Imaging cell interactions with native and crosslinked polyelectrolyte multilayers. *Cell Biochemistry and Biophysics* **2006,** 44, (2), 273-285.

133. Richert, L.; Engler, A. J.; Discher, D. E.; Picart, C., Elasticity of Native and Cross-Linked Polyelectrolyte Multilayer Films. *Biomacromolecules* **2004,** 5, (5), 1908-1916.

134. Lee, I. C.; Wu, Y.-C., Facilitating neural stem/progenitor cell niche calibration for neural lineage differentiation by polyelectrolyte multilayer films. *Colloids and Surfaces B: Biointerfaces* **2014,** 121, 54-65.

135. Neto, A. I.; Cibrão, A. C.; Correia, C. R.; Carvalho, R. R.; Luz, G. M.; Ferrer, G. G.; Botelho, G.; Picart, C.; Alves, N. M.; Mano, J. F., Nanostructured Polymeric Coatings Based on Chitosan and Dopamine-Modified Hyaluronic Acid for Biomedical Applications. *Small* **2014,** 10, (12), 2459-2469.

136. Benkirane-Jessel, N.; Schwinté, P.; Falvey, P.; Darcy, R.; Haïkel, Y.; Schaaf, P.; Voegel, J. C.; Ogier, J., Build-up of Polypeptide Multilayer Coatings with Anti-Inflammatory Properties Based on the Embedding of Piroxicam–Cyclodextrin Complexes. *Advanced Functional Materials* **2004,** 14, (2), 174-182.

137. Kashiwagi, K.; Ito, K.; Haniuda, H.; Ohtsubo, S.; Takeoka, S., Development of Latanoprost-Loaded Biodegradable Nanosheet as a New Drug Delivery System for GlaucomaLatanoprost-Loaded Nanosheet for Glaucoma. *Investigative Ophthalmology & Visual Science* **2013,** 54, (8), 5629-5637.

138. Redolfi Riva, E.; Desii, A.; Sartini, S.; La Motta, C.; Mazzolai, B.; Mattoli, V., PMMA/Polysaccharides Nanofilm Loaded with Adenosine Deaminase Inhibitor for Targeted Anti-inflammatory Drug Delivery. *Langmuir* **2013,** 29, (43), 13190-13197.

139. Lu, H.; Hu, N., Loading Behavior of {Chitosan/Hyaluronic Acid}n Layer-by-Layer Assembly Films toward Myoglobin: An Electrochemical Study. *The Journal of Physical Chemistry B* **2006,** 110, (47), 23710-23718.

140. Tang, Z.; Wang, Y.; Podsiadlo, P.; Kotov, N. A., Biomedical Applications of Layer-by-Layer Assembly: From Biomimetics to Tissue Engineering. *Advanced Materials* **2006,** 18, (24), 3203-3224.

141. Kotov, N. A.; Dekany, I.; Fendler, J. H., Layer-by-Layer Self-Assembly of Polyelectrolyte-Semiconductor Nanoparticle Composite Films. *The Journal of Physical Chemistry* **1995,** 99, (35), 13065-13069.

142. Paterno, L. G.; Fonseca, F. J.; Alcantara, G. B.; Soler, M. A. G.; Morais, P. C.; Sinnecker, J. P.; Novak, M. A.; Lima, E. C. D.; Leite, F. L.; Mattoso, L. H. C., Fabrication and characterization of nanostructured conducting polymer films containing magnetic nanoparticles. *Thin Solid Films* **2009,** 517, (5), 1753-1758.

143. Pichon, B. P.; Louet, P.; Felix, O.; Drillon, M.; Begin-Colin, S.; Decher, G., Magnetotunable Hybrid Films of Stratified Iron Oxide Nanoparticles Assembled by the Layer-by-Layer Technique. *Chemistry of Materials* **2011,** 23, (16), 3668-3675.

144. Boddohi, S.; Almodóvar, J.; Zhang, H.; Johnson, P. A.; Kipper, M. J., Layer-by-layer assembly of polysaccharide-based nanostructured surfaces containing polyelectrolyte complex nanoparticles. *Colloids and Surfaces B: Biointerfaces* **2010,** 77, (1), 60-68.

145. Wang, Z.; Dong, L.; Han, L.; Wang, K.; Lu, X.; Fang, L.; Qu, S.; Chan, C. W., Self-assembled Biodegradable Nanoparticles and Polysaccharides as Biomimetic ECM Nanostructures for the Synergistic effect of RGD and BMP-2 on Bone Formation. *Scientific Reports* **2016,** 6, 25090.

146. Yu, D.-G.; Lin, W.-C.; Yang, M.-C., Surface Modification of Poly(l-lactic acid) Membrane via Layer-by-Layer Assembly of Silver Nanoparticle-Embedded Polyelectrolyte Multilayer. *Bioconjugate Chemistry* **2007,** 18, (5), 1521-1529.

147. Zhong, X.; Song, Y.; Yang, P.; Wang, Y.; Jiang, S.; Zhang, X.; Li, C., Titanium Surface Priming with Phase-Transited Lysozyme to Establish a Silver Nanoparticle-Loaded Chitosan/Hyaluronic Acid Antibacterial Multilayer via Layer-by-Layer Self-Assembly. *PLOS ONE* **2016,** 11, (1), e0146957.

148. Redolfi Riva, E.; Desii, A.; Sinibaldi, E.; Ciofani, G.; Piazza, V.; Mazzolai, B.; Mattoli, V., Gold Nanoshell/Polysaccharide Nanofilm for Controlled Laser-Assisted Tissue Thermal Ablation. *ACS Nano* **2014,** 8, (6), 5552-5563.

149. Gil, S.; Silva, J. M.; Mano, J. F., Magnetically Multilayer Polysaccharide Membranes for Biomedical Applications. *ACS Biomaterials Science & Engineering* **2015,** 1, (10), 1016-1025.

150. Zan, X.; Su, Z., Polyelectrolyte multilayer films containing silver as antibacterial coatings. *Thin Solid Films* **2010,** 518, (19), 5478-5482.

151. Dykman, L.; Khlebtsov, N., Gold nanoparticles in biomedical applications: recent advances and perspectives. *Chemical Society Reviews* **2012,** 41, (6), 2256-2282.

152. Zhang, X., Gold Nanoparticles: Recent Advances in the Biomedical Applications. *Cell Biochemistry and Biophysics* **2015,** 72, (3), 771-775.

153. Pankhurst, Q. A.; Connolly, J.; Jones, S. K.; Dobson, J., Applications of magnetic nanoparticles in biomedicine. *Journal of Physics D: Applied Physics* **2003,** 36, (13), R167.

154. Frimpong, R. A.; Hilt, J. Z., Magnetic nanoparticles in biomedicine: synthesis, functionalization and applications. *Nanomedicine* **2010,** 5, (9), 1401-1414.

155. Leite, Á. J.; Sher, P.; Mano, J. F., Chitosan/chondroitin sulfate multilayers as supports for calcium phosphate biomineralization. *Materials Letters* **2014,** 121, 62-65.

156. Ball, V.; Bernsmann, F.; Betscha, C.; Maechling, C.; Kauffmann, S.; Senger, B.; Voegel, J.-C.; Schaaf, P.; Benkirane-Jessel, N., Polyelectrolyte Multilayer Films Built from Poly(l-lysine) and a Two-Component Anionic Polysaccharide Blend. *Langmuir* **2009,** 25, (6), 3593-3600.

157. Hwang, J. J.; Jelacic, S.; Samuel, N. T.; Maier, R. V.; Campbell, C. T.; Castner, D. G.; Hoffman, A. S.; Stayton, P. S., Monocyte activation on polyelectrolyte multilayers. *Journal of Biomaterials Science, Polymer Edition* **2005,** 16, (2), 237-251.

158. Boulmedais, F.; Tang, C. S.; Keller, B.; Vörös, J., Controlled Electrodissolution of Polyelectrolyte Multilayers: A Platform Technology Towards the Surface-Initiated Delivery of Drugs. *Advanced Functional Materials* **2006,** 16, (1), 63-70.

159. Tsai, H.-A.; Wu, R.-R.; Lee, I. C.; Chang, H.-Y.; Shen, C.-N.; Chang, Y.-C., Selection, Enrichment, and Maintenance of Self-Renewal Liver Stem/Progenitor Cells Utilizing Polypeptide Polyelectrolyte Multilayer Films. *Biomacromolecules* **2010,** 11, (4), 994-1001.

160. Vautier, D.; Karsten, V.; Egles, C.; Chluba, J.; Schaaf, P.; Voegel, J.-C.; Ogier, J., Polyelectrolyte multilayer films modulate cytoskeletal organization in chondrosarcoma cells. *Journal of Biomaterials Science, Polymer Edition* **2002,** 13, (6), 712-731.

161. Chluba, J.; Voegel, J.-C.; Decher, G.; Erbacher, P.; Schaaf, P.; Ogier, J., Peptide Hormone Covalently Bound to Polyelectrolytes and Embedded into Multilayer Architectures Conserving Full Biological Activity. *Biomacromolecules* **2001,** 2, (3), 800-805.

162. Larkin, A. L.; Davis, R. M.; Rajagopalan, P., Biocompatible, Detachable, and Free-Standing Polyelectrolyte Multilayer Films. *Biomacromolecules* **2010,** 11, (10), 2788-2796.

163. Ye, S.; Wang, C.; Liu, X.; Tong, Z., Multilayer nanocapsules of polysaccharide chitosan and alginate through layer-by-layer assembly directly on PS nanoparticles for release. *Journal of Biomaterials Science, Polymer Edition* **2005,** 16, (7), 909-923.

164. Ye, S.; Wang, C.; Liu, X.; Tong, Z.; Ren, B.; Zeng, F., New loading process and release properties of insulin from polysaccharide microcapsules fabricated through layer-by-layer assembly. *Journal of Controlled Release* **2006,** 112, (1), 79-87.

165. Fujie, T.; Matsutani, N.; Kinoshita, M.; Okamura, Y.; Saito, A.; Takeoka, S., Adhesive, Flexible, and Robust Polysaccharide Nanosheets Integrated for Tissue-Defect Repair. *Advanced Functional Materials* **2009,** 19, (16), 2560-2568.

166. Song, Z.; Yin, J.; Luo, K.; Zheng, Y.; Yang, Y.; Li, Q.; Yan, S.; Chen, X., Layer-by-Layer Buildup of Poly(L-glutamic acid)/Chitosan Film for Biologically Active Coating. *Macromolecular Bioscience* **2009,** 9, (3), 268-278.

CHAPTER 3

Materials and methods

In this chapter the main details of the starting polymers, the synthesis and characterization of an alginate-based magnetic ferrofluid which will be employed in the chapters 5 and 6 and the experimental methods employed throughout this thesis are presented.

3.1. MATERIALS

This section summarizes the main characteristics of the polymers and nanoparticles employed to prepare multilayer films via layer-by-layer assembly. Also the reasons why each polymer has been selected are explained. The fabrication of multilayer films through LbL techniques as well as their properties and applications will be studied in the following chapters.

3.1.1. Starting polymers

Polysaccharides

- *Chitosan (Chi)*

Chitosan (Chi), composed of *N*-acetyl D-glucosamine and D-glucosamine units, is obtained from N-deacetylation of chitin, a biopolymer found in shells of crustacean or fungal mycelia.[1] It is biodegradable, biocompatible, bioadhesive and non-toxic.[2, 3] Chi has a pKa of 6.3 which implies that at pH values lower than 6.3 is positively charged being able to act as polycation for building up multilayer films via LbL assembly.[4]

The chemical structure of Chi is illustrated in the Figure 3.1.

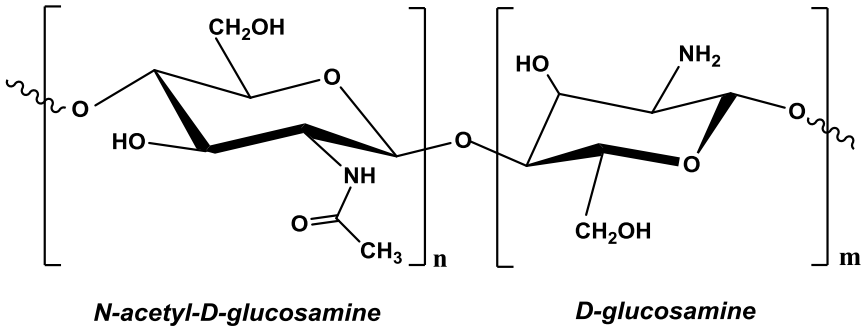

Figure 3.1. Chemical structure of chitosan.

For the fabrication of the LbL films reported on this PhD work, low molecular weight chitosan (Chi) was employed (Aldrich 448869, lot SLBG1673V). According to the fabricant, viscosity was 20 – 300 cps (1 %wt in acetic acid, 25 °C, Brookfield). Purified using the procedure

described by Signini and Campana Filho,[5] Chi was dissolved in acetic acid 1 %w/v with magnetic stirring for 22 h and filtered through filter paper. Then, precipitation of Chi was obtained by addition of 6.25 M NaOH drop by drop. After that, Chi was filtered and washed with distilled water until neutral pH. At the end, it was rinsed with ethanol and dried in an oven at 55°C for 17 h.

- *Alginate (Alg)*

Alginate (Alg) is extracted from brown seaweed and it is constituted of (1, 4) linked α-L-guluronic acid and β-D-mannuronic acid. It is also biodegradable, biocompatible, bioadhesive and non-toxic, characteristic that makes it an excellent candidate for biomedical applications.[3] The pKa of the carboxylic acid group is 3.5 providing a negative charge to alginate at pH values higher than pKa. In these conditions Alg can act as polyanion for building up multilayer films via LbL assembly.[4]

The chemical structure of alginate is illustrated in Figure 3.2.

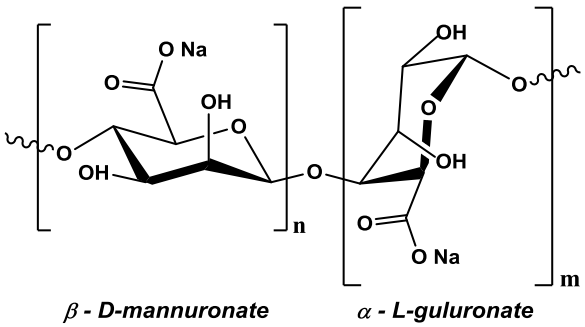

Figure 3.2. Chemical structure of sodium alginate.

For the fabrication of the LbL materials in this PhD work, sodium alginate (Alg) was supplied by Sigma-Aldrich (A2158, lot 090M0092V) and used as received without further purification. According to the fabricant, its viscosity was 136 cps (2 %w/v in water at 25 °C).

- *Hyaluronic acid (HA)*

Hyaluronic acid (HA) is a glycosaminoglycan formed by β-1,3-*N*-acetyl glucosamine-β-1,4-Glucuronic acid disaccharide repeating units which is present in the basal membrane of connective tissues.[6] HA is the major constituent of the skin, it is metabolized in the epidermis and participates in cell proliferation and acts as a space-filling material in the extracellular spaces in the dermis.[7] The pKa is ~3 which means that at physiological pH the carboxyl groups are

ionized.[7] It is used as a polyanion in the LbL assembly due to the fact that it can be used as a surface to support cell cultures[8] and it can control the tissue hydration and inflammatory response after a trauma.[9]

The chemical structure of hyaluronic acid is illustrated in Figure 3.3.

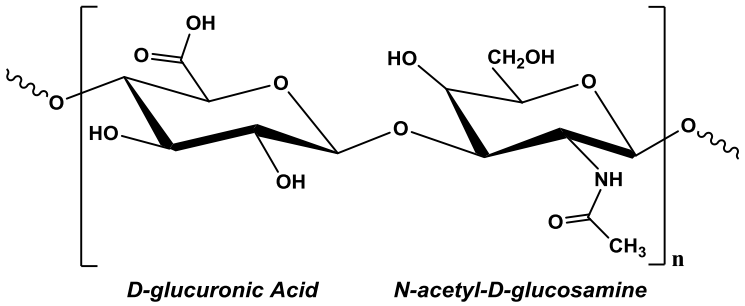

Figure 3.3. Chemical structure of hyaluronic acid.

Hyaluronic acid was supplied by Soliance (Primalhyal 400, lot 12274F) and used as received without further purification. Molecular weight was 472000 with a polydispersity index of 1.55.

- *Chondroitin sulphate (ChS)*

Chondroitin sulphate (ChS) is a glycosaminoglycan formed by alternating units of β-1,3-*N*-acetyl-D glucosamine and β-1,4-Glucuronic acid which is abundant in the extracellular matrix (ECM) and responsible, in many cases, for the mechanical resistance of tissues through the electrostatic repulsions of its sulphate groups, making it attractive *e.g.*, for cartilage or intervertebral disk regeneration. It also plays roles in biological pathways including wound healing and morphogenesis.[10]

The chemical structure of chondroitin sulphate is illustrated in Figure 3.4.

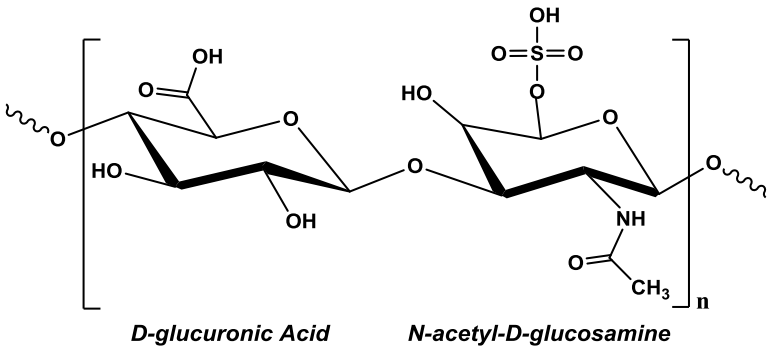

Figure 3.4. Chemical structure of chondroitin sulphate.

Chondroitin sulphate A sodium salt from bovine trachea was purchased from Sigma Aldrich (C9819) and used as received.

Proteins

- *Gelatin (GL)*

Gelatin (GL) is a fibrous protein obtained by partial denaturation of collagen which is the major source of protein biopolymer. The composition and sequence of amino acids differs among sources, *e.g.*, amino acids in porcine skin gelatin do not contain cysteine but they have a high content of glycine (Gly). Porcine skin gelatin is the only one that contains aspartic acid and glutamic acid. The structural unit contains repeating sequences of Gly-X-Y-triplets being X and Y the proline and hydroxyproline amino acids. Gelatin type A is obtained through an acidic pre-treatment which does not affect the amide groups. Gelatin shows high biocompatibility and biodegradability being widely employed for biomedical applications.[11]

The chemical structure of gelatin amino acids functional groups and terminal amino groups is illustrated in Figure 3.5.

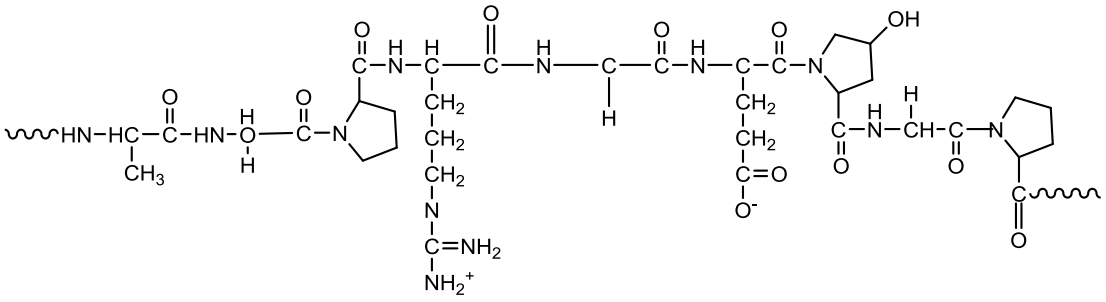

Figure 3.5. Chemical structure of gelatin.

Gelatin type A from porcine skin was purchased from Sigma Aldrich (G1890) and used as received.

Synthetic polymers

- *Poly(allylamine hydrochloride) (PAH)*

Poly(allylamine hydrochloride) (PAH) is a synthetic polycation obtained by the polymerization of allylamine. It is biocompatible, non-biodegradable and insensitive to the action of intracellular proteases which confers the robust property to the LbL structure in biomedical applications.[12, 13]

The chemical structure of poly(allylamine hydrochloride) is illustrated in Figure 3.6.

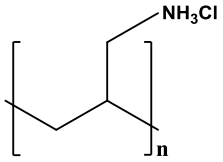

Figure 3.6. Chemical structure of poly(allylamine hydrochloride).

Poly(allylamine hydrochloride) with a molecular weight was 58000 Da was supplied by Aldrich (283223, lot MKBJ4277V) and used as received without further purification.

- *Polyethylenimine (PEI)*

Polyethylenimine (PEI) is a polycation formed by repeating units of amine groups and two aliphatic carbons. It is an important polymer in medicinal chemistry; it has been used in gene therapy and for DNA complexation and transfection in several cell lines and tissues. However, it is cytotoxic.[14, 15] In LbL technique, PEI is used as an adhesion promoter base layer giving rise to a positively charged substrate with an even coating in order to minimize the influence of the surface on the growth of successive layers.[16]

The chemical structure of polyethylenimine is illustrated in Figure 3.7.

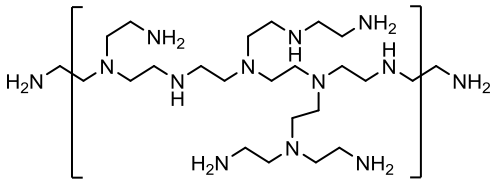

Figure 3.7. Chemical structure of polyethylenimine.

Poly(ethylenimine) (PEI) with a molecular weight of 25000 Da was supplied by Aldrich and used as received.

3.1.2. Characterization of polysaccharides, chitosan and alginate

Determination of the molecular weight by viscosimetry

Chitosan and alginate are natural polymers that come from shells of crustacean or fungal mycelia[1] and brown seaweed,[3] respectively; so that, properties of every lot can be different. It is

well known that some polymer characteristics such as molecular weight have great influence in the properties of the final product. Due to that, the molecular weight of these polymers was determined by viscosimetry at 25 ºC using a capillary viscosimeter Ubbelohde I Schott (ϕ = 0.63mm).

In the case of chitosan, aqueous solutions of chitosan in acetic acid 0.3M/sodium acetate 0.2M with different concentrations, 0.2, 0.25, 0.35, 0.4 and 0.5 mg/mL were prepared. For alginate, the polymer was dissolved in aqueous solutions of sodium chloride 0.1M at different concentrations, 0.4, 0.6, 0.8, 1.0, 1.52 and 2.0 mg/mL.

Viscosity average molecular weight, $\overline{M_v}$, was determined using the Mark-Houwink equation.

$$[\eta] = k \cdot \overline{M_v}^{\,a} \qquad (eq.\,3.1)$$

where $[\eta]$ is the intrinsic viscosity and *k* and *a* are constants for the same system polymer-solvent at 25 °C. For chitosan,[17] these parameters are $k = 74 \cdot 10^{-5}$ dL/g, $a = 0.76$ and for alginate,[18] $k = 2 \cdot 10^{-5}$ dL/g, and $a = 1.0$. $[\eta]$ is obtained from the representation of the reduced viscosity versus the polymer concentration by extrapolation of reduced viscosity to zero concentration.[19]

As can be observed in Figure 3.8, experimental data can be fitted to a linear curve whose ordinate corresponds to intrinsic viscosity. The intrinsic viscosity of chitosan is 3.45 dL/g and its viscosity average molecular weight is obtained using the equation 3.1 achieving a value of 67100 Da. In the case of alginate (Figure 3.8b), the intrinsic viscosity is 3.31 dL/g and the viscosity average molecular weight calculated with the equation 3.1 is 165500 Da.

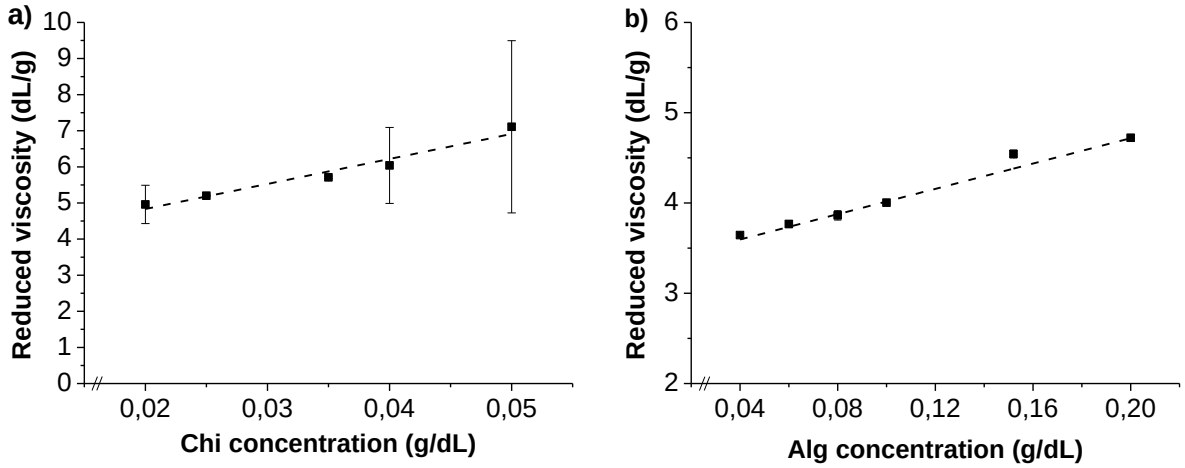

Figure 3.8. Reduced viscosity versus concentration of a) chitosan and b) alginate. Dashed lines represent the linear fit to the experimental data.

Determination of the chitosan deacetylation degree by nuclear magnetic resonance (NMR)

The deacetylation degree (DD) is an important structural parameter to differentiate chitosan, which has a high number of amino groups, from chitin, which has a high number of acetamide groups. It is used to define the properties of chitosan, specially its solubility in water, which influences in a decisive way its biomedical applications. As DD increases, solubility, viscosity, biocompatibility, mucoadhesion, analgesic, antimicrobial, antioxidant and hemostatic properties increase and crystallinity and biodegradability decrease.[20]

The deacetylation degree (DD) of purified chitosan was determined by Nuclear Magnetic Resonance (NMR) in a Bruker Avance 300 at 70 °C. For that, 5 mg of chitosan were dissolved in 1 mL of 2 %wt CD_3COOD in D_2O water. The resulting solutions were filtered with cotton before measurement by NMR.

Chemical structure of chitosan is shown in Figure 3.9. There are two different structural units, D-glucosamine (deacetylated) and N-acetyl-D-glucosamine (acetylated). The three methyl protons of the N-acetyl-D-glucosamine unit (H_a) and the proton of the D-glucosamine unit (H_b) are marked in green.

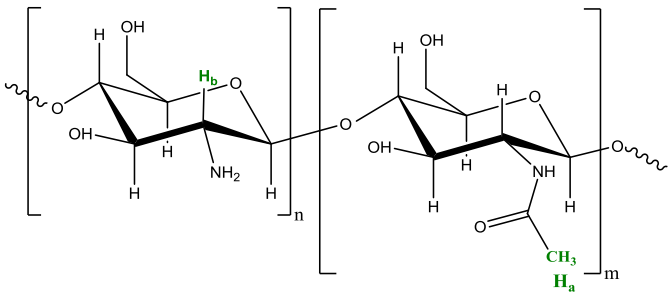

Figure 3.9. Chemical structure of chitosan with the signals of three methyl protons (H_a) and the proton (H_b) marked in green.

Figure 3.10 exhibits the ^{1}H-NMR spectrum of chitosan in CD_3COOD/D_2O carried out at 70 ºC. The signal at 2.48 ppm (H_a) corresponds to the three methyl protons of the structural unit N-acetilglucosamine and the signal at 3.59 ppm (H_b) belongs to the proton of the structural unit D-glucosamine. Bands located at 4 and 5 ppm correspond to anomeric protons of chitosan which have similar electronic densities and chemical shifts and its signals are overlapped in the spectrum of linear chitosan. The peak at 4.71 ppm belongs to the solvent.

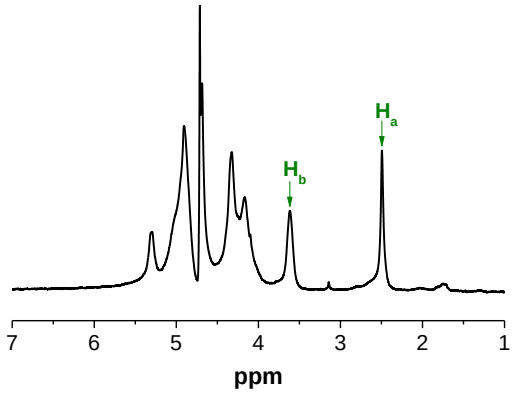

Figure 3.10. [1]H-NMR spectrum of purified chitosan at 70 °C.

The DD is calculated from equation 3.2 taking into account the relative intensity of the signal corresponding to the three methyl protons of the acetamide group (CH_3) represented as H_a and the intensity of the D-glucosamine fraction represented as H_b in the Figure 3.9.[21]

$$DD(\%) = \left(1 - \left(\frac{\frac{1}{3} I_{CH_3}}{\frac{1}{3} I_{CH_3} + I_H}\right)\right) \cdot 100 \qquad (eq. 3.2)$$

The DD obtained is 81 %.

Determination of the thermal stability

A thermogravimetric analysis (TGA) of purified chitosan and alginate was carried out in a TGA Q500 (TA Instruments) from 50 °C to 650 °C at a heating rate of 10 °C/min under air atmosphere. Figure 3.11 displays the weight loss of these polymers versus temperature.

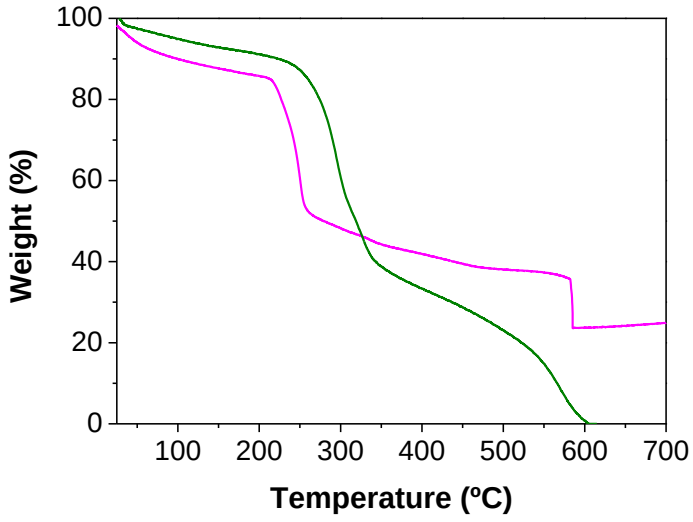

Figure 3.11. Thermogravimetric curves of chitosan (green) and alginate (pink).

The TGA curve of chitosan exhibits three weight losses. The first one takes place in the interval between 50 – 170 ºC and it is due to the evaporation of absorbed water in the sample (8.9 %). The second, between 170 – 400 ºC, is related to depolymerization of chitosan chains, decomposition of pyranose rings by dehydration and deamination and ring-opening reactions. The last one between 400 – 600 ºC is due to decomposition of oxidized chitosan, chain scissions and formation of volatile degradation products.[22, 23 23] Ashes above 600 ºC forms a waste of 0.03% which indicates that chitosan is free from metal traces and impurities, therefore the purification process was carried out correctly.

The alginate spectrum also shows three weight losses. The first one, between 25 – 170 ºC, is due to evaporation of absorbed water in the sample (11.0 %). The second, between 170 – 500 ºC, is related to the decomposition of alginate. The last one between 500 – 600 ºC is due to the formation of Na_2CO_3.[24] The waste formed by Na_2CO_3 constitutes 23.9%.

Results obtained from TGA analysis, onset degradation temperature, percentage of weight loss and percentage of ashes calculated at 650 °C, are collected in Table 3.1.

Table 3.1. Onset temperature, weight loss and ashes obtained from TGA of chitosan and alginate.

Sample	Onset temperature (ºC)	Weight loss (%)	Ashes (%)
Chitosan	260 536	8.9 51.9 39.1	0.1
Alginate	206 446	11.0 50.7 14.4	23.9

3.1.3. Alginate based magnetic ferrofluid

Synthesis of alginate based magnetic ferrofluid

For the preparation of an alginate based magnetic ferrofluid, Fe_3O_4 magnetic nanoparticles (NPs) were synthetized by a coprecipitation method carried out in an alginate aqueous solution following the experimental procedure shown in Scheme 3.1. Briefly, 0.834 g of iron (II) sulfate heptahydrate ($FeSO_4 \cdot 7H_2O$) and 1.6218 g of iron (III) chloride hexahydrate ($FeCl_3 \cdot 6H_2O$) were dissolved in 10 mL of Milli-Q water under N_2 atmosphere. Then, the mixture was added to a three-necked flask containing 40 mL of alginate (2.5 mg/mL) under N_2 atmosphere with

mechanical stirring at 350 rpm using a teflon stirrer and heated at 80 °C for 1 hour. After that, this mixture was added dropwise under constant stirring to other three-necked flask containing 50 mL of ammonium hydroxide (NH_4OH), taking place the color change of the mixture from yellow orange to black. The mixture was held with stirring for 2 hours at 80 °C under N_2 atmosphere. Afterwards, the solution was cooled in an ice bath and washed with Milli-Q water until neutral pH by magnetic decantation. To obtain the final ferrofluid, this slurry was redispersed either in 130 or 65 mL of Milli-Q water giving rise to different magnetite concentrations (ferrofluid 1 and 2, respectively). The Scheme 3.1 includes a photograph corresponding to the ferrofluid 2 whose colloidal stability was assessed by the inverted tube test.

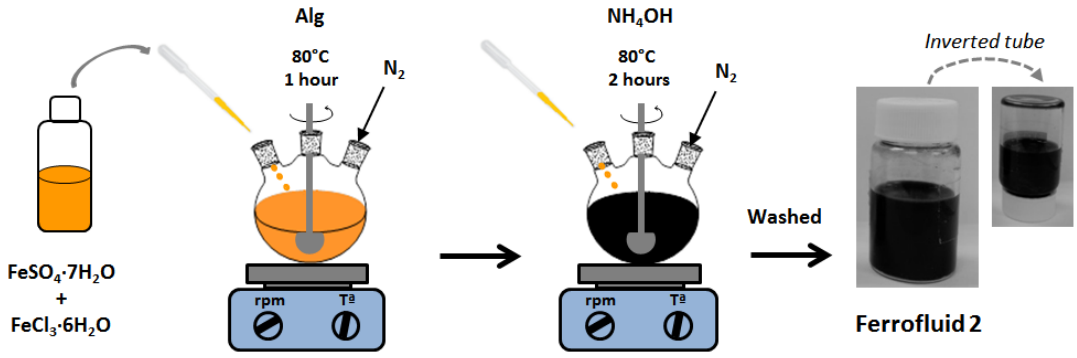

Scheme 3.1. Sequential process followed for the synthesis of the alginate based magnetic ferrofluid with the photograph corresponding to the ferrofluid 2. Note that the inverted tube test is showed to assess the colloidal stability of the synthetized ferrofluid.

Characterization of alginate based magnetic ferrofluid

- *Determination of the iron content*

Iron content was determined by UV-vis transmission spectrophotometry using the thiocyanate complexation reaction and measuring the absorbance of the iron-thiocyanate complex at 478 nm wavelength.

$$Fe^{3+}_{(aq)} + 6\,SCN^{-}_{(aq)} \rightarrow [Fe(SCN)_6]^{3-}_{(aq)}$$

Firstly, an aliquot of 100 µL of ferrofluid was dissolved in 1:1 v/v HCl 6M/HNO_3 (65%) for 2h and, after that, potassium thiocyanate 1.5M was added to the solution to form the iron-thiocyanate complex. Afterwards, the magnetite concentration of ferrofluid was determined by comparing the sample absorbance to a calibration curve. The magnetite concentrations of ferrofluids 1 and 2 were 4.0 and 8.0 mg/mL, respectively.

To determine the mass of alginate in relation to the iron content, a thermogravimetric analysis (TGA) was carried out on previously freeze-dried alginate based magnetic ferrofluid using an analyzer TA Q-500 from 25 ºC to 750 ºC at a heating rate of 10 ºC/min under nitrogen atmosphere. Figure 3.12 shows the weight loss divided in two steps, one in the range from 25 to 100 ºC and another from 100 to 350 ºC. The first weight loss (2 %wt) corresponds to the evaporation of water absorbed in the NPs. The second and more significant weight loss (10 %wt) is due to decomposition of sodium alginate used as surfactant of NPs in water.[25, 26] The total weight loss was 12 %wt and the waste obtained at temperatures above 400 ºC forms 88 %wt of sample and corresponds to the amount of iron content.[27]

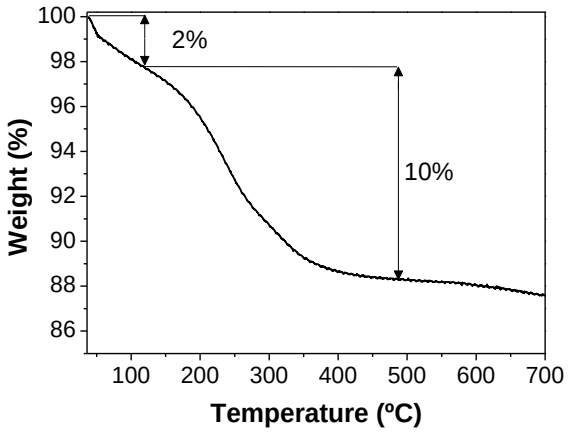

Figure 3.12. Thermogravimetric analysis of freeze-dried ferrofluid under nitrogen atmosphere.

- *Determination of the chemical structure*

Fourier transform infrared spectroscopy (FTIR) was performed on alginate and previously freeze-dried ferrofluid using a spectrometer Perkin Elmer Spectrum One DT-IR from 4000 to 450 cm^{-1} with a resolution of 0.5 cm^{-1}. Figure 3.13 displays FTIR spectra corresponding to the ferrofluid (black line) and alginate (pink line). In the spectrum of the ferrofluid. there is a strong absorption band at 585 cm^{-1} which is attributed to the vibration of Fe–O and shows the formation of magnetite nanoparticles. Peaks at 1420 and 1624 cm^{-1}, attributed to the stretching vibration of C–O bond, and peak at 2924 cm^{-1}, due to the stretching vibration of C–H bond, are also presented in the alginate spectrum. This fact allows to demonstrate the presence of both components, alginate and iron, in the ferrofluid. The broad band centered at 3430 cm^{-1} is assigned to the O–H stretching vibration arising from surface hydroxyl groups adsorbed on nanoparticles.[25, 26, 28]

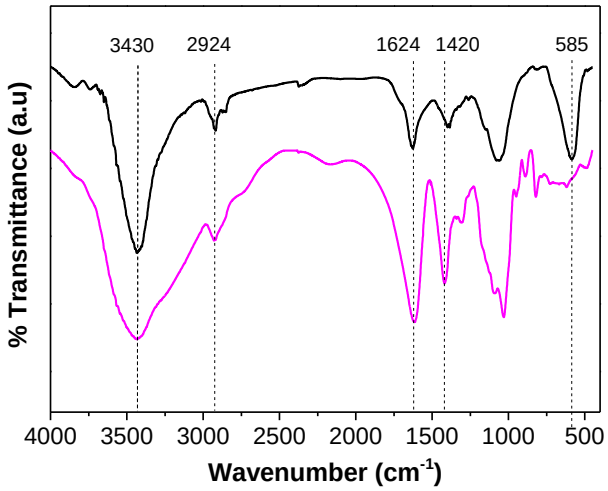

Figure 3.13. FTIR transmittance spectra of freeze-dried ferrofluid (black line) and alginate (pink line).

- *Morphological characterization*

For the determination of the morphology, distribution and average size of the NPs, an aliquot of the ferrofluid was diluted in ethanol and analyzed by transmission electron microscopy (TEM) using a TECNAI T20 transmission electron microscope equipped with a CCD-camera Veleta 2Kx2K and operating at an acceleration voltage of 200 kV with LaB_6 filament.

Figure 3.14a shows a TEM image of NPs which reveals that Fe_3O_4 NPs were quasi-spherical and their size distribution is relatively homogenous. From this TEM image, it is possible to determine the average particle size and particle size distribution. The histogram (Figure 3.14b) was obtained from this TEM image by counting 100 particles using the software ImageJ. The fitting Gaussian curve (orange line) was used to obtain the average size of NPs that was 7.3 ± 1.1 nm.

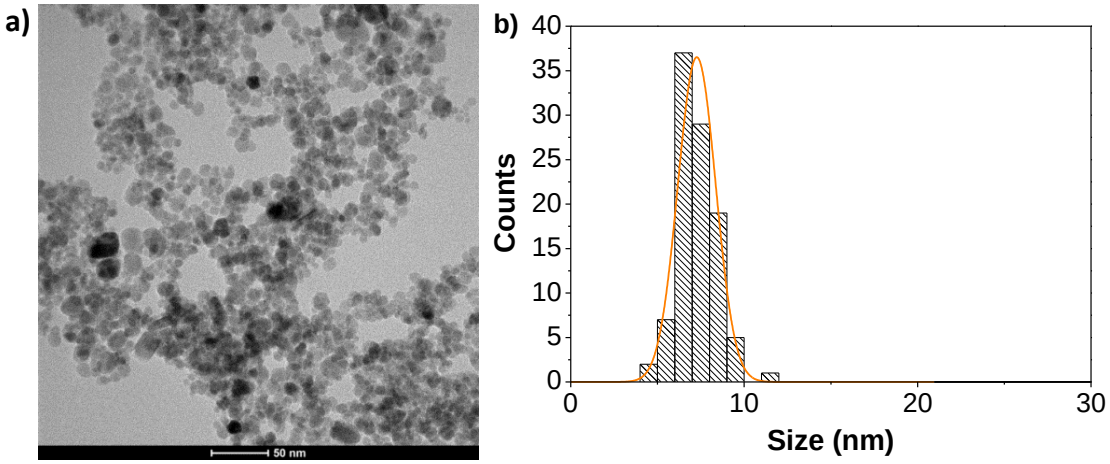

Figure 3.14. a) TEM image of NPs showing the morphology and the general distribution of particle size and b) histogram and the fitting Gaussian curve in orange.

To determine the hydrodynamic average size, the polydispersity index (PDI) and the zeta potential of NPs dispersed in water (ferrofluid), the technique of Dynamic Light Scattering was employed using a Malvern Nanosizer NanoZS instrument equipped with a 4 mW He-Ne laser (λ = 633 nm) at a scattering angle of 173º. Samples were measured in polystyrene cuvettes (SARSTEDT) at 25 ºC. The autocorrelation function was converted into an intensity particle size distribution with ZetaSizer Software 7.10 by using the Stokes-Einstein equation.

The hydrodynamic diameter and polydispersity of ferrofluids prepared at two different magnetite concentrations, 4.0 and 8.0 mg/mL, are collected in the Table 3.2. The hydrodynamic diameter (D_{hyd}) increases with the concentration of magnetite from 83.1 ± 11.0 nm to 103.5 ± 1.3 nm, probably due to the aggregation of magnetic nanoparticles. The polydispersity also increases with the magnetite concentration.

Table 3.2. Dependence of hydrodynamic size and polidispersity with the magnetite concentration.

[Fe_3O_4] (mg/mL)	**D_{hyd} (nm)**	**PDI**
4.0	83.1 ± 11.0	0.141 ± 0.030
8.0	103.5 ± 1.3	0.198 ± 0.016

Figure 3.15a shows the hydrodynamic diameter of NPs dispersed in water (ferrofluid) with a concentration of 8.0 mg/mL as a function of pH to study the influence of this parameter in the colloidal stability. NPs have a hydrodynamic diameter around 100 nm with a polydispersity

about 0.2 for a pH range from 4.9 to 10. Finally, the electrophoretic mobility of NPs dispersed in Milli-Q water was measured at 25 ºC increasing pH from 3 to 10. All measurements were repeated three times. The electrophoretic mobility was transformed into zeta potential using the Smoluchowski equation and results are exhibited in Figure 3.15b. Zeta potential decreases from –8.5 mV to –43 mV as pH increases from 3 to 5.7 until reach a *plateau*. Zeta potential is negative as expected due to the negative charge of carboxylic groups (COO^-) of alginate at the pH measured.[29, 30] At pH higher than 5, alginate-coated NPs are stable due to the presence of charged carboxylate groups on their surface which provides electrostatic repulsion. On the contrary, at pH 4 these ionizable groups underwent protonation giving rise to aggregation and consequent precipitation of the NPs.[31]

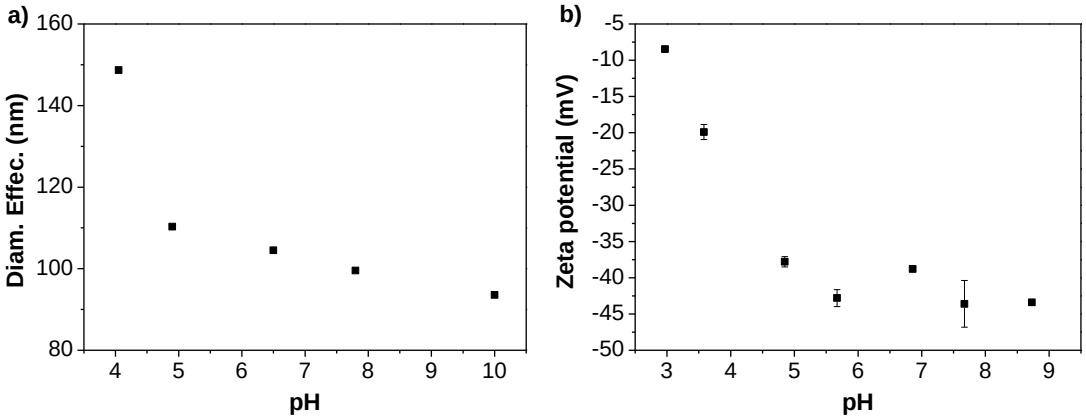

Figure 3.15. a) Hydrodynamic diameter and b) zeta potential of the ferrofluid as function of pH.

- *Determination of crystalline properties*

The crystalline structure of the NPs previously freeze-dried was determined by X-Ray diffraction (XRD) using a X-Ray diffractometer Bruker D8 Advance at a voltage of 40 kV, an intensity of 40 mA and a rate of 0.5 s/step and its spectrum is showed in Figure 3.16.

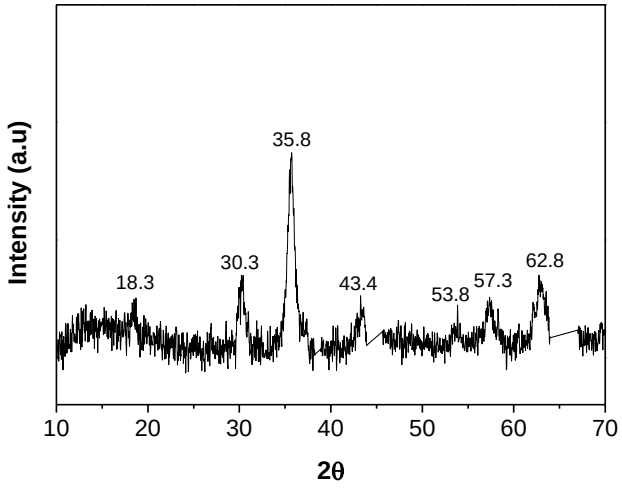

Figure 3.16. X-Ray diffraction spectrum of NPs.

Characteristics peaks at 18.3 (D 1 1 1), 30.3 (D 2 2 0), 35.8 (D 3 1 1), 43.4 (D 4 0 0), 53.8 (D 4 2 2), 57.3 (D 5 1 1) and 62.8 (D 4 4 0) correspond with those previously reported for crystalline magnetite (JCPDS# 19-629). The peak broadening of XRD spectrum indicates the small size of the resulting nanoparticles. It is difficult to distinguish magnetite (Fe_3O_4) from maghemite (γ-Fe_2O_3) because maghemite has a crystal structure and a lattice spacing similar to magnetite, but the absence of other characteristic peaks of maghemite in the XRD spectrum and the black color of the synthetized NPs verifies that it contents mainly Fe_3O_4 and not γ-Fe_2O_3 which has a brown color.[25, 32]

From the XRD spectrum, the average size of NPs can be estimated using the Debye-Scherrer equation.[28]

$$D = \frac{K\,\lambda}{\beta\,cos\theta} \qquad (eq.\,3.3)$$

where D is the average particle size (nm), K is the Scherrer's constant (0.89), λ is the X-ray wavelength (0,154 nm), β is the peak full width at half maximum (FWHM) of the highest diffraction peak in radians and θ is the Bragg diffraction angle.[28] The most intense peak (3 1 1) was used to calculate the average particle size which is 6.8 nm. This value is consistent with the size determined by TEM image (Figure 3.14) 7.3 ± 1.1 nm.

3.1.4. Conclusions

The purification and characterization of chitosan were carried out obtaining the following data: the deacetylation degree (DD) of chitosan, determined by RMN-^{1}H, reached a value of 81% and its molecular weight, determined by capillary viscosimetry at 25°C, was 67100 Da. Besides, the molecular weight of alginate was determined on the same basis achieving a value of 165500 Da.

The synthesis and characterization of an alginate-based ferrofluid was carried out through a coprecipitation method. The obtained ferrofluid possessed colloidal stability at neutral pH with an average particle size of ~ 7 nm and a hydrodynamic diameter around 100 nm for a magnetite concentration of 8.0 mg/mL. From pH 5 the hydrodynamic diameter and the zeta potential reached stationary values around 100 nm and -40 mV, respectively. For lower pHs, both parameters increased until 150 nm and -8 mV, respectively due to the aggregation and precipitation of the magnetic NPs.

3.2. CHARACTERIZATION TECHNIQUES

This following section describes the most relevant characterization techniques employed to study the growth, morphology and structure of multilayer films built up via LbL assembly. Some techniques which have been used occasionally to characterize the properties of materials used in this work, as for example transmission electron microscopy (TEM), Raman microscopy, X-ray diffraction (XRD), etc., are not going to be developed in this section and their experimental procedure will be described in the corresponding section.

3.2.1. Characterization techniques to follow the growth of LbL films

Ellipsometry

Ellipsometry is a non-destructive optical technique to determine the thickness of thin films. A linearly polarized light beam having p-polarized and s-polarized components is incident on a sample at an incidence angle α to the normal. The reflected wave is, in general, elliptically polarized (Figure 3.17).[33] Ellipsometry measures this change in polarized light upon light reflection on a sample (or light transmission by a sample). This change provides information related to optical properties of the sample such as refraction index, thickness and roughness. Single-wavelength ellipsometry employs a monochromatic light source, usually a laser in the visible spectral region at a wavelength of 632.8 nm allowing to focus the beam on a small spot size.[34] One of the most important restrictions of ellipsometry measurements is that the surface

roughness of samples has to be small (<30%) because light scattering of rough surfaces reduces the reflected light intensity and therefore, the ellipsometry measurement becomes difficult.[35]

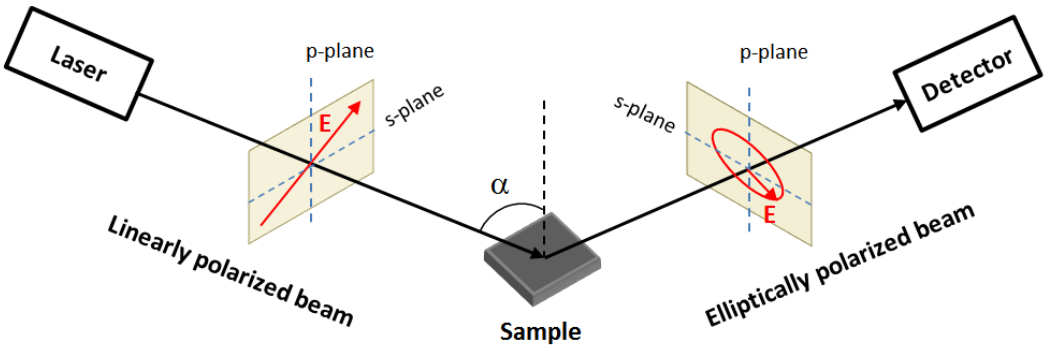

Figure 3.17. Schematic representation of a spectroscopic ellipsometry measurement with the change of polarized light from linear to elliptical after reflection off of the sample.

In the case of multilayer films,[36] the final reflected wave is formed by light reflected on all interphases as shown in Figure 3.18. The light firstly hits in the interphase air-polymer layer being a part of this light reflected and other transmitted through the polymer film thickness until the next interphase polymer layer-substrate, where it takes place a phase difference β which is related to the polymer layer thickness by the following equation.

$$\beta = 2\pi\left(\frac{d}{\lambda}\right) N_2 \cos\alpha_2 \qquad (eq.\,3.4)$$

where d is the polymer layer thickness, λ is the wavelength of the incident light, α_2 is the incidence angle and N_2 is the complex refraction index of the polymer layer.

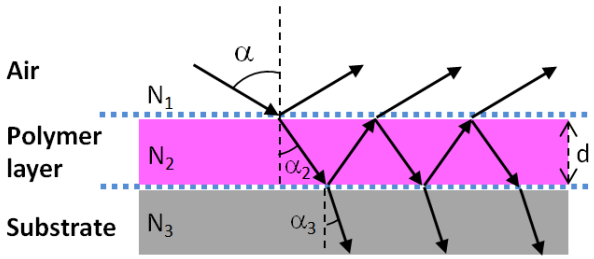

Figure 3.18. Schematic representation of light reflection upon a film supported on a substrate.

Ellipsometry does not directly measure the refraction coefficients but measures two values, the amplitude ratio (ψ) and phase difference (Δ) between light waves known as p-polarized and s-polarized light waves.[35] These two parameters are related by the parameter ρ expressed as.[35, 37]

$$\rho = \frac{r_p}{r_s} = tan\psi \exp(i\Delta) \qquad (eq. 3.5)$$

where r_p and r_s are the complex refraction coefficients for the perpendicular and parallel polarization, respectively. In the case of multilayer films, these coefficients are expressed as:

$$r_p = \frac{r_{12_p} + r_{23_p}\exp(-i2\beta)}{1 + r_{12_p} + r_{23_p}\exp(-i2\beta)} \; ; \; r_s = \frac{r_{12_s} + r_{23_s}\exp(-i2\beta)}{1 + r_{12_s} + r_{23_s}\exp(-i2\beta)} \qquad (eq. 3.6)$$

The optical parameters such as the refraction index, *n*, the extinction coefficient, *k*, and the thickness, *d*, can be related to parameters ψ and Δ measured by ellipsometry through different mathematical models. In the case of polymer thin films, models where the dependence of the wavelength of the real part of the refraction index is fitted to the Cauchy equation (eq. 3.7) are accurate.[38]

$$n(\lambda) = A_n + \frac{B_n}{\lambda^2} \qquad (eq. 3.7)$$

where *n* is the refraction index, λ is the wavelength and A and B are the Cauchy parameters.

Measurements of the film thickness presented in this thesis were carried out with a PLASMOS SD 2300 ellipsometer operating at the single wavelength of 632.8 nm and a constant angle of 70°. This technique was employed during a short stay in the group of Prof. Fouzia Boulmedais in the Institute Charles Sadron, CNRS, Strasbourg.

Quartz Crystal Microbalance (QCM)

The buildup of multilayer films can be followed in situ by a quartz crystal microbalance (QCM). QCM is a nanogram sensitive technique introduced by Sauerbrey that employs the change in the frequency of a single quartz crystal resonator to measure the mass of a rigid film deposited on the quartz resonator surface.[39]

$$\Delta m = -\frac{h_q \rho_q}{f_0}\frac{\Delta f_v}{\nu} = -c\,\frac{\Delta f_v}{\nu} \qquad (eq. 3.8)$$

where h_q is the thickness of the quartz, ρ_q is the density of quartz (~17.7ng·cm^{-2}·Hz^{-1} for a crystal of 5-MHz), f_0 is the fundamental resonant frequency of quartz (5 MHz), ν is the overtone number and *c* the mass sensitivity constant.

The use of QCM for liquid applications reveals that the liquid phase often incorporates viscous and elastic contributions to the frequency change contradicting the Sauerbrey's assumption that the adsorbed mass must be rigidly adsorbed, being necessary a new approach to describe the mass deposits with frictional dissipative losses due to their viscoelastic character. This gave rise to QCM with dissipation monitoring (QCM-D) which allows to simultaneously measure the changes in the resonant frequency and in the viscoelastic properties (dissipation) when a film is adsorbed at the quartz crystal surface.[40] A decrease in $\Delta f/\nu$ is usually associated to an increase of the mass adsorbed on the quartz and a decrease of dissipation (D) at constant mass is usually associated to a stiffer (less elastic) film.[41]

The dissipation parameter is given by equations 3.9 (dimensional) and 3.10 (dimensionless).[40]

$$D = \frac{1}{\pi f \tau} \qquad (eq. 3.9)$$

$$D = \frac{E_{dissipated}}{2\pi E_{stored}} \qquad (eq. 3.10)$$

where τ is the time constant of the amplitude decay of the oscillating crystal as the driving voltage over the crystal is turned off, $E_{dissipated}$ is the energy dissipated during one oscillatory cycle and E_{stored} the energy stored in the oscillating system.

The QCM-D method allows to test f and D values at its fundamental frequency (~ 5 MHz) as well as at several overtones. The QCM-D response of a viscoelastic film can be modelled using the Voigt model to extract meaningful parameters such as thickness, viscosity or shear modulus.[40, 41] This model assumes that the film covers homogenously all the active area of the sensor, has uniform thickness and density under no slip conditions and the medium in which the sensor is resonating is a bulk Newtonian fluid. Taking into account these assumptions, the resonant frequency and the dissipation can be described by the equations 3.11 and 3.12 respectively.[42]

$$\Delta f \approx -\frac{1}{2\pi\rho_q h_q}\left\{\frac{\eta_B}{\delta_B} + h_l\rho_l\left(\frac{\eta_B}{\delta_B}\right)^2 \frac{\eta_l\omega^2}{\mu_l^2 + \omega^2\eta_l^2}\right\} \qquad (eq. 3.11)$$

$$\Delta D \approx \frac{1}{2\pi f\rho_q h_q}\left\{\frac{\eta_B}{\delta_B} + 2h_l\left(\frac{\eta_B}{\delta_B}\right)^2 \frac{\mu_l\omega}{\mu_l^2 + \omega^2\eta_l^2}\right\} \qquad (eq. 3.12)$$

where ω is the angular frequency of the oscillation, ρ_q and h_q are the density and thickness of the quartz crystal respectively, h_l, ρ_l, η_l and μ_l are the thickness, density, viscosity and shear modulus of the adsorbed layer respectively, η_B and ρ_B are the viscosity and density of the bulk liquid and δ_B the viscous penetration depth of the shear wave in the bulk liquid calculated by the following equation.

$$\delta_B = \left(\frac{2\eta_B}{\rho_B \omega}\right)^{1/2} \qquad (eq.3.13)$$

QCM measurements described in this PhD work were carried out on a Q-sense D300 apparatus from Q-Sense AB (Gothenburg, Sweden) during a short stay in the group of Prof. Fouzia Boulmedais in the Institute Charles Sadron, CNRS, Strasbourg.

Fourier transform Infra-Red spectroscopy (FTIR)

Fourier transform Infra-Red spectroscopy (FTIR) is other technique that allows to follow the growth of multilayer films.

Infrared (IR) spectroscopy is based on the interaction of IR light with matter. The infrared region considered is the mid-infrared (4500 cm^{-1} to 400 cm^{-1}). IR light passes through a sample and certain frequencies of the light are absorbed by the chemical bonds of the substance leading to molecular vibrations. The frequencies and intensities of absorbed IR light depend on the specific bond strengths and atoms of that molecule, being the absorption pattern known as a spectrum, unique for each material. An absorption band is characterized by the wavelength at which maximum absorption takes place and the intensity of absorption at this wavelength. In addition, the intensity of this band is proportional to the number of molecules of the material, so that IR spectrum provides not only qualitative, but also quantitative information. Taking into account these characteristics, the layer-by-layer deposition process can be followed by FTIR spectroscopy through recording the FTIR spectra after deposition of one or more polymer layers. The growth process is determined following the absorbance of one or more characteristic bands of the polymer or polymers that are being assembled. If the absorbance of these bands increases their intensity with the number of deposited layers, the growth of the film takes place.

FTIR measurements presented in this thesis were carried out in a Perkin Elmer Spectrum One FTIR Spectrometer. For the follow-up of the LbL process, the deposition of the polymer solutions was carried out on a polystyrene (PS) substrate with a thickness of 70 µm. The signal corresponding to PS was subtracted from the multilayer spectra.

3.2.2. Characterization techniques to determine morphological properties

Scanning Electron Microscopy (SEM)

Scanning electron microscopy (SEM) is a technique to examine and analyze the surface morphology of samples.

The electron beam from an electron gun column is demagnified by condenser lenses into a fine spot as small as 1 nm of diameter which is scanned across a selected area of the sample surface. Interactions between the electron beam and the sample give rise to different intensity signals which are collected by detectors and stored in the computer memory to be subsequently mapped as variations in brightness on the image display. The most widely used signal produced by the interaction of the primary electron beam with the sample is the secondary electron emission signal which varies with the topography of the sample surface being dark for recesses and bright for edges. The magnification of the image is determined by the ratio of the size of the displayed image to the size of the area scanned on the sample.[43, 44]

In this work a FESEM Hitachi model SU8000 with TE detector operated at 0.5-30 kV was employed.

Atomic Force Microscopy (AFM)

The operation method of an AFM is based on the surface forces acting on a sharp tip in close proximity to a surface.[45] Because of the long-range nature of the interaction forces, the vertical resolution of an AFM is typically less than a nanometer whereas the lateral resolution is determined by the tip radius and sample roughness. The sharp tip is usually supported at the end of a cantilever that is scanned over the surface of a sample. Information about the sample surface can be obtained by measuring how the deflection of the cantilever, which is caused by interactions between the tip and the surface, varies with position. In dynamic force microscopy the cantilever is made to vibrate at a specific frequency and the deflection of the tip is measured at this frequency. To measure cantilever motion while scanning, a laser is focused on the cantilever and the reflected light is directed onto a segmented photodiode.[45, 46]

When discussing the nature of the interaction force between tip and substrate, it is often convenient to approximate the tip as a sphere with radius R. This sphere then interacts with the sample via a number of possible forces that cause the cantilever to deflect. In contact mode, the tip exerts a force directly on the sample as it is scanned across it. In intermittent-contact or

tapping mode, the tip vibrates at its resonance frequency by action of a piezoelectric giving rise to a sinusoidal motion of the cantilever that is accurately monitored by the AFM control electronics.[45] This mode allows the characterization of soft materials such as polymers without damaging them.[46]

In this work AFM experiments were carried out in two different equipments. Multimode Scanning probe microscope (Veeco/Bruker), with a di NanoScope IVa Controller using the conventional height mode (tapping mode, normal AFM) at 320 kHz resonant frequency and a nominal force constant of 42 N/m in the Instituto de Ciencia y Tecnología de Polímeros, CSIC. Bruker Multimode 8, with a NanoScope V controller using the conventional height mode (tapping mode, normal AFM) at a scan rate of 0.5 and 1.5 in the group of Prof. T. Ezquerra in the Instituto de Estructura de la Materia, CSIC. The analysis of data was performed using the software NanoScope Analysis 1.5.

3.2.3. Characterization techniques to determine mechanical properties

Atomic Force Microscopy (AFM) nanoindentation measurements

AFM nanoindentation measurements were carried out using a Bruker Multimode 8, with a Nanoscope V controller in the group of Prof. T. Ezquerra in the Instituto de Estructura de la Materia, CSIC.

PeakForce Quantitative Nanomechanical Mapping (PF-QNM) is a contact AFM protocol which is based on the force-volume method. Force-distance curves are collected by nanoindentation of the sample in a point-by-point fashion. In this method, the piezo-scanner is oscillated at 2 kHz while the probe remains at rest. This fact enables a high speed and simultaneous capture of force-distance curves and topographic images.[47] The maximum force (peak force) is controlled at each pixel to obtain force-distance curves which are then used as feedback signal.

Figure 3.19 shows an example of the PF-QNM force-distance curve obtained from a measurement of a polymer film. The Z-axis reflects the distance ramped by the piezo-scanner in the vertical direction. The trace curve is obtained when the tip is approaching the surface of the sample and the retrace curve when the tip is withdrawing from it. As it can be observed, an attractive force appears when the tip is approaching the sample followed by an elastic regime in which the force is proportional to the deformation. The adhesion force is related to the minimum of the retrace force-distance curve (upon withdrawal) and the dissipation is the area between the trace and retrace of the force-distance curves.

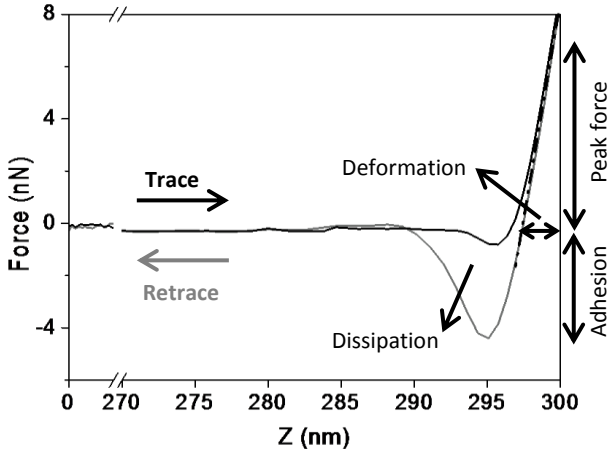

Figure 3.19. Force-distance curve while approaching the surface (trace) and withdrawal (retrace). The dashed line corresponds to fitting of the experimental results to the DMT model.

For the determination of the nanomechanical properties of multilayer films shown in Chapter 5, every tip radius was calibrated against a polystyrene standard of known elastic modulus (Bruker), considering the Derjaguin-Muller-Toporov (DMT) model[48] through equation 3.14.

$$E_r = \frac{3\left(F_{tip} - F_{adh}\right)}{4\sqrt{Rd^3}} \qquad (eq.3.14)$$

where E_r is the reduced Young modulus, F_{tip} is the force on the tip, F_{adh} is the adhesive force between the AFM tip and the sample, R is the AFM tip radius and d is the penetration depth. Provided that the tip Young modulus is much higher than the sample modulus, the reduced modulus (E_r) and the Young modulus of the sample (E_s) are related through equation 3.15.

$$E_s = \frac{E_r}{1 - \nu_s^2} \qquad (eq.3.15)$$

where ν is the Poisson's ratio value.

Analysis of the force-distance curves is automatically performed by a software and allows to extract the height, elastic modulus, adhesion force, deformation and dissipation simultaneously by application of the DMT model. The employment of the DMT model is justified by the fact that the chosen regime of applied forces allows us to study the nanomechanical response of multilayer films in the elastic regime, *i.e.*, without permanent deformation of the sample's surface. The Young´s Modulus is obtained by fitting the retrace curve using equations (3.14) and (3.15) and a Poisson´s ratio of 0.3.[48] Note in Figure 3.19 that the part of the force-distance curve

used to estimate the DMT modulus superimposed in both loading and unloading regime. To data analysis the software NanoScope Analysis 1.5 was employed.

3.2.4. Characterization techniques to determine the structure of LbL films

Grazing-incidence small-angle X-ray scattering (GISAXS)

GISAXS is a powerful technique to study nanostructures at the surface and in buried structures of thin films. GISAXS can provide information about lateral structures with sizes from few nanometers to few hundred nanometers. The incident X-ray beam impinges the sample at shallow angles (<1º), thus total external reflection on the surface may take place. By changing slightly the incident angle it is possible to vary the depth of the incident beam into the sample allowing to study the structural changes with the thickness. Due to the fact that the diffraction in GISAXS experiments is induced by a weak evanescent superficial wave, the use of X-ray synchrotron radiation is especially advantageous.[49, 50]

As can be shown in Figure 3.20, in a GISAXS experiment an X-ray beam impinges under an incident angle (α_i) onto the film surface. The intensity dispersed by the sample is collected by a 2D detector. α and ω are the scattering angles in vertical and horizontal direction. Both the direct beam and the reflected beam are blocked by a beam stop which protects the detector. The dispersion at low angles (GISAXS) takes place when the detector is far away from the sample and the maximum dispersion angle collected by it is low.[51]

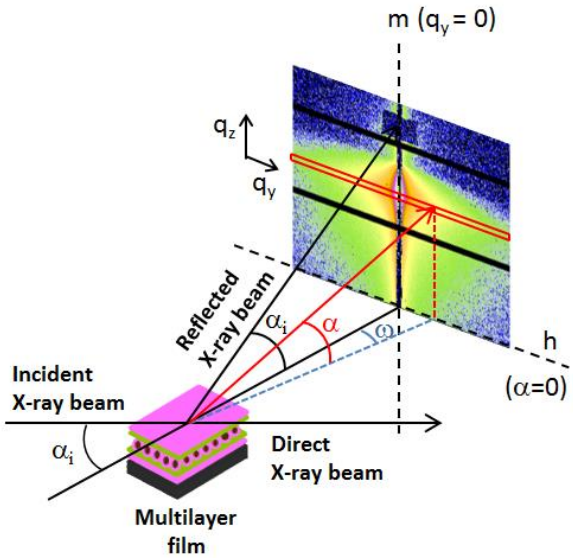

Figure 3.20. Schematic representation of a GISAXS experiment including a 2D GISAXS pattern of a multilayer film.

The information collected from these experiments can be interpreted as a function of the two orthogonal scattering vectors, q_y and q_z, which give information about structural correlations parallel and perpendicular to the plane of the sample, respectively.[50, 51]

$$q_y = \frac{2\pi}{\lambda} sin\omega cos\alpha \qquad (eq. 3.16)$$

$$q_z = \frac{2\pi}{\lambda} (sin\alpha_i + sin\alpha) \qquad (eq. 3.17)$$

Lateral correlation between scattering objects on the film surface can induce some scattered intensity which can be observed out of the meridian (line m) and generate intensity maximums related to the correlation maximums.[51]

GISAXS experiments reported in this thesis were carried out at BM26 beamline of the European Synchrotron Radiation Facility (ESRF) sited in Grenoble (France), using a wavelength of λ = 0,103 nm and a camera of 981 x 1043 pixels (size of the pixel 172 x 172 μm^2) to data acquisition. The detector employed was a PILATUS 1M and the distance sample-detector used in this work was 6.87 m. To data analysis the FIT2D software was employed.

Dual-Beam (Focused Ion Beam (FIB) – Scanning Electron Microscopy (SEM))

To determine the inner organization of the polymer films, dual beam FIB/SEM was employed.

The dual beam incorporates in a single system two columns, a focused ion beam (FIB) column and a scanning electron microscopy column (SEM). This combination is well suited for cross-section studies due to the fact that ion beam mills normal to the sample surface and the electron beam views the cross-section face. These two beams intersect with the sample in a coincident point allowing the ion milling and electron imaging of the same region. In addition, other components such as gas injectors and energy-dispersive X-ray spectroscopy (EDX) are also aligned in this position to achieve an optimum operation. The image obtained from a dual beam is a combination of the electron beam imaging and the ion beam imaging. Although the electron beam is the primary imaging tool which produces images with high resolution, the ion beam can improve it giving rise to a strong image contrast.[52]

These experiments were carried out in a Nova 200 NanoLab, FEI Company during my stay in the group of Prof. Gerardo Goya in the Institute of Nanoscience of Aragon. Films were coated with platinum for imaging with the FIB-SEM. SEM images were taken at 5 kV with a Field

Emission Gun (FEG) column, and a combined Ga-based 30 kV (10 pA) ion beam was used to cross-sectioning films. These investigations were completed by energy-dispersive X-ray spectroscopy (EDX) for chemical analysis.

Figure 3.21. Dual beam Nova 200 NanoLab, FEI Company installed in the Institute of Nanoscience of Aragon.

3.3. REFERENCES

1. Croisier, F.; Jérôme, C., Chitosan-based biomaterials for tissue engineering. *European Polymer Journal* **2013,** 49, (4), 780-792.

2. Xu, C.; Lei, C.; Meng, L.; Wang, C.; Song, Y., Chitosan as a barrier membrane material in periodontal tissue regeneration. *Journal of Biomedical Materials Research Part B: Applied Biomaterials* **2012,** 100, (5), 1435-1443.

3. Cook, M. T.; Tzortzis, G.; Khutoryanskiy, V. V.; Charalampopoulos, D., Layer-by-layer coating of alginate matrices with chitosan–alginate for the improved survival and targeted delivery of probiotic bacteria after oral administration. *Journal of Materials Chemistry B* **2013,** 1, (1), 52-60.

4. Lawrie, G.; Keen, I.; Drew, B.; Chandler-Temple, A.; Rintoul, L.; Fredericks, P.; Grøndahl, L., Interactions between alginate and chitosan biopolymers characterized using FTIR and XPS. *Biomacromolecules* **2007,** 8, (8), 2533-2541.

5. Signini, R.; Campana Filho, S. P., On the preparation and characterization of chitosan hydrochloride. *Polymer bulletin* **1999,** 42, (2), 159-166.

6. Amado, I. R.; Vázquez, J. A.; Pastrana, L.; Teixeira, J. A., Microbial production of hyaluronic acid from agro-industrial by-products: Molasses and corn steep liquor. *Biochemical Engineering Journal* **2017,** 117, Part A, 181-187.

7. Mero, A.; Campisi, M., Hyaluronic acid bioconjugates for the delivery of bioactive molecules. *Polymers* **2014,** 6, (2), 346-369.

8. Larkin, A. L.; Davis, R. M.; Rajagopalan, P., Biocompatible, detachable, and free-standing polyelectrolyte multilayer films. *Biomacromolecules* **2010,** 11, (10), 2788-2796.

9. Richert, L.; Lavalle, P.; Payan, E.; Shu, X. Z.; Prestwich, G. D.; Stoltz, J.-F.; Schaaf, P.; Voegel, J.-C.; Picart, C., Layer by layer buildup of polysaccharide films: physical chemistry and cellular adhesion aspects. *Langmuir* **2004,** 20, (2), 448-458.

10. Thiele, J.; Ma, Y.; Bruekers, S.; Ma, S.; Huck, W. T., 25th Anniversary article: designer hydrogels for cell cultures: a materials selection guide. *Advanced Materials* **2014,** 26, (1), 125-148.

11. Su, K.; Wang, C., Recent advances in the use of gelatin in biomedical research. *Biotechnology letters* **2015,** 37, (11), 2139-2145.

12. Palama, I. E.; Musaro, M.; Coluccia, A. M.; D'Amone, S.; Gigli, G., Cell uptake and validation of novel PECs for biomedical applications. *Journal of drug delivery* **2011,** 2011.

13. Szarpak, A.; Cui, D.; Dubreuil, F. d. r.; De Geest, B. G.; De Cock, L. J.; Picart, C.; Auzély-Velty, R., Designing hyaluronic acid-based layer-by-layer capsules as a carrier for intracellular drug delivery. *Biomacromolecules* **2010,** 11, (3), 713-720.

14. Lungu, C. N.; Diudea, M. V.; Putz, M. V.; Grudziński, I. P., Linear and Branched PEIs (Polyethylenimines) and Their Property Space. *International Journal of Molecular Sciences* **2016,** 17, (4), 555.

15. Vicennati, P.; Giuliano, A.; Ortaggi, G.; Masotti, A., Polyethylenimine in medicinal chemistry. *Current medicinal chemistry* **2008,** 15, (27), 2826-2839.

16. Brunot, C.; Ponsonnet, L.; Lagneau, C.; Farge, P.; Picart, C.; Grosgogeat, B., Cytotoxicity of polyethyleneimine (PEI), precursor base layer of polyelectrolyte multilayer films. *Biomaterials* **2007,** 28, (4), 632-640.

17. Rinaudo, M.; Milas, M.; Dung, P. L., Characterization of chitosan. Influence of ionic strength and degree of acetylation on chain expansion. *International Journal of Biological Macromolecules* **1993,** 15, (5), 281-285.

18. King, K., Changes in the functional properties and molecular weight of sodium alginate following γ irradiation. *Food hydrocolloids* **1994,** 8, (2), 83-96.

19. Pamies, R.; Cifre, J. G. H.; Martínez, M. d. C. L.; de la Torre, J. G., Determination of intrinsic viscosities of macromolecules and nanoparticles. Comparison of single-point and dilution procedures. *Colloid and Polymer Science* **2008,** 286, (11), 1223-1231.

20. Dash, M.; Chiellini, F.; Ottenbrite, R. M.; Chiellini, E., Chitosan—A versatile semi-synthetic polymer in biomedical applications. *Progress in Polymer Science* **2011,** 36, (8), 981-1014.

21. Arteche Pujana, M. Nanogeles de quitosano modificados con entrecruzantes biocompatibles para su aplicación en la liberación selectiva de fármacos anticancerígenos. Universidad del País Vasco, Leioa, **2013**.

22. Zawadzki, J.; Kaczmarek, H., Thermal treatment of chitosan in various conditions. *Carbohydrate polymers* **2010,** 80, (2), 394-400.

23. Bengisu, M.; Yilmaz, E., Oxidation and pyrolysis of chitosan as a route for carbon fiber derivation. *Carbohydrate polymers* **2002,** 50, (2), 165-175.

24. Soares, J. P.; Santos, J. E.; Chierice, G. O.; Cavalheiro, E. T. G., Thermal behavior of alginic acid and its sodium salt. *Eclética Química* **2004,** 29, 57-64.

25. Cai, W.; Wan, J., Facile synthesis of superparamagnetic magnetite nanoparticles in liquid polyols. *Journal of Colloid and Interface Science* **2007,** 305, (2), 366-370.

26. Sundar, S.; Mariappan, R.; Piraman, S., Synthesis and characterization of amine modified magnetite nanoparticles as carriers of curcumin-anticancer drug. *Powder Technology* **2014,** 266, 321-328.

27. Khalkhali, M.; Rostamizadeh, K.; Sadighian, S.; Khoeini, F.; Naghibi, M.; Hamidi, M., The impact of polymer coatings on magnetite nanoparticles performance as MRI contrast agents: a comparative study. *DARU Journal of Pharmaceutical Sciences* **2015,** 23, (1), 1.

28. Yan, H.; Zhang, J.; You, C.; Song, Z.; Yu, B.; Shen, Y., Influences of different synthesis conditions on properties of Fe 3 O 4 nanoparticles. *Materials Chemistry and Physics* **2009,** 113, (1), 46-52.

29. Jiang, W.; Chen, X.; Niu, Y.; Pan, B., Spherical polystyrene-supported nano-Fe3O4 of high capacity and low-field separation for arsenate removal from water. *Journal of Hazardous Materials* **2012,** 243, 319-325.

30. Calatayud, M. P.; Sanz, B.; Raffa, V.; Riggio, C.; Ibarra, M. R.; Goya, G. F., The effect of surface charge of functionalized Fe3O4 nanoparticles on protein adsorption and cell uptake. *Biomaterials* **2014,** 35, (24), 6389-6399.

31. Bloemen, M.; Brullot, W.; Luong, T. T.; Geukens, N.; Gils, A.; Verbiest, T., Improved functionalization of oleic acid-coated iron oxide nanoparticles for biomedical applications. *Journal of Nanoparticle Research* **2012,** 14, (9), 1100.

32. Iida, H.; Takayanagi, K.; Nakanishi, T.; Osaka, T., Synthesis of Fe 3 O 4 nanoparticles with various sizes and magnetic properties by controlled hydrolysis. *Journal of Colloid and Interface Science* **2007,** 314, (1), 274-280.

33. Woollam, J. A.; Snyder, P. G., Fundamentals and applications of variable angle spectroscopic ellipsometry. *Materials Science and Engineering: B* **1990,** 5, (2), 279-283.

34. Cobet, C., Ellipsometry: A Survey of Concept. In *Ellipsometry of functional organic surfaces and films*, Springer: Heidelberg, 2014; pp 1-26.

35. Fujiwara, H., Introduction to Spectroscopic Ellipsometry. In *Spectroscopic Ellipsometry: Principles and Applications*, John Wiley & Sons, Ltd: Chichester, 2007; pp 1-11.

36. Bermejo, J. S. Modificación química y caracterización de superficies poliméricas. Determinación del perfil de profundidad. Universidad Complutense de Madrid, Madrid, **2001**.

37. Garcia-Caurel, E.; Ossikovski, R.; Foldyna, M.; Pierangelo, A.; Drévillon, B.; De Martino, A., Advanced Mueller Ellipsometry Instrumentation and Data Analysis. In *Ellipsometry at the Nanoscale*, Springer: Heidelberg, 2013; pp 31-144.

38. Poelman, D.; Smet, P. F., Methods for the determination of the optical constants of thin films from single transmission measurements: a critical review. *Journal of Physics D: Applied Physics* **2003,** 36, (15), 1850.

39. Sauerbrey, G., Verwendung von Schwingquarzen zur Wägung dünner Schichten und zur Mikrowägung. *Zeitschrift für Physik* **1959,** 155, (2), 206-222.

40. Dixon, M. C., Quartz crystal microbalance with dissipation monitoring: enabling real-time characterization of biological materials and their interactions. *Journal of Biomolecular Techniques* **2008,** 19, (3), 151-158.

41. Alves, N. M.; Picart, C.; Mano, J. F., Self Assembling and Crosslinking of Polyelectrolyte Multilayer Films of Chitosan and Alginate Studied by QCM and IR Spectroscopy. *Macromolecular Bioscience* **2009,** 9, (8), 776-785.

42. Boudou, T.; Crouzier, T.; Auzély-Velty, R.; Glinel, K.; Picart, C., Internal Composition versus the Mechanical Properties of Polyelectrolyte Multilayer Films: The Influence of Chemical Cross-Linking. *Langmuir* **2009,** 25, (24), 13809-13819.

43. Vernon-Parry, K., Scanning electron microscopy: an introduction. *III-Vs Review* **2000,** 13, (4), 40-44.

44. Aharinejad, S. H.; Lametschwandtner, A., Fundamentals of Scanning Electron Microscopy. In *Microvascular Corrosion Casting in Scanning Electron Microscopy*, Springer: Wien, 1992; pp 44-51.

45. Reifenberger, R., Introduction to Scanning Probe Microscopy. In *Fundamentals of Atomic Force Microscopy. Part I: Foundations*, World Scientific: Singapore, 2015; Vol. 4, pp 1-20.

46. Garcia, R.; Herruzo, E. T., The emergence of multifrequency force microscopy. *Nature nanotechnology* **2012,** 7, (4), 217-226.

47. Marius, C.; Seth, L. Y.; Vladimir, V. T., Recent advances in micromechanical characterization of polymer, biomaterial, and cell surfaces with atomic force microscopy. *Japanese Journal of Applied Physics* **2015,** 54, 1-13.

48. Derjaguin, B. V.; Muller, V. M.; Toporov, Y. P., Effect of contact deformations on the adhesion of particles. *Journal of Colloid and Interface Science* **1975,** 53, 314-326.

49. Santoro, G.; Yu, S., Grazing Incidence Small Angle X-Ray Scattering as a Tool for In- Situ Time-Resolved Studies. In *X-ray Scattering*, InTech: Rijeka, 2017; pp 29-52.

50. Roth, S. V., A deep look into the spray coating process in real-time—the crucial role of x-rays. *Journal of Physics: Condensed Matter* **2016,** 28, (40), 403003.

51. Rebollar, E.; Pérez, S.; Hernández, J. J.; Martín-Fabiani, I.; Rueda, D. R.; Ezquerra, T. A.; Castillejo, M., Assessment and formation mechanism of laser-induced periodic surface structures on polymer spin-coated films in real and reciprocal space. *Langmuir* **2011,** 27, (9), 5596-5606.

52. Young, R. J.; Moore, M. V., Dual-Beam (FIB-SEM) Systems. . In *Introduction to Focused Ion Beams: Instrumentation, Theory, Techniques and Practice*, Springer US: Boston, 2005; pp 247-268.

CHAPTER 4

Layer-by-layer films from natural polymers. Study of the growth mechanism

In this chapter the LbL assembly of two different multilayer systems based on natural polymers was studied. In the first one comprising alginate and chitosan, the optimal conditions for the spray LbL assembly, concentration and pH, were evaluated and the growth mechanism for films built up through spray LbL was studied. In addition, a comparison between dipping assisted LbL and spray assisted LbL was stablished. In the second system, the optimal conditions for the LbL assembly of hyaluronic acid and poly(allylamine hydrochloride), the kind of assembly process and the influence of a third component, alginate-Fe^{2+}, in the buildup process were analyzed.

4.1. INTRODUCTION

In recent decades, layer-by-layer (LbL) assembly has attracted an increasing attention to fabricate polymeric films due to its simplicity, versatility and nanoscale control of film thickness.[1] The fundamentals and differences between spray LbL and dipping LbL techniques were described in detail in the chapter 2.

The growth of multilayer structures can be determined by multiple techniques. Besides the employment of ellipsometry,[2] quartz crystal microbalance[3] and FTIR spectroscopy[4] fully explained in the chapter 3, there are other techniques to follow the multilayer deposition process. Confocal laser microscopy (CLSM) which determines the thickness between fluorescently-labeled polyelectrolytes assembled into the multilayer structure has been employed to determine the thickness corresponding to the Alg layer incorporated between in PLL/HA or PAH/PSS multilayers by utilization of fluorescent PLL or PAH layers.[5, 6] Surface plasmon resonance (SPR) is highly sensitive to refractive index changes at the surface and can be used to monitor the adsorption process and cyclic voltammetry is an electrochemical procedure used to follow the growth by acquiring information on the redox behavior of electrochemically active species.[7, 8] Other useful technique to follow the multilayer assembly process is dual-polarization interferometry (DPI), which measures changes in the thickness and the refractive index of adsorbed layers in situ. In the case of PLL/PGA films, DPI data for the thickness and refractive index were more consistent than these ones obtained by ellipsometry.[9] Optical waveguide lightmode spectroscopy (OWLS) is a highly sensitive method (precision ~ 1 ng/cm^2) for measuring macromolecular adsorption kinetics of multilayer films at the solid-liquid interface. Detection system is based on excitation of guided modes through a polarized laser beam directed at the surface of the sample. Afterwards, the mass and thickness of every layer can be determined making use of an optical model.[10] Scanning angle reflectometry (SAR) is other optical technique to study the structural parameters characterizing thin macromolecular adsorbed

films. It measures the changes in the reflected intensity of a TM-wave around the Brewster angle before and after each deposition step.[11] In the case of polyelectrolyte multilayers films which can be are formed by an homogeneous and isotropic monolayer, their optical properties can be defined using the monolayer model in both techniques, SAR and OWLS. However, for multilayer films more complex, the experimentally determined parameters depend strongly on the model used for the analysis and there are significant differences between methods, the mass and the thickness are model independent for OWLS and extremely sensitive to the model for SAR.[11] The growth process can also be studied by UV-Vis spectroscopy which determines the cumulative absorption attributed to stepwise deposition of UV-active polyelectrolytes during the LbL adsorption following the absorbance of one or more characteristic bands of the polymer or polymers that we are assembling.[12] For the assembly of oppositely charged polyelectrolytes, the buildup process can be followed by charge reversal changes through the zeta potential measurement by Dynamic light scattering (DLS). As an example, the assembly of anionic poly(4-styrenesulfonic acid) and cationic poly(diallyldimethylammonium chloride) has been followed employing this technique, but it has the disadvantage that it is difficult to translate the zeta potential measurement to a real surface charge density, especially due to the fact that the surface charge is spread out into a thin film.[13] The growth of multilayer polymer structures can be also monitored by measuring the wettability of every assembled polymer layer through contact angle measurements of polymers with different hydrophobicity, as it is the case of poly(methacrylic acid) (PMAA) and poly(4-vinylpyridine-co-(aminopropyl)methacrylamide) (PVP-NH_2) which have contact angles of ~15º and ~30º, respectively.[14] In contrast to optical techniques, although zeta potential and contact angle allow to follow the deposition process, the thickness of every deposited layer cannot be obtained.

Most of these techniques allow to determine the thickness of every layer and/or the global thickness of the multilayer structure. In addition to these, Atomic force microscopy (AFM) is other useful technique to obtain the thickness by making a scratch on the sample and recording height profile of the transition zone, then the thickness is obtained from the depth profile of this image.[2] Scanning electron microscopy also allows to determine the thickness of multilayer films by measuring their cross-section.[4]

To the best of our knowledge, first studies regarding to the multilayer assembly of chitosan (Chi) and alginate (Alg), the main polymer system employed in this PhD work, were carried out over particulate substrates by dipping LbL with a centrifugation step after each deposited layer.[15, 16] The buildup of multilayer Chi/Alg films on planar substrates through dipping LbL was carried

out later to study the effect of the assembly pH on the kinetics and surface composition of these Chi/Alg films in situ through surface plasmon resonance (SPR) spectroscopy.[17] More studies related to the assembly of Alg/Chi films have been explained in detail in the chapter 2.

With regards to HA/PAH films, one of the most important properties is their swelling behavior which influences the hydration of the film and the loading and release performance. The influence of the polymer concentration and pH on the HA/PAH assembly by dipping and later swelling was studied with the objective of using these multilayer films for potential applications of controlled release, membrane filtration and biomaterial coatings.[18, 19] Assembly of HA/PAH by dipping has been also used to make multilayer microcapsules with the ability of remaining stable outside cells and breaking open once internalized by cells which allows to use them as carriers for intracellular drug delivery.[20, 21]

The aim of this chapter is the determination of the growth mechanism of multilayer films fabricated from two different polymer systems, Chi/Alg and PAH/HA. The main experimental probes were ellipsometry and quartz crystal microbalance. As a first step, the determination of the experimental conditions for the LbL assembly was evaluated through precipitation tests. Multilayer Alg/Chi films obtained here will be employed in the chapters 5, 6 and 7 in order to study their nanomechanical properties as well as their use in biomedical applications. In the second system formed by PAH and HA, a gel-like layer made of Alg-Fe^{2+} was incorporated in an intermediate position with the goal of investigate the use of these nanostratified films as drug delivery systems in the future.

4.2. EXPERIMENTAL PART

4.2.1. Materials

Low molecular weight chitosan (Chi) (448869, lot SLBG1673V), sodium alginate (Alg) (A2158, lot 090M0092V), poly(allylamine hydrochloride) (283223, lot MKBJ4277V), iron(II) chloride tetrahydrate, poly(ethylenimine) (PEI) with a molecular weight (M_w) of 25000 and acetic acid were supplied by Aldrich. Sodium acetate anhydrous was purchased from Panreac. Hyaluronic acid was supplied by Soliance (Primalhyal 400, lot 12274F). More information about these materials is detailed in the chapter 3.

4.2.2. Fabrication of multilayer films through LbL assembly

Two different multilayer films have been prepared through LbL assembly and characterized afterwards. The first system was based on the assembly of alginate (polyanion) and chitosan (polycation) and, the second one, was formed by hyaluronic acid (polyanion) and poly(allylamine hydrochloride) (polycation). In the last system, the influence of the introduction of a gel-like layer, Alg-Fe^{2+}, in the buildup process was also studied.

Precipitation studies

A series of precipitation studies were first carried out to determine the optimal conditions of concentration and pH for the formation of interactions between the polycation and the polyanion which appear through the formation of a precipitate.

In the case of the assembly of alginate and chitosan, different buffer solutions at pH 3 and pH 5 were used to dissolve alginate and chitosan. These buffer solutions were prepared from acetic acid 0.1M and sodium acetate 0.1M. Both polymers were dissolved at three different concentrations, 1.0, 3.0 and 5.0 mg/mL. Aliquots of 1 mL of both polymer solutions varying the concentrations and pH of alginate and chitosan were mixed in a vial and precipitation results were observed after 72 hours.

With regards to the assembly of hyaluronic acid and poly(allylamine hydrochloride), both polymers were dissolved in NaCl 0.15M at two different concentrations for each polymer, 1.2 and 2.5 mg/mL for HA and 1.0 and 2.0 mg/mL for PAH. Aliquots of 1 mL of both polymer solutions varying the concentrations of PAH and HA were mixed in a vial and precipitation results were observed after 24 hours at room temperature. A particular PAH/HA/Alg-Fe^{2+} multilayer system was prepared by formation of a gel-like layer in an intermediate position of the PAH/HA multilayer structure giving rise to nanostratified films. The gel-like layer was formed by an alginate gel crosslinked through ions Fe^{2+}. Therefore, the interactions between Alg and ions Fe^{2+} were also studied. Aliquots of 1 mL of both solutions varying the Fe^{2+} concentration from 10 to 40 mg/mL and using a fixed alginate concentration of 5.0 mg/mL were mixed in a vial and results corresponding to the formation of a gel were observed after 24 hours by the inverted tube method.

Preparation of the substrates

All multilayer films were built on a substrate. Three different kinds of substrates were employed, polystyrene, silicon and glass depending on the kind of characterization technique used.

Glass substrates with diameters of 12 and 14 mm were supplied by Marienfeld-Superior and cleaned with ethanol. Silicon substrates were purchased from Siegert, cleaned with piranha solution (3:1 H_2SO_4/H_2O_2) for 10 minutes and, then, rinsed extensively with water. Polystyrene (PS) substrates with a thickness of 70 μm were obtained by solvent casting of 5 mL of a polystyrene solution (5 %w/v in tetrahydrofuran (THF)) in a Petri dish of 60 mm diameter.

As these substrates are neutral or negatively charged, a first layer of polyethylenimine (PEI) was deposited providing a positively charged homogenous substrate. For that purpose, substrates were immersed in a solution of 1.0 mg/mL PEI for 5 min, rinsed in a solution of Milli-Q water for 2 min and subsequently dried with pressurized air at 1-1.5 bar.

Multilayer films obtained through spray assisted LbL

Multilayer films fabricated in this chapter as well as in chapters 5 and 6 were built up manually using the spray equipment shown in the Figure 4.1.

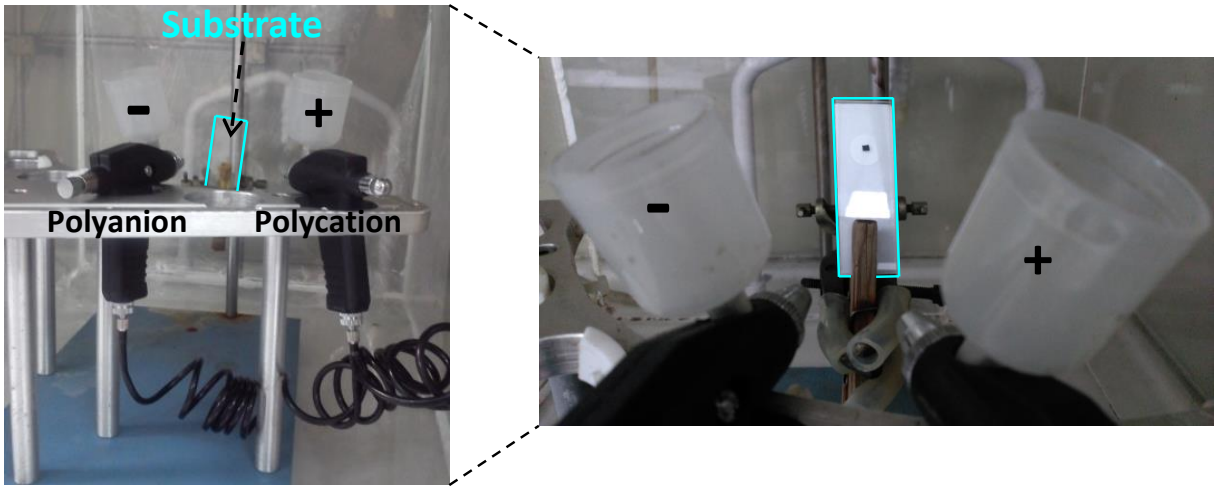

Figure 4.1. Image of the manual spray deposition system installed in the laboratory and magnification of the substrate area.

Multilayer films were built on a substrate (polystyrene, silicon or glass) functionalized with PEI. During the spraying process, the substrate was inclined 45° with respect to the vertical to allow

the drainage of the solution. The multilayer films were built by a sequential spraying of the polyanion and polycation solutions as can be observed in the Scheme 4.1. The spray process was carried out manually and the repeatability is guaranteed because the air brush is placed at a fixed distance in relation to the sample (100 mm) and the spray of the polymer solutions is controlled by the air pressure (150 bar) and the deposition time (5 s).

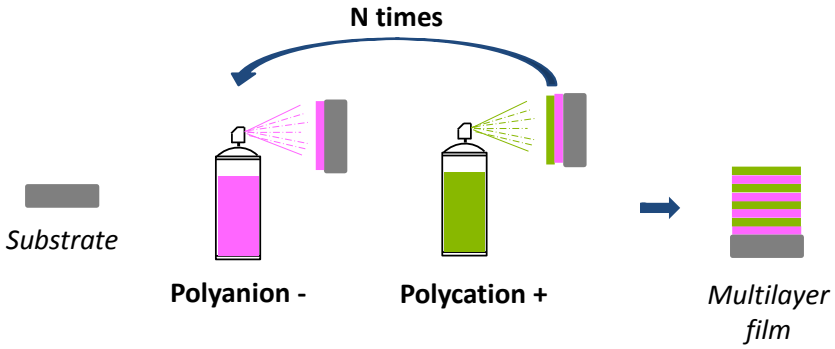

Scheme 4.1. Schematic diagram of the sequential assembly process through spray LbL followed for the preparation of multilayer films.

In the case of multilayer films composed by alginate and chitosan, the Alg solution was sprayed onto the substrate for 5 s. After a waiting time of 15 s, Chi solution was sprayed for 5 s. After an additional waiting time of 15 s, the cycle was repeated until obtaining the desired number of bilayers. Samples were denoted as $(Alg/Chi)_n$ where *n* stands for the number of bilayers. Note that a bilayer is the basic unit of the system, composed of a layer of each polymer. These films will also be employed in the chapters 5, 6 and 7.

For the buildup of multilayer films based on hyaluronic acid and poly(allylamine hydrochloride), HA and PAH solutions were sprayed sequentially onto the substrate for 5 s with a waiting time of 15 s between deposition steps. The cycle was repeated until obtaining the desired number of bilayers and samples were denoted as $(HA/PAH)_n$ where *n* stands for the number of bilayers.

Multilayer nanocomposite Alg/Chi films with magnetic nanoparticles (NPs) will be built up in chapters 5 and 6 using this technique.

Note. At the end of this thesis, an automatic spray deposition equipment (ND-SP spray coater from Nadetech innovations, Spain) has been bought (Figure 4.2). Multilayer Alg/Chi films with tamoxifen will be fabricated in the chapter 7 using this equipment and following the same procedure above mentioned with the same experimental conditions, an air brush-sample distance of 100 mm, air pressure (150 bar) and deposition time (5 s).

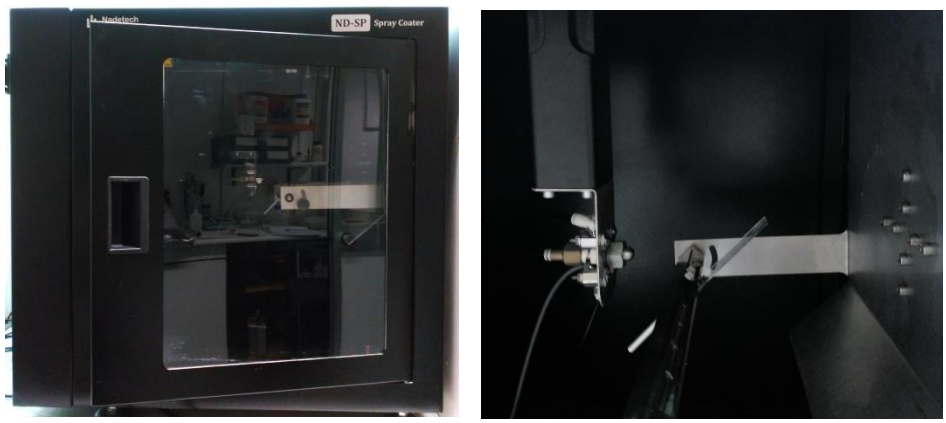

Figure 4.2. Image of the automatic spray deposition system installed in the laboratory.

Multilayer films obtained through dipping assisted LbL

Multilayer films were built by sequential dipping of the substrate in the polyanion and polycation solutions with a rinsing step between them, as can be observed in the Scheme 4.2. Note that the deposition takes place on both sides of the substrate; in the schematic representation it is only shown one side but it must be taken into account that on the other side it occurs the same.

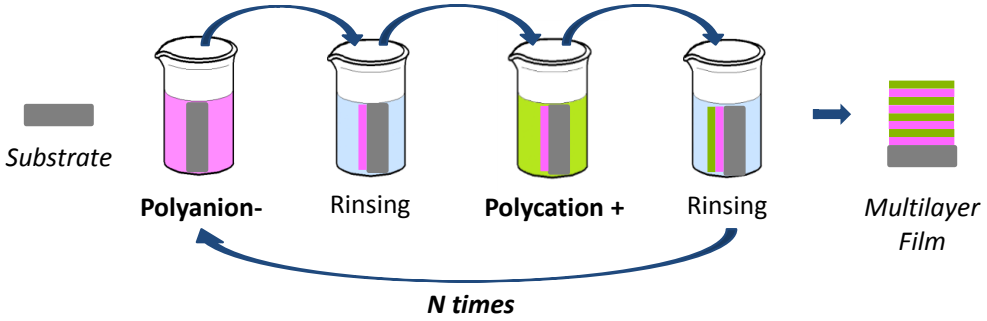

Scheme 4.2. Schematic diagram of the sequential assembly process through dipping LbL for the preparation of multilayer films.

In the case of multilayer films based on alginate and chitosan, the silicon substrate functionalized with PEI was immersed in Alg solution (1.0, 2.5 and 5.0 mg/mL) for 5 min and then in buffer pH 3 solution for 2 min. After that, it was immersed in Chi solution (1.0 mg/mL) for 5 min and then in buffer pH 5 for 2 min. The cycle was repeated until obtaining the desired number of bilayers. Samples were denoted as $(Alg/Chi)_n$ where *n* stands for the number of bilayers. Note that a bilayer is the basic unit of the system, composed of a layer of each polymer. These films will also be employed in the chapter 5.

Another multilayer system composed of Alg/Chi with alginate-based magnetic ferrofluid (Alg/Chi/NPs) will be reported in chapter 5.

With regards to multilayer films formed by hyaluronic acid and poly(allylamine hydrochloride), the silicon substrate functionalized with PEI was immersed in the HA solution (1.2 and 2.5 mg/mL) for 5 minutes and rinsed by immersion in NaCl 0.15M for 2 minutes. After that, the film was immersed in the PAH solution (1.0 and 2.0 mg/mL) for 5 minutes and, then rinsed by immersion in NaCl 0.15M for 2 minutes. The cycle could be repeated until getting the desired number of bilayers. Samples were denoted as $(HA/PAH)_n$ where *n* stands for the number of bilayers.

4.2.3. Determination of the thickness

Ellipsometry

Measurements of the film thickness were carried out with a PLASMOS SD 2300 ellipsometer operating at the single wavelength of 632.8 nm and a constant angle of 70°. Due to the inherent limit of ellipsometry to simultaneously determine the refractive index and the film thickness for very thin films, the refractive index of all films was assumed to be constant at 1.465.[22] While this procedure will lead to slightly incorrect values with respect to the absolute film thicknesses, it allows for the quick and precise determination of relative film thicknesses. Thickness values obtained with the assumption of a fixed refractive index for all films are of better precision than required for the comparison of film growth data as in this PhD work. For each substrate studied, 10 different thickness measurements were randomly taken on different film regions over an area of a few cm^2 of the film surface.

Scanning electron microscopy (SEM)

The cross section of films was observed by scanning electron microscopy (SEM) using a Hitachi SU 8000 microscope operating at 0.8 kV. The average thickness was determined by measuring the width of the cross section in the SEM micrographs in five different points.

Quartz crystal microbalance

The buildup of $(HA/PAH)_n$ films on a gold quartz crystal was followed in situ by quartz crystal microbalance-dissipation (QCM-D) on a Q-sense D300 apparatus from Q-Sense AB (Gothenburg, Sweden) at room temperature. This technique has been described in the Chapter 3.

At the beginning, the crystal was put into contact with NaCl 0.15M (buffer baseline) for 10 min. After that and before starting the experiment, a first layer of PEI (1.0 mg/mL) was deposited for 5 min. The multilayer $(HA/PAH)_5$ film was built through alternate adsorption of the polyelectrolyte solutions, HA (1.2 mg/mL) and PAH (0.3 mg/mL), on the crystal for 5 min approximately, until reaching a *plateau*. A rinsing step of 5 min with NaCl 0.15M was included between the adsorptions of each polyelectrolyte. These durations were sufficient to reach constant values for the frequency changes and hence a constant amount of deposited polyelectrolyte. After 5 HA/PAH bilayers, a layer of Alg with a concentration of 5.0 mg/mL was adsorbed for 5 min and then, without rinsing, the iron solution (20 mg/mL) was injected for 5 min with the objective of interact with alginate to form a gel.[23] After that, a new cycle of *m* bilayers PAH/HA was carried out. Samples were denoted as $(HA/PAH)_5Alg\text{-}Fe^{2+}(PAH/HA)_m$, where *m* stands for the number of bilayers after the Alg deposition.

The Δf and ΔD results obtained from QCM experiments were analyzed with the software QTools 3 data analysis. This software was also used to numerically fit the data to the Voigt model to obtain the thickness and viscosity of the film. The fixed parameters used for this model were the bulk liquid density (ρ_B=1000 kg/m^3), the bulk liquid viscosity (η_B= 1 mPa·s) and a fixed layer density (ρ_l= 1000 kg/m^3).

4.3. RESULTS AND DISCUSSION

4.3.1. Multilayer Alg/Chi films

Optimization of the experimental conditions for LbL assembly

It is expected that negatively charged Alg and positively charged Chi interact electrostatically under determined pH conditions (Scheme 4.3). Chi has a pKa of 6.3 and at a pH lower than pKa, it is positively charged. On the other hand, Alg has a pKa of 3.5 attributed to the carboxylic acid group which provides a negative charge even at low pH due to its deprotonation at pH > pKa.[24]

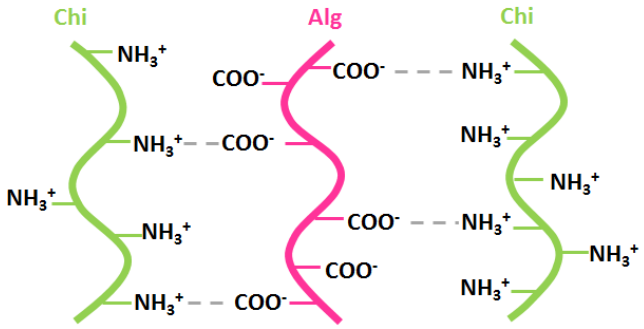

Scheme 4.3. Schematic representation of the electrostatic interactions between alginate (Alg) and chitosan (Chi).

The interactions between the carboxylate group of alginate (COO^-) and the protonated amine of chitosan (NH_3^+) through electrostatic forces can give rise to the formation of a precipitate.[24]

Chi and Alg solutions with concentrations from 1.0 to 5.0 mg/mL and pH 3 and 5 were mixed in all possible combinations (pH and concentration) and kept at room temperature up to 72 hours, to establish the conditions which produced greater amount of precipitate and, therefore, higher number of electrostatic interactions. These results are illustrated in the Figure 4.3.

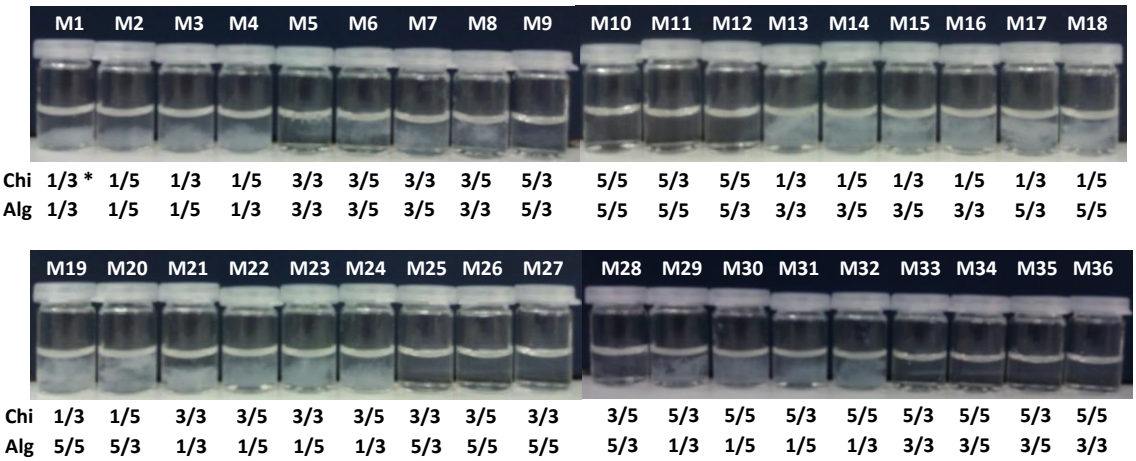

Figure 4.3. Experimental conditions used to carry out precipitation tests. *1/3, the first number indicates the concentration in mg/mL and the second refers to pH.* M1 (Chi 1/3, Alg 1/3) corresponds to a mixture of chitosan whose concentration is 1 mg/mL and pH 3, with alginate, whose concentration is 1 mg/mL and pH 3.

As can be observed in Figure 4.3, when alginate and chitosan concentrations are coincident, samples were transparent (M1-M12) assessing that precipitate is not formed. In the cases where Alg and Chi concentrations were 3.0 and 5.0 mg/mL respectively (M25-M28), the precipitate is not observed indicating that minimum number of interactions takes place. These conditions are similar for Alg and Chi concentrations of 5.0 and 3.0 mg/mL, respectively (M33-M36). An

increase in polymer-aggregation precipitation is observed in samples with a Chi concentration of 1.0 mg/mL and alginate concentrations of 3.0 and 5.0 mg/mL (M13-M20), which show the highest amount of precipitate. The precipitate induced by the polymer aggregation was also observed in samples with Alg concentration of 1.0 mg/mL and Chi concentrations of 3.0 and 5.0 mg/mL (M21-M24, M29-M32) but in lower extension.

The greatest amount of precipitate was obtained when chitosan concentration was 1.0 mg/mL indicating that a higher number of interactions took place. For that reason, it was the concentration chosen for the next LbL experiments. With regards to alginate, only with precipitation tests, we could not discard between 3.0 and 5.0 mg/mL.

Concerning the pH effect, at pH 3 for both polymer solutions, precipitate was formed when Chi concentration was 1.0 mg/mL and Alg concentrations 3.0 and 5.0 mg/mL. At pH 5 for both polymer solutions, the formation of a precipitate took place for Alg concentration of 1.0 mg/mL and Chi concentrations of 3.0 and 5.0 mg/mL. With these results, it is not possible to choose the pH conditions. Taking into account the previous results obtained by other authors for $(Alg/Chi)_n$ films built up via dipping LbL,[3, 25] knowing that the higher growth of these films took place at pH 5 for chitosan and pH 3 for alginate,[4] as well as the fact that when the assembly pH of alginate is 3, the assembled structure is relatively homogeneous due to alginate molecules are adsorbed homogeneously on the surface,[26] we selected the following conditions to carry out the layer-by-layer deposition process, Chi with a concentration of 1.0 mg/mL at pH 5 and Alg with concentrations from 1.0 to 5.0 mg/mL at pH 3.

Determination of interactions between Alg and Chi in LbL films

In order to determine the presence of interactions between Alg and Chi in the multilayer films, a FTIR analysis was carried out. FTIR spectra of chitosan, sodium alginate and a multilayer $(Alg/Chi)_{40}$ film are shown in Figure 4.4.

Chitosan (green line), with a deacetylation degree of 81%, shows a band at 1574 cm^{-1} assigned to amide II and amine and a shoulder at 1650 cm^{-1} corresponding to amide I.[24] In addition, it can be observed the C-O-C vibrations and C-N vibrations at 1152 cm^{-1} as well as the CH_2 flexion at 1412 cm^{-1}. Peaks in the region 1081 – 1014 cm^{-1} are attributed to the skeletal vibrations involving C-O stretching.[27]

Sodium alginate (pink line) exhibits two characteristics peaks at 1611 and 1415 cm^{-1} assigned to the asymmetric and symmetric vibrations of carboxylate group, respectively.[24] The bands located

at 1125, 1091, 1031 and 948 cm^{-1} are assigned to C-C stretching, C-O stretching, C-O-C stretching and C-O stretching, respectively.[27]

In the multilayer film spectrum (blue line), two new bands appears at 1710 y 1735 cm^{-1} which are not observed in the polymer spectra. The band at 1710 cm^{-1} is attributed to acetic acid residues in the film and the peak at 1735 cm^{-1} is due to the protonation of the carboxylate group of the alginate. The shoulder at 1530 cm^{-1} indicates that amine group of chitosan is protonated. The band located at 1618 cm^{-1} is attributed to the amide II of chitosan which is, in turn, overlapped with the band corresponding to the amine of chitosan together with the asymmetric vibration of the carboxylate group of alginate. This band decreases their intensity due to the electrostatic interactions between the amine groups of Chi and the carboxylate group of Alg. The presence of the peak at 1416 cm^{-1}, characteristic of the carboxylate group of alginate (COO^-), together with the shoulder at 1530 cm^{-1}, belonging to the protonated amine group of chitosan (NH_3^+), point out to the existence of electrostatic interactions between both polymers.[24] The new band at 1735 cm^{-1} corroborates the existence of electrostatic interactions between both polymers in the multilayer film.[27]

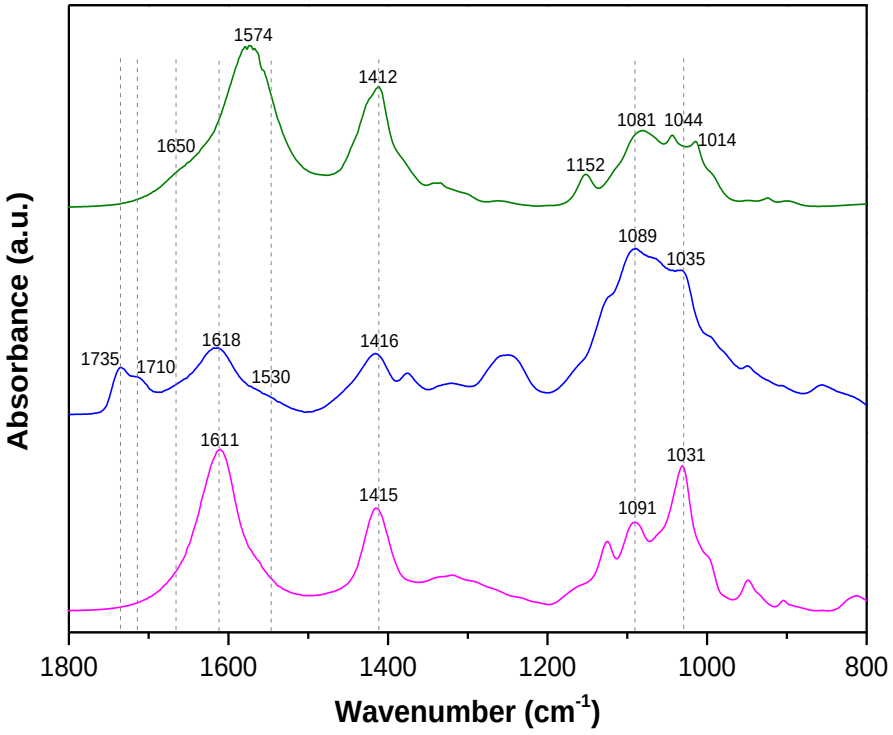

Figure 4.4. FTIR spectra of chitosan (green line), alginate (pink line) and multilayer $(Alg/Chi)_{40}$ film (blue line) with their characteristic peaks in the range 1800 – 800 cm^{-1}.

Determination of the thickness as a function of the number of bilayers

Multilayer systems formed by Chi and Alg have been prepared with different conditions of concentration and number of bilayers as well as two different LbL fabrication techniques, spray or dipping.

- *Influence of the method of preparation (spray vs. dipping)*

The influence of the method of preparation, spray LbL or dipping LbL, on the growth of multilayer $(Alg/Chi)_n$ films was studied for films prepared with concentrations of Alg and Chi fixed at 5.0 mg/mL and 1.0 mg/mL, respectively. Figure 4.6 shows the evolution of the thickness of $(Alg5/Chi)_n$ films as a function of the number of bilayers (n).

As it can be observed, the thickness of $(Alg5/Chi)_n$ films increases linearly with the number of bilayers, up to 5 bilayers, for both preparation methods being much higher in the case of spray LbL. Films grow at a rate of 2 nm/layer in the dipping method whereas in the spray LbL growth rate is 20 nm/layer, one order of magnitude greater. The total thickness of a film with 5 bilayers is 23.4 ± 0.9 nm using dipping LbL and 217.2 ± 15.9 nm employing spray LbL.

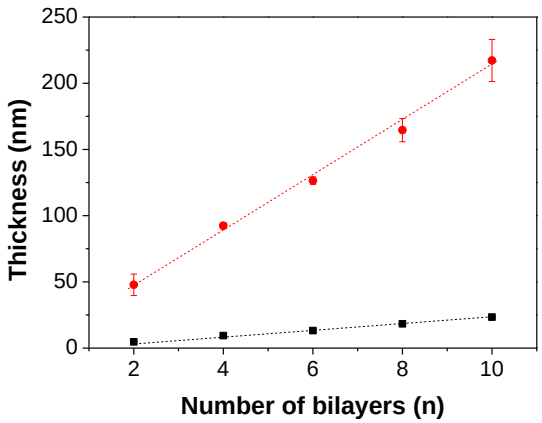

Figure 4.6. Evolution of $(Alg5/Chi)_n$ film thickness, measured by ellipsometry, vs. the number of bilayers. The films were obtained by dipping LbL (■) and spray assisted LbL (●) with Alg concentration at 5.0 mg/mL. Dashed lines are a guide to the eye.

Morphological changes in the cross section of $(Alg5/Chi)_n$ films prepared by spray LbL and dipping LbL can be analyzed by SEM. Figure 4.7 shows the cross section micrographs of representative $(Alg5/Chi)_{20}$ films built up by dipping LbL (Figure 4.7a) and spray LbL (Figure 4.7b). The average thicknesses of these films, determined by measuring the cross section in the SEM micrographs in five different points using the software ImageJ, are 352 ± 90 nm and 1837

± 659 nm, respectively. As can be observed, films prepared by dipping are thinner and less roughs than those prepared by spray LbL. This is mainly due to the rinsing step between polymer layers which is necessary in dipping but not in spray giving rise to thinner and more homogeneous layers in the dipping process.

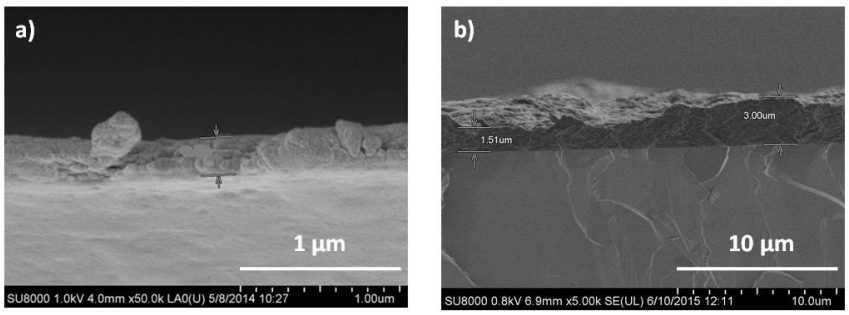

Figure 4.7. SEM micrographs corresponding to $(Alg5/Chi)_{20}$ films built up by a) dipping and b) spray LbL.

Taking into account the inherent restrictions of dipping method, such as the long-time of deposition of every layer (minutes) and the subsequent rinse step after every deposited layer, as well as the favorable results obtained here for spray that provide a high growth rate, spray was the LbL technique selected for building up Alg/Chi films in the following chapters with the aim of studying their properties and applications.

- *Influence of the alginate concentration*

In order to optimize the buildup conditions of the films via spray assisted LbL, $(Alg\mathit{x}/Chi)_n$ films were prepared at different concentrations of Alg solution keeping the concentration of Chi solution fixed at 1.0 mg/mL. Figure 4.5 shows the evolution of the thickness of $(Alg\mathit{x}/Chi)_n$ films, measured by ellipsometry, as a function of the number of bilayers for different Alg concentrations, where *n* stands for the number of bilayers and *x* refers to Alg concentration (1, 2.5 and 5 mg/mL).

As it can be observed, the thickness of multilayer $(Alg\mathit{x}/Chi)_n$ films increases linearly with the number of bilayers for all concentrations studied, up to 5 bilayers, with a slope that increases with the concentration of Alg solution. Alg1/Chi film grows at a rate of 4 nm/layer whereas Alg2.5/Chi and Alg5/Chi films grow at a similar rate of 20 nm/layer. Previous reports have shown a linear increase of the thickness of Alg/Chi films with the number of layers when they are prepared by dipping LbL at a rate of 3 nm/layer which corresponds to a total thickness of ~35 nm (5 bilayers) for Alg and Chi concentrations of 0.5 mg/mL at pH 5.5.[3, 28] The growing of the

film with the number of bilayers for the two highest concentrations of Alg, 2.5 and 5.0 mg/mL, is similar and much higher than that obtained for 1.0 mg/mL of alginate. It is worth mentioning that 5.0 mg/mL Alg solutions tend to clog the spray. Therefore, this concentration was discarded for the next experiments. So, the following experiments are focused on $(Alg\mathit{x}/Chi)_n$ films prepared with x = 1.0 and 2.5 mg/mL and a fixed concentration of 1.0 mg/mL for the chitosan solution.

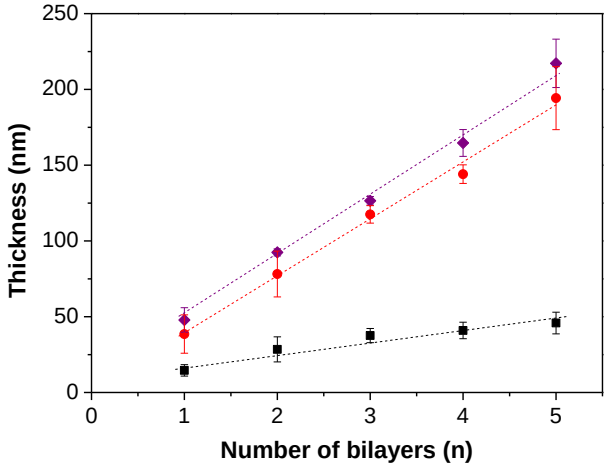

Figure 4.5. Evolution of $(Alg\mathit{x}/Chi)_n$ film thickness, measured by ellipsometry, vs. the number of bilayers. The films were obtained by spray assisted LbL with Alg concentration at x = 1.0 (■), x = 2.5 (●) and x = 5.0 mg/mL (♦). Dashed lines are a guide to the eye.

- *Determination of the growth mechanism*

Figure 4.8 displays the evolution of the thickness of $(Alg1/Chi)_n$ and $(Alg2.5/Chi)_n$ films as a function of the number of bilayers up to n = 40. Due to the ellipsometry restrictions to determine film thicknesses of more than 8 bilayers, the thickness of films with n = 10, 20 and 40 bilayers was determined by SEM through the measurement of their cross section. In order to visualize the cross section of Alg/Chi films, a representative SEM micrograph $(Alg2.5/Chi)_{20}$ has been included in the inset of Figure 4.8. It can be observed that the thickness increases linearly up to 5 bilayers, exponentially from 5 to 20 deposited bilayers and then slightly increases toward a *plateau*.

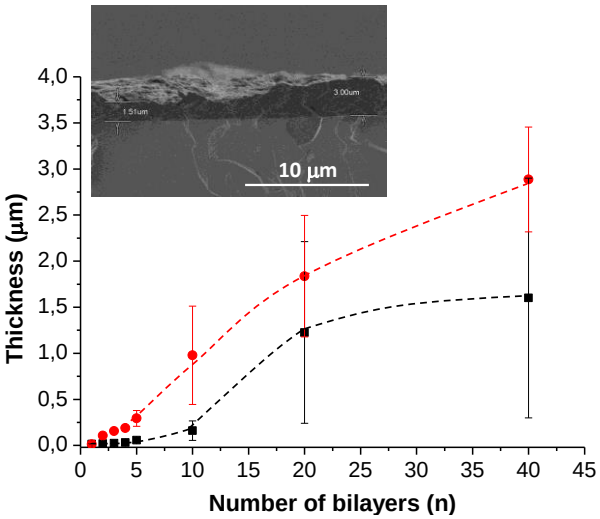

Figure 4.8. a) Evolution of $(Alg1/Chi)_n$ (■) and $(Alg2.5/Chi)_n$ (●) film thickness, measured by SEM, vs. number of bilayers. Dashed lines are a guide to the eye. The inset of the figure is a representative SEM micrograph corresponding to the cross section of a film $(Alg2.5/Chi)_{20}$.

Previous studies have shown that the multilayer growth regime is related to the internal structure of the multilayer film.[28, 29] For polymer films comprising several layers, the growth profile typically proceeds either linearly or exponentially. A detailed description of both mechanisms is provided in Chapter 2. Exponential film growth is currently understood to arise from the diffusion of adsorbed species 'in' and 'out' of the multilayer film. In this process, macromolecules first adsorb from solution to the exposed surface of the film via attractive intermolecular interactions; then they diffuse through the bulk toward the substrate. Diffusion from the bulk of the film toward the film surface also occurs during this process. In the case of $(Algx/Chi)_n$ films reported in this study, the exponential growth could be due to the diffusion of chitosan 'in' and 'out' of the film during the deposition process. The diffusion of chitosan during the buildup process in different polyelectrolytes systems has been proved for chitosan/hyaluronic acid[30] and chitosan/heparin[31] up to 10 bilayers. The change of growth from exponential to linear at a number of bilayers higher than 20 might be due to the gradual rearrangement of the polymer chains in the film which makes the film less penetrable for the diffusion process, so that the growth becomes linear with the number of deposited bilayers when the time allowed for deposition is constant.[32]

4.3.2. Polyallylamine/hyaluronic acid films

Optimization of the experimental conditions for LbL assembly

The capacity of polyallylamine and hyaluronic acid to form a polyelectrolyte complex (PEC) through electrostatic interaction is studied through the formation of a precipitate. In order to study the effect of the polymer concentrations in the buildup process, diverse precipitation tests were carried out at different concentrations of hyaluronic acid, 1.2 and 2.5 mg/mL, and polyallylamine, 1.0 and 2.0 mg/mL, and results are exhibited in the Figure 4.9. The precipitate can be formed due to the ionic interaction between the carboxylic groups of hyaluronic acid and the amine groups of polyallylamine through electrostatic forces.[18] Due to the fact that the formation of a precipitate is observed in all cases under study, this test is not enough to discard any concentration and all of them are going to be tested in the buildup process studied by ellipsometry.

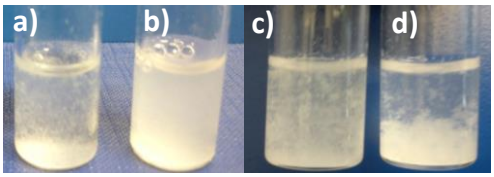

Figure 4.9. Photograph of precipitation tests corresponding to mixtures of: a) 1.2 mg/mL HA and 1.0 mg/mL PAH, b) 1.2 mg/mL HA and 2.0 mg/mL PAH, c) 2.5 mg/mL HA and 1.0 mg/mL PAH and d) 2.5 mg/mL HA and 2.0 mg/mL PAH.

A multilayer system composed by PAH/HA and an intermediate gel-like layer (Alg-Fe^{2+}) has also been explored with the aim of being employed as a drug reservoir in future applications.

Previous to evaluate the influence of the introduction of Alg-Fe^{2+} into the multilayer buildup of HA and PAH, the interaction between Alg and ions Fe^{2+} was studied. Therefore, a series of mixtures of alginate (5.0 mg/mL) and Fe^{2+} at different concentrations, 10, 20, 30 and 40 mg/mL, were made and results are shown in the Figure 4.10a. The formation of a gel was tested by the inverted tube method after 24 hours (Figure 4.10b) proving that only the mixture corresponding to 5.0 mg/mL Alg and 20 mg/mL Fe^{2+} formed a gel. The formation of a gel is induced by iron cations and it is attributed to a combination of ionotropic gelation, due to the binding of Fe^{2+} and free COO^- groups of alginate, and acid gelation, typical of alginic acid salts.[23]

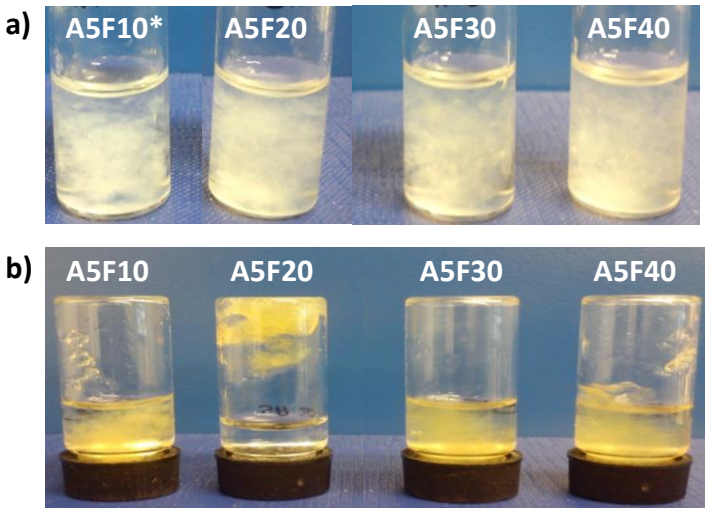

Figure 4.10. Gel formation of samples with a fixed alginate concentration of 5.0 mg/mL and different iron concentrations, 10, 20, 30 and 40 mg/mL a) as prepared and b) inverted tube after 24 h. *A5F10, the letters A and F indicates the alginate and iron respectively and the number following refers to the concentration in mg/mL.

Determination of the thickness

- *Influence of the method of preparation (spray vs. dipping)*

To elucidate the most adequate LbL technique for the assembly of $(HA/PAH)_n$ films, spray experiments were carried out with different concentrations of HA, 1.2 and 2.5 mg/mL, and PAH, 1.0 and 2.0 mg/mL, solutions. The evolution of the thickness with the number of layers followed by ellipsometry is shown in Figure 4.12. As can be observed, the growth of the films does not take place by spray assisted LbL. Maybe this is due to the fact that PAH and HA are not given enough time in contact to interact between them. Considering these results, the most appropriate method for the preparation of $(HA/PAH)_n$ films is dipping LbL.

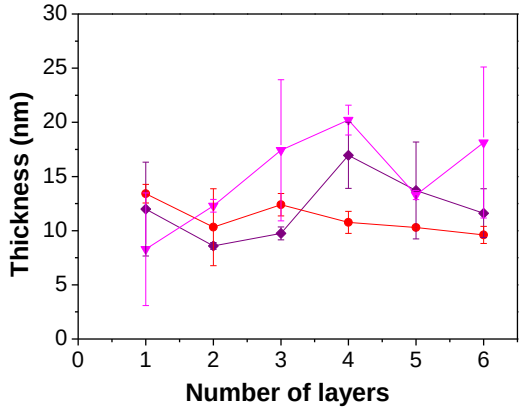

Figure 4.12. Evolution of the thickness vs. number of layers measured by ellipsometry of $(HA1.2/PAH0.6)_n$ (♦), $(HA1.2/PAH1.0)_n$ (●) and $(HA2.5/PAH2.0)_n$ (▼) films prepared through spray LbL.

- *Influence of the HA and PAH concentrations*

To optimize the buildup conditions of $(HA/PAH)_n$ films via dipping LbL, multilayer films were prepared with different concentrations of HA, 1.2 and 2.5 mg/mL, and PAH, 1.0 and 2.0 mg/mL, solutions. Figure 4.11 shows the evolution of the thickness of $(HAx/PAHy)_n$ films, determined by ellipsometry, as a function of the number of bilayers, where *n* stands for the number of bilayers, *x* refers to HA concentration (1.2 and 2.5 mg/mL) and *y* to PAH concentration (1.0 and 2.0 mg/mL). As can be observed, the thickness of multilayer $(HA/PAH)_n$ films increases exponentially with the number of bilayers up to 5 bilayers in all cases. This increase is more pronounced for films with the highest concentration of HA (2.5 mg/mL). Keeping constant the HA concentration, the growth of films is higher for the highest PAH concentration (2.0 mg/mL) in both cases. The exponential growth was attributed to the presence of NaCl in the assembly process since films assembled without NaCl showed a linear growth as it has been previously reported.[20, 33] Films with exponential growth are dynamic entities where diffusion and exchange processes of at least one of the two polyelectrolytes through the whole film thickness at each deposited bilayer takes place.[7] In our case, the exponential growth could be related to the diffusion of PAH within the multilayer film structure,[21] so that a higher concentration of PAH provides more amine groups to diffuse into the structure increasing the thickness.

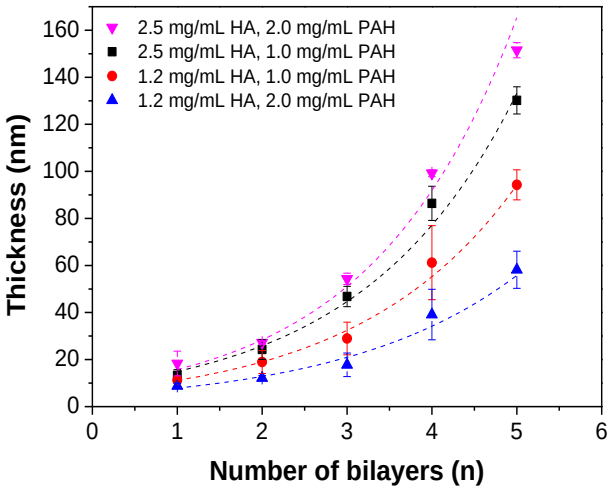

Figure 4.11. Evolution of the thickness vs. number of bilayers of $(HA1.2/PAH1.0)_n$ (●), $(HA1.2/PAH2.0)_n$ (▲), $(HA2.5/PAH1.0)_n$ (■) and $(HA2.5/PAH2.0)_n$ (▼) films prepared through dipping LbL and measured by ellipsometry. Dashed lines are a guide to the eye.

- *Study of the buildup process of nanostratified HA/PAH/Alg-Fe^{2+} systems*

A stratified system composed by a multilayer HA/PAH film with an intermediate gel-like layer, Alg-Fe^{2+}, was explored and studied by QCM.

Quartz crystal microbalance with dissipation monitoring (QCM-D) was employed to study the changes in the frequency and dissipation during the LbL process of HA and PAH in wetting conditions. Figure 4.13a exhibits the evolution of $\Delta f/v$ with the time which provides information about mass changes due to the adsorption or desorption of the polyelectrolyte on the film[33] during the buildup of a multilayer $(HA/PAH)_5$Alg-$Fe^{2+}(PAH/HA)_m$ film with 5 bilayers HA/PAH followed by a gel-like layer of Alg-Fe^{2+} and then another multilayer $(PAH/HA)_m$ structure. As can be observed, $\Delta f/v$ decreases with each HA or PAH deposition step and this $\Delta f/v$ decay is more pronounced for lower overtones. On the other hand, Figure 4.13b depicts the variation of ΔD with the time providing information about the viscoelasticity of the film. An increase of ΔD takes place after each HA or PAH deposition. Taking into account that the decrease of normalized frequencies, $\Delta f/v$, is different for every overtone under study and do not overlap as well as the increase in the dissipation, it can be concluded that the adsorbed layer does not obey the Sauerbrey equation (eq. 3.8 in Chapter 3) as a consequence of the viscoelastic behavior of the adsorbed film.[3] This is corroborated by the representation of dissipation (ΔD_3) versus frequency for the third overtone ($\Delta f_3/3$) in the Figure 4.13c. The high slope ($\Delta D/\Delta f$) of this curve also indicates the softness of the film.

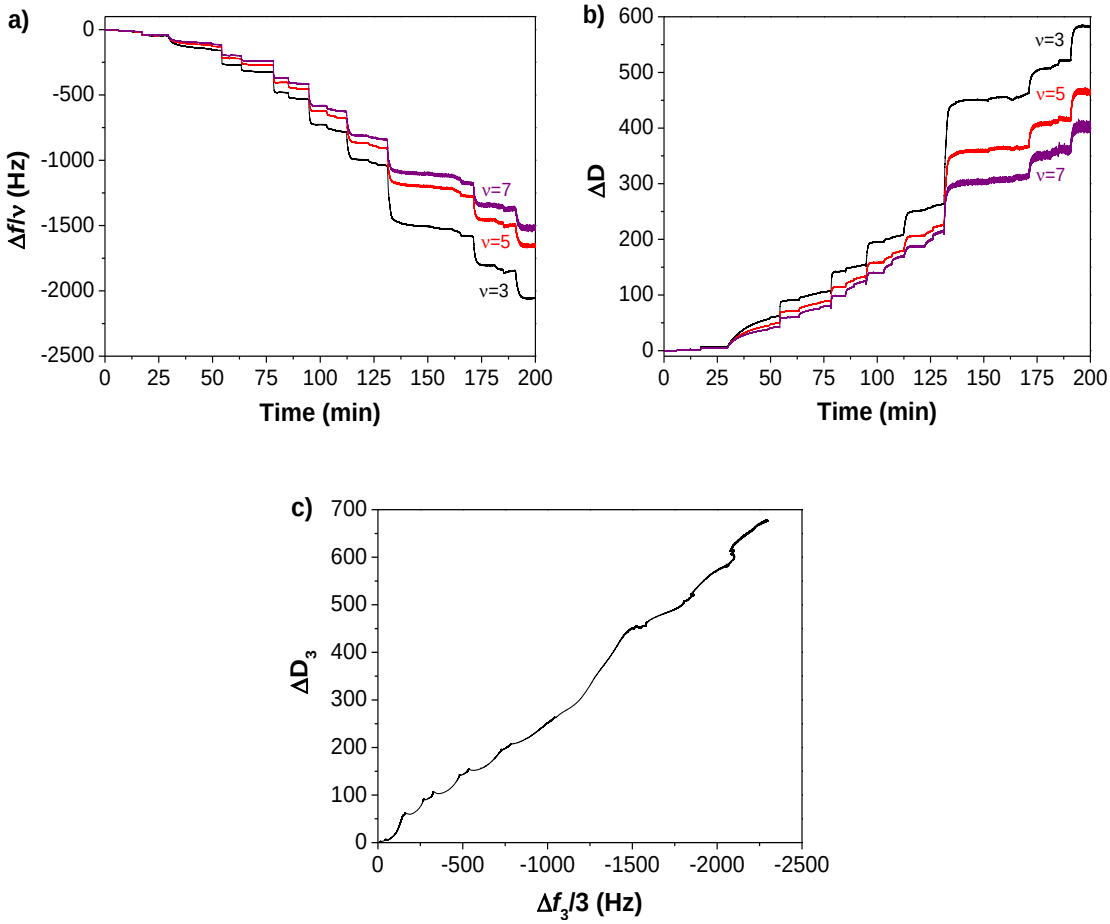

Figure 4.13. a) Normalized frequency ($\Delta f/\nu$) and b) dissipation changes measured by QCM during the buildup of a $(HA/PAH)_5$Alg-$Fe^{2+}(HA/PAH)_3$ film with a concentration of 1.2 mg/mL HA and 0.3 mg/mL PAH. c) Dissipation changes (ΔD_3) versus frequency ($\Delta f_3/3$) for the third overtone.

Thickness and viscoelastic properties of the films can be obtained applying the Voigt model and the results corresponding to the third overtone are illustrated in Figure 4.14. Figure 4.14a shows the exponential evolution of the film thickness with the number of HA/PAH deposited layers before and after deposition of the gel-like layer Alg-Fe^{2+}. The deposition of this gel-like layer Alg-Fe^{2+} (5.0 mg/mL Alg and 20 mg/mL Fe^{2+}) gives rise to a high increase of the thickness from 300 nm to 570 nm. Considering that every adsorbed layer has an uniform thickness, the multilayer $(HA/PAH)_n$ film grows at a rate of ~30 nm/layer before and after Alg-Fe^{2+} deposition and the Alg-Fe^{2+} layer has a thickness of 270 nm. The thickness of the HA layer is higher than the PAH layer during the LbL process. This might be due to the fact that the concentration of PAH (0.3 mg/mL) is much lower than HA (1.2 mg/mL). Figure 4.14b exhibits the viscosity of the film. Viscosity increases exponentially with the number of layers and it is much higher for every HA deposited layer (~1.6 mPa·s) than PAH layer (~0.4 mPa·s) which means that the HA

layer is more rigid than PAH layer and, as we mentioned above, this might be caused by differences between PAH and HA concentrations, 0.3 mg/mL and 1.2 mg/mL, respectively.

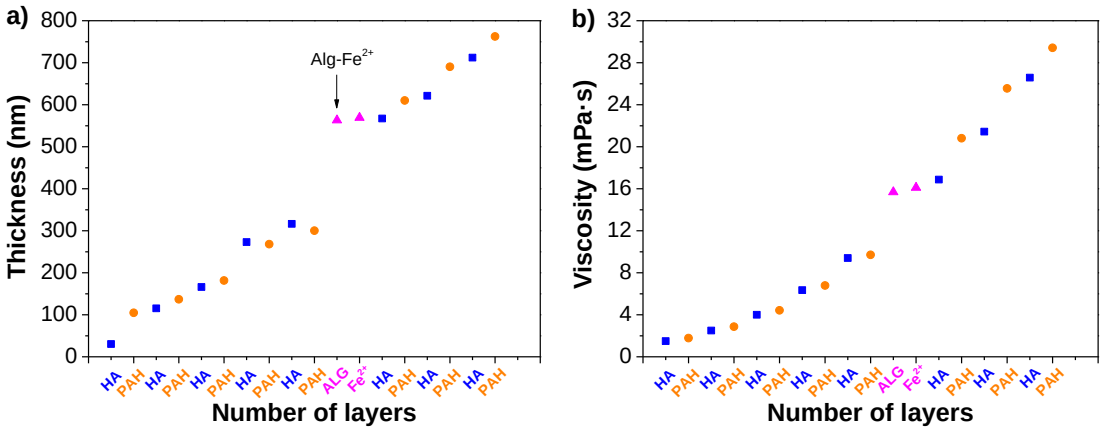

Figure 4.14. a) Thickness of the growing $(HA/PAH)_5Alg\text{-}Fe^{2+}(HA/PAH)_3$ film, where the incorporation of the gel-like layer $Alg\text{-}Fe^{2+}$ is marked with an arrow, and b) viscosity as a function of the number of layers calculated with the Voigt model. Note that every polymer layer is marked with a different color, HA in blue, PAH in orange and Alg and Fe^{2+} in pink.

4.4. CONCLUSIONS

In the study of the growth mechanism of layer-by-layer films obtained from natural polymers, the following conclusions can be drawn:

The experimental conditions for spray LbL assembly were determined by precipitation tests and follow up the layer by layer growth process was followed through ellipsometry.

In the case of films made of alginate and chitosan, differences in the growth of $(Alg5/Chi)_n$ films up to 5 bilayers fabricated by two different LbL deposition methods, spray and dipping, were determined by ellipsometry. The growth was linear in both cases, but the growth rate of films built up by dipping was 2 nm/layer, one order of magnitude lower than films fabricated by spray which was 20 nm/layer. Besides to a high growth rate, spray LbL allows a considerable time saving to build up $(Alg/Chi)_n$ films due to the fact that the deposition time of a layer (seconds) is lower than the dipping deposition time (minutes). In the case of films made of hyaluronic acid and poly(allylamine hydrochloride), ellipsometry allowed to discard spray LbL technique, because the growth of $(HAx/PAHy)_n$ films did not take place. Therefore, dipping LbL was employed to fabricate these films.

The growth of (Alg*x*/Chi)$_n$ films prepared by spray assisted LbL was studied by ellipsometry up to 5 bilayers for a fixed Chi concentration (1.0 mg/mL) and three different Alg concentrations (*x* = 1.0, 2.5 and 5.0 mg/mL). The thickness of these films showed a linear increase with the number of deposited bilayers being higher as Alg concentration increased. However, the growth rate for the two highest Alg concentrations, 2.5 and 5.0 mg/mL, was similar at 20 nm/layer. To follow the growth above 5 bilayers, SEM was employed and a change of tendency from linear to exponential was exhibited from 5 to 20 bilayers to continue with a slight increase towards a *plateau* at a number of bilayers above 20 due to the rearrangements of polymer chains during the deposition process. The experimental conditions to build up (HA*x*/PAH*y*)$_n$ films were optimized following the growth of the films up to 5 bilayers by ellipsometry for two different concentrations of HA (1.2 and 2.5 mg/mL) and PAH (1.0 and 2.0 mg/mL). The growth of these films was exponential for all concentrations due to the presence of NaCl and the diffusion of PAH within the multilayer film structure. The growth was higher for 2.5 mg/mL HA and 2.0 mg/mL PAH.

Finally, the development of a nanostratified system based on HA/PAH multilayers with a gel-like layer Alg-Fe^{2+} incorporated in an intermediate position was probed by QCM-D. This technique also allowed to determine the growth of (HA1.2/PAH0.3)$_n$ films in wetting conditions as well as the thickness of the nanostratified system, up to a higher number of deposited layers, using the Voigt model. In addition, the viscoelastic properties were determined revealing that the thickness and rigidity of HA layers were higher than those of PAH layers.

4.5. REFERENCES

1. Richardson, J. J.; Björnmalm, M.; Caruso, F., Technology-driven layer-by-layer assembly of nanofilms. *Science* **2015,** 348, (6233).

2. Lefort, M.; Boulmedais, F.; Jierry, L.; Gonthier, E.; Voegel, J. C.; Hemmerlé, J.; Lavalle, P.; Ponche, A.; Schaaf, P., Simultaneous Spray Coating of Interacting Species: General Rules Governing the Poly(styrene sulfonate)/Poly(allylamine) System. *Langmuir* **2011,** 27, (8), 4653-4660.

3. Alves, N. M.; Picart, C.; Mano, J. F., Self Assembling and Crosslinking of Polyelectrolyte Multilayer Films of Chitosan and Alginate Studied by QCM and IR Spectroscopy. *Macromolecular Bioscience* **2009,** 9, (8), 776-785.

4. Caridade, S. G.; Monge, C.; Gilde, F.; Boudou, T.; Mano, J. F.; Picart, C., Free-Standing Polyelectrolyte Membranes Made of Chitosan and Alginate. *Biomacromolecules* **2013,** 14, (5), 1653-1660.

5. Mjahed, H.; Porcel, C.; Senger, B.; Chassepot, A.; Netter, P.; Gillet, P.; Decher, G.; Voegel, J.-C.; Schaaf, P.; Benkirane-Jessel, N.; Boulmedais, F., Micro-stratified architectures based on successive stacking of alginate gel layers and poly(l-lysine)-hyaluronic acid multilayer films aimed at tissue engineering. *Soft Matter* **2008,** 4, (7), 1422-1429.

6. Kerdjoudj, H.; Boulmedais, F.; Berthelemy, N.; Mjahed, H.; Louis, H.; Schaaf, P.; Voegel, J. C.; Menu, P., Cellularized alginate sheets for blood vessel reconstruction. *Soft Matter* **2011,** 7, (7), 3621-3626.

7. Ball, V.; Hübsch, E.; Schweiss, R.; Voegel, J.-C.; Schaaf, P.; Knoll, W., Interactions between Multivalent Ions and Exponentially Growing Multilayers: Dissolution and Exchange Processes. *Langmuir* **2005,** 21, (18), 8526-8531.

8. Díaz, B.; Freire, L.; Montemor, M. F.; Nóvoa, X. R., Oxide film growth by CSV on AISI 316L: a combined electrochemical and analytical characterization. *Journal of the Brazilian Chemical Society* **2013,** 24, 1246-1258.

9. Halthur, T. J.; Claesson, P. M.; Elofsson, U. M., Immobilization of Enamel Matrix Derivate Protein onto Polypeptide Multilayers. Comparative in Situ Measurements Using Ellipsometry, Quartz Crystal Microbalance with Dissipation, and Dual-Polarization Interferometry. *Langmuir* **2006,** 22, (26), 11065-11071.

10. Wittmer, C. R.; Phelps, J. A.; Saltzman, W. M.; Van Tassel, P. R., Fibronectin Terminated Multilayer Films: Protein Adsorption and Cell Attachment Studies. *Biomaterials* **2007,** 28, (5), 851-860.

11. Picart, C.; Ladam, G.; Senger, B.; Voegel, J.-C.; Schaaf, P.; Cuisinier, F. J. G.; Gergely, C., Determination of structural parameters characterizing thin films by optical methods: A comparison between scanning angle reflectometry and optical waveguide lightmode spectroscopy. *The Journal of Chemical Physics* **2001,** 115, (2), 1086-1094.

12. Dante, S.; Hou, Z.; Risbud, S.; Stroeve, P., Nucleation of Iron Oxy-Hydroxide Nanoparticles by Layer-by-Layer Polyionic Assemblies. *Langmuir* **1999,** 15, (6), 2176-2182.

13. Ferriz-Mañas, M.; Schlenoff, J. B., Zeta Potential of Polyelectrolyte Multilayers Using the Spinning Disk Method. *Langmuir* **2014,** 30, (29), 8776-8783.

14. Wang, Y.; Kozlovskaya, V.; Arcibal, I. G.; Cropek, D. M.; Kharlampieva, E., Highly swellable ultrathin poly(4-vinylpyridine) multilayer hydrogels with pH-triggered surface wettability. *Soft Matter* **2013,** 9, (39), 9420-9429.

15. Ye, S.; Wang, C.; Liu, X.; Tong, Z., Multilayer nanocapsules of polysaccharide chitosan and alginate through layer-by-layer assembly directly on PS nanoparticles for release. *Journal of Biomaterials Science, Polymer Edition* **2005,** 16, (7), 909-923.

16. Ye, S.; Wang, C.; Liu, X.; Tong, Z.; Ren, B.; Zeng, F., New loading process and release properties of insulin from polysaccharide microcapsules fabricated through layer-by-layer assembly. *Journal of Controlled Release* **2006,** 112, (1), 79-87.

17. Yuan, W.; Dong, H.; Li, C. M.; Cui, X.; Yu, L.; Lu, Z.; Zhou, Q., pH-Controlled Construction of Chitosan/Alginate Multilayer Film: Characterization and Application for Antibody Immobilization. *Langmuir* **2007,** 23, (26), 13046-13052.

18. Burke, S. E.; Barrett, C. J., Swelling behavior of hyaluronic acid/polyallylamine hydrochloride multilayer films. *Biomacromolecules* **2005,** 6, (3), 1419-1428.

19. Burke, S. E.; Barrett, C. J., pH-dependent loading and release behavior of small hydrophilic molecules in weak polyelectrolyte multilayer films. *Macromolecules* **2004,** 37, (14), 5375-5384.

20. Szarpak, A.; Pignot-Paintrand, I.; Nicolas, C.; Picart, C.; Auzély-Velty, R., Multilayer assembly of hyaluronic acid/poly (allylamine): control of the buildup for the production of hollow capsules. *Langmuir* **2008,** 24, (17), 9767-9774.

21. Szarpak, A.; Cui, D.; Dubreuil, F. d. r.; De Geest, B. G.; De Cock, L. J.; Picart, C.; Auzély-Velty, R., Designing hyaluronic acid-based layer-by-layer capsules as a carrier for intracellular drug delivery. *Biomacromolecules* **2010,** 11, (3), 713-720.

22. Burke, S. E.; Barrett, C. J., pH-Responsive Properties of Multilayered Poly(l-lysine)/Hyaluronic Acid Surfaces. *Biomacromolecules* **2003,** 4, (6), 1773-1783.

23. Hernández, R.; Sacristán, J.; Mijangos, C., Sol/Gel Transition of Aqueous Alginate Solutions Induced by Fe2+ Cations. *Macromolecular Chemistry and Physics* **2010,** 211, (11), 1254-1260.

24. Lawrie, G.; Keen, I.; Drew, B.; Chandler-Temple, A.; Rintoul, L.; Fredericks, P.; Grøndahl, L., Interactions between alginate and chitosan biopolymers characterized using FTIR and XPS. *Biomacromolecules* **2007,** 8, (8), 2533-2541.

25. Silva, J. M.; Duarte, A. R. C.; Caridade, S. G.; Picart, C.; Reis, R. L.; Mano, J. F., Tailored Freestanding Multilayered Membranes Based on Chitosan and Alginate. *Biomacromolecules* **2014,** 15, (10), 3817-3826.

26. Yao, K.; Li, J.; Yao, F.; Yin, Y., Formation of chitosan-based hydrogels network. In *Chitosan-based hydrogels. Functions and applications*, CRC Press: 2012; pp 183-197.

27. Kulig, D.; Zimoch-Korzycka, A.; Jarmoluk, A.; Marycz, K., Study on Alginate–Chitosan Complex Formed with Different Polymers Ratio. *Polymers* **2016,** 8, (5), 167.

28. Sham, A. Y. W.; Notley, S. M., Graphene–polyelectrolyte multilayer film formation driven by hydrogen bonding. *Journal of Colloid and Interface Science* **2015,** 456, 32-41.

29. Shenoy, D. B.; Antipov, A. A.; Sukhorukov, G. B.; Möhwald, H., Layer-by-Layer Engineering of Biocompatible, Decomposable Core−Shell Structures. *Biomacromolecules* **2003,** 4, (2), 265-272.

30. Richert, L.; Lavalle, P.; Payan, E.; Shu, X. Z.; Prestwich, G. D.; Stoltz, J.-F.; Schaaf, P.; Voegel, J.-C.; Picart, C., Layer by Layer Buildup of Polysaccharide Films: Physical Chemistry and Cellular Adhesion Aspects. *Langmuir* **2004,** 20, (2), 448-458.

31. Lundin, M.; Blomberg, E.; Tilton, R. D., Polymer Dynamics in Layer-by-Layer Assemblies of Chitosan and Heparin. *Langmuir* **2010,** 26, (5), 3242-3251.

32. Porcel, C.; Lavalle, P.; Ball, V.; Decher, G.; Senger, B.; Voegel, J.-C.; Schaaf, P., From Exponential to Linear Growth in Polyelectrolyte Multilayers. *Langmuir* **2006,** 22, (9), 4376-4383.

33. Pettersson, T. r.; Pendergraph, S. A.; Utsel, S.; Marais, A.; Gustafsson, E.; Wågberg, L., Robust and Tailored Wet Adhesion in Biopolymer Thin Films. *Biomacromolecules* **2014,** 15, (12), 4420-4428.

CHAPTER 5

Determination of the structure-properties relationship in Alg/Chi films

In this chapter, as a first step, the morphological and nanomechanical properties of multilayer Alg/Chi films developed in the Chapter 3 have been determined. In addition, these properties were also determined for nanocomposite Alg/Chi films with magnetic nanoparticles and crosslinked Alg/Chi films which will be employed for different biomedical applications in Chapters 6 and 7, respectively. As a second step, the inner structure of nanocomposite Alg/Chi films was studied by Grazing incidence small-angle X-ray scattering.

5.1. INTRODUCTION

Over the last few years, multilayer polymer films and nanocomposite films, obtained through their combination with nanoparticles, have drawn a lot of attention for the development of several applications in organic microelectronics, as biosensors or scaffolds for tissue engineering.[1, 2] The control of the mechanical properties of these films is specifically attractive in the biomaterials area where the mechanical properties of polymer films allow to modulate cellular behaviors regarding adhesion, proliferation and cell differentiation.[3-5]

Until now, most of the mechanical studies performed on LbL polymer films and nanocomposite multilayer films have been accomplished by macroscopic stress-strain experiments. Focusing on multilayer Alg/Chi films, measurements of their mechanical strength using the bulge test have revealed an increase in the elastic modulus with the film thickness for films in the range of tens of nanometers.[6] Very recently, it was shown that the incorporation of magnetic nanoparticles within free-standing multilayer Alg/Chi films gave rise to an increase in the elastic moduli measured in the wet state by stress-strain measurements.[7] Probe-based indentation is a versatile method to study local mechanical properties of materials from the nanoscale to the macroscale.[8-10] Within this method, nanoindenter and atomic force microscopy (AFM) are the most used techniques.[11] An early study reported the employment of AFM indentation, with 2.5 μm radius sphere, to determine the mechanical properties of hydrated multilayer PLL/HA films in the micron range either native or crosslinked and supported by an underlying glass coverslip.[12] However, this technique presents some drawbacks such as poor lateral resolution and the large time required to obtain the quantitative mechanical mapping of the surface.[8-10]

To solve these problems, two AFM modes for mapping mechanical properties have been introduced, HarmoniX and PeakForce (PF) Quantitative Nanomechanical Mapping (QNM).[8-10] These modes use the Derjaguin-Muller-Toporov (DMT) model[13] to obtain the elastic modulus from the force-indentation curves. It is important to note that the employment of regular sharp

probes may cause overestimation of the film modulus by the DMT method. An approach would be using special probes, such as colloidal ones for example, that would allow increasing the applied force without producing large penetration. However, in that case, lateral resolution would be compromised.[8] There are only few studies aimed to determine the nanomechanical properties of LbL multilayer films by means of (PF-QNM) AFM, mainly focused on determining the effect of the number of deposited layers on the elastic moduli on LbL polymer films and the effect of the stiff underlying substrate[14, 15] and, none of them, deal with the determination of the nanomechanical properties of films fully fabricated from polysaccharides.

In this chapter, the nanomechanical properties (elastic moduli, deformation and adhesion values) of multilayer Alg/Chi films will be determined. To achieve this aim, not only the effect of the number of deposited bilayers on the resulting mechanical properties was considered, but it was also considered the effect of crosslinking and the effect of the incorporation of nanoparticles to obtain nanocomposite films during the buildup of the films. All of these parameters are known to influence the performance of these materials in biomedical applications. Specifically, nanocomposite Alg/Chi films with magnetic nanoparticles will be explored as pads for local magnetic hyperthermia in chapter 6 and the cell adhesion properties of Alg/Chi films will be examined in the chapter 7.

Small-angle X-ray scattering (SAXS) is proved to be a powerful tool for studying the inner structure of multilayer films by measuring changes into the structure during the buildup process.[16] In addition to this, Grazing-incidence small-angle X-ray scattering (GISAXS) is a powerful technique to study nanostructures at the surface and in buried structures of thin films, by changing slightly the incident angle it is possible to vary the depth of the incident beam into the sample allowing to study the structural changes with the thickness.[17] There are other two X-ray techniques, XRD and Grazing-incidence X-ray diffraction (GIXD), which can be applied to the study of the inner structure of multilayer polymer films, with the difference that GIXD controls the penetration depth through the incident angle.[17]

Regarding the inner structure of nanocomposite Alg/Chi films, to the best of our knowledge, it has not been previously reported although recent results has pointed to the feasibility of performing GISAXS experiments on spray deposited arrays of polymer nanoparticles.[18, 19] It is generally accepted that films formed from synthetic polymers, such as poly(styrene sulfonate) and poly(allylamine hydrochloride) (PSS/PAH) are stratified in layers whereas some degree of interpenetration is present in natural polymers,[20] such as chitosan and hyaluronic acid

(Chi/HA).[21] In this context, the distribution of NPs within polysaccharidic films could vary from films with well separated monolayers to films with dispersed NPs all over the thickness. In the chapter 4 it was described the exponential growth of multilayer films based on alginate and chitosan (Alg/Chi) which was attributed to a possible diffusion of chitosan along the structure. In multilayer polymer films containing inorganic nanoparticles, the distribution of NPs and structuration of NPs layers inside films influence the final properties of the resulting nanocomposite materials. A varying architecture in multilayer films fabricated from polymers and magnetic NPs have revealed different magnetic properties depending on the distance between NPs layers.[22]

The incorporation of magnetic nanoparticles into the bulk structure of different diblock copolymer films has been studied by neutron reflection,[23] neutron scattering[24] and grazing incident small-angle X-ray scattering (GISAXS).[25, 26] Grazing incident small-angle X-ray scattering (GISAXS) allows to determine structural information on the arrangement of polymers and nanoparticles in the direction perpendicular to the free surface, as it has been previously reported for polymer thin films.[27, 28] In this chapter, GISAXS will be employed to elucidate the internal structure of nanocomposite multilayer films based on alginate and chitosan with magnetic nanoparticles (NPs) incorporated.

5.2. EXPERIMENTAL PART

5.2.1. Materials

Chitosan (Chi) of low molecular weight (448869, lot SLBG1673V), sodium alginate (Alg) (A2158, lot 090M0092V), poly(ethylenimine) (PEI) with a molecular weight (M_w) of 25000 and acetic acid were supplied by Aldrich and used as received. Sodium acetate anhydrous was supplied by Panreac. More information about these materials is detailed in the chapter 3.

A lab-made alginate based magnetic ferrofluid containing the iron oxide nanoparticles (NPs) with a magnetite concentration of 8.0 mg/mL, whose characteristics have been described in the Chapter 3, was employed for the preparation of nanocomposite Alg/Chi films.

5.2.2. Preparation of Alg/Chi films

All films were built on silicon wafers (20 × 40 mm, Siegert) following the procedure corresponding to spray assisted LbL deposition described in the Chapter 4 using a fixed Chi concentration (1 mg/mL) and two different Alg concentrations, 1.0 and 2.5 mg/mL. Samples

were denoted as (Alg*x*/Chi)$_n$ where *n* stands for the number of bilayers (*n* = 5, 10, 20 or 40) and *x* refers to Alg concentration (*x* = 1.0 or 2.5 mg/mL).

5.2.3. Preparation of crosslinked Alg/Chi films

For the preparation of crosslinked Alg/Chi films, (Alg*x*/Chi)$_n$ films were thermally crosslinked in an oven at 120 ºC for 2 hours.

5.2.4. Preparation of nanocomposite Alg/Chi films

Nanocomposite Alg/Chi films were obtained by spraying a bilayer of alginate and chitosan followed by a bilayer of a lab-made alginate based magnetic ferrofluid containing the iron oxide NPs and a chitosan layer (Scheme 5.1). In this case, fixed chitosan and alginate concentrations of 1.0 mg/mL and 2.5 mg/mL, respectively, were used and each layer was sprayed for 5 s. Three nanocomposite films were obtained by applying different number of cycles and samples were denoted as (Alg/Chi)$_3$/(NPs/Chi)$_2$, (Alg/Chi)$_5$/(NPs/Chi)$_5$ and (Alg/Chi)$_{10}$/(NPs/Chi)$_{10}$. Note that the sample, (Alg/Chi)$_3$/(NPs/Chi)$_2$, has not the ending NPs/Chi bilayer.

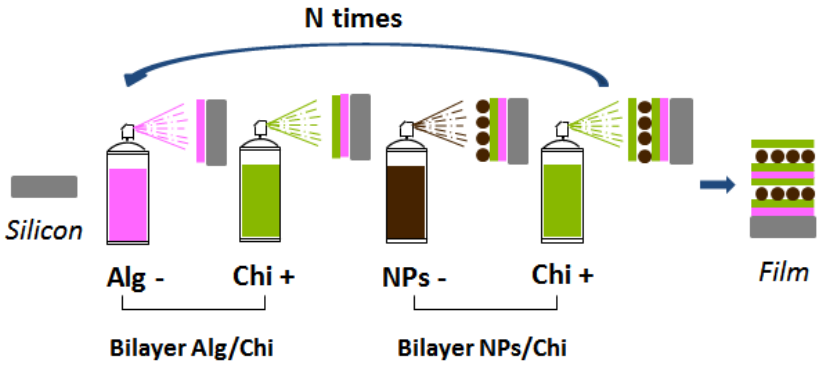

Scheme 5.1. Schematic diagram of the sequential spraying process followed for the preparation of nanocomposite Alg/Chi films.

For the GISAXS experiment, an additional nanocomposite Alg/Chi film was prepared through dipping following the procedure shown in the Scheme 5.2. The silicon substrate was sequentially immersed in Alg (2.5 mg/mL) and Chi (1.0 mg/mL) solutions to build up a bilayer Alg/Chi and then it was immersed in the alginate based magnetic ferrofluid and Chi solutions to build up a bilayer NPs/Chi. The time of immersion was 5 min for every deposited layer with a subsequent rinsing step of 2 min. The obtained nanocomposite film was denoted as (Alg/Chi)$_2$/(NPs/Chi)$_1$.

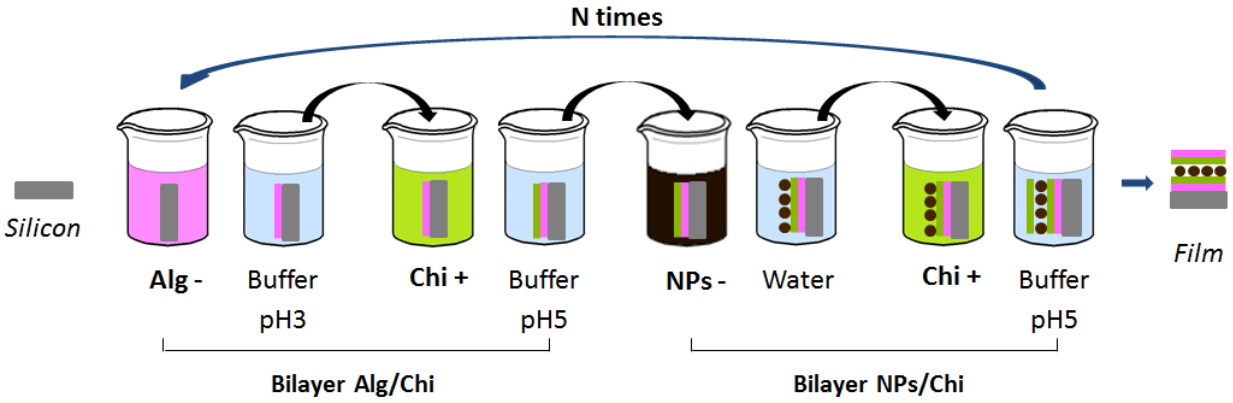

Scheme 5.2. Schematic diagram of the sequential dipping process followed for the preparation a nanocomposite $(Alg/Chi)_2/(NPs/Chi)_1$ film.

5.2.5. Morphological characterization

The topography and surface roughness were measured by Atomic Force Microscopy (AFM) using a Bruker Multimode 8, with a Nanoscope V controller. All measurements were performed in air, at room temperature, on films supported on silicon wafers. Samples $(Algx/Chi)_n$ were scanned over square regions of 2 μm size and nanocomposite $(Alg/Chi)_n/(NPs/Chi)_m$ films over square regions of 1 μm size. The average roughness (R_a) was calculated from the height images in four different square points of 1μm × 1μm.

The cross section of films was observed by scanning electron microscopy (SEM) using a Hitachi SU 8000 microscope operating at 0.8 kV. The average thickness was determined by measuring the width of the cross section in the SEM micrographs in five different points using the software ImageJ.

5.2.6. Mechanical properties

The mechanical properties of films were evaluated using a Bruker Multimode 8, with a Nanoscope V controller, by the PeakForce Quantitative Nanomechanical Mapping (PF-QNM) method. All measurements were performed in air, at room temperature, on films supported on silicon wafers. Samples $(Algx/Chi)_n$ were scanned over square regions of 2 μm size and nanocomposite $(Alg/Chi)_n/(NPs/Chi)_m$ films over square regions of 1 μm size. All quantitative measurements were carried out with different probes depending on the actual mechanical properties of every sample. In particular, TAP150 and RTESPA525 probes (Bruker) were employed. Cantilever spring constants for each probe were measured by the thermal tune method

and found to be around 1-5 and 50-100 N/m for TAP150 and RTESPA525, respectively. More details about this technique can be consulted in the Chapter 3.

The precise experimental procedure was the following: an initial force on the tip, F_{tip}, was set, and an initial estimation of the tip radius, based on the provider specifications was considered. The F_{tip} was chosen to produce a deformation depth of about 5 nm. Under these experimental conditions, the adhesive force, F_{adh}, between the tip and the sample can be neglected. With this, an experiment on the polystyrene standard was carried out. The tip radius value was modified systematically until the measured elastic modulus of the reference matched the one provided by the provider. The obtained value for the tip radius was typically around 10 nm. The same sample was measured with different tips, after careful calibration for tip radius, for cantilever deflection sensitivity and also at different times. In addition, the z distance in the piezo is regularly calibrated using a grating of known depth.

Analysis of the force-distance curves is automatically performed by a software program, NanoScope Analysis 1.5, which allows to extract the height, elastic modulus, adhesion force, deformation and dissipation simultaneously by application of the DMT model.

5.2.7. Characterization of the inner structure of nanocomposite films

To study the inner structure of nanocomposite films, GISAXS measurements were carried on $(Alg/Chi)_n$ films and nanocomposite $(Alg/Chi)_n(NPs/Chi)_m$ films prepared by spray and dipping LbL on BM26 beamline of the European Synchrotron Radiation Facility (ESRF) sited in Grenoble (France). A two-dimensional (2D) detector (Pilatus 1M) and a camera of 981 x 1043 pixels (size of the pixel 172 x 172 μm^2) was used at a sample to detector distance of 6.87 m to data acquisition. The X-ray beam had a wavelength of $\lambda = 0.103$ nm. The angle of incidence (α_i) was varied between 0.1 and 0.4º. To data analysis the FIT2D software program was employed. More details about this technique can be accessed in the Chapter 3.

5.3. RESULTS AND DISCUSSION

5.3.1. Morphological characterization

The effect of the number of layers, the alginate concentration, as well as the crosslinking and the incorporation of NPs, in the thickness and surface average roughness (R_a) of $(Alg/Chi)_n$ films were studied by AFM and SEM.

Effect of the number of deposited layers, alginate concentration and crosslinking

Results corresponding to the surface average roughness (R_a), determined from the AFM height images, and the thickness, determined by SEM through the measurement of the cross-section of $(Algx/Chi)_n$ films are shown in Table 5.1. Multilayer $(Alg2.5/Chi)_n$ films were subjected to a thermal treatment at 120 ºC for 2 hours in order to induce crosslinking through formation of amide bonds between the amine groups of chitosan and the carboxylic acid groups of alginate.[29] The thickness and average roughness (R_a) are also shown in Table 5.1 as a function of the number of bilayers.

Table 5.1. Evolution of the thickness and average roughness (R_a) of non-crosslinked $(Algx/Chi)_n$ films and crosslinked $(Alg2.5/Chi)_n$ films as a function of the number of bilayers (n).

n	**$(Alg1.0/Chi)_n$ films**		**$(Alg2.5/Chi)_n$ films**		**Crosslinked $(Alg2.5/Chi)_n$ films**	
	Thickness (μm)	R_a (nm)	Thickness (μm)	R_a (nm)	Thickness (μm)	R_a (nm)
5	0.13 ± 0.10	18.4 ± 5.3	0.29 ± 0.09	8.9 ± 3.6	0.43 ± 0.21	4.8 ± 3.6
10	0.16 ± 0.11	13.8 ± 6.5	0.82 ± 0.06	17.1 ± 3.4	0.85 ± 0.75	3.8 ± 0.6
20	1.23 ± 0.98	33.1 ± 5.0	1.75 ± 1.34	29.8 ± 11.9	1.04 ± 0.98	22.3 ± 8.9
40	1.59 ± 0.65	35.6 ± 7.3	3.06 ± 1.71	49.0 ± 17.5	2.15 ± 1.25	18.5 ± 0.5

For non-crosslinked films, the thickness increases with the number of bilayers (n) from 0.13 ± 0.10 μm (n =5) to 1.59 ± 0.65 μm (n = 40) for films with an alginate concentration of 1.0 mg/mL. In the case of films with a higher alginate concentration, 2.5 mg/mL, the thickness also increases with the number of bilayers from 0.29 ± 0.09 μm (n =5) to 3.06 ± 1.71 μm (n = 40), but in a two-fold scale with regards to films with 1.0 mg/mL alginate. Concerning the average roughness, an increase can be detected with the number of deposited bilayers for both alginate concentrations without showing significant differences between them. For example, in the case of non-crosslinked $(Alg2.5/Chi)_n$ films, R_a increases from 8.9 ± 3.6 to 49.0 ± 17.5 nm when the number of bilayers increases from 5 to 40. This might be attributed to the self-assembly of opposite charges between alginate and chitosan that gives rise to their aggregation resulting in rougher surfaces as the number of bilayers increases.[30]

The R_a values obtained for crosslinked films, 4.8 ± 3.6 (n = 5) and 18.5 ± 0.5 (n = 40), are lower than those corresponding to native $(Alg2.5/Chi)_n$ films in agreement with previous reports in

which it was demonstrated that the crosslinking of multilayer films did not significantly change the thickness in the dry state, giving rise to more uniform films due to the reorganization of the film.[31] Notice that R_a values obtained after crosslinking do not follow a clear trend with the number of deposited bilayers probably due to the fact that R_a arises during the process of the preparation of the films before the crosslinking step.

Effect of the presence of nanoparticles

Figure 5.1 shows AFM topographic images corresponding to two samples prepared with the same number of total bilayers, $(Alg2.5/Chi)_{10}$ and nanocomposite $(Alg/Chi)_5/(NPs/Chi)_5$ films, which provide information on their morphology and their roughness. The film without NPs displays finer grain texture and a more homogeneous surface morphology, with an average roughness of 17.1 ± 3.4 nm, than the nanocomposite film, which exhibits aggregated NPs and an average roughness of 42 ± 3.4 nm. The formation of aggregates is attributed to the roughness accumulation induced by the inner NPs layers. Cluster formation could also be influenced by the aggregation of small particles during the spray of a colloidal solution.[32]

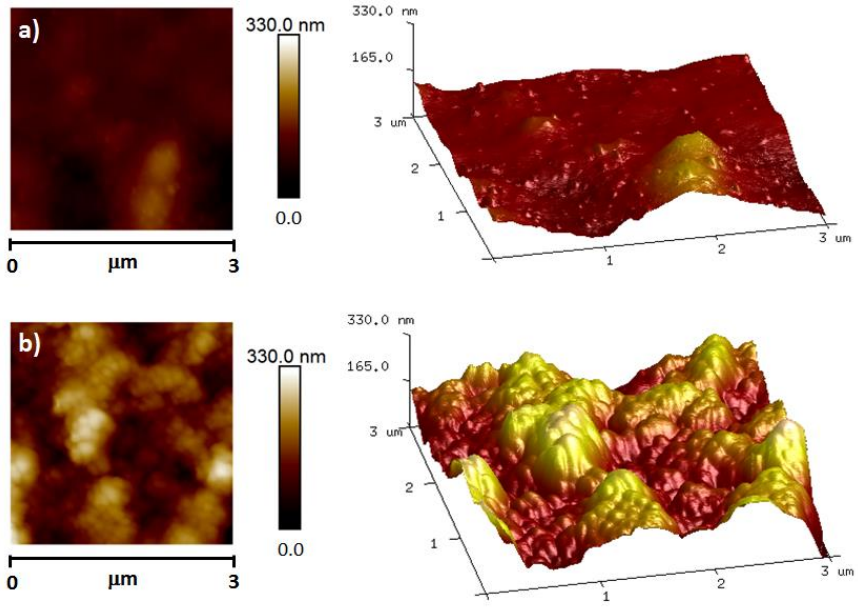

Figure 5.1. AFM topographic images (3µm × 3µm) corresponding to a representative sample a) $(Alg2.5/Chi)_{10}$ and b) nanocomposite $(Alg/Chi)_5/(NPs/Chi)_5$ films.

5.3.2. Mechanical properties

To characterize the nanomechanical properties of Alg/Chi LbL films by means of (PF-QNM) AFM, the number of bilayers and the alginate concentration were varied. The effect of the crosslinking and the incorporation of NPs were also studied.

Effect of the alginate concentration and thermal crosslinking

Representative (PF-QNM) AFM images corresponding to the height, elastic modulus, deformation and adhesion of $(Alg1.0/Chi)_{20}$ films are shown in Figure 5.2a. Results of mechanical properties are obtained by analysis of the cross sectional profiles in four different points of each image, marked with different colored lines, corresponding to areas with different height profiles, in order to obtain an average measurement of every mechanical property (Figure 5.2b).

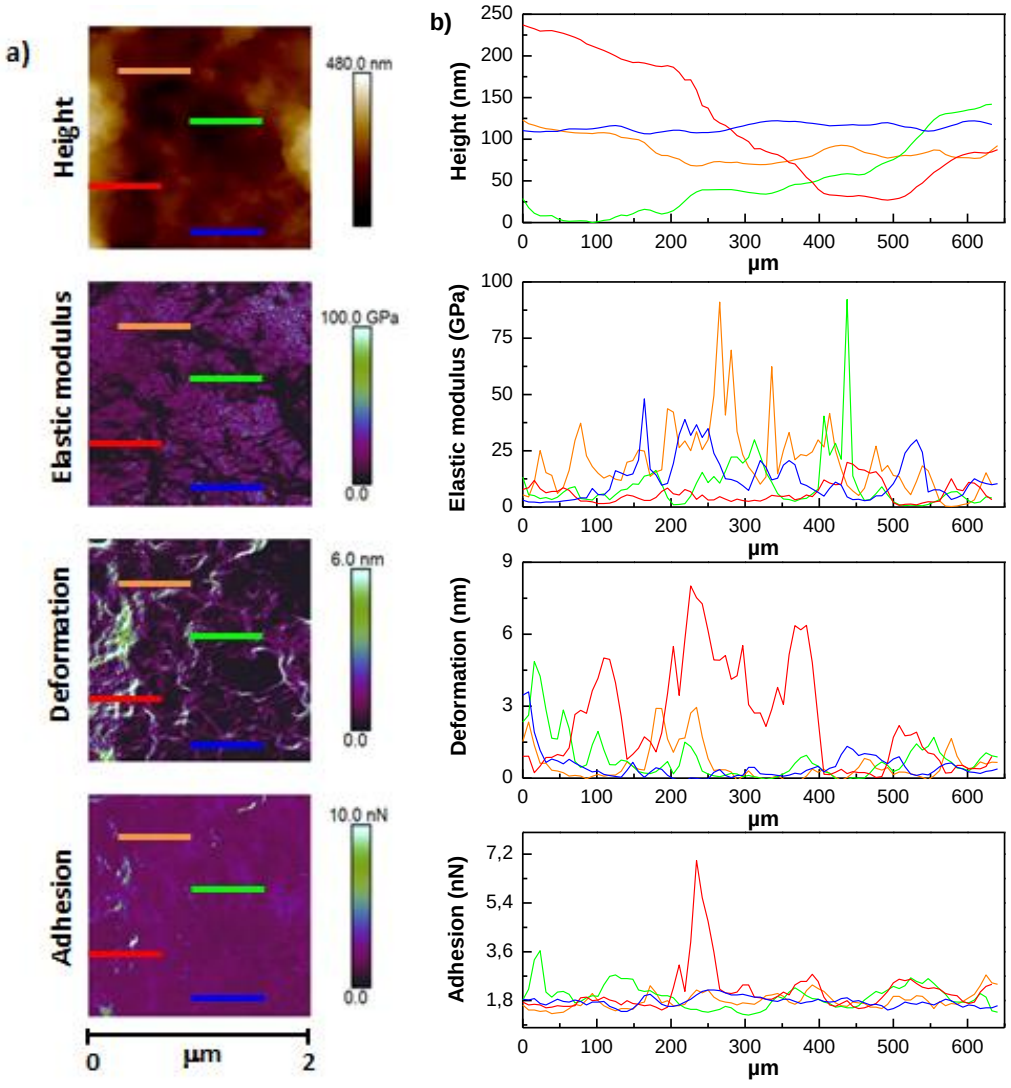

Figure 5.2. a) (PF-QNM) AFM images (2µm × 2µm), height, elastic modulus, deformation and adhesion corresponding to $(Alg1.0/Chi)_{20}$ films with colored lines incorporated and situated in the zones where the cross sectional profiles were taken and b) variation of height, elastic modulus, deformation and adhesion along the different cross sectional profiles marked with their specific color in the AFM images (left).

A comparison of the AFM height images and those corresponding to the mechanical properties (elastic modulus, deformation and adhesion) allows to observe that the topography of the

samples is not associated to changes of the mechanical properties. For example, centering our attention in green and blue lines which represent areas of the sample with different height according to the different color scale, there are not significant differences in the elastic modulus and the values of deformation and adhesion are similar.

Figure 5.3 illustrates representative (PF-QNM) AFM images corresponding to $(Alg2.5/Chi)_{20}$ films before and after thermal crosslinking. As in the previous case, the topography of the samples is not associated to changes of the mechanical properties and this is more evident for crosslinked $(Alg2.5/Chi)_{20}$ films. For easier visualization, a white square (500 nm× 500 nm) was placed in the same position within the height AFM image and that corresponding to the determination of elastic modulus. As it can be observed, this region presents an homogeneous roughness whereas differences in the elastic moduli can be observed according to the different color scale. This result suggests the presence of heterogeneous regions which might be related to regions of different degree of crosslinking arising from differences on the rearrangement of the polymer layers after thermal crosslinking or even from inhomogeneous deposition of the polymers, regions with more polymer mass give rise to a higher number of crosslinking points. In addition, there is a correlation between AFM images corresponding to deformation and those corresponding to adhesion: regions that deform more are those that show a higher tip-adhesion force. This might be attributed to the establishment of more effective interactions, probably of Van der Waals nature, between the tip and the polymer surface.

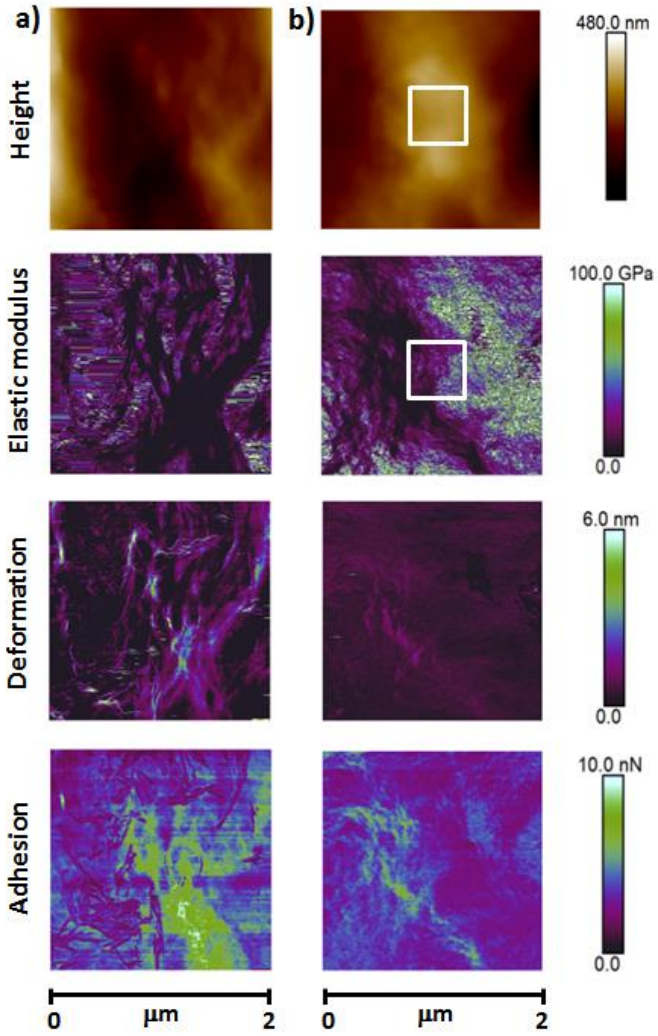

Figure 5.3. (PF-QNM) AFM images (2µm × 2µm), height, elastic modulus, deformation and adhesion, corresponding to (Alg2.5/Chi)$_{20}$ films a) before and b) after crosslinking. For the sake of discussion, the white square (500 nm × 500 nm) placed in the same position within the height AFM image and the elastic moduli AFM image indicates a small roughness region with differences in the elastic moduli.

The mechanical properties (elastic modulus, deformation and adhesion), quantified at four different positions, of native (Alg*x*/Chi)$_n$ films as a function of the number of bilayers are shown in Figure 5.4a.

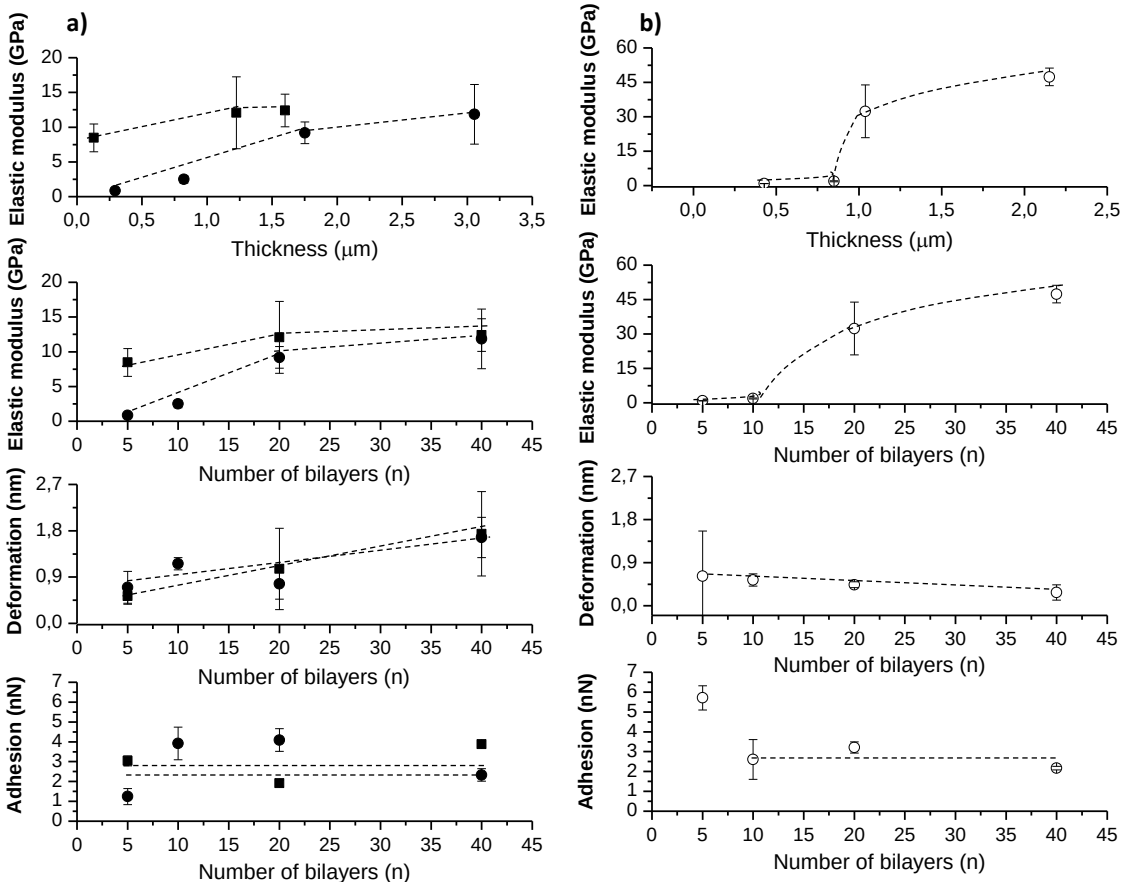

Figure 5.4. Evolution of the elastic modulus, deformation and adhesion of a) $(Alg1.0/Chi)_n$ (■) and $(Alg2.5/Chi)_n$ films (●) and b) crosslinked $(Alg2.5/Chi)_n$ films (○) vs. film thickness and number of bilayers. Dashed lines are a guide to the eye.

The elastic modulus of $(Alg1/Chi)_n$ films slightly increases with the number of bilayers being 8.5 ± 2.0 GPa for 5 Alg/Chi bilayers and 12.4 ± 2.3 GPa for 40 Alg/Chi bilayers. The increase in the elastic moduli with the number of bilayers from 5 to 40 Alg/Chi bilayers is more significant in the case of $(Alg2.5/Chi)_n$ increasing from 0.8 ± 0.1 GPa to 11.8 ± 4.3 GPa, respectively. The elastic moduli obtained for $(Alg2.5/Chi)_n$ films are lower than those corresponding to $(Alg1.0/Chi)_n$ ones. For both alginate concentrations, the elastic moduli reach a *plateau* value of ~12GPa at 40 bilayers. Note that this value is similar to those reported and literature obtained by bulge tests carried out on free-standing Alg/Chi films prepared by spray assisted LbL which showed that the elastic modulus of Alg/Chi films with 35 nm was 1.1 ± 0.4 GPa and increased to similar values for Alg/Chi films with thicknesses of 75 nm and 114 nm (8.1± 2.5 GPa and 11.0 ± 1.6 GPa, respectively). For these samples, Fujie et al.[6] obtained a linear increase in the thickness with a single Alg/Chi bilayer of approximately 3.3 nm thickness, suggesting that each polysaccharide layer constitutes an almost single molecular layer. In our study, spray assisted LbL of $(Alg1.0/Chi)_n$ and $(Alg2.5/Chi)_n$ films present a thickness of a single Alg/Chi bilayer of ~

7.8 nm and ~ 42.4 nm, respectively and a *plateau* value for the elastic modulus of 12.4 ± 2.3GPa and 11.8 ± 4.3GPa, respectively is obtained for (Alg*x*/Chi)$_n$ films with thicknesses above 1 μm, *i.e.*, above 20 bilayers. This fact may be attributed to the change in growth mechanism from exponential to linear that takes place above 20 bilayers as it was shown in the Chapter 4. Thus, it follows that the effective interaction established between Alg and Chi is weaker for sprayed LbL than for spin-coated LbL. It was proposed that the initial exponential growth observed in Figure 4.8 (Chapter 4) is controlled by the interdiffusion of both Alg and Chi leading to a significant increase of the elastic moduli with the increase of bilayers. Once the thickness of the sprayed LbL film reaches a certain value, the buildup changes from an exponential to linear growth due to a hindering of the diffusion process and the elastic modulus tends to a *plateau* value.

The deformation of Alg/Chi films is almost constant with the number of bilayers and only varies in a range between 0.5 and 1.5 nm due to the similar peak force used for all measurements. Similarly, adhesion values are independent of the number of deposited bilayers with values ranging between 1 and 4 nN. This is expected, as the adhesion is derived from the pull off force that is a measure of the attractive forces between the tip and outermost layers of the samples, *i.e.*, the adhesion measurements are sensitive only to the surface and thus they should be similar for all the samples. Moreover, there are no differences in deformation and adhesion between films prepared at the two concentrations of Alg.

Now, we turn our attention to the effect of the crosslinking on the mechanical properties measured on (Alg2.5/Chi)$_n$ films as a function of the number of bilayers (*n*) (Figure 5.4b). For $n<10$, the elastic moduli of crosslinked films are similar to those of the native ones. However, as the number of bilayers increases, the elastic moduli drastically increase to reach a maximum value of ≈ 47.4 ± 3.8 GPa at 40 Alg/Chi bilayers. In addition, the deformation values of crosslinked (Alg2.5/Chi)$_n$ films remain below 0.9 nm regardless the number of bilayers. Adhesion values are on the same range as those encountered for native films with the exception of (Alg2.5/Chi)$_5$ film for which the adhesion force increases to 6 nN. Although no conclusive explanation for this effect exists, it can be speculated about a lower chemical heterogeneity for the crosslinked sample at low number of bilayers arising from a lower degree of interpenetration between alginate and chitosan as shown in Figure 4.8 (Chapter 4). This result would imply that the adhesion promoted by the final chitosan layer would be higher than that resulting from the interpenetration with alginate. It is important to note that in ambient conditions, the values of adhesion are likely facilitated by capillary forces of a surface adsorbed water layer in air.[33] This

is especially relevant in the case of hydrophilic polymers such as chitosan that constitutes the last layer of all the samples under study.[34, 35]

To partially summarize, crosslinked films present a higher elastic modulus and less deformation than native films. As expected, crosslinking increases the stiffness of the multilayer films provoking an increase in the elastic modulus. This is due to the fact that thermal crosslinking results in an amidization reaction between the carboxylate groups of alginate (COO^-) and the ammonium groups of the chitosan (NH_3^+) to form amide crosslinks (NHCO) that rigidify the multilayers.[36] The crosslinking reduces the molecular mobility of polymer chains because it decreases the intermolecular space between these chains.[7] The effect of film crosslinking on the elastic moduli was expected since the degree of crosslinking is known to influence the mechanical properties of multilayer films. As an example, in a recent study, the Young Modulus of Alg/Chi films, determined on 31.7 ± 4.7 μm film thickness by dynamic mechanical analysis in a hydrated environment at 37°C, increased from 4.8 to 56.4 MPa after crosslinking with genipin.[31]

Effect of the presence of nanoparticles

In this section, the effect of the presence of iron oxide nanoparticles (NPs), inside the multilayer structures as well as on the outermost layer, on the mechanical properties is discussed.

In a first step, the presence of NPs inside multilayer films is studied. Representative (PF-QNM) AFM images corresponding to nanocomposite $(Alg/Chi)_{10}/(NPs/Chi)_{10}$ films are shown in Figure 5.5. The mechanical properties (elastic modulus, deformation and adhesion) were analyzed in four different points of these images. It is worth to emphasize that the analysis was carried out in 1 μm^2 regions.

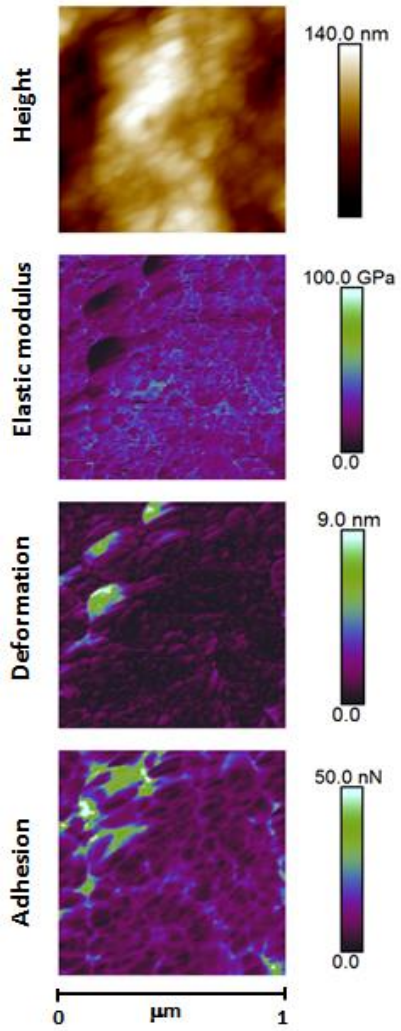

Figure 5.5. (PF-QNM) AFM images (1µm × 1µm), height, elastic modulus, deformation and adhesion, corresponding to a nanocomposite $(Alg/Chi)_{10}/(NPs/Chi)_{10}$ film.

Table 5.2 summarizes the results corresponding to the thickness, determined by SEM, and the mechanical properties, determined by (PF-QNM)-AFM, for three nanocomposite $(Alg/Chi)_n/(NPs/Chi)_m$ films with Chi as ending layer.

Table 5.2. Summary of mechanical properties of nanocomposite $(Alg/Chi)_n/(NPs/Chi)_m$ films determined by (PF-QNM) AFM and thickness determined by SEM.

Samples	Thickness (μm)	Elastic modulus (GPa)	Deformation (nm)	Adhesion (nN)
$(Alg/Chi)_3/(NPs/Chi)_2$	0.24 ± 0.10	18.8 ± 6.3	1.1 ± 0.9	2.3 ± 1.5
$(Alg/Chi)_5/(NPs/Chi)_5$	0.38 ± 0.13	34.4 ± 5.6	1.1 ± 0.2	21.4 ± 2.8
$(Alg/Chi)_{10}/(NPs/Chi)_{10}$	1.11 ± 0.34	26.2 ± 3.9	0.8 ± 0.2	11.7 ± 3.9

As it can be observed, for the same number of bilayers, nanocomposite $(Alg/Chi)_n/(NPs/Chi)_m$ films present a higher elastic moduli than $(Alg2.5/Chi)_n$ films (results depicted in Figure 5.4a). These results corroborate that the mechanical properties, found by (PF-QNM) AFM, are consistent with intrinsic properties of the sample and are not influenced by the substrate properties. It is interesting to note that the values of deformation increased significantly in nanocomposite films with respect to Alg/Chi films for which the values of deformation range between 0.5 and 1.5 nm. A careful examination of the results depicted in Figure 5.5 for the $(Alg/Chi)_{10}/(NPs/Chi)_{10}$ film shows that regions that deform more correspond to regions with no NPs. It might be hypothesized that the incorporation of NPs might decrease the number of interactions between polyelectrolyte layers, thus promoting the formation of 'empty regions' in between polymer layers which might lead to the increase of deformation. In fact, previous reports on the incorporation of NPs during the buildup of the multilayer film have revealed that the deposition process can give rise to islands that create empty regions into the internal structure of the film.[37, 38] For the nanocomposite films under study, SEM images shown in Figure 5.6 corroborate the formation of empty spaces or islands during the spray deposition. The film with a lower number of NPs layers (Figure 5.6a) presents separated islands on different points of the surface of the film. As the number of bilayers increases, islands decrease their size and the deposition becomes more homogeneous (Figures 5.6b and c).

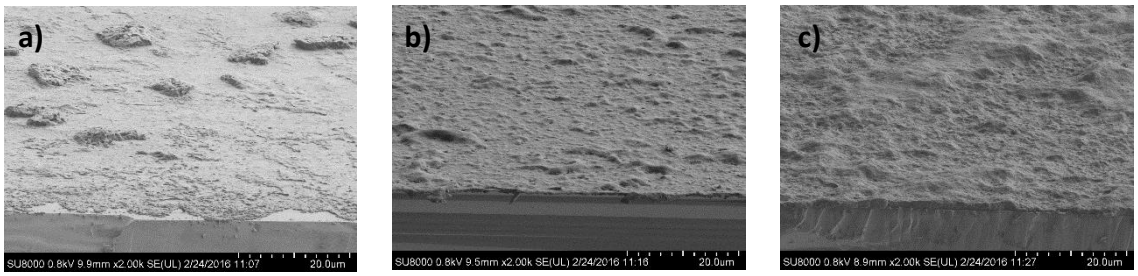

Figure 5.6. SEM micrographs corresponding to the surface of nanocomposite films a) $(Alg/Chi)_3/(NPs/Chi)_2$; b) $(Alg/Chi)_5/(NPs/Chi)_5$ and c) $(Alg/Chi)_{10}/(NPs/Chi)_{10}$.

Furthermore, it is noteworthy that the adhesion value is a factor of 2−3 higher when iron oxide NPs are incorporated within Alg/Chi films (see Table 5.2) compared to native Alg/Chi films (results depicted in Figure 5.4), indicating that NPs play a significant role on the adhesion values. As shown in Figure 5.1, the roughness of nanocomposite films increases with respect to films without nanoparticles. As previously described for samples without nanoparticles, adhesion values are likely to be influenced by the formation of a water neck between the AFM tip and the sample due to capillary condensation and adsorption of thin water films at surface. In addition, surface roughness has also a great influence on the adhesion force measured through AFM although this effect is hard to quantify.[33] In the case of nanocomposite films, which show higher values of roughness with respect to films without nanoparticles, it might be hypothesized that the formation of empty spaces or islands during the spray deposition might induce an increase in the contact area between the tip and the surface which would have an effect on the increase of the adhesion values found for these samples.

The effect of the presence of NPs on the outermost layer of nanocomposite films on the mechanical properties was also evaluated. Figure 5.7 shows representative (PF-QNM) AFM images for nanocomposite $(Alg/Chi)_5/(NPs/Chi)_5$ (Figure 5.7a) and $(Alg/Chi)_5/(NPs/Chi)_5$-NPs (Figure 5.7b) films with the same number of bilayers, but with different ending layer, Chi and NPs, respectively.

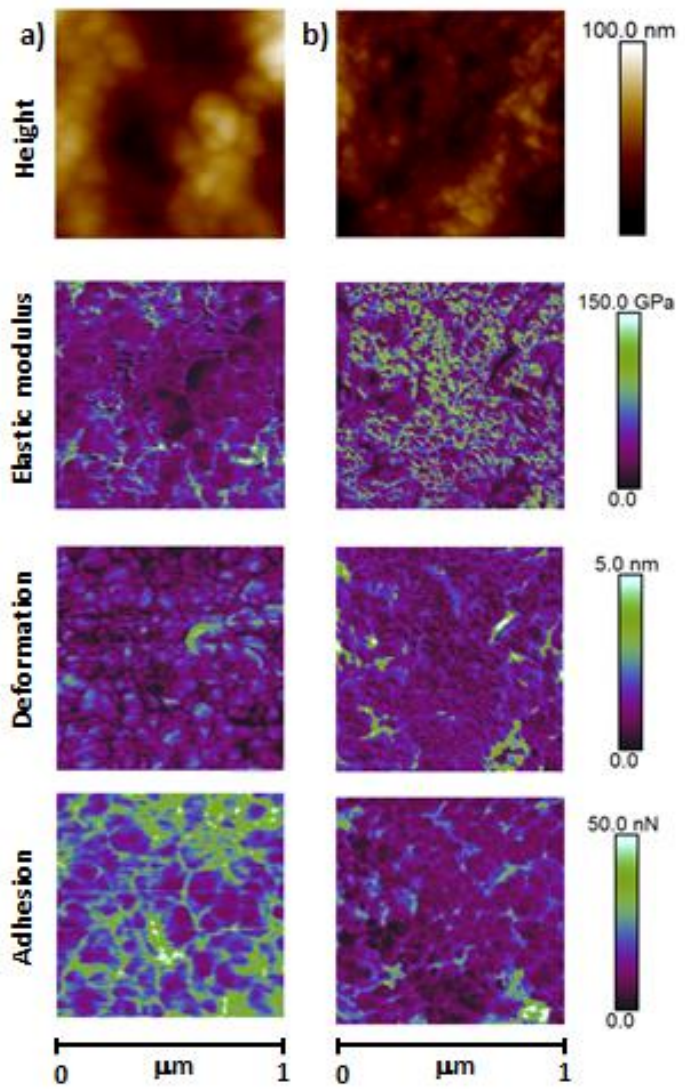

Figure 5.7. (PF-QNM) AFM images (1µm × 1µm), height, elastic modulus, deformation and adhesion corresponding to nanocomposite a) $(Alg/Chi)_5/(NPs/Chi)_5$ and b) $(Alg/Chi)_5/(NPs/Chi)_5$-NPs films.

The incorporation of an additional NPs layer on the top of the nanocomposite films increases their thickness from 0.38 ± 0.13 µm to 0.76 ± 0.23 µm. The elastic modulus of nanocomposite $(Alg/Chi)_5(NPs/Chi)_5$-NP_s films in which the iron oxide nanoparticles are incorporated on the last layer takes values of 50.0 ± 7.5 GPa, showing a two-fold increase with respect to nanocomposite $(Alg/Chi)_5(NPs/Chi)_5$ films in which the last layer is chitosan (Table 5.2) due to the fact that NPs are stiffer than chitosan. This has been corroborated for other polymer systems. The deposition of a layer of gold nanoparticles on the surface of multilayer films of hyaluronic acid and poly-L-Lysine, $(HA/PLL)_{24}$-AuNPs, gave rise to a 16-fold increase of the elastic modulus with regards to films without metallic nanoparticles on the surface.[39] In addition, the high values of elastic modulus obtained here (up to 50 GPa) for iron oxide nanoparticles as

ending layer are in agreement with the order of magnitude of elastic modulus of other metallic nanoparticles, such as gold or silver.[40]

The deformation values, 1.3 ± 0.1 nm, almost remain constant in nanocomposite films whether the last layer is chitosan or NPs. This corroborates that deformation is more influenced by empty spaces into the multilayer structure than the number of layers or the nature of the outermost layer.

The presence of NPs on the top of multilayer films decreases the adhesion to 11.3 ± 1.4 nm. Taking into account that the adhesion values are sensitive to attractive interactions between the tip and the sample surface, as mentioned above, this result suggests that chitosan has higher adhesion than magnetic nanoparticles.

5.3.3. Study of the inner structure of nanocomposite films

Grazing incident small-angle X-ray scattering (GISAXS) is able to examine the lateral structure at the surface and the morphology inside the films. In addition, GISAXS provides information about inner structures of thin films at the nanoscale along a macroscopic area, on the contrary to direct imaging techniques such as SEM and AFM, which only gives information about the surface morphology along a small region of the sample.[27, 28]

The influence of the method of preparation, spray and dipping LbL, and the number of NPs layers in the inner structure of nanocomposite films has been evaluated by GISAXS.

Figure 5.8 (left) shows the 2D GISAXS patterns at an incident angle of 0.4º of a film $(Alg/Chi)_5$ prepared by spray LbL (Figure 5.8a) and nanocomposite $(Alg/Chi)_n(NPs/Chi)_m$ films prepared by dipping LbL (Figure 5.8b) and spray LbL (Figure 5.8c). The scattering pattern corresponding to a $(Alg/Chi)_5$ film prepared by dipping LbL is similar to this one prepared by spray LbL and for that reason it is not displayed. The horizontal black bars are caused by the intermodular detector gap (IDG) between adjacent modules of the detector. The vertical streak in the center of the pattern indicates the reflection plane where the horizontal component of the scattering vector equals zero ($q_y = 0$). In these images the specular beam stop (SBS) to prevent the damage of the detector is observed. The intensity maximum observed in these patterns corresponds to the Yoneda peak[41] which appears at the critical angle of the scattering material. To visualize this zone in more detail, Figure 5.8 (right) shows a zoom corresponding to the area delimited by a dashed red rectangle performed along the q_y and q_z directions which are directly related to ω and α, respectively as it was described in the chapter 3. As can be observed, the scattering intensity at

the Yoneda peak position increases in nanocomposite films (Figures 5.8 b and c) due to the presence of NPs with regards to the film without NPs (Figure 5.8a). In the case of a film without NPs, the ring of intensity around the Yoneda peak represents the isotropic orientation of the domains in the film.[42] With regards to films with one NPs layer, spray LbL deposition gives rise to certain anisotropy in the q_y direction (Figure 5.8c), whereas the scattering pattern corresponding to films prepared by dipping LbL shows the isotropic character of the sample (Figure 5.8b).

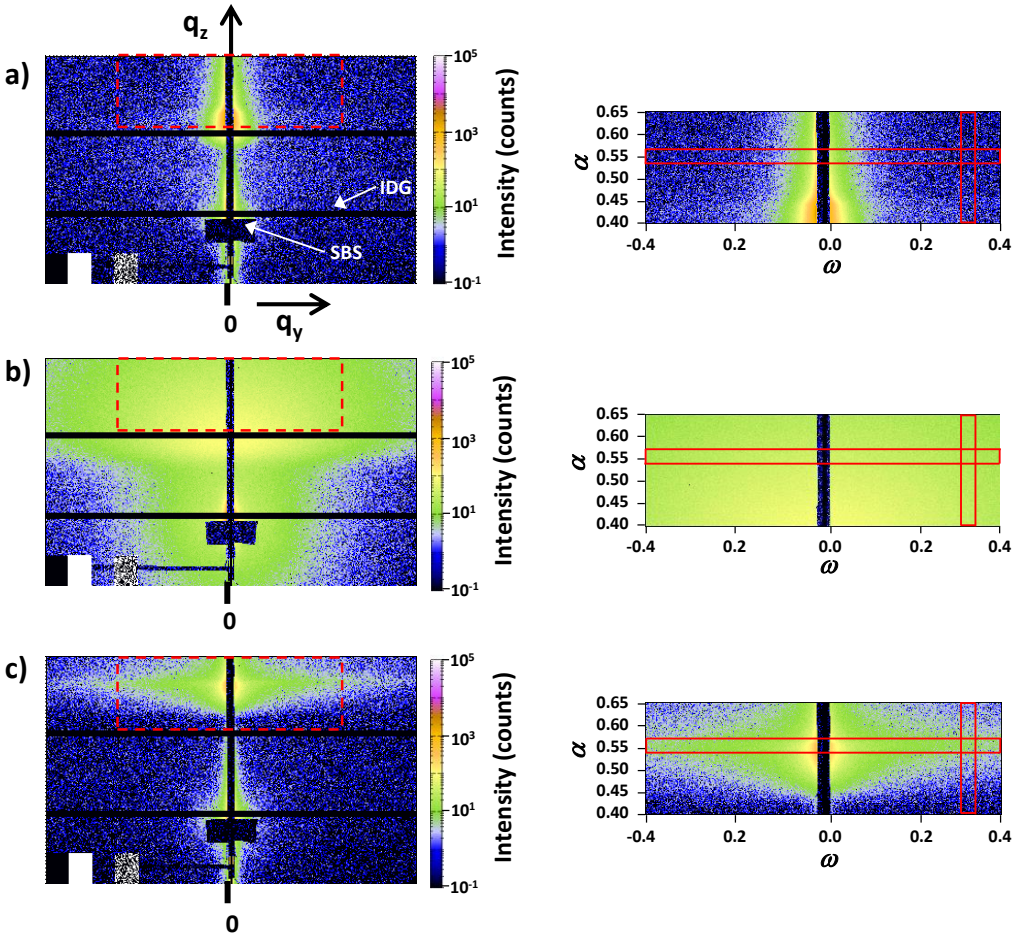

Figure 5.8. GISAXS patterns at α_i = 0.4º of a) $(Alg/Chi)_5$ film prepared by spray LbL, b) $(Alg/Chi)_2/(NPs/Chi)_1$ film prepared by dipping LbL and c) $(Alg/Chi)_2/(NPs/Chi)_1$ film prepared by spray LbL (left) and zoom in at the Yoneda peak region with horizontal cuts at α = 0.57º and vertical cuts at ω = 0.3º corresponding to areas delimited by a red rectangle in the GISAXS patterns (right).

With the aim of analyzing these patterns in more detail and extract lateral structure information from inside multilayer films, horizontal cuts at α = 0.57º and vertical cuts at ω = 0.3º were integrated over 20 pixels and performed along the ω and α directions, respectively and results are shown in Figure 5.9.

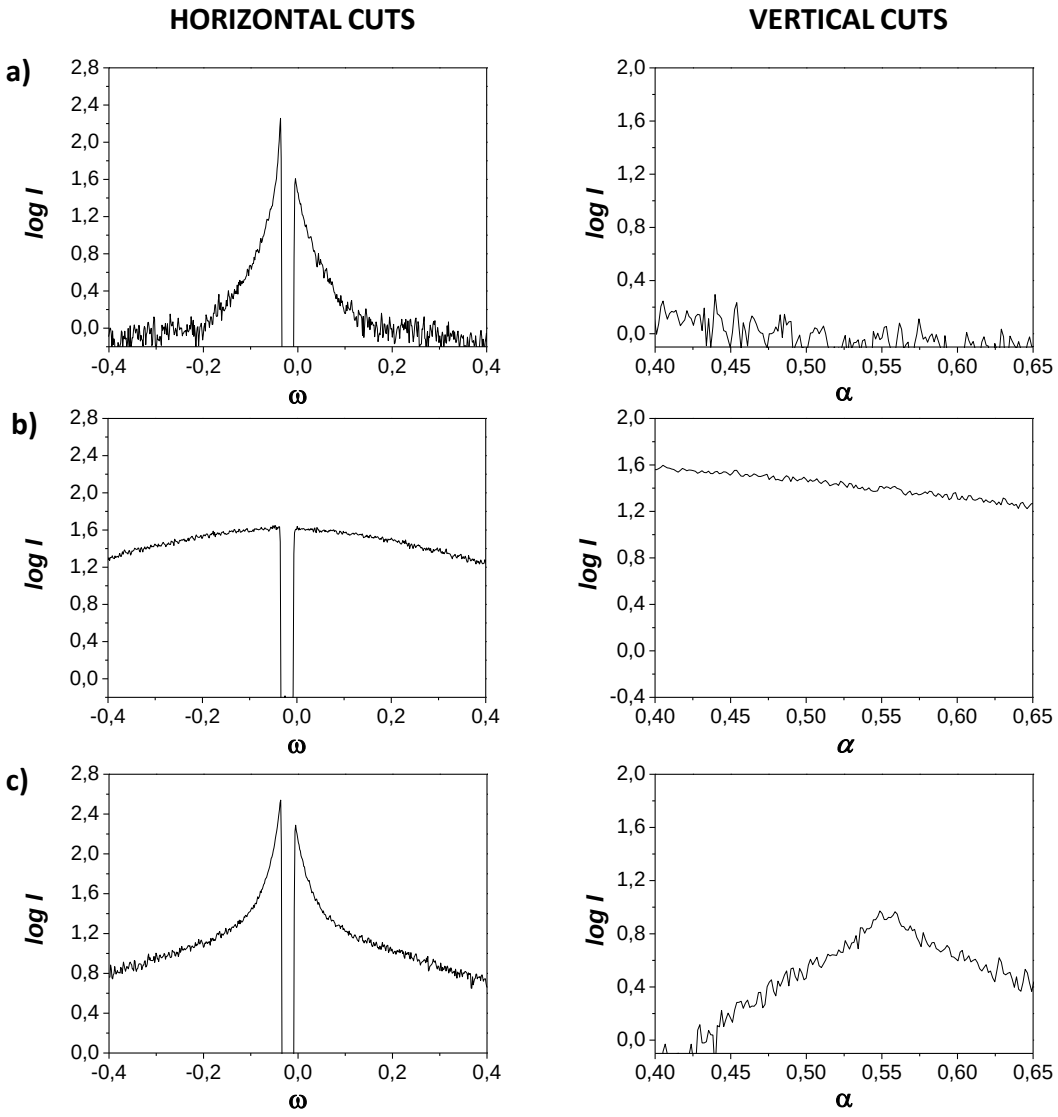

Figure 5.9. Horizontal cuts at $\alpha = 0.57^{o}$ (left) and vertical cuts at $\omega = 0.3^{o}$ (right) from GISAXS patterns at $\alpha_i = 0.4^{o}$ of a) $(Alg/Chi)_5$ film prepared by spray LbL, b) $(Alg/Chi)_2/(NPs/Chi)_1$ film prepared by dipping LbL and c) $(Alg/Chi)_2/(NPs/Chi)_1$ film prepared by spray LbL.

The representations of log I versus ω, obtained from the horizontal cuts, do not show any scattering intensity maxima out of the meridiam ($\omega \neq 0$) for any sample. However, the graphic displays of log I versus α, obtained from vertical cuts, show a maximun in scattering intensity around $\alpha = 0{,}55^{o}$ in Figures 5.9 c and d.

To clarify what is intended to be analyzed with every cut, the Scheme 5.3 illustrates a picture of a nanocomposite film with one NPs layer (Scheme 5.3a) and their corresponding horizontal (Scheme 5.3b) and vertical (Scheme 5.3c) cuts in an ideal process where every layer is deposited as a monolayer without interpenetration between them or diffussion of NPs along the multilayer structure.

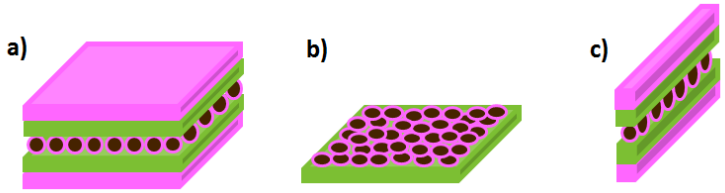

Scheme 5.3. a) Schematic representation of a nanocomposite film with one NPs layer, b) horizontal cut and c) vertical cut of this film.

The absence of any scattering intensity maximum in the horizontal cuts (Figure 5.9 left) might be attributed to the scattering of structureless objects due to the presence of the NPs and the roughness of the films. In the vertical cuts (Figure 5.9 right), there are significant differences between films built up by dipping and spray LbL. In the case of nanocomposite films with one NPs layer prepared by dipping LbL (Figure 5.9b), the scattering intensity remains constant corroborating the isotropic character of the sample which could be attributed to the diffusion of the NPs throught the whole structure. In samples built up by spray LbL (Figure 5.9c), the appearence of a scattering intensity maximum indicates that there is some anisotropy in the vertical direction that could be attributed to a certain degree of ordering of NPs within the multilayer structure and they could be positioned in an intermediate layer. The broadening of this maximum indicates a high dispersion of NPs maybe due to the roughness of the films.

A qualitative model that illustrates the inner structure of Alg/Chi films obtained by spray and dipping LbL is shown in Scheme 5.4. Multilayer films are inherently rough, even more when they are fabricated by spray LbL (Scheme 5.4a). These results could indicate that NPs deposited by spray LbL does not diffuse along the structure (Scheme 5.4b) whereas those deposited by dipping LbL diffuse throught the structure during the deposition time (Scheme 5.4c). In contrast, spray LbL is a quicker deposition technique, providing less time for the diffusion of NPs nd giving rise to some degree of ordering of the NPs layers.

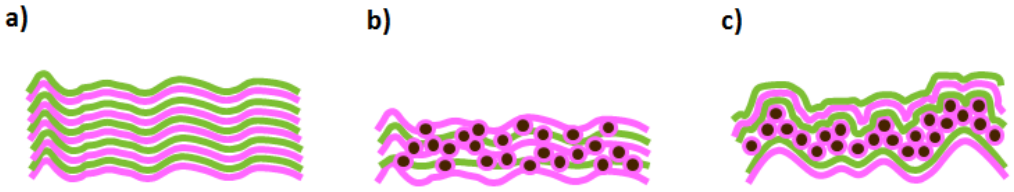

Scheme 5.4. Schematic representation showing the structural morphology proposed for a) $(Alg/Chi)_5$ film, b) $(Alg/Chi)_2/(NPs/Chi)_1$ film built up by dipping LbL and c) $(Alg/Chi)_2/(NPs/Chi)_1$ film prepared by spray LbL.

5.4. CONCLUSIONS

The influence of three different experimental parameters, alginate concentration, thermal crosslinking and number of NPs layers, on the thickness and mechanical properties of multilayer Alg/Chi films, crosslinked Alg/Chi films and nanocomposite Alg/Chi films built up via spray LbL were determined by SEM and (PF-QNM) AFM, respectively.

The elastic moduli increased with the number of deposited bilayers up to a value of ~12 GPa for alginate concentrations of 1.0 and 2.5 mg/mL. Thermal crosslinking of Alg/Chi films reduced the roughness of multilayer films and increased the elastic modulus. This increase was much more significant for films obtained with higher alginate concentration. For both series of samples, non-crosslinked and crosslinked Alg/Chi films, deformation values are below 2 nm and the adhesion force varies between 1 and 4 nN regardless the number of bilayers or the concentration of alginate. This was attributed to the fact that the composition of the outer layer is similar for all the studied samples and the adhesion measurements were sensitive only to the surface.

The incorporation of iron oxide NPs within the multilayer films increased their roughness and induced an increase of the elastic moduli of the resulting films. The increase in the values of deformation found for nanocomposite Alg/Chi films with respect to Alg/Chi films suggested the presence of empty spaces originated from the fabrication process of the films.

Adhesion values of nanocomposite films were higher than those corresponding to $(Alg/Chi)_n$ films which pointed to a significant effect of the presence of nanoparticles on the adhesion values found for nanocomposite films. The incorporation of NPs on the last layer of nanocomposite films gave rise to a two-fold increase in the elastic modulus with respect to nanocomposite films in which the last layer is chitosan, whereas the deformation was not affected.

The study of the inner structure of nanocomposite films by GISAXS revealed that films assembled by dipping LbL gave rise to an isotropic structure, whereas these ones assembled by spray LbL could form separated NPs layers with dispersion of NPs along the structure due to the inherent roughness of these films. These results were visualized with the aid of a proposed qualitative model.

5.5. REFERENCES

1. Langhe, D.; Ponting, M., Introduction to Multilayered FIlms. In *Manufacturing and Novel Applications of Multilayer Polymer Films*, William Andrew Publishing: Boston, 2016; pp 1-15.

2. Wong, H. C.; Higgins, A. M.; Wildes, A. R.; Douglas, J. F.; Cabral, J. T., Patterning Polymer–Fullerene Nanocomposite Thin Films with Light. *Advanced Materials* **2013,** 25, (7), 985-991.

3. Wang, L.-m.; Chang, H.; Zhang, H.; Ren, K.-f.; Li, H.; Hu, M.; Li, B.-c.; Martins, M. C. L.; Barbosa, M. A.; Ji, J., Dynamic stiffness of polyelectrolyte multilayer films based on disulfide bonds for in situ control of cell adhesion. *Journal of Materials Chemistry B* **2015,** 3, (38), 7546-7553.

4. Ventrelli, L.; Fujie, T.; Turco, S. D.; Basta, G.; Mazzolai, B.; Mattoli, V., Influence of nanoparticle-embedded polymeric surfaces on cellular adhesion, proliferation, and differentiation. *Journal of Biomedical Materials Research Part A* **2014,** 102, (8), 2652-2661.

5. Discher, D. E.; Mooney, D. J.; Zandstra, P. W., Growth Factors, Matrices, and Forces Combine and Control Stem Cells. *Science* **2009,** 324, (5935), 1673.

6. Fujie, T.; Matsutani, N.; Kinoshita, M.; Okamura, Y.; Saito, A.; Takeoka, S., Adhesive, Flexible, and Robust Polysaccharide Nanosheets Integrated for Tissue-Defect Repair. *Advanced Functional Materials* **2009,** 19, (16), 2560-2568.

7. Gil, S.; Silva, J. M.; Mano, J. F., Magnetically Multilayer Polysaccharide Membranes for Biomedical Applications. *ACS Biomaterials Science & Engineering* **2015,** 1, (10), 1016-1025.

8. Dokukin, M. E.; Sokolov, I., Quantitative Mapping of the Elastic Modulus of Soft Materials with HarmoniX and PeakForce QNM AFM Modes. *Langmuir* **2012,** 28, (46), 16060-16071.

9. Martínez-Tong, D. E.; Najar, A. S.; Soccio, M.; Nogales, A.; Bitinis, N.; López-Manchado, M. A.; Ezquerra, T. A., Quantitative mapping of mechanical properties in polylactic acid/natural rubber/organoclay bionanocomposites as revealed by nanoindentation with atomic force microscopy. *Composites Science and Technology* **2014,** 104, 34-39.

10. Schön, P.; Bagdi, K.; Molnár, K.; Markus, P.; Pukánszky, B.; Julius Vancso, G., Quantitative mapping of elastic moduli at the nanoscale in phase separated polyurethanes by AFM. *European Polymer Journal* **2011,** 47, (4), 692-698.

11. Nguyen, H. K.; Fujinami, S.; Nakajima, K., Elastic modulus of ultrathin polymer films characterized by atomic force microscopy: The role of probe radius. *Polymer* **2016,** 87, 114-122.

12. Richert, L.; Engler, A. J.; Discher, D. E.; Picart, C., Elasticity of Native and Cross-Linked Polyelectrolyte Multilayer Films. *Biomacromolecules* **2004,** 5, (5), 1908-1916.

13. Derjaguin, B. V.; Muller, V. M.; Toporov, Y. P., Effect of contact deformations on the adhesion of particles. *Journal of Colloid and Interface Science* **1975,** 53, (2), 314-326.

14. Sham, A. Y. W.; Notley, S. M., Graphene–polyelectrolyte multilayer film formation driven by hydrogen bonding. *Journal of Colloid and Interface Science* **2015,** 456, 32-41.

15. Fernández, R.; Ocando, C.; Fernandes, S. C. M.; Eceiza, A.; Tercjak, A., Optically Active Multilayer Films Based on Chitosan and an Azopolymer. *Biomacromolecules* **2014,** 15, (4), 1399-1407.

16. Tian, Y.; Li, L.; Han, H.; Wang, W.; Wang, Y.; Ye, Z.; Guo, X., Modification of Spherical Polyelectrolyte Brushes by Layer-by-Layer Self-Assembly as Observed by Small Angle X-ray Scattering. *Polymers* **2016,** 8, (4), 145.

17. Singh, M. A.; Groves, M. N., Depth profiling of polymer films with grazing-incidence small-angle X-ray scattering. *Acta Crystallographica Section A: Foundations of Crystallography* **2009,** 65, (Pt 3), 190-201.

18. Zhang, P.; Santoro, G.; Yu, S.; Vayalil, S. K.; Bommel, S.; Roth, S. V., Manipulating the Assembly of Spray-Deposited Nanocolloids: In Situ Study and Monolayer Film Preparation. *Langmuir* **2016,** 32, (17), 4251-4258.

19. Herzog, G.; Benecke, G.; Buffet, A.; Heidmann, B.; Perlich, J.; Risch, J. F. H.; Santoro, G.; Schwartzkopf, M.; Yu, S.; Wurth, W.; Roth, S. V., In Situ Grazing Incidence Small-Angle X-ray Scattering Investigation of Polystyrene Nanoparticle Spray Deposition onto Silicon. *Langmuir* **2013,** 29, (36), 11260-11266.

20. Ho, T. T. M.; Bremmell, K. E.; Krasowska, M.; MacWilliams, S. V.; Richard, C. J. E.; Stringer, D. N.; Beattie, D. A., In Situ ATR FTIR Spectroscopic Study of the Formation and Hydration of a Fucoidan/Chitosan Polyelectrolyte Multilayer. *Langmuir* **2015,** 31, (41), 11249-11259.

21. Picart, C., Polyelectrolyte multilayer films: from physico-chemical properties to the control of cellular processes. *Current medicinal chemistry* **2008,** 15, (7), 685-697.

22. Pichon, B. P.; Louet, P.; Felix, O.; Drillon, M.; Begin-Colin, S.; Decher, G., Magnetotunable Hybrid Films of Stratified Iron Oxide Nanoparticles Assembled by the Layer-by-Layer Technique. *Chemistry of Materials* **2011,** 23, (16), 3668-3675.

23. Lauter-Pasyuk, V.; Lauter, H.; Gordeev, G.; Müller-Buschbaum, P.; Toperverg, B. P.; Petry, W.; Jernenkov, M.; Petrenko, A.; Aksenov, V., Parallel and perpendicular lamellar phases in copolymer–nanoparticle multilayer structures. *Physica B: Condensed Matter* **2004,** 350, (1–3, Supplement), E939-E942.

24. Lauter-Pasyuk, V.; Lauter, H. J.; Gordeev, G. P.; Müller-Buschbaum, P.; Toperverg, B. P.; Jernenkov, M.; Petry, W., Nanoparticles in Block-Copolymer Films Studied by Specular and Off-Specular Neutron Scattering. *Langmuir* **2003,** 19, (19), 7783-7788.

25. Kashem, M. M. A.; Perlich, J.; Schulz, L.; Roth, S. V.; Müller-Buschbaum, P., Correlated Roughness in Polymer Films Containing Maghemite Nanoparticles. *Macromolecules* **2008,** 41, (6), 2186-2194.

26. Abul Kashem, M. M.; Perlich, J.; Diethert, A.; Wang, W.; Memesa, M.; Gutmann, J. S.; Majkova, E.; Capek, I.; Roth, S. V.; Petry, W.; Müller-Buschbaum, P., Array of Magnetic Nanoparticles via Particle Co-operated Self-Assembly in Block Copolymer Thin Film. *Macromolecules* **2009,** 42, (16), 6202-6208.

27. Song, L.; Wang, W.; Körstgens, V.; González, D. M.; Yao, Y.; Minar, N. K.; Feckl, J. M.; Peters, K.; Bein, T.; Fattakhova-Rohlfing, D.; Santoro, G.; Roth, S. V.; Müller-Buschbaum, P., Spray Deposition of Titania Films with Incorporated Crystalline Nanoparticles for All-Solid-State Dye-Sensitized Solar Cells Using P3HT. *Advanced Functional Materials* **2016,** 26, (10), 1498-1506.

28. Philipp, M.; Körstgens, V.; Magerl, D.; Heller, C.; Yao, Y.; Wang, W.; Santoro, G.; Roth, S. V.; Müller-Buschbaum, P., Sorption of Water and Initial Stages of Swelling of Thin PNIPAM Films Using in Situ GISAXS Microfluidics. *Langmuir* **2015,** 31, (35), 9619-9627.

29. Rydzek, G.; Schaaf, P.; Voegel, J.-C.; Jierry, L.; Boulmedais, F., Strategies for covalently reticulated polymer multilayers. *Soft Matter* **2012,** 8, (38), 9738-9755.

30. Luo, H.; Shen, Q.; Ye, F.; Cheng, Y.-F.; Mezgebe, M.; Qin, R.-J., Structure and properties of layer-by-layer self-assembled chitosan/lignosulfonate multilayer film. *Materials Science and Engineering: C* **2012,** 32, (7), 2001-2006.

31. Silva, J. M.; Duarte, A. R. C.; Caridade, S. G.; Picart, C.; Reis, R. L.; Mano, J. F., Tailored Freestanding Multilayered Membranes Based on Chitosan and Alginate. *Biomacromolecules* **2014,** 15, (10), 3817-3826.

32. Taccola, S.; Desii, A.; Pensabene, V.; Fujie, T.; Saito, A.; Takeoka, S.; Dario, P.; Menciassi, A.; Mattoli, V., Free-Standing Poly(l-lactic acid) Nanofilms Loaded with Superparamagnetic Nanoparticles. *Langmuir* **2011,** 27, (9), 5589-5595.

33. Butt, H.-J.; Cappella, B.; Kappl, M., Force measurements with the atomic force microscope: Technique, interpretation and applications. *Surface Science Reports* **2005,** 59, (1–6), 1-152.

34. Nogales, A.; Ezquerra, T. A.; Rueda, D. R.; Martinez, F.; Retuert, J., Influence of water on the dielectric behaviour of chitosan films. *Colloid and Polymer Science* **1997,** 275, (5), 419-425.

35. Stukalov, O.; Murray, C. A.; Jacina, A.; Dutcher, J. R., Relative humidity control for atomic force microscopes. *Review of Scientific Instruments* **2006,** 77, (3), 033704.

36. Yang, S. Y.; Rubner, M. F., Micropatterning of Polymer Thin Films with pH-Sensitive and Cross-linkable Hydrogen-Bonded Polyelectrolyte Multilayers. *Journal of the American Chemical Society* **2002,** 124, (10), 2100-2101.

37. Huang, H.; Spaepen, F., Tensile testing of free-standing Cu, Ag and Al thin films and Ag/Cu multilayers. *Acta Materialia* **2000,** 48, (12), 3261-3269.

38. He, J.; Kanjanaboos, P.; Frazer, N. L.; Weis, A.; Lin, X.-M.; Jaeger, H. M., Fabrication and Mechanical Properties of Large-Scale Freestanding Nanoparticle Membranes. *Small* **2010,** 6, (13), 1449-1456.

39. Schmidt, S.; Madaboosi, N.; Uhlig, K.; Köhler, D.; Skirtach, A.; Duschl, C.; Möhwald, H.; Volodkin, D. V., Control of cell adhesion by mechanical reinforcement of soft polyelectrolyte films with nanoparticles. *Langmuir* **2012,** 28, (18), 7249-7257.

40. Guo, D.; Xie, G.; Luo, J., Mechanical properties of nanoparticles: basics and applications. *Journal of Physics D: Applied Physics* **2013,** 47, (1), 013001.

41. Yoneda, Y., Anomalous Surface Reflection of X Rays. *Physical Review* **1963,** 131, (5), 2010-2013.

42. Busch, P.; Posselt, D.; Smilgies, D. M.; Rauscher, M.; Papadakis, C. M., Inner Structure of Thin Films of Lamellar Poly(styrene-b-butadiene) Diblock Copolymers As Revealed by Grazing-Incidence Small-Angle Scattering. *Macromolecules* **2007,** 40, (3), 630-640.

CHAPTER 6

In vitro study of nanocomposite Alg/Chi films for applications in magnetic hyperthermia

This chapter describes the potential application of nanocomposite Alg/Chi films for magnetic hyperthermia therapy. The iron content of nanocomposite Alg/Chi films described in the Chapter 5 and their heating induced by an alternating magnetic field were determined. It was also evaluated the human neuroblastoma SH-SY5Y cell adhesion onto these films and their application for *in vitro* magnetic hyperthermia treatment through a proof of concept using neuroblastoma cells. In addition to this, the specific power absorption of the alginate based magnetic ferrofluid described in the Chapter 3 and the effect of its immobilization in a gel-like material were determined.

6.1. INTRODUCTION

Magnetic nanoparticles (NPs) provide LbL films with the ability to respond to a magnetic field.[1-3] In biomedical applications, magnetic responsive polymers also find applications in controlled drug release mediated through external magnetic fields[4] and magnetic hyperthermia therapies (MHT).[5] Hyperthermia is a treatment in which the temperature of the body tissue is increased in a range between 42 – 45 ºC to kill cancer cells.[6, 7] The three main kinds of treatments for clinical applications of MHT therapy are: *i)* the whole-body hyperthermia where the entire body is heated up, *ii)* the regional hyperthermia which is applied by perfusion of a limb, organ or body cavity with heated fluids and *iii)* the local hyperthermia where the heat is applied in a localized area.[8] In local hyperthermia, heat is applied to small and superficial tumor areas with the aim of reaching temperatures up to 42 ºC for one hour within the cancer tumor to cause cell death, being a less invasive technique as compared with regional and whole hyperthermia. Clinical cases where local hyperthermia is a viable alternative include chest wall recurrences, superficial malignant melanoma lesions and head/neck tumors.[9, 10] There are several approaches for the application of local hyperthermia including superficial applicators of different shapes and kinds that can be heated by the action of external energy sources such as radiofrequencies, microwave, ultrasound or near infrared radiation laser.[11-13] Polymer films with embedded gold nanoparticles have been succesfully employed for tissue laser ablation when placed in contact with the tissue to be treated inducing local exogeneus hyperthermia. While the photothermal therapy offers the possibility to control the energy dose delivered to the target area by both the intensity of the laser beam and the concentration of NPs, this technique is limited by the short penetration depth of the NIR wavelength into the human body (~0.3 cm in breast tissue) even at the known ‘optical window’ of water.[14]

Magnetic hyperthermia (MHT) is based on the employment of an alternating magnetic field (AMF) to increase the temperature of magnetic nanoparticles used as heating agents.[15-18] The potential of magnetic NPs to be used as heating agents depends on their specific power absorption (SPA), defined as the power absorbed by unit mass of NPs which it is released to the surrounding medium to generate heat. Iron oxide nanoparticles (NPs) have been reported to have SPA values large enough to heat macroscopic tumors, and also to display lower toxicity than other heating materials investigated (*e.g.*, Co, Ni and their oxides).[19] There exist multiple research approaches for the design of polymer materials, *e.g.*, in the form of nanogels, nanoparticles or micelles, able to encapsulate NPs in order to promote selective internalization into tumor cells and hence, promote intracellular magnetic hyperthermia.[16-18] Currently, there are very promising results regarding the application of intracellular magnetic hyperthermia for clinical oncology.[20, 21]

Intracellular hyperthermia consist of using magnetic nanoparticles to remotely induce local heat when an alternating magnetic field is applied giving rise to the required temperature increase of 42 - 45 ºC to induce cell apoptosis in the tumor site (tissues and organs).[22] Cancer cells are more sensitive to temperature oscillations than normal cells due to the fact that tumor cells show an increased metabolism, higher rates of glycolysis and enhanced radiosensitivity than normal cells, which makes them more vulnerable to hyperthermia therapy. In order to be used for intracellular hyperthermia therapy, NPs have to be non-toxic, biocompatible and injectable.[23] The main disadvantages of this technique are: the difficulty to drive them to the target of interest, the difficulty to internalize a concentration of NPs enough to achieve an effective treatment. At this point it has to be considered the surface functionalization of NPs which influences their attachment to target species (cells, tissues, organs) and the NPs size, because the bigger size of NPs the higher magnetic heating produced, but if NPs are too big they could not be able to cross the endothelial barrier and if they are too small could not produce enough heating to induce cell death.[16, 23] An alternative approach to apply MHT therapy could be the incorporation of NPs inside a polymer film in order to control the concentration of NPs, directly related to the increase of temperature achieved through the application of MHT. Such thermomagnetic films (TMFs) could be placed in contact with the tissue affected by cancer disease to induce exogenous magnetic hyperthermia.

The exogenous heating strategy using magnetic fields that it is described in this chapter can deliver energy density values to the target area that are lower than the typical values produced by photothermal therapy. However, as biological tissues essentially do not interact with ac magnetic

fields of 100-500 kHz, the energy can be delivered essentially into any depth of the human body. This property makes our strategy based on the employment of thermomagnetic polymer films (TMFs) more adapted to subcutaneous or deeper applications. To the best of our knowledge, such approach has not been undertaken before. In the chapter 5 the incorporation of magnetic nanoparticles within multilayer polymer films obtained from chitosan and alginate through spray assisted LbL was described and in this chapter, their thermal effect and their application in magnetic hyperthermia treatment was evaluated through a proof of concept on human neuroblastoma SH-SY5Y cells. The neuroblastoma-derived SH-SY5Y cell line was selected as a model of human malignant metastatic neuroblastoma which exhibits a notable resistance to hyperthermic stress.[24]

6.2. EXPERIMENTAL PART

6.2.1. Materials

Chitosan (Chi) of low molecular weight (448869, lot SLBG1673V), sodium alginate (Alg) (A2158, lot 090M0092V), poly(ethylenimine) (PEI) with a molecular weight (M_w) of 25000 and acetic acid were supplied by Aldrich. Sodium acetate anhydrous was supplied by Panreac. More information about these materials is detailed in the chapter 3.

It was also employed a lab-made alginate based magnetic ferrofluid containing the iron oxide nanoparticles (NPs) with a magnetite concentration of 8.0 mg/mL whose characteristics have been described in the Chapter 3.

Live/Dead viability/cytotoxicity kit, for mammalian cells was supplied by Molecular Probes, ThermoFisher scientific (L3224). The kit contains calcein AM (4 mM in anhydrous DMSO) and ethidium homodimer-1 (2 mM in DMSO/H_2O 1:4 (v/v)).

6.2.2. Preparation of nanocomposite Alg/Chi films

All multilayer films were built on functionalized glass slides (12 mm ϕ) by spray assisted layer-by-layer (LbL) of aqueous solutions of alginate (2.5 mg/mL), chitosan (1 mg/mL) and a lab-made alginate-based magnetic ferrofluid containing the NPs (8.0 mg/mL) following the procedure described in chapter 5 with some variations, such as the waiting time after the deposition of the NPs layer and the increase of the NPs/Chi bilayers with regards to Alg/Chi bilayers, as shown in Scheme 6.1. The spray time was fixed at 5 s with a waiting time of 15 s between layers of chitosan and alginate and 30 s between NPs and Chitosan layers. The

structural unity was formed by a bilayer Alg/Chi followed by four bilayers NPs/Chi repeated as many times as necessary until the desired number of layers was obtained. Samples were denoted as $(Alg/Chi)_n(NPs/Chi)_m$ where *n* stands for the number of Alg/Chi bilayers (*n* = 2, 4, 8, 12, 20 and 40) and *m* for the corresponding number of NPs/Chi bilayers (*m* = 8, 16, 32, 48, 80 and 160).

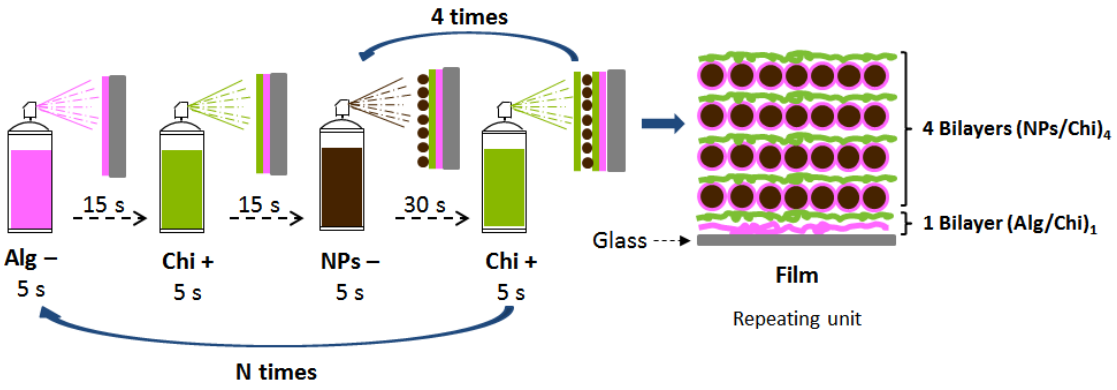

Scheme 6.1. Schematic representation of the spray assisted layer-by-layer procedure and the repeating structural unit of the nanocomposite $(Alg/Chi)_n/(NPs/Chi)_m$ multilayer films.

In order to achieve free-standing films, a polyvinyl alcohol (PVA) layer with a concentration of 100 mg/mL was deposited over the multilayer films with a pipette and dried for 24 hours until become robust. The resulting multilayer film with the ending PVA layer was peeled from the glass substrate with tweezers; after that, the resulting free-standing film was immersed in Milli-Q water and the PVA layer was removed by dissolution in water (Scheme 6.2).

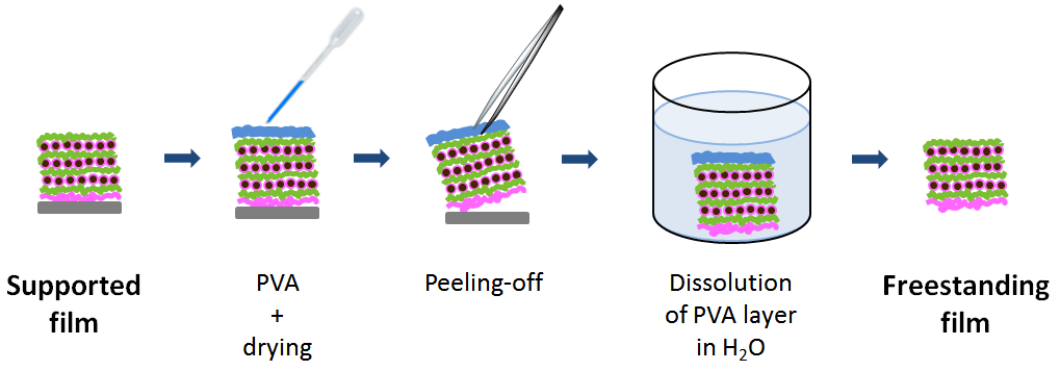

Scheme 6.2. Schematic representation to obtain a free-standing film using a PVA sacrificial layer.

6.2.3. Characterization of nanocomposite Alg/Chi films

Determination of the iron content

The determination of the iron content of $(Alg/Chi)_n(NPs/Chi)_m$ films was carried out through UV-Vis transmission spectrophotometry using the thiocyanate complexation reaction and measuring the absorbance of the iron-thiocyanate complex at 478 nm wavelength.

$$Fe^{3+}_{(aq)} + 6\,SCN^{-}_{(aq)} \rightarrow [Fe(SCN)_6]^{3-}_{(aq)}$$

$(Alg/Chi)_n(NPs/Chi)_m$ free-standing films were dissolved in HCl 6M/HNO_3 (65%) for 2h. After that, potassium thiocyanate was added to the solution to form the iron-thiocyanate complex. The magnetite content was determined by comparing the sample absorbance to a calibration curve (Annex I, Figure A.I.1).

Morphological studies

To determine the inner organization of the polymer films, dual beam FIB/SEM (Nova 200 NanoLab, FEI Company) was carried out on nanocomposite $(Alg/Chi)_n(NPs/Chi)_m$ films. Films were coated with platinum for imaging with the FIB-SEM. SEM images were taken at 5 kV with a Field Emission Guns (FEG) column, and a combined Ga-based 30 kV (10 pA) ion beam was used to cross-sectioning films. These investigations were completed by energy-dispersive X-ray spectroscopy (EDX) for chemical analysis.

Determination of magnetic remote heating

The magnetic heating was determined separately for the alginate based magnetic ferrofluid and for the nanocomposite films.

The heating capacity of the *as prepared* ferrofluid under alternating magnetic fields (AMF) was measured using a commercial magnetic field applicator (DM-100, nB Nanoscale Biomagnetics, Spain) (Figure 6.1) at frequencies $250 < f < 820$ kHz and field amplitudes $0 \leq H \leq 24$ kA/m. The fluoroptic thermometer integrated into this equipment allowed to measure the temperature as a function of time.

Figure 6.1. Magnetic field applicator DM-100, nB Nanoscale Biomagnetics.

The heating of nanocomposite $(Alg/Chi)_n(NPs/Chi)_m$ films was remotely induced by an alternating magnetic field (AMF) using a commercial induction heating station (EasyHeat, Ambrell B.V., The Netherlands) working at f = 180 kHz and field amplitude of H = 35 kA/m. The AMF was applied over the samples placed at the center of 11-turn solenoid. The samples were thermalized at 37 ºC by a water-heated jacket, which has also the function of thermally detach the samples from the joule heating at the coil. The temperature was measured using a thermal camera (FLIR Systems, USA) in a zenithal position over the film. Before each experiment, the samples were placed within the solenoid and allowed to thermalize at 37 ºC for 5 min before the AMF was turned on. After that, the heating time for each sample was 5 min. A photograph of this experimental setup in the Institute of Nanoscience of Aragon is shown in Figure 6.2.

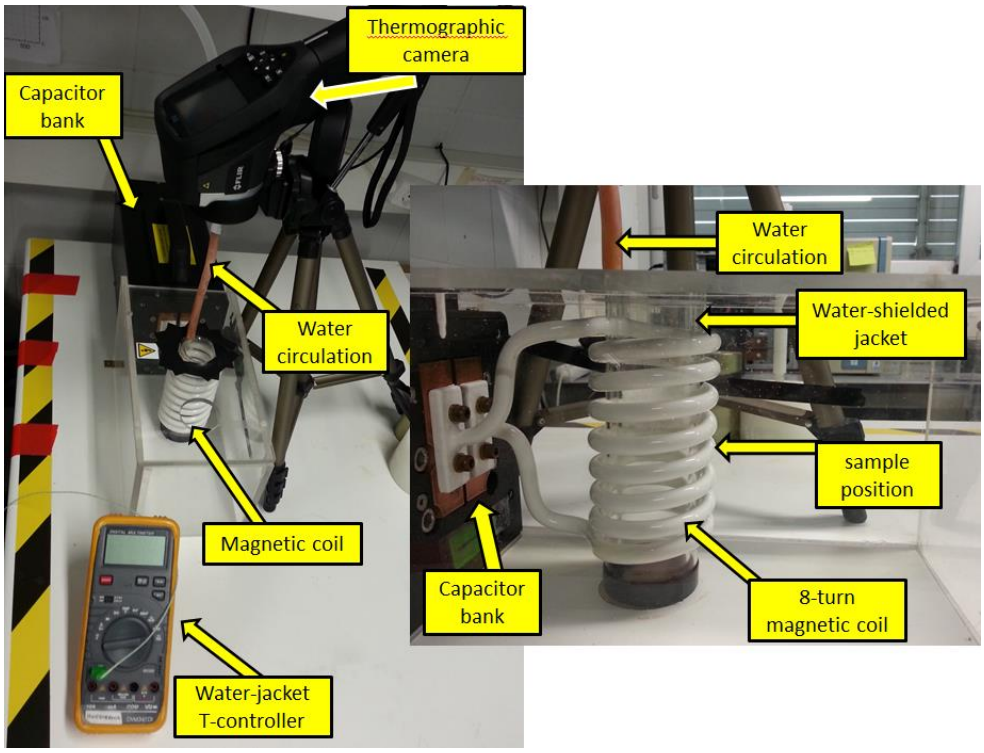

Figure 6.2. Experimental setup for the measurements of the magnertic remote heating of nanocomposite films as well as for the application of *in vitro* magnetic hyperthermia and magnification of solenoid.

6.2.4. *In vitro* magnetic hyperthermia experiments

Study of adhesion of neuroblastoma cells

Direct contact assays to test cell adhesion were carried out on $(Alg/Chi)_n(NPs/Chi)_m$ films with different number of layers. Films were sterilized under UV light for 5 hours. Human neuroblastoma SH-SY5Y cells (ATCC CRL-26) were cultured in Dulbecco's modified Eagle's medium (DMEM) and Ham's F12 (1:1) with 15% fetal bovine serum, 100 IU/mL penicillin, 100 μg/mL streptomycin and 2 mM L-glutamine. Cells were maintained at 37 ºC in a saturated humidity atmosphere containing 95% air and 5% of CO_2. At confluence, cells were trypsinized and seeded on the films surface with a cellular density of 1.5 x 10^5 cells. Cells were cultured for 48 hours. For adhesion tests, the cell growth was followed at 24 and 48 hours by scanning electron microscopy (Nova 200 NanoLab, FEI Company). For that, cells adhered onto the films were fixed with 2 %v/v glutaraldehyde for 2 h at 4°C, treated with 2.5 %v/v potassium ferrocyanate and 1 %v/v osmium tetroxide. Later, SH-SY5Y cells were dehydrated and coated with platinum for imaging with the FIB-SEM. SEM images were taken at 5 kV with a FEG column, and a combined Ga-based 30 kV (10 pA) ion beam was used to cross-sectioning single cells. These investigations were completed by energy-dispersive X-ray spectroscopy (EDX) for chemical analysis.

Experimental setup and conditions for *in vitro* magnetic hyperthermia experiments

In order to test nanocomposite $(Alg/Chi)_n(NPs/Chi)_m$ films as a suitable material for magnetic hyperthermia (MHT) applications, human neuroblastoma SH-SY5Y cells with a cellular density of 1.5 x 10^5 cells were cultured on the film surface for 48 hours in an Ibidi dish at 37 ºC in a saturated humidity atmosphere containing 95% air and 5% of CO_2. After that, the film was subjected to 1 cycle of MHT (f = 180 kHz, H = 35 kA/m, t = 30 min) as shown in Scheme 6.3a. In the case of application of more than one cycle of MHT, the waiting time between cycles was 5 h and samples were maintained at 37 ºC in a saturated humidity atmosphere 95% air and 5% CO_2.

A second experimental protocol (Scheme 6.3b) consisted on placing a thermomagnetic film above human neuroblastoma SH-SY5Y cells with a cellular density of 1.5 x 10^5 cells cultured on an Ibidi dish for 48h at 37 ºC in a saturated humidity atmosphere containing 95% air and 5% of CO_2. After that, the Ibidi dish was subjected to two cycles of MHT (f = 180 kHz, H = 35 kA/m, t = 30 min, waiting time between cycles = 5h).

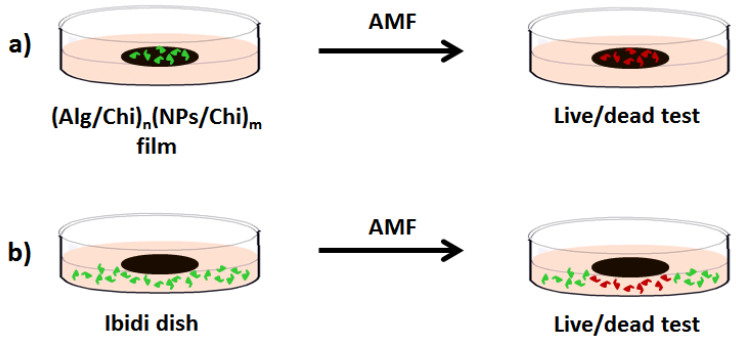

Scheme 6.3. Schematic representation of the two different experimental protocols employed to measure *in vitro* magnetic hyperthermia.

Determination of cell viability after magnetic hyperthermia experiments

Viability of cells cultured on $(Alg/Chi)_n(NPs/Chi)_m$ films and subjected to hyperthermia treatment was determined with the Live/Dead viability/cytotoxicity kit 12 hours after the application of the last MHT cycle in the first experimental protocol and after 3 hours in the second experimental protocol. Cells were washed with 1 mL of PBS, after that, 1 mL of the stain kit was added and kept for 30 minutes at room temperature in darkness. The Live/Dead kit contains calcein AM (4 mM in anhydrous DMSO) and ethidium homodimer-1 (2 mM in DMSO/H_2O 1:4 (v/v)) which allows staining live cell in green and dead cells in red, respectively. The stained cells were visualized with a Leica SP2 AOBS confocal scanning microscope. Images were collected using the microscope in sequential mode with a 20x (lens specification, HCPL FLUOTAR NA 0.50; Leica), a line average of 16 and a format of 1024x1024 pixels. The confocal pinhole was 1 Airy unit.

6.3. RESULTS AND DISCUSSION

The characterization of multilayer films fabricated with different number of NPs layers, from 8 to 160, is carried out in order to prove their application in magnetic hyperthermia therapy *in vitro* with neuroblastoma cells at the end of this chapter.

6.3.1. Determination of iron content of nanocomposite Alg/Chi films

Previous to determine the iron content of nanocomposite films, the incorporation of NPs within the multilayer structure of Alg/Chi films was assessed visually (Figure 6.3a). All nanocomposite $(Alg/Chi)_n(NPs/Chi)_m$ films under study present an homogeneous colour which suggests a good dispersion of NPs within the films and they become darker with the increase in the number of

NPs layers. The magnetite content (Fe_3O_4) incorporated within the multilayer films was determined by UV-Vis transmission spectrophotometry and plotted in Figure 6.3b as a function of the number of NPs layers. The magnetite content increases linearly with the number of NPs layers and could be fitted with the following equation

$$f(Fe_3O_4) = -0.44 + 0.052N \qquad (eq.\,6.1)$$

where N is the number of NPs layers.

The linear trend observed up to the maximum number of NPs layers deposited suggests that the final Fe_3O_4 concentration per unit area could be even increased, although there is likely a limit in the mechanical integrity of the films over N = 200. However, as discussed within this chapter, the deposition of the NPs layers during the buildup process of multilayer polymer films was enough to produce a high temperature increase during the magnetic hyperthermia experiments.

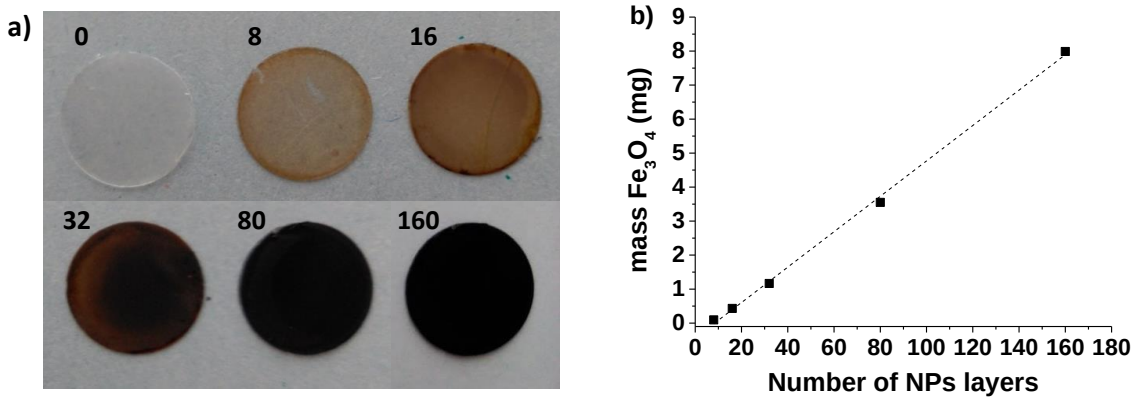

Figure 6.3. a) Image of films assembled on glass substrates with different number of NPs layers from 0 to 160 as indicated in the figure. b) Determination of Fe_3O_4 content as a function of the number of NPs layers deposited. Dashed line represents the linear fit of the data.

6.3.2. Inner morphology of nanocomposite Alg/Chi films

The inner structural organization of multilayer $(Alg/Chi)_n(NPs/Chi)_m$ films was characterized through dual-beam (FIB-SEM) images. Representative results corresponding to the cross section of sample $(Alg/Chi)_8(NPs/Chi)_{32}$ are shown in Figure 6.4a. A magnification of the SEM image shown in Figure 6.4b showed that the thickness of the sample is about 1 μm and it is nanostructured in layers, each of them with an average thickness of ~50 nm. An EDX analysis of these cross-sectioned samples revealed the layered distribution of the NPs (Figure 6.4c and 6.4d-f) as shown from elementary Fe mapping of the material. These results demonstrate not only the incorporation of Fe_3O_4 NPs into the multilayers but also their ordered intercalation between

layers in the film. The carbon is due to the polysaccharides, alginate and chitosan. The results are in agreement with those obtained by GISAXS reported in Chapter 5.

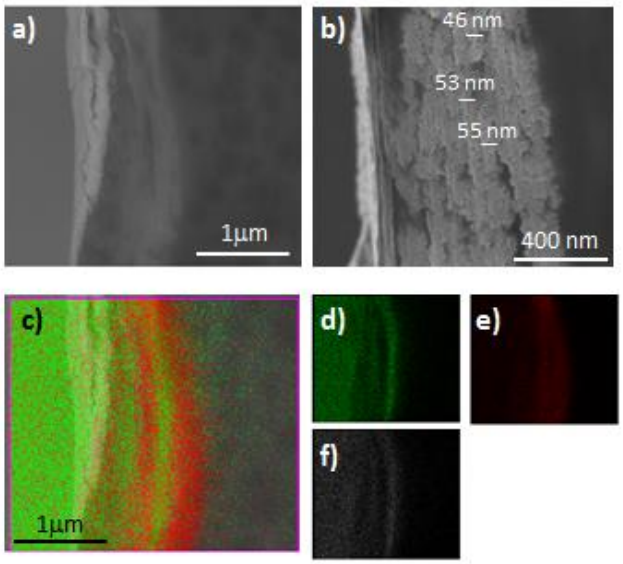

Figure 6.4. Dual beam FIB-SEM micrographs corresponding to the cross-sectional view of the $(Alg/Chi)_8(NPs/Chi)_{32}$ film (a) scale bar 1µm and b) scale bar 400 nm. (c) EDX spectrum and area of individual components of EDX spectrum, carbon (d), iron (e) and oxygen (f).

6.3.3. Determination of magnetic remote heating

Determination of the Specific Power Absorption (SPA) as a function of different experimental parameters

Previous to the measurements of the magnetic remote heating of nanocomposite films, a study of the alginate based magnetic ferrofluid, whose preparation and characterization were described in Chapter 3, was carried out.

To measure the efficiency of the ferrofluid as a heating agent under alternating magnetic fields, it is necessary to know its specific power absorption (SPA), defined as the power absorbed by unit mass of the magnetic material. SPA was measured in a commercial equipment DM-100 (Nanoscale Biomagnetics, NB). This equipment measures the heating of NPs dispersed in Milli-Q water (ferrofluid) with the time when an alternating magnetic field (AMF) is applied. Figure 6.5 shows the heating curve of a ferrofluid with a concentration of 8.0 mg/mL applying a magnetic field amplitude of 24 kA/m and a frequency of 570 kHz. The temperature increases from 23 to 27 ºC in 10 seconds (dashed arrow).

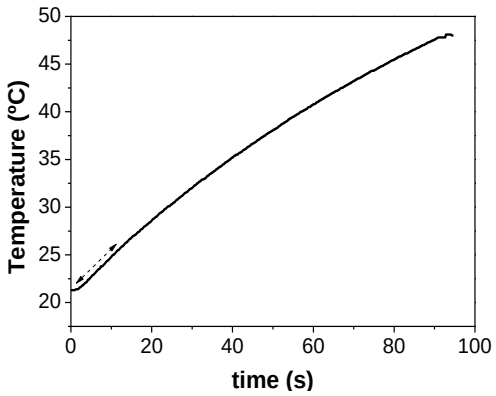

Figure 6.5. Magnetic heating of ferrofluid with a concentration of 8.0 mg/mL of magnetite in water in the commercial equipment DM-100 (Nanoscale Biomagnetics) at f = 571 kHz and H = 24 kA/m. The part of the curve employed to determine the SPA is indicated by the dashed arrow.

SPA value is obtained from the slope of the heating curve using the following equations,[25]

$$SPA = \left(\frac{m_l \cdot Ce_l + m_p \cdot Ce_p}{m_p}\right) \cdot \left(\frac{\Delta T}{\Delta t}\right)_{max} \qquad (eq.6.2)$$

where Ce and m are the specific heat and the mass, respectively and the subscripts p and l, denotes the nanoparticles and the liquid carrier, respectively. Taking into account that the concentration of NPs is less than 1 %wt, this equation can be approximated by

$$SPA = \left(\frac{\rho_l \cdot Ce_l}{\phi}\right) \cdot \left(\frac{\Delta T}{\Delta t}\right)_{max} \qquad (eq.6.3)$$

where ρ_l is the density of the liquid carrier and ϕ is the weight concentration of the NPs in the ferrofluid. In this case, the liquid carrier is water with $\rho_l = 10^3$ kg/m^3 and $Ce_l = 4.18$ kcal/kgºC.

Ferrofluids were tested at different frequencies and magnetic field amplitudes and every measurement was repeated three times. Figure 6.6a shows the SPA variation with the magnetic field amplitude at a fixed frequency of 571 kHz for two different ferrofluid concentrations, 4.8 and 8.0 mg/mL, as prepared and after 4 months for the ferrofluid with higher magnetite concentration. Figure 6.6b depicts the SPA variation with the frequency at a fixed magnetic field amplitude of 24 kA/m for two different ferrofluid concentrations (ϕ), 4.8 and 8.0 mg/mL, as prepared and after 4 months for the ferrofluid with higher concentration.

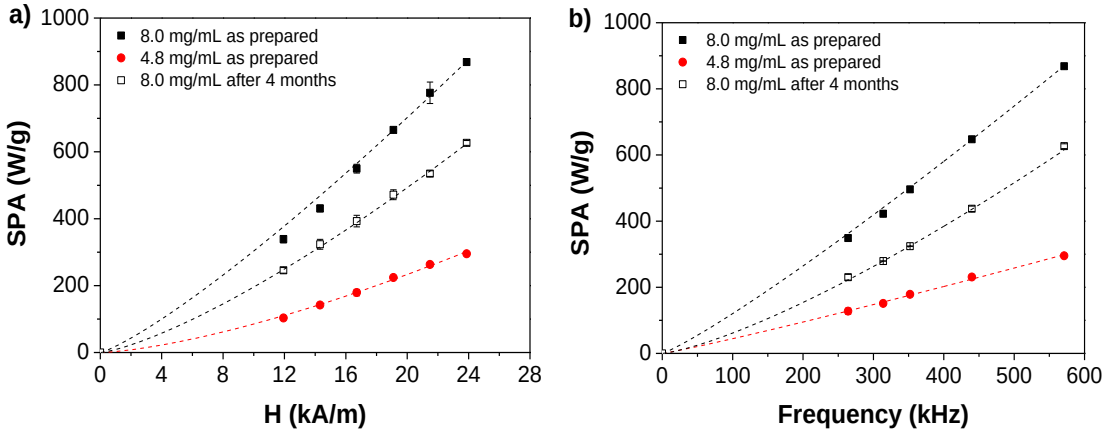

Figure 6.6. SPA dependence with a) magnetic field amplitude at *f* = 571 kHz and b) frequency at H = 24 kA/m for ferrofluids with 4.8 mg/mL as prepared (●) and 8.0 mg/mL as prepared (■) and after 4 months (□). Dashed lines are a guide to the eye.

As can be observed, SPA increases with the magnetic field amplitude and the frequency and it is highly influenced by the magnetite concentration. Focusing the attention in the SPA at H = 24 kA/m and *f* = 571 kHz, in the case of the highest concentration of magnetite (8.0 mg/mL) SPA is 868.4 ± 1.9 W/g and for the lowest concentration (4.8 mg/mL) SPA decreases up to 295.3 ± 3.5 W/g.

To study the effect of the aging in the SPA, the ferrofluid with a magnetite concentration of 8.0 mg/mL was measured 4 months after its preparation and results are also shown in the Figure 6.6. After 4 months, SPA follows the same tendency with the frequency and with the magnetic field amplitude as immediately after its preparation; however, the SPA values are lower. For example, at *f* =571 kHz and H = 24 kA/m the SPA is 868.4 ± 1.9 W/g immediately after its synthesis and 626.7 ± 7.2 W/g 4 months after its preparation. These results suggest the loss of magnetic properties of the ferrofluid probably due to some degree of oxidation of the NPs.

Note that the movement of magnetite NPs in the ferrofluid is not restricted, whereas in nanocomposite multilayer films they are immobilized. As an approach, to study the influence of the immobilization of these NPs on the heating properties, the SPA of NPs immobilized in gelatin was evaluated. To that aim, 500 µL of ferrofluid with a concentration of 8.0 mg/mL were precipitated at 14500 rpm for 15 min, then the supernatant was removed and NPs were dispersed in 1mL of 1 %w/v or 2 %w/v gelatin in a vortex for 1 min and kept at -4 ºC for 1 hour to form the gel. After that, SPA was measured in the commercial equipment DM-100 (NanoScale Biomagnetics) at a frequency of 571 kHz and a magnetic field amplitude of 24 kA/m and results are shown in Figure 6.7.

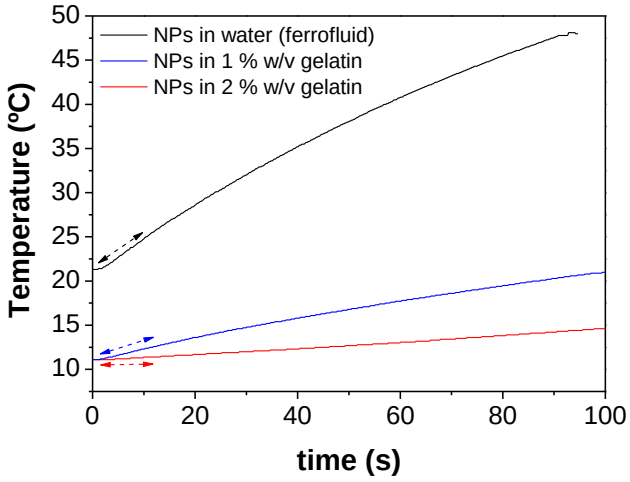

Figure 6.7. Magnetic heating of NPs in water (black line) and in 1%w/v (blue line) and 2 %w/v gelatin (red line) at *f* = 571 kHz and H = 24 kA/m. The part of the curve employed to determine the SPA is showed by the dashed arrow.

SPA is obtained from the initial slope of the curves exhibited in Figure 6.7 and results are provided in Table 6.1. SPA decreases when nanoparticles are immobilized in gelatin and this decrease is higher as gelatin concentration increases. The exposition of magnetic NPs to a radio-frequency magnetic field gives rise to a single domain particle that aligns its magnetic moment M to the field H to decrease the interaction free energy. There are two dissipation mechanisms, Brownian relaxation and Néel relaxation, which influence the magnetization of ferrofluids when they are exposed to external time varying magnetic fields. Brownian relaxation is due to the physical rotation of the nanoparticles against viscous torques from the surrounding media, *i.e.*, carrier liquid, films, etc., and Néel relaxation is caused by the rotation of the magnetic moment inside the magnetic core.[26, 27]

Due to the fact that both mechanisms take place simultaneously in the dissipation mechanism of the ferrofluid, the immobilization of NPs in gelatin tends to block the physical rotation of NPs as gelatin concentration increases and, subsequently, the Brownian contribution to the SPA value decreases being the Néel relaxation the main dissipation mechanism. It is expected that the same physical process will take place when NPs are encapsulated into the multilayer films based on chitosan and alginate as it will be discussed in next section.

Table 6.1. SPA of NPs dispersed in water and in 1%w/v and 2 %w/v gelatin.

Sample	ΔT/t (ºC/min)	SPA (W/g)
NPs in water	10.1	868.4 ± 1.9
NPs in 1%w/v gelatin	4.8	130.5 ± 6.3
NPs in 2%w/v gelatin	1.9	77.2 ± 0.1

Remote heating of nanocomposite Alg/Chi films

To assess the efficiency of the thermomagnetic films produced, a series of $(Alg/Chi)_n(NPs/Chi)_m$ films with different number of NPs layers were heated under a fixed AMF amplitude and frequency. The temperature was measured using a thermal camera (FLIR Systems, USA) in a zenithal position over the film. Figure 6.8 illustrates the sequential photographs obtained with this camera during the heating process of two different films, $(Alg/Chi)_{20}(NPs/Chi)_{80}$ (Figure 6.8a) and $(Alg/Chi)_{40}(NPs/Chi)_{160}$ (Figure 6.8b).

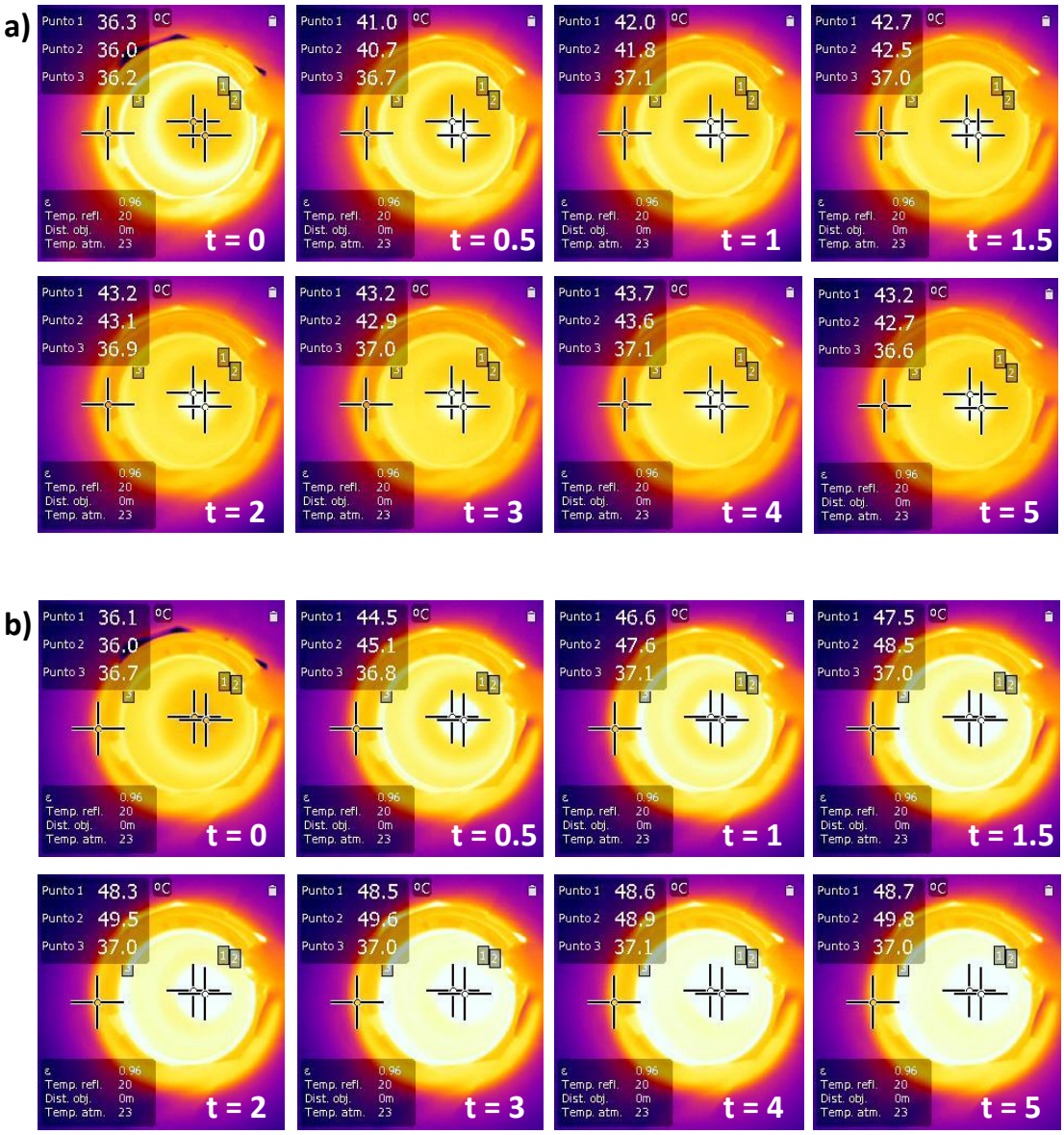

Figure 6.8. Sequential photographs obtained by a thermal camera (FLIR Systems, USA) during the heating of a) a film $(Alg/Chi)_{20}(NPs/Chi)_{80}$ and b) a film $(Alg/Chi)_{40}(NPs/Chi)_{160}$. Points 1 and 2 represent two different points of the sample and point 3 represents the temperature of the water-heated jacket.

The temperature increase, ΔT, measured from the basal value T_0 = 37 ºC, is plotted as a function of time (Figure 6.9a) and as a function of the NPs layers (Figure 6.9b) for the different samples. The heating of the films, from the basal value T_0 = 37 ºC, with time by action of the AMF was followed for 5 minutes for the different samples (Figure 6.9a). As can be observed, temperature increases during the first two minutes, then a *plateau* is reached. It can be seen from Figure 6.9b that ΔT increases linearly with the number of NPs layers (*i.e.*, films with 80 or 160 NPs layers yield ΔT of 6 and 12 ºC, respectively). Notice that the magnetic heating of the ferrofluid with a magnetite concentration of 8.0 mg/mL gave rise to a temperature increase of 48 ºC in 1.5 min (Figure 6.5) and nanocomposite films with 80 and 160 NPs layers give rise to a temperature increase of 5.8 and 11.2 ºC in 1.5 min, respectively (Figure 6.9a). The immobilization of NPs into a multilayer Alg/Chi film through spray LbL produces a similar effect to this observed for the immobilization of NPs into a gel-like material decreasing the temperature increase with respect to the ferrofluid.

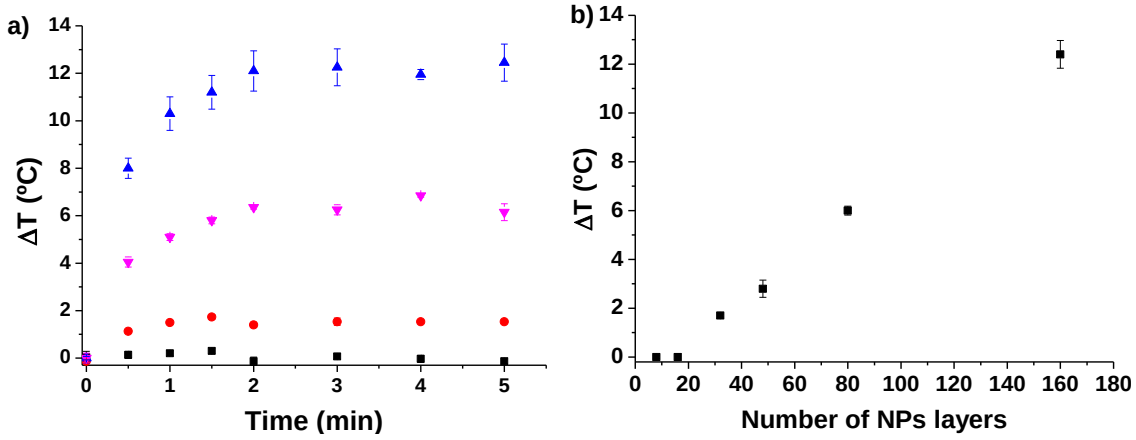

Figure 6.9. a) Temperature increase of $(Alg/Chi)_n(NPs/Chi)_m$ films measured as a function of the number of NPs layers and b) Temperature increase with the time of application of the magnetic field for films with different number of NPs layers: (■) 16, (●) 32, (▼) 80 and (▲) 160.

6.3.4. *In vitro* magnetic hyperthermia experiments

Adhesion studies of neuroblastoma cells

As $(Alg/Chi)_n(NPs/Chi)_m$ films are intended to be employed as adhesive pads for exogenous magnetic hyperthermia treatment, the first step in order to optimize the proposed application was to ascertain the cell adhesion onto the surface of the thermomagnetic films.

To study the influence of NPs on cell adhesion, neuroblastoma cells were cultured on $(Alg/Chi)_n$ and $(Alg/Chi)_n(NPs/Chi)_m$ films and the cell adhesion process was followed at different times, 24 and 48 hours, by optical microscopy and the results are shown in Figure 6.10. At 24 hours the cell adhesion is higher in films with NPs than without NPs and at 48 hours cell confluence is observed in both cases. The presence of NPs within films influences cell adhesion. In the chapter 5 it had been demonstrated that stiffness of $(Alg/Chi)_n(NPs/Chi)_m$ films built up via spray LbL increases as number of NPs increases. This could be one of the reasons why neuroblastoma cell adhesion is higher in films with NPs than in films without NPs.

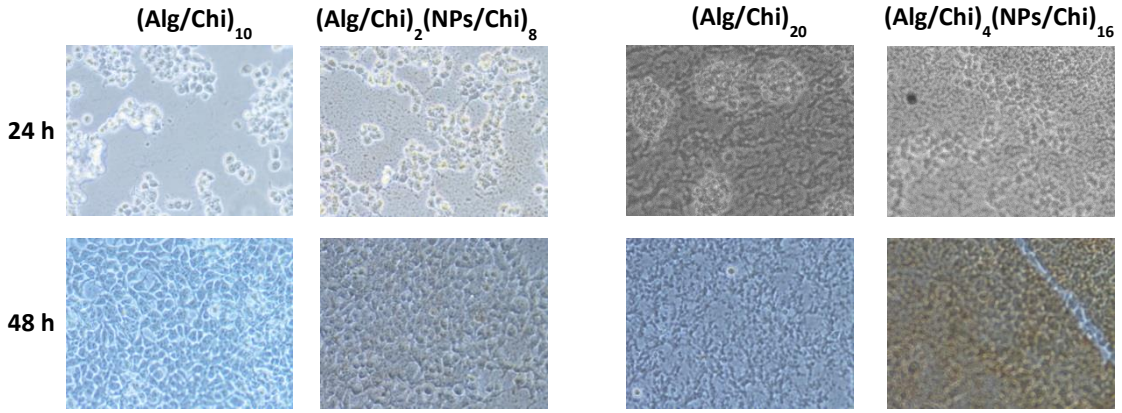

Figure 6.10. Optical micrographs of SH-SY5Y cell adhesion on $(Alg/Chi)_n$ films (n = 10 and 20) and on $(Alg/Chi)_n(NPs/Chi)_m$ films (n = 2, 4 and m =8, 16) after 24 and 48 hours

In the case of $(Alg/Chi)_{20}(NPs/Chi)_{80}$ films with a high number of NPs layers, films become very dark as can be seen in the Figure 6.3a and it is not possible to follow the cell adhesion by optical microscopy. An alternative technique consists of dehydration of samples and visualization by SEM (Figure 6.11). With the aim of checking that similar results are obtained by SEM microscopy, the cell adhesion on $(Alg/Chi)_n(NPs/Chi)_m$ films with different number of layers after 48 hours of culture was studied. Figure 6.12a shows a general view of neuroblastoma cells cultured for 24 h on a $(Alg/Chi)_{20}(NPs/Chi)_{80}$ film and cell adhesion and proliferation can be observed along the film surface. At this point, it is important to note that there are not noticeable differences regarding neuroblastoma cell adhesion and proliferation on $(Alg/Chi)_n(NPs/Chi)_m$ films with different number of NPs layers. In fact, cell confluence is also observed for films with 8 and 16 NPs layers after 24 h (Figure 6.11).

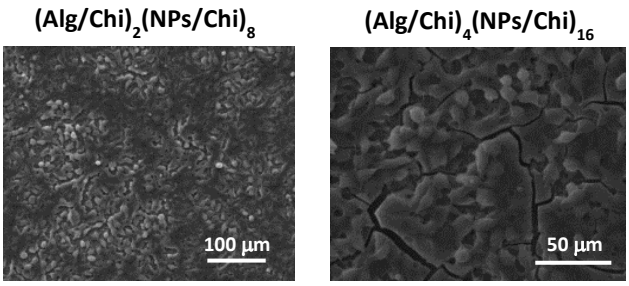

Figure 6.11. SEM micrographs of SH-SY5Y cells cultured on $(Alg/Chi)_n(NPs/Chi)_m$ films (n = 2, 4 and m = 8, 16) for 24 h.

A magnification of the SEM image (Figure 6.12b) allows observing an individual cell adhered onto the film surface. Further information on cell adhesion can be obtained from the cross section of the film. The cell adhered completely to the film surface as can be observed in a lamella cross section of the cell shown (Figure 6.12c). The analysis of the EDX spectrum corresponding to this area (Figure 6.12d) with the different elements, carbon in green (Figure 6.12e), iron in red (Figure 6.12f), oxygen in grey (Figure 6.12g) and silicon in blue (Figure 6.12h) allows to clearly differentiate the iron component embedded on the film (red color) from the nucleus of the cell (black color) marked with the arrow. Note that the presence of silicon is due to the fact that the film is supported on a glass substrate. The composition of the film can be quantitatively determined from the EDX spectrum (Figure 6.12i) where the major component is iron (64.67%), followed by O (28.69%) and C (6.64%).

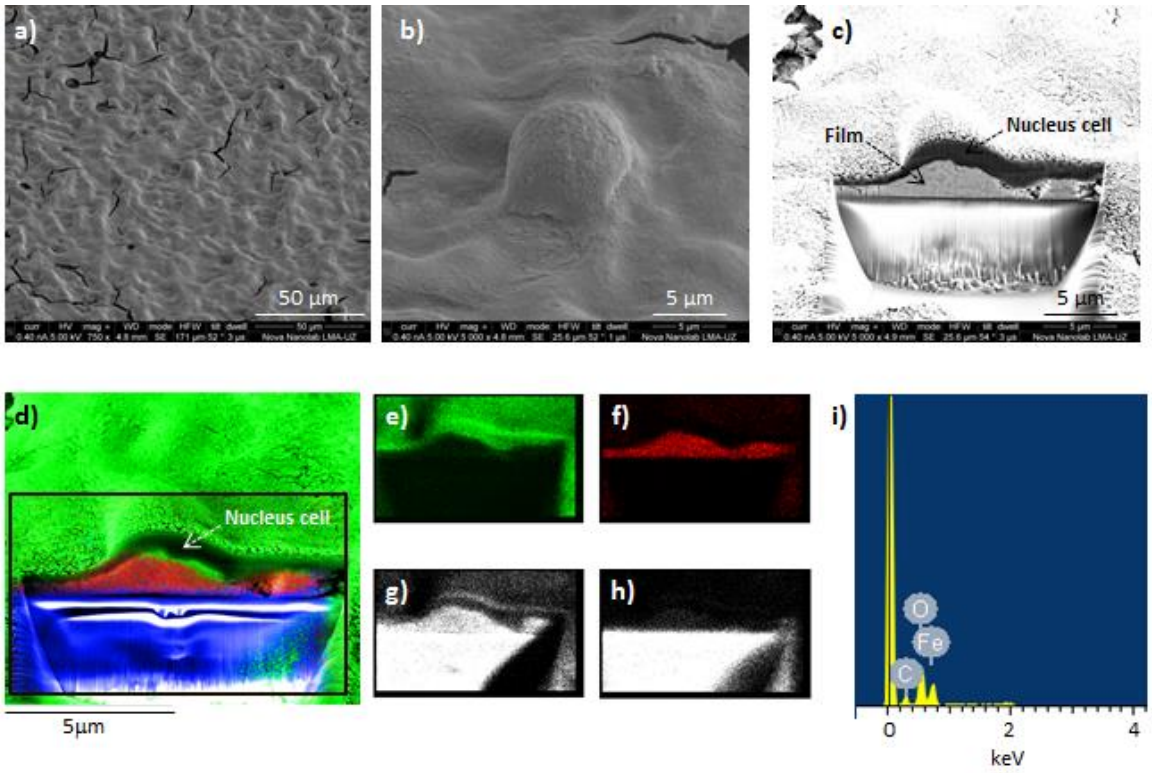

Figure 6.12. SEM micrographs corresponding to neutoblastoma cells cultured on a $(Alg/Chi)_{20}(NPs/Chi)_{80}$ film for 24 hours taken at two different magnifications: (a) 50 µm and (b) 5 µm , (c) FIB-SEM image corresponding to the cross-sectional view of an individual neuroblastoma cell adhered onto a $(Alg/Chi)_{20}(NPs/Chi)_{80}$ film, (d) EDX spectrum and area of individual components of EDX spectrum delimited by a black rectangle, carbon (e), iron (f), oxygen (g) and silicon (h) and EDX spectrum (i).

In vitro hyperthermia studies

The temperature range for activating apoptotic cell mechanisms depends on the cellular type involved, but it can be generalized that above 43-45ºC different metabolic pathways are activated to reverse the effects of the temperature.[16, 28]

Firstly, the effect of magnetic hyperthermia (MHT) on the cell viability was evaluated using the experimental protocol showed in Scheme 6.3a where neuroblastoma cells were cultured on the surface of films with 80 and 160 NPs layers and then, they were subjected to 1 cycle of MHT (H = 35 kA/m and *f* = 180 kHz; 30 min) and 3 cycles of MHT with a waiting time of 5 h between cycles. The results were compared to those obtained for neuroblastoma cells cultured on a control film not subjected to MHT treatment.

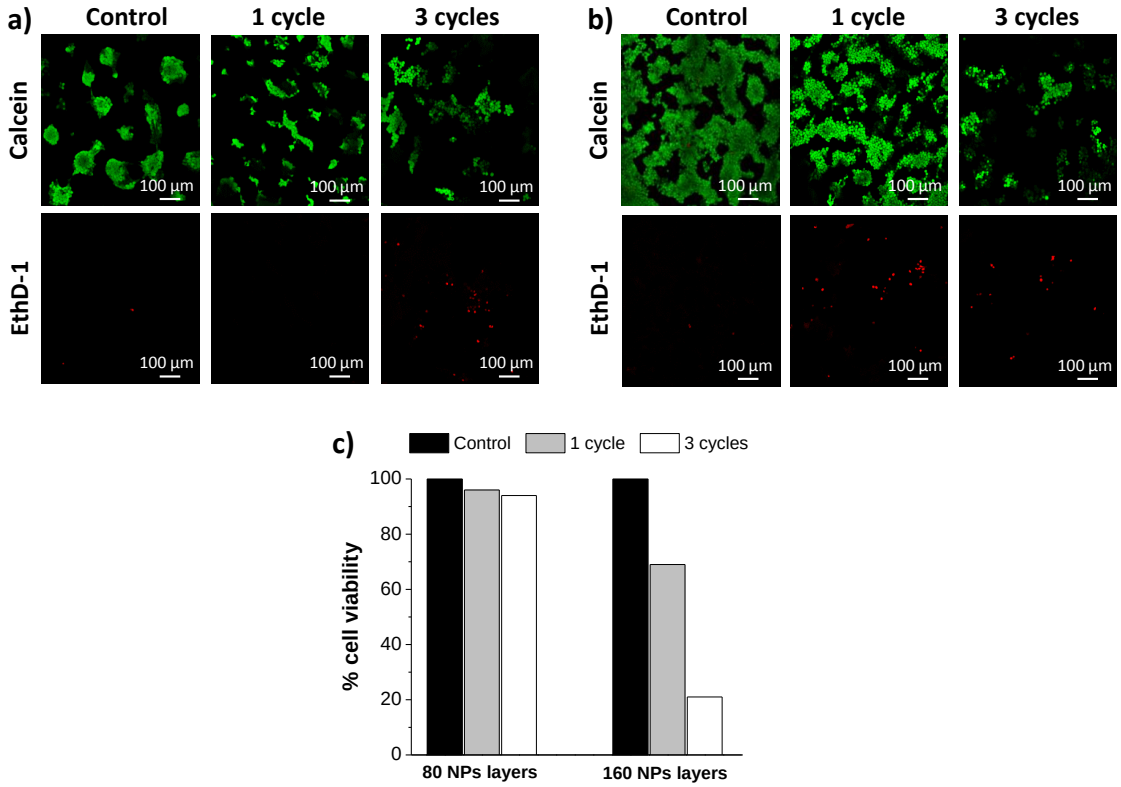

Figure 6.13. Images corresponding to the live/dead test carried out on neuroblastoma cells cultured onto a) $(Alg/Chi)_{20}(NPs/Chi)_{80}$ and b) $(Alg/Chi)_{40}(NPs/Chi)_{160}$ films subjected to 0 cycles of MHT (control), 1 cycle of MHT (30 min) and 3 cycles of MHT (30 min, waiting time between cycles of 5h). Note that cells are labelled with calcein (live cells in green) and EthD-1 (dead cells in red). (c) Determination of % cell viability obtained from the images corresponding to live cells stained in green.

The results corresponding to the live/dead test performed on neuroblastoma cells cultured on films with 80 and 160 NPs layers are shown in Figures 6.13a and 6.13b, respectively. From a qualitative point of view, control experiments carried out on neuroblastoma cells cultured on films with 80 NPs layers and not subjected to MHT, present a lower number of live cells (stained in green) adhered to the film than that observed for cells cultured on films with 160 NPs layers (Figure 6.13b). This is in general agreement with the results found in literature regarding cell adhesion on multilayer films that show that, generally speaking, cells tend to adhere more on films with higher number of layers.[29] Other studies have also shown that the incorporation of nanoparticles into polymer films improved cell adhesion due to the increase in surface roughness.[30, 31] For cells cultured onto films with 80 NPs layers (Figure 6.13a), the application of one and three cycles of MHT does not significantly change the area covered by live cells with respect to the control experiment. In contrast, Figure 6.13b shows that the application of one cycle of MHT on cells cultured on films with 160 NPs layers results in a decrease of area covered by live cell population with respect to the control film, being this decrease much more

noticeable after the application of 3 cycles of MHT. It is worth to note that the percentage of dead cells stained in red (Ethidium homodimer-1 in Figures 6.13a and 6.13b) does not correspond to the total number of dead cells due to the fact that cell death results in the loss of cell adhesion and hence detachment from the film.

As can be observed in Figure 6.13c, the cell viability data (%) obtained from the quantification of the area covered by live cells stained in green cultured on films with 80 NPs layers demonstrates that the application of MHT results in negligible cytotoxic effects after the application of one (96% viable cells) or three MHT cycles (94% viable cells). However, the cell viability data (%) corresponding to neuroblastoma cells cultured on films with 160 NPs decreases to 69% with respect to the control experimental with the application of one cycle of MHT and to 21% with the application of three cycles of MHT. At this point, it is important to take into account the final temperature reached by the TMFs with the application of AMF which is related to the number of NPs layers as shown in Figure 6.9. TMFs with 80 NPs layers reach a final temperature of 42 ºC, which under the experimental protocol employed, is not high enough to induce a cytotoxic effect on neuroblastoma cells whereas the temperature reached by TMFs with 160 NPs layers increases to 49 ºC which induces a decrease of cell viability to 69% with respect to the control experiment. These results demonstrate the importance of controlling the concentration of NPs and hence, the temperature generated during the magnetic field application in order to produce a measurable magnetic hyperthermia effect. The temperature range for activating apoptotic cell mechanisms depends on the cellular type involved, but it can be generalized that above 43-45 ºC different metabolic pathways are activated to reverse the effects of the temperature.[16, 22] For our experiments, the temperature gradient was expected to be large due to the bidimensional nature of the samples (and thus large surfaces for exchanging heat).

It can be observed from Figure 6.13 that films with 80 magnetic layers did not produce enough thermal effect to affect the cell viability even after three application cycles. However, for those films with 160 magnetic layers the application of several cycles increased the cell mortality through MHT. This is consistent with previous studies showing an increase in cell death in cell cultures subjected to several expositions to AMF.[32 33]

Because of the potential therapeutic applications require these polymer films to be placed on the surface of the treated area, we conducted further *in vitro* MHT experiments aimed to test the cell viability of neuroblastoma cells grown underneath the thermomagnetic films. To that aim, human neuroblastoma cells were cultured on the surface of an Ibidi dish for 48 hours and a film

with 80 NPs layers was placed above cells as shown in Figure 6.14. As control experiment, neuroblastoma cells were cultured in an Ibidi dish with cells and not subjected to MHT. Cells were subjected to two cycles of MHT (30 min with a waiting time of 5 hours between cycles; H = 35 kA/m, *f* = 180 kHz) which causes a significant decrease in the calcein signal that corresponds to live cells stained in green. In addition, it is possible to observe that cellular death takes place only within the area in contact with the thermomagnetic film which proves the local effect of the magnetic hyperthermia.

In a recent study reported on the same SH-SY5Y cell line studied here, it was demonstrated that MHT required a lower temperature than an exogenous heating source (*i.e.*, water bath) to provoke a given level of cell death.[34] The results depicted in the inset of Figure 6.13a show a much higher efficiency of the TMFs under study with respect to exogeneous heating provided by a thermalized bath. The quantification of the calcein signal after the application of 2 MHT cycles yields a cell viability of 15% which represents a significant decrease with respect to the control film. It is important to note that the temperature achieved by the TMF after each cycle was 43 ºC (see Figure 6.9a). In the case of the application of hyperthermia through a thermalized water bath, the temperature needed to achieve a similar decrease in cell viability was 52 ºC.[34] Hence, the TMFs under study show a much higher efficiency in the application of exogenous hyperthermia with respect to the results found by an exogenous heating source (*i.e.*, water bath) which can be explained because of the intimate contact of the cells with the heating element.

Secondly, taking into account that the potential therapeutic applications require these polymer films to be placed on the surface of the treated area, *in vitro* MHT experiments aimed to test the cell viability of neuroblastoma cells grown underneath the thermomagnetic films were conducted following the protocol showed in Scheme 6.3b. To that aim, human neuroblastoma cells were cultured on the surface of an Ibidi dish for 48 hours and a film $(Alg/Chi)_{20}(NPs/Chi)_{80}$ was placed above cells as shown in Figure 6.14. As control, neuroblastoma cells were cultured in an Ibidi dish with cells and not subjected to MHT. Cells were subjected to two cycles of MHT (30 min with a waiting time of 5 hours between cycles; H = 35 kA/m, *f* = 180 kHz). The quantification of the calcein signal yields a cell viability of 15% which represents a significant decrease with respect to the control film. In addition, it is possible to observe that cellular death takes place only within the area in contact with the thermomagnetic film which proves the local effect of the magnetic hyperthermia. Taking into account that the temperature achieved by $(Alg/Chi)_{20}(NPs/Chi)_{80}$ with the application of the AMF is T = 43 ºC, the effect of 2 cycles of MHT on cell viability is much higher for thermofilms than that obtained by exogenous

hyperthermia (EHT) and even by local intra-tumoral magnetic hyperthermia for which a T = 52 ºC and 47 ºC respectively are needed to reach a decrease of cell viability of 15%.

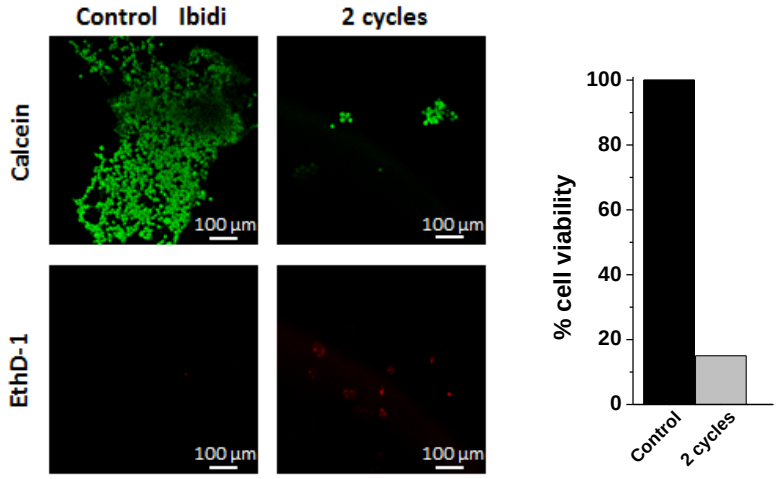

Figure 6.14. Live/dead test carried out on neuroblastoma cells cultured onto an Ibidi dish, covered by a $(Alg/Chi)_{20}(NPs/Chi)_{80}$ film and subjected to 2 cycles of MHT. Neuroblastoma cells cultured on an Ibidi dish and not subjected to MHT are employed as control. Cells are labelled with calcein (live cells in green) and EthD-1 (dead cells in red). The bar chart shows the determination of % cell viability obtained from the images corresponding to live cells stained in green.

6.4. CONCLUSIONS

Thermomagnetic polymer films have been successfully prepared by alternate deposition of chitosan and alginate layers and magnetic nanoparticles using a spray assisted layer-by-layer assembly. Precisely, the presence of NPs into the multilayer structure of these films provides them the ability to response to a magnetic field and allows to use them in magnetic hyperthermia therapies. The incorporation of NPs into the multilayer structure was assessed visually due to a change of colour of films with NPs with regards to films without NPs and the magnetite content was determined by UV-Vis transmission spectrophotometry showing a linear increase of magnetite content with the number of NPs layers deposited.

Dual Beam scanning electron microscopy of the cross section of the films revealed their nanostructuration in layers and the EDX analysis of this area showed the ordered distribution and intercalation of NPs between layers and determined the composition of these films, being the iron the major component in a 65%. The layered structure together with the ordered distribution and intercalation of NPs between layers provided the expected mechanical stability and thermal responsiveness.

The SPA of NPs in Milli-Q water (ferrofluid) with a concentration of magnetite of 8.0 mg/mL applying a magnetic field amplitude of 24 kA/m and a frequency of 571 kHz was 868.4 ± 1.9 W/g. The immobilization of NPs in 2 %w/v gelatin produced a decrease of SPA up to 77.2 ± 0.1 W/g due to the block of the Brownian relaxation.

Thermomagnetic films were heated by application of a magnetic field amplitude of 35 kA/m and a frequency of 180 kHz for 5 minutes from 6 to 12 ºC varying the number of NPs layers from 80 to 160 layers. The ΔT increases linearly with the number of NPs layers, that is with the magnetite content. Indeed, the concentration of NPs (up to ≈ 65 % in mass) into the multilayer structure of these films was enough to reach target temperatures up to 14 ºC above the control samples by the application of AMF.

In vitro experiments showed good adhesion properties to grow neuroblastoma cells on these films with different number of NPs layers as proven by optical microscopy and SEM. By remotely heating the films using ac magnetic fields we induced a reduction in cell viability to 67% and 20% of the control samples for one and three heating cycles, respectively. The results in experimental conditions mimicking *in vivo* applications yielded a reduction of 85% of the cell viability only within the contact area with the film after two cycles of MHT.

6.5. REFERENCES

1. Pichon, B. P.; Louet, P.; Felix, O.; Drillon, M.; Begin-Colin, S.; Decher, G., Magnetotunable Hybrid Films of Stratified Iron Oxide Nanoparticles Assembled by the Layer-by-Layer Technique. *Chemistry of Materials* **2011,** 23, (16), 3668-3675.

2. Paterno, L. G.; Fonseca, F. J.; Alcantara, G. B.; Soler, M. A. G.; Morais, P. C.; Sinnecker, J. P.; Novak, M. A.; Lima, E. C. D.; Leite, F. L.; Mattoso, L. H. C., Fabrication and characterization of nanostructured conducting polymer films containing magnetic nanoparticles. *Thin Solid Films* **2009,** 517, (5), 1753-1758.

3. Schaaf, P.; Voegel, J.-C.; Jierry, L.; Boulmedais, F., Spray-Assisted Polyelectrolyte Multilayer Buildup: from Step-by-Step to Single-Step Polyelectrolyte Film Constructions. *Advanced Materials* **2012,** 24, (8), 1001-1016.

4. Bruvera, I.; Hernández, R.; Mijangos, C.; Goya, G. F., An integrated device for magnetically-driven drug release and in situ quantitative measurements: design, fabrication and testing. *Journal of Magnetism and Magnetic Materials* **2015,** *377*, 446-451.

5. Zamora-Mora, V.; Fernández-Gutiérrez, M.; Román, J. S.; Goya, G.; Hernández, R.; Mijangos, C., Magnetic core–shell chitosan nanoparticles: Rheological characterization and hyperthermia application. *Carbohydrate polymers* **2014,** 102, 691-698.

6. Kerr, J. F. R.; Winterford, C. M.; Harmon, B. V., Apoptosis. Its significance in cancer and cancer Therapy. *Cancer* **1994,** 73, (8), 2013-2026.

7. Mahmoudi, K.; Hadjipanayis, C. G., The application of magnetic nanoparticles for the treatment of brain tumors. *Frontiers in Chemistry* **2014,** 2, 109.

8. Van der Zee, J., Heating the patient: a promising approach? *Annals of oncology* **2002,** 13, (8), 1173-1184.

9. Kok, H. P.; Crezee, J., A comparison of the heating characteristics of capacitive and radiative superficial hyperthermia. *International Journal of Hyperthermia* **2016**, 1-9.

10. Gao, S.; Zheng, M.; Ren, X.; Tang, Y.; Liang, X., Local hyperthermia in head and neck cancer: mechanism, application and advance. *Oncotarget* **2016,** 7, (35), 57367-57378.

11. Wust, P.; Hildebrandt, B.; Sreenivasa, G.; Rau, B.; Gellermann, J.; Riess, H.; Felix, R.; Schlag, P. M., Hyperthermia in combined treatment of cancer. *The Lancet Oncology* **2002,** 3, (8), 487-497.

12. Sardari, D.; Verga, N., Cancer Treatment with Hyperthermia. In *Current Cancer Treatment - Novel Beyond Conventional Approaches*, InTech: 2011; pp 455-474.

13. Habash, R. W. Y.; Bansal, R.; Krewski, D.; Alhafid, H. T., Thermal Therapy, Part 2: Hyperthermia Techniques. *Critical Reviews™ in Biomedical Engineering* **2006,** 34, (6), 491-542.

14. Redolfi Riva, E.; Desii, A.; Sinibaldi, E.; Ciofani, G.; Piazza, V.; Mazzolai, B.; Mattoli, V., Gold Nanoshell/Polysaccharide Nanofilm for Controlled Laser-Assisted Tissue Thermal Ablation. *ACS Nano* **2014,** 8, (6), 5552-5563.

15. P Calatayud, M.; Asin, L.; Tres, A.; F Goya, G.; R Ibarra, M., Cell Bystander Effect Induced by Radiofrequency Electromagnetic Fields and Magnetic Nanoparticles. *Current Nanoscience* **2016,** 12, (3), 372-377.

16. Hervault, A.; Thanh, N. T. K., Magnetic nanoparticle-based therapeutic agents for thermo-chemotherapy treatment of cancer. *Nanoscale* **2014,** 6, (20), 11553-11573.

17. Sailor, M. J.; Park, J.-H., Hybrid Nanoparticles for Detection and Treatment of Cancer. *Advanced Materials* **2012,** 24, (28), 3779-3802.

18. Zamora-Mora, V.; Fernández-Gutiérrez, M.; González-Gómez, Á.; Sanz, B.; Román, J. S.; Goya, G. F.; Hernández, R.; Mijangos, C., Chitosan nanoparticles for combined drug delivery and magnetic hyperthermia: From preparation to in vitro studies. *Carbohydrate polymers* **2017,** 157, 361-370.

19. Cristofolini, L.; Szczepanowicz, K.; Orsi, D.; Rimoldi, T.; Albertini, F.; Warszynski, P., Hybrid Polyelectrolyte/Fe3O4 Nanocapsules for Hyperthermia Applications. *ACS Applied Materials & Interfaces* **2016,** 8, (38), 25043-25050.

20. Maier-Hauff, K.; Rothe, R.; Scholz, R.; Gneveckow, U.; Wust, P.; Thiesen, B.; Feussner, A.; von Deimling, A.; Waldoefner, N.; Felix, R.; Jordan, A., Intracranial Thermotherapy using Magnetic Nanoparticles Combined with External Beam Radiotherapy: Results of a Feasibility Study on Patients with Glioblastoma Multiforme. *Journal of Neuro-Oncology* **2007,** 81, (1), 53-60.

21. Johannsen, M.; Thiesen, B.; Wust, P.; Jordan, A., Magnetic nanoparticle hyperthermia for prostate cancer. *International Journal of Hyperthermia* **2010,** 26, (8), 790-795.

22. IP Soares, P.; MM Ferreira, I.; AGBN Igreja, R.; MM Novo, C.; PMR Borges, J., Application of hyperthermia for cancer treatment: recent patents review. *Recent patents on anti-cancer drug discovery* **2012,** 7, (1), 64-73.

23. Bañobre-López, M.; Teijeiro, A.; Rivas, J., Magnetic nanoparticle-based hyperthermia for cancer treatment. *Reports of Practical Oncology & Radiotherapy* 18, (6), 397-400.

24. Cheng, L.; Smith, D. J.; Anderson, R. L.; Nagley, P., Human neuroblastoma SH-SY5Y cells show increased resistance to hyperthermic stress after differentiation, associated with elevated levels of Hsp72. *International Journal of Hyperthermia* **2011,** 27, (5), 415-426.

25. Gonzalez-Fernandez, M. A.; Torres, T. E.; Andrés-Vergés, M.; Costo, R.; de la Presa, P.; Serna, C. J.; Morales, M. P.; Marquina, C.; Ibarra, M. R.; Goya, G. F., Magnetic nanoparticles for power absorption: Optimizing size, shape and magnetic properties. *Journal of Solid State Chemistry* **2009,** 182, (10), 2779-2784.

26. Sagué, B. S. Study of the cell death induced by magnetic hyperthermia in neural cells using Fe3O4 nanoparticles. Universidad de Zaragoza, Zaragoza, **2015**.

27. Kötitz, R.; Weitschies, W.; Trahms, L.; Semmler, W., Investigation of Brownian and Néel relaxation in magnetic fluids. *Journal of Magnetism and Magnetic Materials* **1999,** 201, (1–3), 102-104.

28. Paula, I. P. S.; Isabel, M. M. F.; Rui, A. G. B. N. I.; Carlos, M. M. N.; Joao, P. M. R. B., Application of Hyperthermia for Cancer Treatment: Recent Patents Review. *Recent patents on anti-cancer drug discovery* **2012,** 7, (1), 64-73.

29. Neto, A. I.; Vasconcelos, N. L.; Oliveira, S. M.; Ruiz-Molina, D.; Mano, J. F., High-Throughput Topographic, Mechanical, and Biological Screening of Multilayer Films Containing Mussel-Inspired Biopolymers. *Advanced Functional Materials* **2016,** 26, (16), 2745-2755.

30. Ventrelli, L.; Fujie, T.; Turco, S. D.; Basta, G.; Mazzolai, B.; Mattoli, V., Influence of nanoparticle-embedded polymeric surfaces on cellular adhesion, proliferation, and differentiation. *Journal of Biomedical Materials Research Part A* **2014,** 102, (8), 2652-2661.

31. Lipski, A. M.; Pino, C. J.; Haselton, F. R.; Chen, I. W.; Shastri, V. P., The effect of silica nanoparticle-modified surfaces on cell morphology, cytoskeletal organization and function. *Biomaterials* **2008,** 29, (28), 3836-3846.

32. Ito, A.; Tanaka, K.; Honda, H.; Abe, S.; Yamaguchi, H.; Kobayashi, T., Complete regression of mouse mammary carcinoma with a size greater than 15 mm by frequent repeated hyperthermia using magnetite nanoparticles. *Journal of Bioscience and Bioengineering* **2003,** 96, (4), 364-369.

33. Balivada, S.; Rachakatla, R. S.; Wang, H.; Samarakoon, T. N.; Dani, R. K.; Pyle, M.; Kroh, F. O.; Walker, B.; Leaym, X.; Koper, O. B.; Tamura, M.; Chikan, V.; Bossmann, S. H.; Troyer, D. L., A/C magnetic hyperthermia of melanoma mediated by iron(0)/iron oxide core/shell magnetic nanoparticles: a mouse study. *BMC Cancer* **2010,** 10, 119-119.

34. Sanz, B.; Calatayud, M. P.; Torres, T. E.; Fanarraga, M. L.; Ibarra, M. R.; Goya, G. F., Magnetic hyperthermia enhances cell toxicity with respect to exogenous heating. *Biomaterials* **2017,** 114, 62-70.

CHAPTER 7

Study of cell adhesion and applications in drug delivery of Alg/Chi films

This chapter firstly investigates the influence of the number of bilayers, surface chemistry and crosslinking of multilayer Alg/Chi films obtained through spray assisted LbL on cell adhesion of human dermal fibroblasts (HDF) and human caucasian breast adenocarcinoma (MCF-7). Secondly, the employment of these films for drug delivery applications was evaluated by incorporation of an anticancer drug (tamoxifen) in different intermediate positions of multilayer Alg/Chi films to study its controlled release over time.

7.1. INTRODUCTION

Multilayer films prepared through layer-by-layer (LbL) assembly of polyelectrolytes are extensively employed in biomedical applications.[1-5] For example, LbL technique allows the encapsulation of different therapeutic drugs into multilayer films by direct assembly during the buildup process.[4-8] Taking into account that this assembly is carried out in aqueous solutions under mild conditions, the activity of the loaded drugs is retained in the films.[9] Thanks to the control of the thickness, composition and surface chemistry, as well as the satisfactory adhesion ability, LbL assembled polymer films can be specifically customized to function as a promising platform for sustained drug delivery.[10, 11] Compared with the traditional oral drug delivery systems, such as tablets or liquid formulations, polymer films can be attached to the pathological site of the target organ or tissue for direct drug delivery of the therapeutic agent which enhances therapeutic activity, increases the efficacy of drugs, reduces the dose frequency, minimizes side effects to normal tissue, improves patient compliance and reduces gastrointestinal side effects.[5, 10, 12] In addition to this, multilayer polymer films offer the possibility of providing sustained drug delivery over the time as a function of the number of layers.[13] These characteristics increase their potential clinical applications. Different therapeutic drugs have been encapsulated in multilayer films for biomedical applications.[4, 8, 13-15] An hydrophobic anti-inflammatory drug, adenosine deaminase inhibitor, was assembled in the middle of a multilayer $(Chi/Alg)_{10}$ film built up via spin-coating LbL to treat localized inflammatory bowel disease.[4] An anti-fibrotic agent, pirfenidone, was encapsulated in a $(Chi/Alg)_{15}$ film via dipping LbL for excisional wound healing. In the ocular field, latanoprost isopropyl ester was cast on the surface of $(Chi/Alg)_n$ films (n = 5, 10 and 20) to reduce intraocular pressure[13] and norfloxacin and timolol were loaded in multilayer $(Ha/Chi)_{10}$ films built up via dipping LbL to decrease the wearing hydrogel contact lenses.[14] Curcumin, which has a pleiotropic therapeutic effect in cancer, was dissolved in nanocrystalline cellulose (NCC) and multilayer films (Chi/NCC) were made by dipping LbL.[8] Another important biomedical application of multilayer polymer films is their employment as

model surfaces for the study of the adhesion of living cells provided that the chemical and physical surface properties of the films are key to the modulation of cell adhesion.[16-19]. In fact, LbL allows to tune the final biological and physicochemical properties of multilayer films by changing the nature of the outermost layer and the thickness and roughness of the films through the number of deposited layers.[20] These features make LbL a powerful technique to modulate cell adhesion on the surface of a multilayer film.[17]

In chapter 4, the fabrication of multilayer films based on chitosan and alginate by means of spray assisted LbL assembly was described. Then, the nanomechanical properties of these multilayer Alg/Chi films were studied in the chapter 5 concluding that the elastic modulus increased with the number of deposited bilayers and with the thermal crosslinking process at 120 ºC, whereas the deformation remained constant. Multilayer $(Alg/Chi)_n$ films built up through spray assisted LbL possess chemical and physical properties for exploring cell adhesion. Cells are sensible to the elasticity or rigidity of the surface, for that reason nanomechanical properties of the films are of crucial importance in their adhesion.[21] Among the different parameters that affect to the elastic modulus of a surface and influence cell adhesion, crosslinking is one of the most decisive leading to an increase of the stiffness and cell attachment in many cases.[22] Lee et al.[23] demonstrated that different types of cells, human umbilical artery endothelial cells (HUAECs), 3T3 fibroblasts, osteoblasts MC3T3-E1 and HeLa (epithelial) cells grew at similar rates on different poly(dimethylsiloxane) surfaces regardless of the stiffness for surfaces having elastic moduli ranging from 0.6 to 2.6 MPa. On the contrary, Silva et al.[22] observed that $(Chi/Alg)_{100}$ films built up via dipping LbL increased their elastic modulus from 4.8 MPa to 12.8 and 56.4 MPa after crosslinking with two different genipin concentrations and probed that the adhesion of fibroblasts L929 cells was sensitive to the stiffness of films increasing a ~15% and 40% with regards to non-crosslinked films.

In this chapter, *in vitro* cell adhesion studies will be carried out with dermal fibroblast and human breast cancer MCF-7 cells aimed to elucidate the influence of physicochemical properties and different architectures of multilayer Alg/Chi films on cell adhesion. To that aim, it was varied the number of deposited bilayers and the outermost layer, alginate or hyaluronic acid, and the effect of crosslinking was studied in order to elucidate the influence of these variables on cell adhesion properties. Taking into account that these multilayer films are intended to be used as patches for sustained drug delivery, the encapsulation of tamoxifen, a therapeutic drug to treat the breast cancer, was carried out within different intermediate positions of the multilayer $(Alg/Chi)_n$ films and results corresponding to *in vitro* drug release are also presented.

7.2. EXPERIMENTAL PART

7.2.1. Materials

Chitosan (Chi) of low molecular weight (448869, lot SLBG1673V), sodium alginate (Alg) (A2158, lot 090M0092V), poly(ethylenimine) (PEI) with a molecular weight (M_w) of 25000 were supplied by Aldrich and used as received. Hyaluronic acid (HA) was supplied by Lifecore Biomedical (lot 024276, part HA500K-5). More information about these materials is detailed in the chapter 3.

Acetic acid, tamoxifen citrate salt ≥99% (TMX), 1-Ethyl-3-(3-dimethylaminopropyl)-carbodiimide (EDC) and N-Hydroxysuccinimide (NHS) (Aldrich) were supplied by Aldrich and used as received. Sodium acetate anhydrous was purchased from Panreac.

For biological assays, phosphate buffered solution (PBS) of pH 7.4 (Sigma-Aldrich) and fetal bovine serum (FBS) (Gibco) were used as received. Tissue culture media, additives, trypsin, glutaraldehyde and Tween 80 were purchased from Sigma-Aldrich. Alamar Blue reagent was supplied from Invitrogen, DAPI (4',6-Diamidino-2-Phenylindole, Dihydrochloride) fluorescent stain was purchased by Molecular Probes and crystal violet was supplied by Prolab diagnostics.

7.2.2. Preparation of multilayer films with tamoxifen

All films were built on functionalized glass slides (14 mm ϕ) through spray assisted layer-by-layer (LbL) technique of aqueous solutions of alginate (2.5 mg/mL) and chitosan (1.0 mg/mL) using an automatic ND-SP spray coater from Nadetech innovations (Spain). Three different systems were prepared. *i)* Alg/Chi films was prepared following the procedure described in the chapter 4 to obtain $(Alg/Chi)_n$ films. In order to study the influence of the surface chemistry, a layer of Alg or HA was deposited at the end of the cycle for 5 s and samples were denoted as $(Alg/Chi)_nAlg$ and $(Alg/Chi)_nHA$ films, where *n* stands for the number of bilayers. *ii)* The second type of samples was obtained by crosslinking of the previously prepared $(Alg/Chi)_nAlg$ and $(Alg/Chi)_nHA$ films by immersing them in a solution prepared dissolving 30 mg EDC and 19.9 mg NHS in 1 ml of Milli-Q water for 1 hour at 4 ºC and then they were washed in deionized water for 30 min three times to remove crosslinking NHS-ester residues. Samples were denoted as crosslinked (CL) $(Alg/Chi)_nAlg$ and crosslinked $(Alg/Chi)_nHA$ films. *iii)* For the third series of samples which tamoxifen incorporated in an intermediate position, it was followed the same procedure, but in the middle of the preparation process a layer of tamoxifen (200 µL of a

solution of 1.0 mg/mL of TMX in ethanol) was deposited with a pipette and, after a waiting time of 2 hours to evaporate the solvent, the spray deposition process was followed (Scheme 7.1). Samples were denoted as $(Alg/Chi)_5TMX(Chi/Alg)_m$ where *m* stands for the number of (Chi/Alg) bilayers after deposition of TMX.

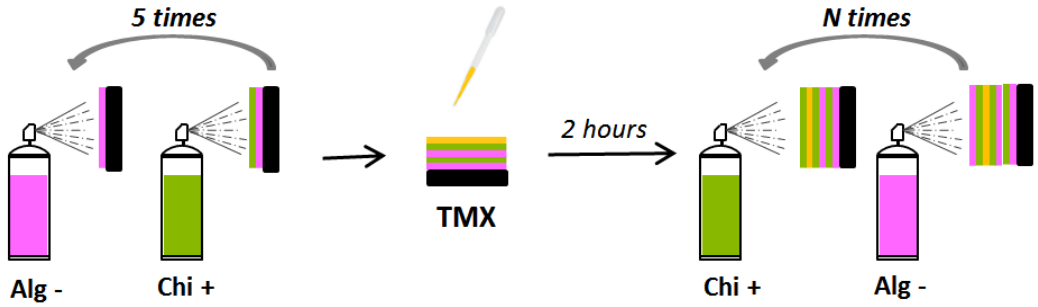

Scheme 7.1. Sequential process followed for the preparation of $(Alg/Chi)_5TMX(Chi/Alg)_m$ films.

7.2.3. Characterization

Morphological characterization

The topography and surface roughness of films were evaluated using a Multimode Scanning probe microscope (Veeco/Bruker), with a di NanoScope IVa Controller using the conventional height mode (tapping mode, normal AFM) at 320 kHz resonant frequency and a nominal force constant of 42 N/m. All measurements were performed in air, at room temperature, on films supported on silicon wafers. Non-crosslinked and crosslinked $(Alg/Chi)_nAlg$ and $(Alg/Chi)_nHA$ films were scanned over square regions of 2 μm size and the average roughness (R_a) was calculated from the height images.

Contact angle

To determine films hydrophilicity, sessile drop air/water contact angle measurements were carried out on the surface of non-crosslinked and crosslinked $(Alg/Chi)_nAlg$ and $(Alg/Chi)_nHA$ films with different number of bilayers at room temperature using a goniometer KSV tetha (KSV instruments, Ltd., Finland) with water droplets of 3 μL. The average contact angle was determined by measuring three different points of every film.

Degradation assay

The degradation of non-crosslinked and crosslinked $(Alg/Chi)_{10}Alg$ and $(Alg/Chi)_{10}HA$ films over time was performed by immersing the film in a vial containing 3 mL of culture medium at 37 ºC in a shaker plate at 30 rpm. At different times, 4, 8 and 15 days, the surface of films was observed by Scanning Electron Microscopy using a Hitachi SU 8000 microscope operating at 1.5 kV. The same experimental protocol was employed in order to evaluate the influence of the encapsulation and drug delivery of TMX in the degradation process of $(Alg/Chi)_5TMX(Chi/Alg)_n$ films (n = 5, 10 and 20).

Biological behavior

The biological response of the as-prepared materials was tested with human dermal fibroblasts (HDF, Innoprot) and human caucasian breast adenocarcinoma (MCF-7, ECACC) cells. The culture medium was Dulbecco's Modified Eagle's Medium, enriched with 4500 mg/mL of glucose (DMEM) supplemented with 10% fetal bovine serum (FBS), 200 mM L-glutamine, 100 units/mL penicillin and 100 mg/mL streptomycin, modified with 4-(2-hydroxyethyl)-1-piperazineethanesulfonic acid (HEPES).

The culture medium was changed at selected time intervals with little disturbance to culture conditions. Glass slides (14 mm ϕ) were used as a negative control. Samples were sterilized under UV light (HNS OSRAM, 263 nm, 3.6UVC/W) at a power of 11W for 2 hours.

- *Cytotoxicity assay*

Cytotoxicity assay was carried out on $(Alg/Chi)_{10}Alg$ films. Films were immersed in a falcon tube of 15 mL containing 5 mL of culture medium and placed in a shaker plate (30 rpm) at 37 ºC. At predetermined intervals, 2, 4, 8 and 11 days, the medium was removed and replaced with other 5 mL. All the extracts were obtained under sterile conditions. Cells were seeded at a density of 9×10^4 cells/mL in complete medium in a sterile 96 well culture plate and incubated to confluence. After 24 h of incubation, the medium was replaced with the corresponding extracts and incubated at 37 ºC in humidified air with 5% CO_2 for 24 h.

A solution of Alamar Blue (AB) (10 %v/v) was prepared in warm DMEM without phenol red (Gibco). Then, 100 μL of this solution were added to each well and the plates were incubated at 37 °C for 3 h. After that, fluorescence was measured with a Biotek Synergy HT detector using an

emission wavelength of 590 nm and an excitation wavelength of 530 nm. Cell viability (CV) was calculated with the following equation:

$$CV = \left(\frac{FD_S - FD_B}{FD_C - FD_B}\right) \cdot 100 \qquad (eq.7.1)$$

where FD_S, FD_B and FD_C are the fluorescence density of the AB for the sample (S), blank (B) (culture medium without cells) and control (C), respectively.

- *Adhesion and morphology assays*

Direct contact assays to test cell adhesion were carried out on non-crosslinked and crosslinked $(Alg/Chi)_nAlg$ and $(Alg/Chi)_nHA$ films with different number of bilayers. Glass slides were used as negative controls. At confluence, cells were trypsinized and seeded on the surface of films with a cellular density of 4.9 x 10^4 cells. For adhesion tests, the cell growth was followed after 3 days in culture by optical microscopy (Nikon eclipse TE2000-S). After that, a solution of AB (10 %v/v), prepared in a warm medium without phenol red, was added to the plate and incubated at 37 ºC for 3 h. Finally, fluorescence was measured with a Biotek Synergy HT detector and cell viability (CV) was calculated with equation 7.1.

To observe cellular adhesion and morphology of cells onto the surface of films, cells were stained with different dyes according to the following protocol. Films were washed with PBS and fixed with glutaraldehyde 2.5 %v/v in PBS for 10 min at room temperature. After that, glutaraldehyde was removed and film was rinsed with PBS again. In the case of cellular adhesion, the cell nuclei were stained with 10 µL/mL of DAPI dye solution and left it for 10 min at room temperature in the darkness and, for cellular morphology; cell cytoskeletal was stained with crystal violet solution (0.02 %w/v) and kept it for 10 min at room temperature. Finally, stained cells were observed using an epifluorescence microscope (Nikon eclipse TE2000-S) and three different filters.

In vitro release of TMX

The release of TMX from $(Alg/Chi)_5TMX(Chi/Alg)_n$ films with n = 5, 10 and 15 bilayers was performed by immersing the film in a vial containing 3 mL of PBS pH 7.4 with 1% w/v Tween 80 at 37 ºC in a shaker plate at 30 rpm. At predetermined intervals, the solution was replaced by a fresh one to ensure constant release conditions. The amount of TMX released was evaluated measuring the absorbance at 277 nm in PBS with 1 %w/v Tween 80 using a UV-Vis

spectrophotometer (NanoDrop One/One^{c}, Thermo scientific). The cumulative amount of released TMX was determined from the standard calibration curve of TMX in PBS with 1 %w/v Tween 80 (Annex II, Figure A.II.1). All experiments were repeated three times. The total amount of TMX loaded into the films was determined by dissolving films in 5 mL buffer pH5 (acetic acid 0.1M/sodium acetate 0.1M) with magnetic stirring, the resulting solution was freeze-dried and solved in 4 mL of PBS with 1 %w/v Tween 80 to measure the absorbance at 277 nm.

For *in vitro* assays of tamoxifen delivery in contact with HDF and MCF-7 cells, the following experimental protocol was carried out. $(Alg/Chi)_5TMX(Chi/Alg)_n$ films with n = 5, 10 and 15 bilayers and $(Alg/Chi)_n$ films with n = 10, 15 and 20 bilayers were immersed in falcon tubes of 15 mL containing 3 mL of culture medium and placed in a shaker plate (30 rpm) at 37 ºC. At predetermined intervals, 1, 2, 4 and 8 hours, the medium was removed and replaced with other 3 mL. All the extracts were obtained under sterile conditions. Cells were seeded at a density of 6 $x10^4$ cells/mL in complete medium in a sterile 96 well culture plate and incubated to confluence. After 24 h of incubation, the medium was replaced with the corresponding extracts and incubated at 37 ºC in humidified air with 5% CO_2 for 24 h. Afterwards, the medium was removed, wells were washed with PBS and fixed with glutaraldehyde 2.5 %v/v in PBS for 10 min at room temperature. After that, glutaraldehyde was removed and wells were rinsed with PBS again. Then, 100 µL of crystal violet solution at 10%w/v were added to each well and kept at room temperature for 15 min. After that, the solution was removed and wells were washed with Milli-Q water to remove the excess of dye. After drying at room temperature, 100 µL of acetic acid (10 %v/v in PBS) were added to each well and absorbance was measured with a Biotek Synergy HT detector using an emission wavelength of 690 nm and an excitation wavelength of 620 nm. Cell viability (CV) was calculated using the equation 7.2.

$$CV = \left(\frac{AD_S - AD_B}{AD_C - AD_B}\right) \cdot 100 \qquad (eq.7.2)$$

where AD_S, AD_B and AD_C are the absorbance density of the crystal violet for the sample (S), blank (B) (culture medium without cells) and control (C), respectively.

7.3. RESULTS AND DISCUSSION

7.3.1. Morphological characterization of Alg/Chi films by AFM

Figure 7.1 shows representative AFM images corresponding to the topography of multilayer polymer films with the same number of bilayers in which the last layer is Alg ($(Alg/Chi)_{10}Alg$, Figure 7.1a) or HA ($(Alg/Chi)_{10}HA$, Figure 7.1b) and the corresponding crosslinked samples (Figures 7.1c and 7.1d respectively). AFM images corresponding to non-crosslinked and crosslinked $(Alg/Chi)_nAlg$ and $(Alg/Chi)_nHA$ films (n = 5, 7, 15 and 25) can be accessed in the Annex III (Figure A.III.1).

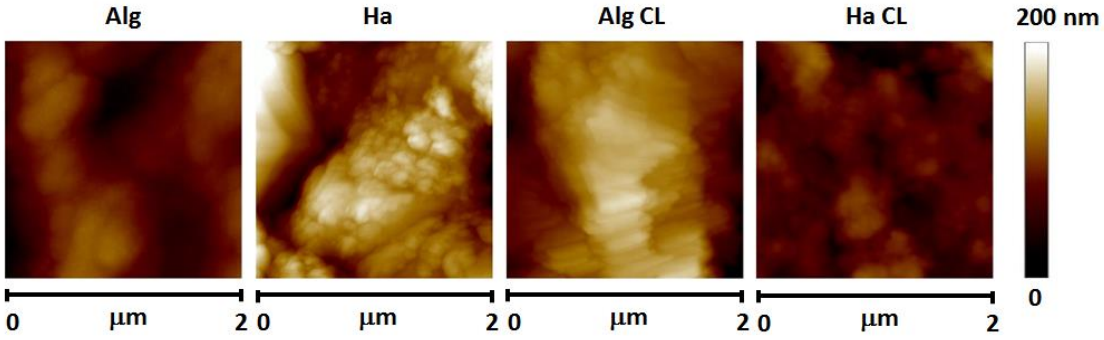

Figure 7.1. Representative AFM topographic images corresponding to non-crosslinked and crosslinked $(Alg/Chi)_{10}Alg$ and $(Alg/Chi)_{10}HA$ films to calculate the average roughness (Ra).

The analysis of AFM topographic images of non-crosslinked and crosslinked $(Alg/Chi)_nAlg$ and $(Alg/Chi)_nHA$ films with different number of bilayers allows to obtain the average roughness (R_a) of the films. The results corresponding to the average roughness of the films under study are tabulated in Table 7.1. As can be observed, R_a increases with the number of deposited bilayers for all samples under study regardless surface chemistry (ending layer, HA or Alg) or chemical crosslinking, but not in great extension. At first deposited bilayers, the roughness is attributed to the formation of islands which decrease their size as the number of deposited bilayers increases. In this case, the roughness is also influenced by the spraying deposition process and by the absence of additional external ionic strength (*e.g.*, NaCl).[24, 25] The surface chemistry produces differences in the roughness being $(Alg/Chi)_nHA$ films rougher than $(Alg/Chi)_nAlg$ films, whereas after crosslinking there are not differences between both. Conversely, it is not possible to find a general trend regarding the influence of crosslinking on roughness for films with the same surface chemistry.

Table 7.1. Evolution of the average roughness (R_a) of non-crosslinked and crosslinked $(Alg/Chi)_nAlg$ and $(Alg/Chi)_nHA$ films as a function of the number of bilayers (n).

Number of bilayers (n)	**R_a (nm)**			
	$(Alg/Chi)_nAlg$ films	$(Alg/Chi)_nHA$ films	Crosslinked $(Alg/Chi)_nAlg$ films	Crosslinked $(Alg/Chi)_nHA$ films
5	8.7 ± 1.2	7.2 ± 1.2	7.2 ± 2.2	15.0 ± 4.0
7	13.4 ± 3.7	14.9 ± 3.8	10.1 ± 3.2	9.9 ± 4.3
10	16.9 ± 3.9	27.1 ± 6.3	18.2 ± 4.3	17.2 ± 2.3
15	16.3 ± 2.4	31.7 ± 9.8	26.1 ± 7.0	24.1 ± 4.6
25	14.7 ± 7.8	25.2 ± 1.4	32.0 ± 1.3	31.2 ± 6.0

7.3.1. Degradation essay

Taking into account the increasing interest and the great number of applications of these multilayer polymer films, it is important to know the degradation behavior in fluids that resemble biological media.[26] The degradation of non-crosslinked and crosslinked $(Alg/Chi)_{10}Alg$ and $(Alg/Chi)_{10}HA$ films in culture medium (DMEM) at 37 ºC was evaluated by physical changes within the surface of multilayer films by SEM for a period of 15 days at different time intervals of 4 and 8 days as can be observed in Figure 7.2.

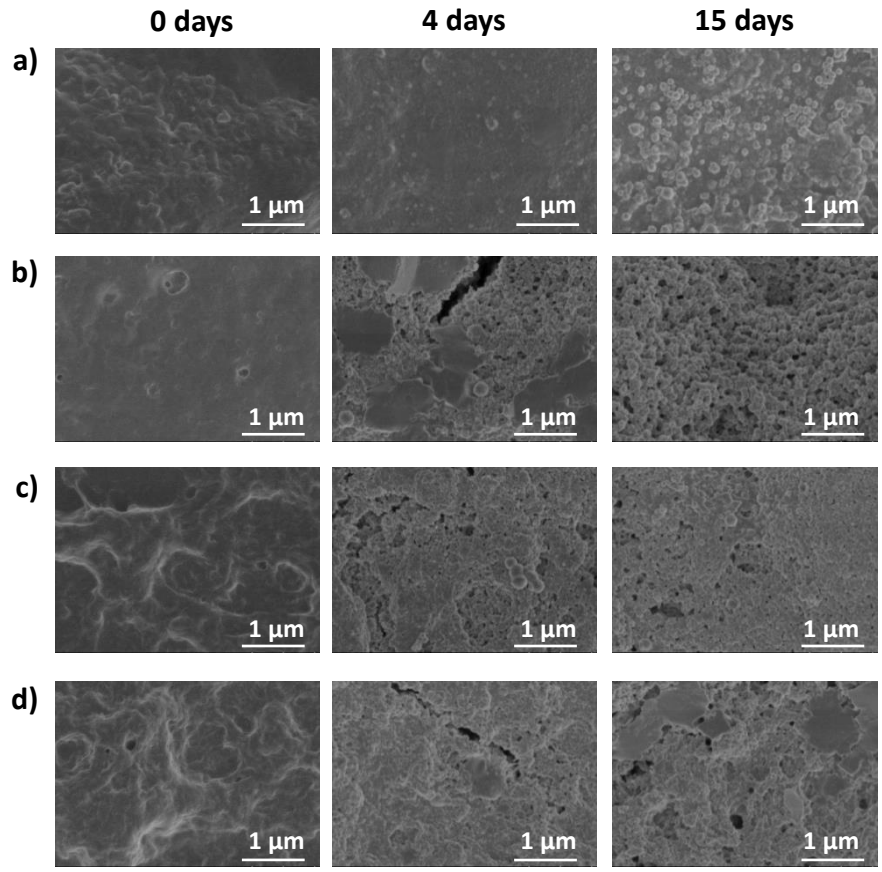

Figure 7.2. SEM micrographs of non-crosslinked a) $(Alg/Chi)_{10}Alg$ and b) $(Alg/Chi)_{10}HA$ films and crosslinked c) $(Alg/Chi)_{10}Alg$ and d) $(Alg/Chi)_{10}HA$ films in contact with DMEM at 37ºC during different time intervals.

In the case of non-crosslinked films, when Alg is the outermost layer (Figure 7.2a), small spherical objects are noted with time but there are not cracks on the surface. On the contrary, when HA is the last layer (Figure 7.2b), cracks and voids are observed after 4 days. After 15 days, the surface has completely changed, indicating that films ending in HA are more prone to degradation. For crosslinked films (Figures 7.2 c and d), although cracks appear after 4 days, less degradation is observed after 15 days with respect to non-crosslinked films, reflecting a decrease in the degradation process.

7.3.2. *In vitro* cell adhesion studies

Cytotoxicity assay

In this work, chemical crosslinking of $(Alg/Chi)_n$ films was carried out through carbodiimide chemistry, using EDC and NHS as chemical crosslinkers. Considering that EDC has been reported to be cytotoxic in literature,[27] as a first step it was evaluated the biocompatibility of non-crosslinked and crosslinked $(Alg/Chi)_nAlg$ films by means of a cytotoxicity assay performed

in vitro with HDF and MCF-7 cells (Figure 7.3). A comparison of the results obtained for non-crosslinked and crosslinked films with the control sample corresponding to cells cultured with culture medium shows that HDF and MCF-7 cell viability remained unaffected up to 11 days in contact with non-crosslinked films. Likewise, the crosslinking of the films with EDC and NHS did not produce a decrease in cell viability over the same period of time. These results demonstrate that non-crosslinked and crosslinked $(Alg/Chi)_{10}Alg$ films are biocompatible and could be incorporated in cell culture applications.

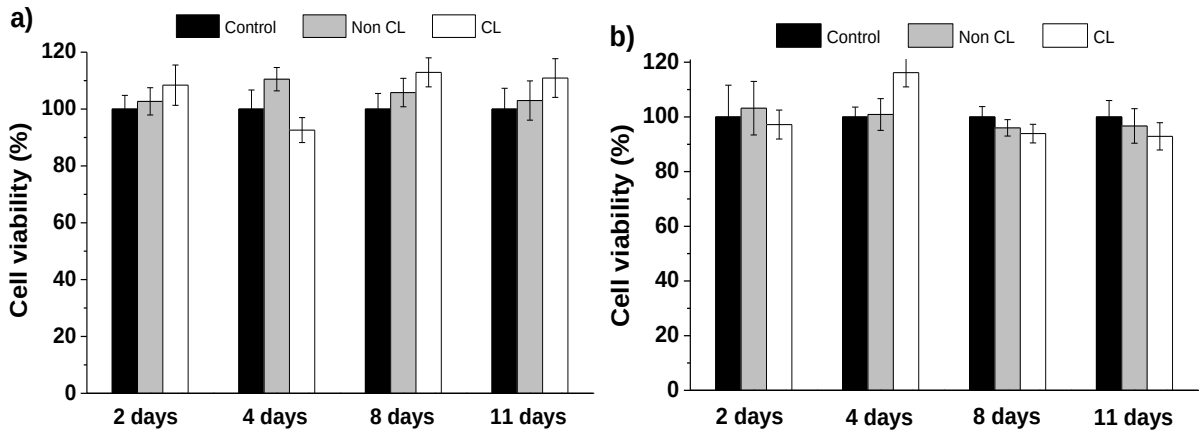

Figure 7.3. Cytotoxicity assay of non-crosslinked and crosslinked $(Alg/Chi)_{10}$ films in contact with a) HDF and b) MCF-7 cells.

Cell adhesion

Taking into account that interactions between cells and multilayer films surface could be influenced by the number of bilayers[21] and the chemical nature of the outermost layer,[28] the spray assisted LbL technique allows to easily change the last deposited layer of the multilayer films keeping constant the overall chemical composition in order to modulate cell adhesion.[29] Hence, it provides a methodology to produce polymer films with tailored physicochemical properties for systematic studies of cell adhesion. Cell adhesion tests were carried out on multilayer $(Alg/Chi)_n$ films built up with the same polyelectrolyte pairs, alginate and chitosan, and spraying the corresponding polyanion solution, alginate or hyaluronic acid, at the end of the spray LbL $(Alg/Chi)_n$ process to obtain films with different ending layer, $(Alg/Chi)_nAlg$ and $(Alg/Chi)_nHA$, in contact with cells. Cells were seeded on the films and kept in culture for three days. Figure 7.4 shows representative images of the cell nuclei stained with DAPI (up) and bright field images (down) of non-crosslinked and crosslinked $(Alg/Chi)_{10}Alg$ and $(Alg/Chi)_{10}HA$ films after three days of culture with HDF (Figure 7.4a) and MCF-7 cells (Figure 7.4b). Images corresponding to non-crosslinked and crosslinked $(Alg/Chi)_nAlg$ and

$(Alg/Chi)_nHA$ films (n = 5, 7, 15 and 25) are shown in the Annex IV (Figures A.IV.1 and A.IV.2). Multilayer films with Alg as ending layer show lower cell attachment compared with multilayer films ending on Ha. The crosslinking process produces an increase of cell adhesion for both kind of cells, HDF and MCF-7, and chemical surfaces, Alg and HA, under study.

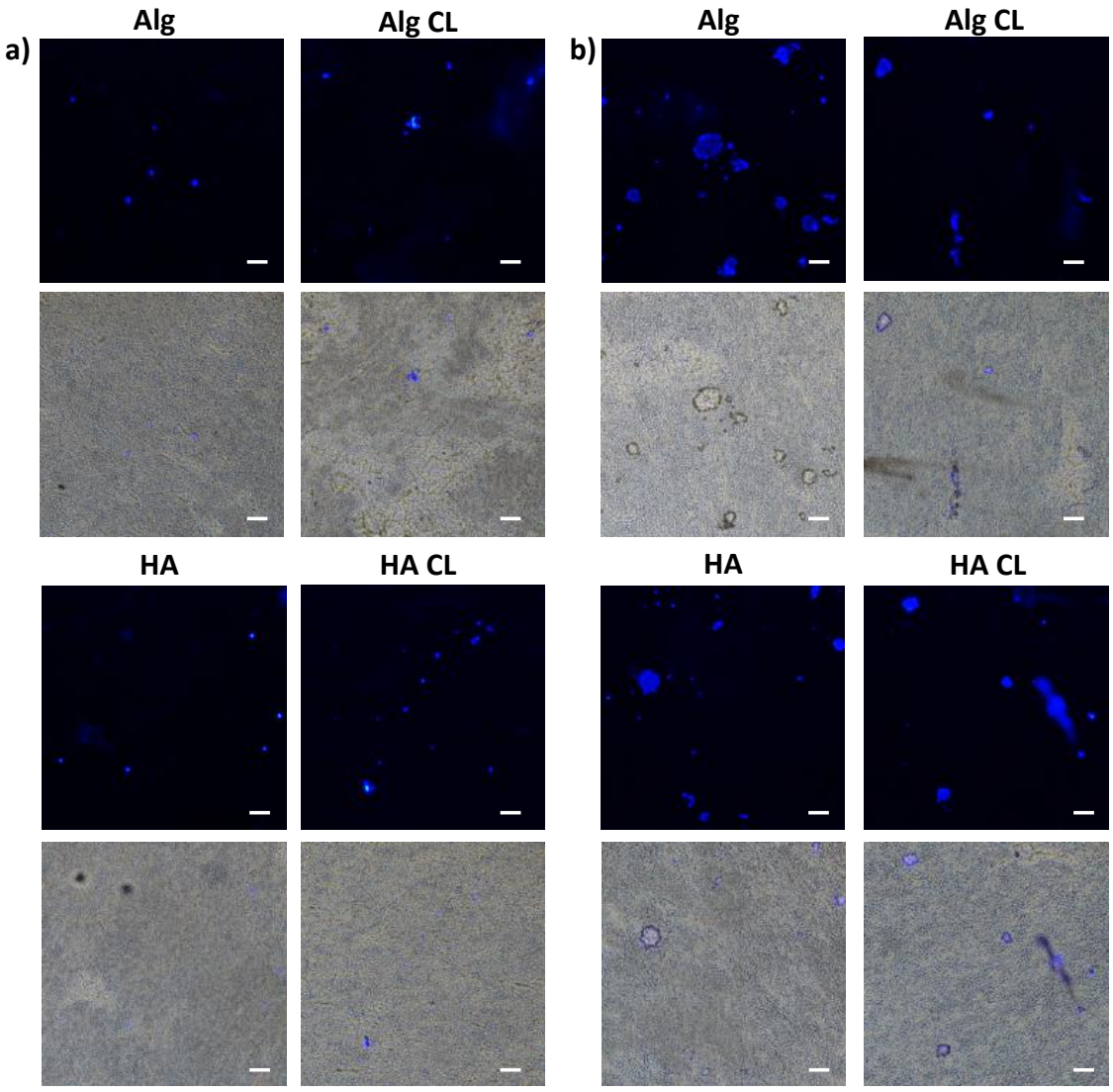

Figure 7.4. Fluorescence microscope images of a) HDF and b) MCF-7 cell adhesion on non-crosslinked and crosslinked $(Alg/Chi)_{10}Alg$ and $(Alg/Chi)_{10}HA$ films after 3 days. Scale bars 100 μm.

Cell adhesion was quantified by means of an Alamar blue assay carried out on $(Alg/Chi)_nAlg$ and $(Alg/Chi)_nHa$ films after three days of cell culture of HDF and MCF-7 cells. Besides the type of cells, HDF or MCF-7, three different experimental parameters were taken into account, namely, number of bilayers, effect of crosslinking and effect of the chemistry of the last layer (alginate or hyaluronic acid) and results are depicted in Figure 7.5.

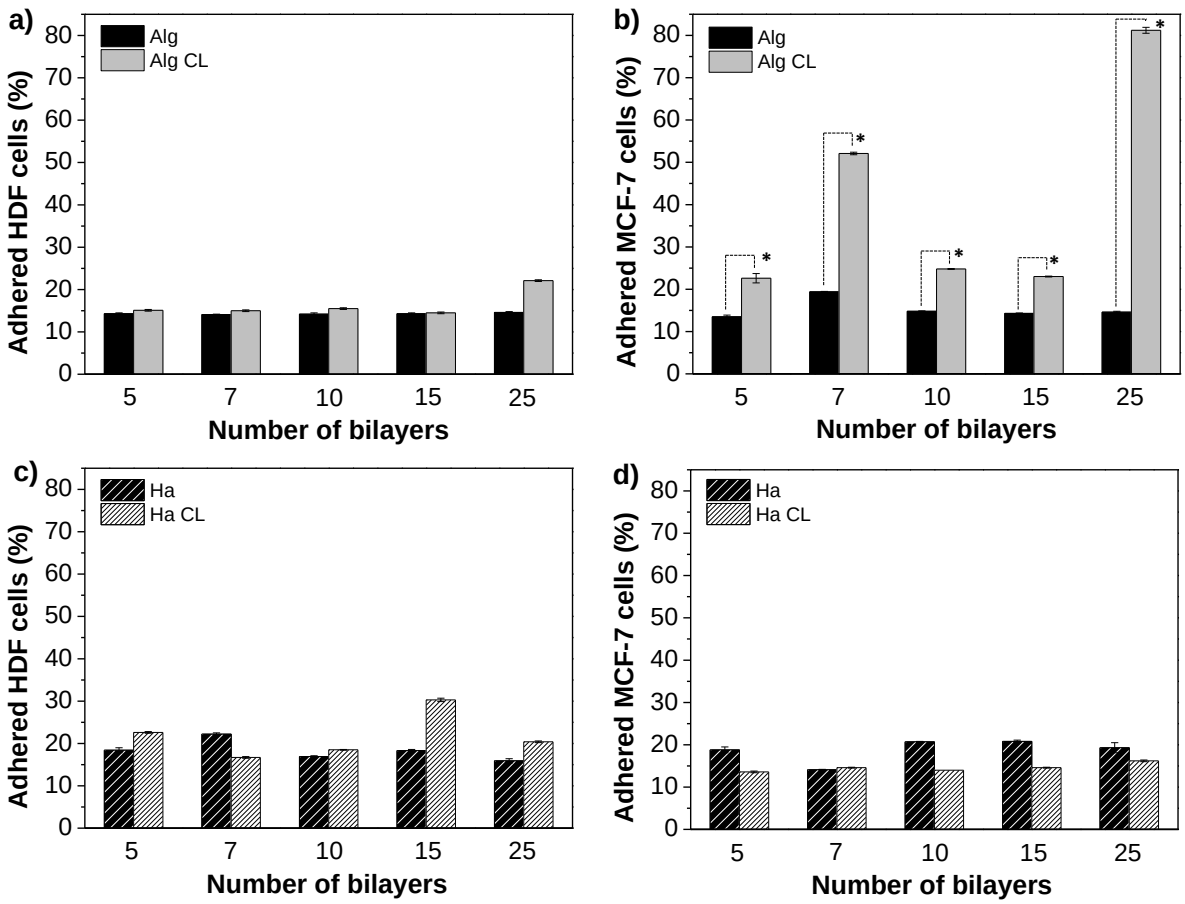

Figure 7.5. a) HDF and b) MCF-7 cell adhesion on non-crosslinked and crosslinked $(Alg/Chi)_nAlg$ films. c) HDF and d) MCF-7 cell adhesion on non-crosslinked and crosslinked $(Alg/Chi)_nHa$ films. The diagrams include the mean, the standard deviation (n = 4) and the ANOVA results at a significance level of * $p < 0.05$.

- *Effect of the number of bilayers*

As shown in Figure 7.5a, the percentage of HDF cells adhered on $(Alg/Chi)_nAlg$ films remains constant at ~14% with the number of bilayers. After crosslinking, the adhesion of HDF cells increases up to 22% only for the sample with 25 bilayers. Likewise, the percentage of MCF-7 adhered cells remains constant (~14%) within the experimental error for $(Alg/Chi)_nAlg$ films with different number of bilayers (Figure 7.5b). However, after crosslinking, there is a remarkable increase in MCF-7 cell adhesion with the number of deposited bilayers increasing from 23% for $(Alg/Chi)_5Alg$ films to 81% for $(Alg/Chi)_{25}Alg$ films.

In the case of $(Alg/Chi)_nHA$ films (Figure 7.5c), the percentage of HDF adhered cells remains constant with the number of bilayers (~18%), being slightly higher than that corresponding to $(Alg/Chi)_nAlg$ films (~14%). Generally speaking, crosslinking gives rise to a slight increase in HDF cell adhesion up to 22% for $(Alg/Chi)_{15}HA$ films with respect to non-crosslinked films.

Similar results were obtained regarding the quantification of MCF-7 adhered cells on $(Alg/Chi)_nHA$ films (Figure 5.7d), that is percentage of adhered cells remains constant with the number of bilayers (~20%). But in this case, crosslinking produces a decrease of MCF-7 cell adhesion that also remains constant with the number of bilayers.

From the results shown in Figure 7.5, it can be concluded that there is no effect of the number of bilayers on cell adhesion, neither for HDF nor for MCF-7 cells. The increase of the number of bilayers in multilayer polysaccharidic films prepared through spray assisted LbL results in a concomitant increase of roughness (Table 7.1). This is in agreement with previous reports, Neto et al.[30] studied the adhesion of L929 cells on the surface of $(Chi/Alg)_n$ films (n = 5, 10, 15) functionalized with fibronectin giving rise to ~5% cell adhesion for all three multilayer films without noting increase of adhesion with the number of bilayers. Elbert et al.[31] studied adhesion of human fibroblast cells on $(PLL/Alg)_n$ films (n = 5, 10, 15) and did not observe changes in the cell adhesion as number of bilayers increased. Cado et al.[32] demonstrated that cell viability and spreading are quite similar for films with different roughness. It follows, that roughness when it is homogeneously distributed throughout the film surface does not have an appreciable effect on cell adhesion for the films under study in this report.

- *Effect of the surface chemistry*

As to the surface chemistry, there are slight differences on cell adhesion between films ending in alginate and those ending in hyaluronic acid. The percentage of HDF adhered cells increase from 14% for $(Alg/Chi)_nAlg$ films to 18% for $(Alg/Chi)_nHA$ films. Similarly, MCF-7 cells adhesion increased from 15% on $(Alg/Chi)_nAlg$ films to 20% on $(Alg/Chi)_nHA$ films. One of the reasons for a higher cell attachment of MCF-7 with respect to HDF could be that HDF cells prefer smoother surfaces to grow[33] and multilayer films built up via spray LbL have a roughness which increases with the number of bilayers. Other kind of cells, *e.g.*, human osteosarcoma cells MG63, exhibit a higher level of adhesion with the increase in surface roughness.[34] A rough surface induces morphological mutations in tumor cells probably due to the fact that this kind of cells are more prone to the invasion of their living environment and can adapt to it more easily. In addition, rougher surfaces tend to form clusters of cells which does not occur when cells are seeded onto smooth surfaces.[35]

- *Effect of crosslinking*

Results point to a significant effect of crosslinking on MCF-7 cell adhesion measured on $(Alg/Chi)_nAlg$ films which increases from 14% to up 81%. Crosslinking gives rise to an increase of the elastic modulus as it was demonstrated by means of PeakForce Quantitative Nanomechanical Mapping atomic force microscopy (PF-QNM) AFM in the chapter 5. The elastic modulus of a film with 20 bilayers increases from 9.2 ± 1.6 GPa to 32.4 ± 11.5 GPa after crosslinking. This increase in the elastic modulus makes the film stiffer and gives advantage to cell adhesion as it has been corroborated by earlier studies about cell adhesion carried out for different types of cells.[1, 30, 36, 37]

Interestingly, it is important to note that crosslinking does not seem to have an effect on HDF cell adhesion which remains almost constant at ~14% on $(Alg/Chi)_nAlg$ films and ~18% on $(Alg/Chi)_nHA$ films.

Contact angle studies

Some studies relate cell adhesion to the contact angle values of the film surface,[34, 38] a sensitive method to the chemical nature and the surface morphology of the last layer in a multilayer film architecture. The wetting properties of non-crosslinked and crosslinked $(Alg/Chi)_nAlg$ and $(Alg/Chi)_nHA$ films were evaluated by water contact angle measurements and results are exhibited in Figure 7.6 as a function of the number of bilayers. In the case of non-crosslinked $(Alg/Chi)_nAlg$ films, there is a linear increase of the contact angle from 17º to 41º up to 10 bilayers and then a *plateau* is reached. For crosslinked films, the same trend is observed, that is the contact angle increases with the number of bilayers from 12º to 44º for $(Alg/Chi)_nAlg$ films up to 10 bilayers and then a *plateau* is reached. However, it is important to highlight that there are not significant differences in the contact angle between non-crosslinked and crosslinked $(Alg/Chi)_nAlg$ films.

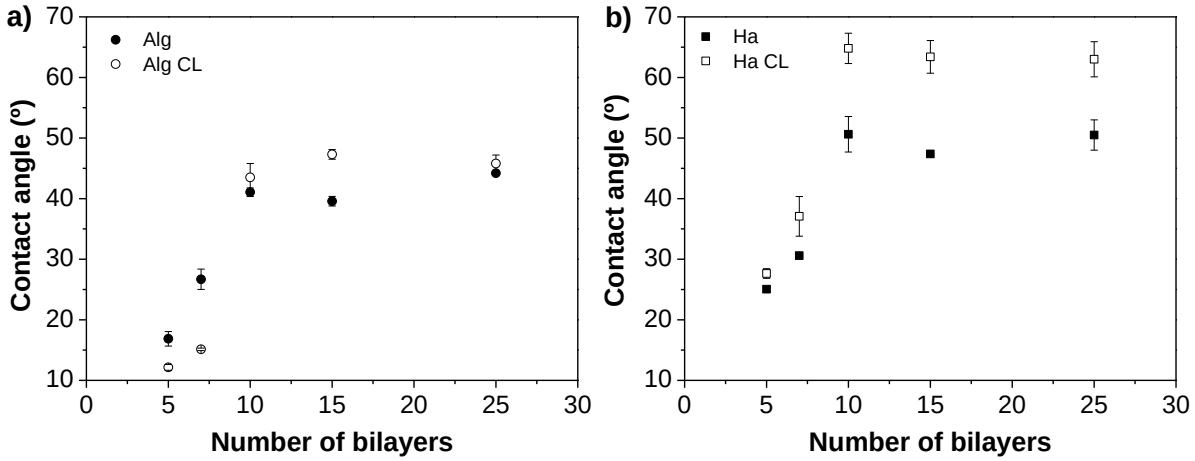

Figure 7.6. Water contact angle measurements on non-crosslinked and crosslinked a) $(Alg/Chi)_nAlg$ and b) $(Alg/Chi)_nHA$ films with different number of bilayers.

Figure 7.6b shows the evolution of the contact angle for non-crosslinked and crosslinked $(Alg/Chi)_nHA$ films as a function of the number of bilayers. The trend is similar to the one found for $(Alg/Chi)_nAlg$ films, that is, for non-crosslinked $(Alg/Chi)_nHA$ films, there is a linear increase of the contact angle from 25º to 50º up to 10 bilayers and then a *plateau* is reached. For crosslinked films, the same trend is observed but the contact angles are higher with regards to non-crosslinked $(Alg/Chi)_nHA$ films, that is the contact angle increases with the number of bilayers from 28º to 65º up to 10 bilayers and then a *plateau* is reached. However, in this case, crosslinking produces an increase of the contact angle in all cases, that is, samples become less hydrophilic with crosslinking, which could alter cell adhesion in some cases as it was observed in the Figure 7.5d.

It is important to note that all films under study are hydrophilic as shown by contact angle values lower than 90º.[27] The hydrophilic character of both polymers, Alg and HA, is attributed to hydroxyl and carboxyl groups.[33] The pKa values of hyaluronic acid and sodium alginate are ~3[39] and ~3.5[40] respectively, so that at physiological pH these groups are ionized. Therefore, the small differences found regarding the contact angle of $(Alg/Chi)_nAlg$ and $(Alg/Chi)_nHA$ films cannot account for the slight differences regarding cell adhesion of HDF. On the contrary, in the case of MCF-7 cell attachment, the hydrophilicity of the surface might play a more important role decreasing the cell attachment on crosslinked $(Alg/Chi)_nHA$ films, where the surface became less hydrophilic.

Although wettability of a surface reflects its surface chemistry, there is not unanimity with regards to cell adhesion. Some authors consider that more hydrophilic surfaces provide a higher

cell adhesion[41] and others report that cells adhered better when the surface is hydrophobic or at intermediate contact angles[33]. Taking into account these considerations, it is possible to think that different kinds of cells will preferentially adhere to surfaces with particular contact angle values. In the case of HDF, cell attachment is slightly higher as increasing hydrophobicity of surfaces being HA the surface where more HDF cells adhered. Maybe this is due to the fact that HA provides an appropriate combination of hydrophilicity and hydrophobicity properties on the adhesion surface which favors the growth of fibroblast cells as reported Wang et al.[33] for L929 cells.

Morphology assay

Not only the percentage of adhered cells but also the cell morphology after adhesion is important for the development of biocompatible polymer patches.[42] Figure 7.7 shows representative images corresponding to the overall cell morphology of HDF and MCF-7 cells adhered on non-crosslinked and crosslinked $(Alg/Chi)_{10}Alg$ and $(Alg/Chi)_{10}HA$ films with two different ending layers, Alg and HA. The morphology of these two cell lines, HDF (Figure 7.7a) and MCF-7 cells (Figure 7.7b), were characterized by visualizing stained cells with crystal violet using an optical microscopy. HDF cells show their characteristic elongated shape[43] with a more slender appearance for Alg ending layer than for HA. Significant differences on morphology were not observed with the crosslinking process. MCF-7 has a cobblestone-like phenotype with strong cell-cell adhesion and exhibit round mass morphology with formation of colonies distinguished from the round morphological grouping.[44] MCF-7 cells show a similar morphology as Alg or HA are the outermost layer. In this case, crosslinking produces a change of morphology decreasing the size of colonies.

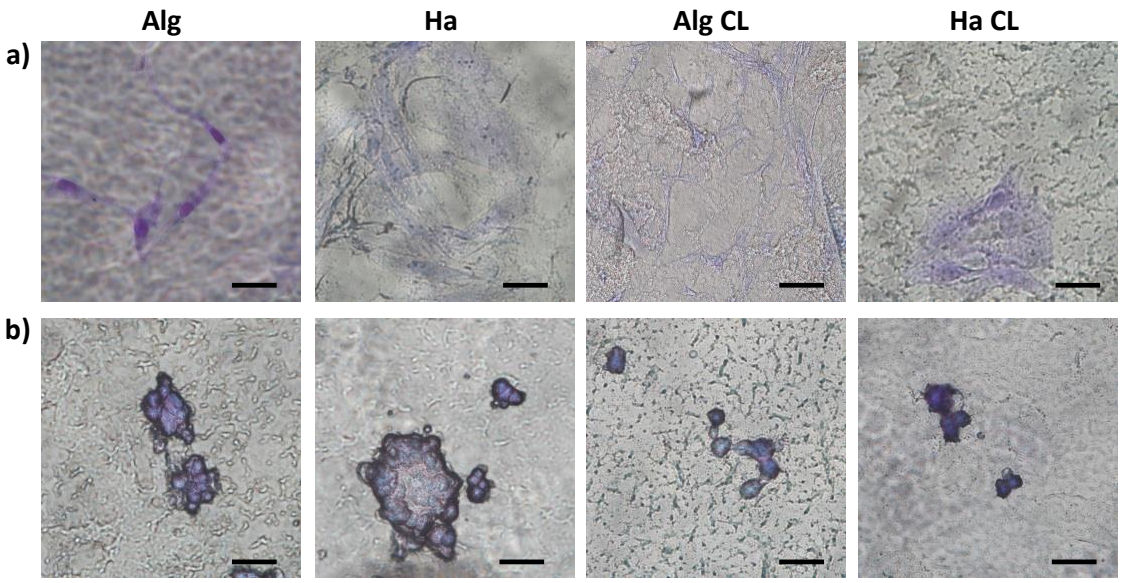

Figure 7.7. Cytoskeletal organization of a) HDF and b) MCF-7 cells on non-crosslinked and crosslinked $(Alg/Chi)_{10}Alg$ and $(Alg/Chi)_{10}HA$ films after 3 days culture. Scale bars 1000 μm.

7.3.3. Drug release experiments

The total amount of TMX loaded into $(Alg/Chi)_5TMX(Chi/Alg)_n$ films was 0.11 ± 0.01 mg TMX in a surface of 14 mm diameter which corresponds to 0.071 mg/cm^2. With this approach, the quantity of loaded drug for the specific application as a function of the film area can be modulated. Prior to test the drug delivery *in vitro* with HDF and MCF-7cells, the TMX release was quantified and results are shown in Figure 7.8 in which the cumulative release profiles of TMX from three different multilayer films, $(Alg/Chi)_5TMX(Chi/Alg)_n$ where n = 5, 10 and 20 bilayers, are compared as a function of time. A fast initial release takes place during the first hour for the three different multilayer films under study; the film with lower number of bilayers (n = 5) releases the 50% of TMX (0.037 mg/cm^2), followed by the film with n = 10 which releases 37% of TMX (0.028 mg/cm^2) and n = 20 with 28% (0.020 mg/cm^2). The complete release of TMX occurred at 2, 5 and 10 days for n = 5, 10 and 20 bilayers respectively. The spray LbL technique allows to modulate the release rate as a function of the number of deposited bilayers being slower and sustained over time as the number of bilayers increases.[13, 45]

The cumulative drug release data up to 0.6 for the two films with higher number of bilayers (n = 10 and 20) were fitted to different diffusion models, Higuchi,[46] Ritger-Peppas,[47] Peppas-Sahlin[48] and zero-order,[49] to elucidate the diffusion release mechanism, being the Ritger-Peppas[47] described by equation 7.3 the most accurate model ($r^2 > 0.99$ in all cases).

$$\frac{M_t}{M_\infty} = k \cdot t^m \qquad (eq. 7.3)$$

where M_t/M_∞ is the released fraction and *k* and *m* are fitting parameters characteristic of the film/solution medium and transport mechanism, respectively. The value of *m* indicates Fickian diffusion (*m* = 0.5), anomalous transport (0.5 < *m* < 1) or Case-II transport (*m* = 1).[48] The inset of the Figure 7.8 shows the fitting to the Ritger-Peppas model up to 0.6 cumulative drug release and the fitting parameters obtained from this model are summarized in Table 7.2. The value of *m* = 0.43 for the film $(Alg/Chi)_5TMX(Chi/Alg)_{20}$ confirms the diffusion controlled drug release mechanism.

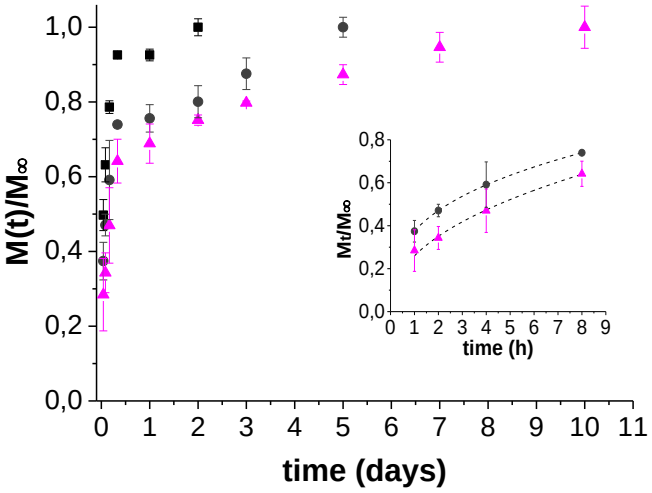

Figure 7.8. Cumulative time-dependent release profiles of TMX from $(Alg/Chi)_5TMX(Chi/Alg)_5$ (■), $(Alg/Chi)_5TMX(Chi/Alg)_{10}$ (●) and $(Alg/Chi)_5TMX(Chi/Alg)_{20}$ (▲) films. The inset shows the fitting with dashed lines to the Ritger-Peppas model up to 0.6 cumulative drug release for $(Alg/Chi)_5TMX(Chi/Alg)_{10}$ (●) and $(Alg/Chi)_5TMX(Chi/Alg)_{20}$ (▲) films.

Table 7.2. Fitting parameters from the Ritger-Peppas model.

Sample	k	m	r^2
$(Alg/Chi)_5TMX(Chi/Alg)_{10}$	0.38 ± 0.00	0.33 ± 0.00	0.999
$(Alg/Chi)_5TMX(Chi/Alg)_{20}$	0.26 ± 0.01	0.43 ± 0.02	0.993

The surface morphology of $(Alg/Chi)_5TMX(Chi/Alg)_n$ films (n = 5, 10 and 20) after the drug delivery experiment is shown in Figure 7.9. No significant differences are observed between films after the drug delivery experiment which seems to indicate the absence of degradation of the films. This result confirms that the release mechanism follows a diffusion controlled mechanism.

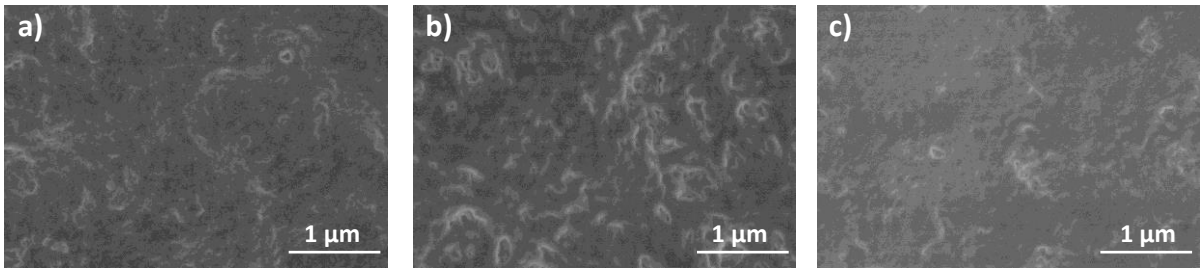

Figure 7.9. SEM micrographs of a) $(Alg/Chi)_5TMX(Chi/Alg)_5$, b) $(Alg/Chi)_5TMX(Chi/Alg)_{10}$ and c) $(Alg/Chi)_5TMX(Chi/Alg)_{20}$ films after drug delivery experiment.

Considering that the higher amount of TMX is released during the first 8 hours, *in vitro* cell viability experiments were evaluated in this period of time. As can be observed in Figure 7.10a, the release of TMX does not decrease the cell viability of non-tumor HDF cells for any film under study up to 8 hours. On the contrary, the delivery of TMX affects significantly the cell viability of breast adenocarcinoma MCF-7 cells (Figure 7.10b), as it was expected due to the fact that TMX is a therapeutic agent against breast cancer. A comparison of the results depicted in Figure 7.10b with the cumulative TMX delivery profile shown in Figure 7.8 allows to observe that cell viability obtained during the first hour correlates well with the amount of TMX released. That is, the highest TMX concentration released, the lowest the cell viability. For films with n=5, the cell viability decreases to~ 36% (release of TMX = 0.037 mg/cm^2), whereas for films with n=10 and n=20 the cell viability decreases to ~29% (0.028 mg/cm^2) and ~27% cell viability (0.020 mg/cm^2), respectively. After 2 hours, the cell viability also decreases with respect to the control for all the films under study but this decrease is lower than that observed after one hour.

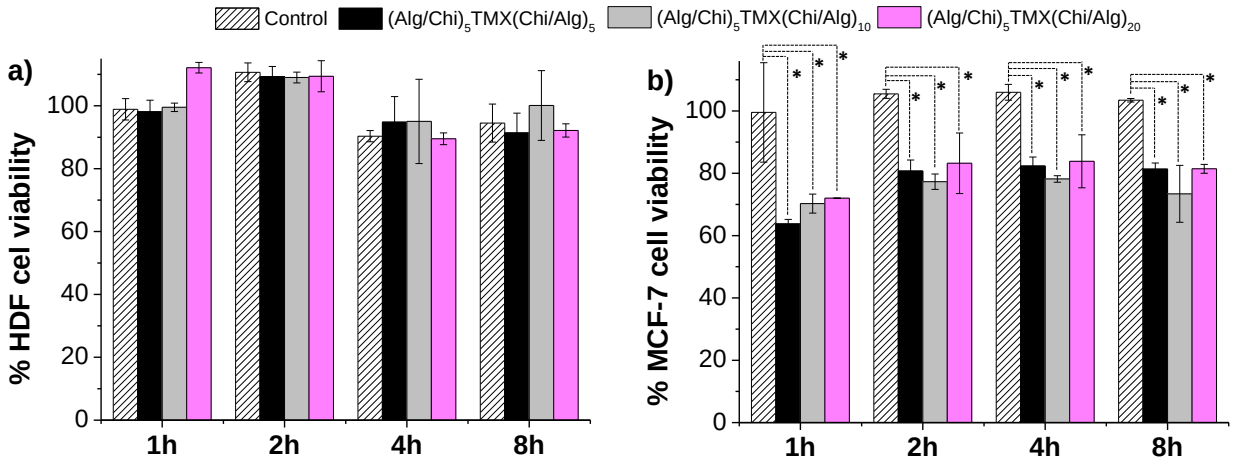

Figure 7.10. a) % HDF cell viability and b) % MCF-7 cell viability after the TMX delivery from $(Alg/Chi)_5TMX(Chi/Alg)_m$ (m = 5, 10 and 20) films at different times comparing with control films without TMX. Diagrams include the mean, the standard deviation (n = 2) and the ANOVA results at a significance level of * $p < 0.05$.

7.4. CONCLUSIONS

The influence of the surface chemistry and the crosslinking on the morphological characteristics, degradation and cell adhesion of multilayer Alg/Chi films has been studied.

The degradation of these multilayer films in physiological environment (DMEM at 37ºC) revealed that films ended in HA were more prone to degradation than films ended in Alg after 15 days. The degradation process could be diminished by crosslinking films with the carbodiimide chemistry.

The cytotoxicity assay showed that non-crosslinked and chemically crosslinked Alg/Chi films were not cytotoxic. It was proven that the number of bilayers of multilayer Alg/Chi films did not influence the cell adhesion of dermal fibroblast (HDF) and breast adenocarcinoma (MCF-7) cells. Non-significant differences on cell adhesion were observed with regards to the roughness of multilayer films. In contrast, the crosslinking process produced an increase of the stiffness of multilayer films favoring the MCF-7 cell adhesion on films whose ending layer was Alg.

Contact angle measurements showed that there are not significant differences between non-crosslinked multilayer films ending on Alg or HA. Chemical crosslinking did not produce any effect on the hydrophilicity of multilayer films ending on Alg, whereas gave rise to an increase of the hydrophobicity of those ending on Alg.

With the objective of using these multilayer films as platforms for sustained drug release, tamoxifen, a therapeutic agent against breast cancer, was assembled in different intermediate positions of the multilayer $(Alg/Chi)_n$ films achieving a more sustained release over time as number of deposited bilayers increases. The release mechanism is controlled diffusion, due to the fact that there was not degradation of these films after the drug delivery experiment, being the Ritger-Peppas model the most accurate to describe the diffusion mechanism. The incorporation of TMX within Alg/Chi films decreased the cell viability of MCF-7 cells whereas the HDF cell viability remained unaffected.

7.5. REFERENCES

1. Silva, J. M.; Duarte, A. R. C.; Caridade, S. G.; Picart, C.; Reis, R. L.; Mano, J. o. F., Tailored freestanding multilayered membranes based on chitosan and alginate. *Biomacromolecules* **2014,** 15, (10), 3817-3826.

2. Pensabene, V.; Taccola, S.; Ricotti, L.; Ciofani, G.; Menciassi, A.; Perut, F.; Salerno, M.; Dario, P.; Baldini, N., Flexible polymeric ultrathin film for mesenchymal stem cell differentiation. *Acta Biomaterialia* **2011,** 7, (7), 2883-2891.

3. Monteiro, I. P.; Shukla, A.; Marques, A. P.; Reis, R. L.; Hammond, P. T., Spray- assisted layer-by- layer assembly on hyaluronic acid scaffolds for skin tissue engineering. *Journal of Biomedical Materials Research Part A* **2015,** 103, (1), 330-340.

4. Redolfi Riva, E.; Desii, A.; Sartini, S.; La Motta, C.; Mazzolai, B.; Mattoli, V., PMMA/Polysaccharides Nanofilm Loaded with Adenosine Deaminase Inhibitor for Targeted Anti-inflammatory Drug Delivery. *Langmuir* **2013,** 29, (43), 13190-13197.

5. Chen, D.; Chen, J.; Wu, M.; Tian, H.; Chen, X.; Sun, J., Robust and flexible free-standing films for unidirectional drug delivery. *Langmuir* **2013,** 29, (26), 8328-8334.

6. Hammond, P. T., Building biomedical materials layer-by-layer. *Materials Today* **2012,** 15, (5), 196-206.

7. Chen, D.; Wu, M.; Chen, J.; Zhang, C.; Pan, T.; Zhang, B.; Tian, H.; Chen, X.; Sun, J., Robust, flexible, and bioadhesive free-standing films for the co-delivery of antibiotics and growth factors. *Langmuir* **2014,** 30, (46), 13898-13906.

8. Mohanta, V.; Madras, G.; Patil, S., Layer-by-layer assembled thin films and microcapsules of nanocrystalline cellulose for hydrophobic drug delivery. *ACS Applied Materials & Interfaces* **2014,** 6, (22), 20093-20101.

9. Su, X.; Kim, B.-S.; Kim, S. R.; Hammond, P. T.; Irvine, D. J., Layer-by-layer-assembled multilayer films for transcutaneous drug and vaccine delivery. *ACS Nano* **2009,** 3, (11), 3719-3729.

10. Vilela, C.; Figueiredo, A. R.; Silvestre, A. J.; Freire, C. S., Multilayered materials based on biopolymers as drug delivery systems. *Expert Opinion on Drug Delivery* **2016**, 1-12.

11. De Villiers, M. M.; Otto, D. P.; Strydom, S. J.; Lvov, Y. M., Introduction to nanocoatings produced by layer-by-layer (LbL) self-assembly. *Advanced drug delivery reviews* **2011,** 63, (9), 701-715.

12. Karki, S.; Kim, H.; Na, S.-J.; Shin, D.; Jo, K.; Lee, J., Thin films as an emerging platform for drug delivery. *Asian Journal of Pharmaceutical Sciences* **2016**.

13. Kashiwagi, K.; Ito, K.; Haniuda, H.; Ohtsubo, S.; Takeoka, S., Development of Latanoprost-Loaded Biodegradable Nanosheet as a New Drug Delivery System for GlaucomaLatanoprost-Loaded Nanosheet for Glaucoma. *Investigative Ophthalmology & Visual Science* **2013,** 54, (8), 5629-5637.

14. Hu, X.; Tan, H.; Li, D.; Gu, M., Surface functionalisation of contact lenses by CS/HA multilayer film to improve its properties and deliver drugs. *Materials Technology* **2014,** 29, (1), 8-13.

15. Jain, A. K.; Swarnakar, N. K.; Godugu, C.; Singh, R. P.; Jain, S., The effect of the oral administration of polymeric nanoparticles on the efficacy and toxicity of tamoxifen. *Biomaterials* **2011,** 32, (2), 503-515.

16. Pavlukhina, S.; Sukhishvili, S., Polymer assemblies for controlled delivery of bioactive molecules from surfaces. *Advanced Drug Delivery Reviews* **2011,** 63, (9), 822-836.

17. Zelikin, A. N., Drug releasing polymer thin films: new era of surface-mediated drug delivery. *ACS Nano* **2010,** 4, (5), 2494-2509.

18. Larkin, A. L.; Davis, R. M.; Rajagopalan, P., Biocompatible, detachable, and free-standing polyelectrolyte multilayer films. *Biomacromolecules* **2010,** 11, (10), 2788-2796.

19. Fujie, T.; Ricotti, L.; Desii, A.; Menciassi, A.; Dario, P.; Mattoli, V., Evaluation of substrata effect on cell adhesion properties using freestanding poly (l-lactic acid) nanosheets. *Langmuir* **2011,** 27, (21), 13173-13182.

20. Costa, R. R.; Alatorre-Meda, M.; Mano, J. F., Drug nano-reservoirs synthesized using layer-by-layer technologies. *Biotechnology advances* **2015,** 33, (6), 1310-1326.

21. Arias, C. J.; Surmaitis, R. L.; Schlenoff, J. B., Cell Adhesion and Proliferation on the "Living" Surface of a Polyelectrolyte Multilayer. *Langmuir* **2016,** 32, (21), 5412-5421.

22. Silva, J. M.; Duarte, A. R. C.; Caridade, S. G.; Picart, C.; Reis, R. L.; Mano, J. F., *Biomacromolecules* **2014,** 15, 3817-3826.

23. Lee, J. N.; Jiang, X.; Ryan, D.; Whitesides, G. M., Compatibility of mammalian cells on surfaces of poly (dimethylsiloxane). *Langmuir* **2004,** 20, (26), 11684-11691.

24. Elosua, C.; Lopez-Torres, D.; Hernaez, M.; Matias, I. R.; Arregui, F. J., Comparative study of layer-by-layer deposition techniques for poly(sodium phosphate) and poly(allylamine hydrochloride). *Nanoscale Research Letters* **2013,** 8, (1), 539-539.

25. Picart, C.; Lavalle, P.; Hubert, P.; Cuisinier, F. J. G.; Decher, G.; Schaaf, P.; Voegel, J. C., Buildup Mechanism for Poly(l-lysine)/Hyaluronic Acid Films onto a Solid Surface. *Langmuir* **2001,** 17, (23), 7414-7424.

26. Pena, J.; Corrales, T.; Izquierdo-Barba, I.; Doadrio, A. L.; Vallet-Regí, M., Long term degradation of poly (ε-caprolactone) films in biologically related fluids. *Polymer Degradation and Stability* **2006,** 91, (7), 1424-1432.

27. Powell, H. M.; Boyce, S. T., EDC cross-linking improves skin substitute strength and stability. *Biomaterials* **2006,** 27, (34), 5821-5827.

28. Caridade, S. G.; Monge, C.; Gilde, F.; Boudou, T.; Mano, J. o. F.; Picart, C., Free-standing polyelectrolyte membranes made of chitosan and alginate. *Biomacromolecules* **2013,** 14, (5), 1653-1660.

29. Sergeeva, Y. N.; Huang, T.; Felix, O.; Jung, L.; Tropel, P.; Viville, S.; Decher, G., What is really driving cell–surface interactions? Layer-by-layer assembled films may help to answer questions concerning cell attachment and response to biomaterials. *Biointerphases* **2016,** 11, (1), 019009.

30. Neto, A. I.; Vasconcelos, N. L.; Oliveira, S. M.; Ruiz- Molina, D.; Mano, J. F., High-Throughput Topographic, Mechanical, and Biological Screening of Multilayer Films Containing Mussel- Inspired Biopolymers. *Advanced Functional Materials* **2016**.

31. Elbert, D. L.; Herbert, C. B.; Hubbell, J. A., Thin polymer layers formed by polyelectrolyte multilayer techniques on biological surfaces. *Langmuir* **1999,** 15, (16), 5355-5362.

32. Cado, G.; Kerdjoudj, H.; Chassepot, A.; Lefort, M.; Benmlih, K.; Hemmerle, J.; Voegel, J.-C.; Jierry, L.; Schaaf, P.; Frere, Y., Polysaccharide films built by simultaneous or alternate spray: a rapid way to engineer biomaterial surfaces. *Langmuir* **2012,** 28, (22), 8470-8478.

33. Wang, Y.-W.; Wu, Q.; Chen, G.-Q., Reduced mouse fibroblast cell growth by increased hydrophilicity of microbial polyhydroxyalkanoates via hyaluronan coating. *Biomaterials* **2003,** 24, (25), 4621-4629.

34. Dowling, D. P.; Miller, I. S.; Ardhaoui, M.; Gallagher, W. M., Effect of surface wettability and topography on the adhesion of osteosarcoma cells on plasma-modified polystyrene. *Journal of biomaterials applications* **2010**.

35. De Vitis, S.; Coluccio, M. L.; Gentile, F.; Malara, N.; Perozziello, G.; Dattola, E.; Candeloro, P.; Di Fabrizio, E., Surface enhanced Raman spectroscopy measurements of MCF7 cells adhesion in confined micro-environments. *Optics and Lasers in Engineering* **2016,** 76, 9-16.

36. Blacklock, J.; Sievers, T. K.; Handa, H.; You, Y.-Z.; Oupický, D.; Mao, G.; Möhwald, H., Cross-linked bioreducible layer-by-layer films for increased cell adhesion and transgene expression. *The Journal of Physical Chemistry B* **2010,** 114, (16), 5283-5291.

37. Picart, C.; Elkaim, R.; Richert, L.; Audoin, F.; Arntz, Y.; Da Silva Cardoso, M.; Schaaf, P.; Voegel, J. C.; Frisch, B., Primary Cell Adhesion on RGD- Functionalized and Covalently Crosslinked Thin Polyelectrolyte Multilayer Films. *Advanced Functional Materials* **2005,** 15, (1), 83-94.

38. Kim, S. H.; Ha, H. J.; Ko, Y. K.; Yoon, S. J.; Rhee, J. M.; Kim, M. S.; Lee, H. B.; Khang, G., Correlation of proliferation, morphology and biological responses of fibroblasts on LDPE with different surface wettability. *Journal of Biomaterials Science, Polymer Edition* **2007,** 18, (5), 609-622.

39. Brown, M.; Jones, S. A., Hyaluronic acid: a unique topical vehicle for the localized delivery of drugs to the skin. *Journal of the European Academy of Dermatology and Venereology* **2005,** 19, (3), 308-318.

40. Hu, L.; Sun, C.; Song, A.; Chang, D.; Zheng, X.; Gao, Y.; Jiang, T.; Wang, S., Alginate encapsulated mesoporous silica nanospheres as a sustained drug delivery system for the poorly water-soluble drug indomethacin. *Asian Journal of Pharmaceutical Sciences* **2014,** 9, (4), 183-190.

41. Altankov, G.; Groth, T., Reorganization of substratum-bound fibronectin on hydrophilic and hydrophobic materials is related to biocompatibility. *Journal of Materials Science: Materials in Medicine* **1994,** 5, (9-10), 732-737.

42. Grover, C. N.; Gwynne, J. H.; Pugh, N.; Hamaia, S.; Farndale, R. W.; Best, S. M.; Cameron, R. E., Crosslinking and composition influence the surface properties, mechanical stiffness and cell reactivity of collagen-based films. *Acta Biomaterialia* **2012,** 8, (8), 3080-3090.

43. Hakkinen, K. M.; Harunaga, J. S.; Doyle, A. D.; Yamada, K. M., Direct comparisons of the morphology, migration, cell adhesions, and actin cytoskeleton of fibroblasts in four different three-dimensional extracellular matrices. *Tissue Engineering Part A* **2010,** 17, (5-6), 713-724.

44. Kenny, P. A.; Lee, G. Y.; Myers, C. A.; Neve, R. M.; Semeiks, J. R.; Spellman, P. T.; Lorenz, K.; Lee, E. H.; Barcellos-Hoff, M. H.; Petersen, O. W.; Gray, J. W.; Bissell, M. J., The morphologies of breast cancer cell lines in three-dimensional assays correlate with their profiles of gene expression. *Molecular oncology* **2007,** 1, (1), 84-96.

45. Su, X.; Kim, B.-S.; Kim, S. R.; Hammond, P. T.; Irvine, D. J., Layer-by-Layer Assembled Multilayer Films for Transcutaneous Drug and Vaccine Delivery. *ACS Nano* **2009,** 3, (11), 3719-3729.

46. Higuchi, T., Mechanism of sustained- action medication. Theoretical analysis of rate of release of solid drugs dispersed in solid matrices. *Journal of pharmaceutical sciences* **1963,** 52, (12), 1145-1149.

47. Ritger, P. L.; Peppas, N. A., A simple equation for description of solute release II. Fickian and anomalous release from swellable devices. *Journal of Controlled Release* **1987,** 5, (1), 37-42.

48. Peppas, N. A.; Sahlin, J. J., A simple equation for the description of solute release. III. Coupling of diffusion and relaxation. *International Journal of Pharmaceutics* **1989,** 57, (2), 169-172.

49. Serra, L.; Doménech, J.; Peppas, N. A., Drug transport mechanisms and release kinetics from molecularly designed poly (acrylic acid-g-ethylene glycol) hydrogels. *Biomaterials* **2006,** 27, (31), 5440-5451.

CHAPTER 8

LbL hydrogels obtained from natural polymers

This chapter is an extension of the LbL assembly from films to hydrogels. Firstly, the multilayer assembly and chemical characterization of layer-by-layer hydrogels based on two natural polymers, gelatin and chondroitin sulphate, is described. Secondly, the internal structure of these LbL hydrogels is studied by a combination of scanning electron microscopy and confocal Raman spectroscopy and the mechanical properties are determined through rheological measurements.

8.1. INTRODUCTION

Hydrogels are polymer networks crosslinked by physical, ionic or covalent interactions that exhibit the ability to swell and retain a significant fraction of water within its structure without being dissolved by it.[1] Hydrogels have received increasing attention in the past 50 years due to the fact that they possess a degree of flexibility very similar to natural tissue, because of their large water content, allowing their use in a wide range of biomedical applications.[2-5]

Hydrogels obtained from natural polymers are currently the focus of considerable scientific research for the development of biomedical applications due to their inherent biocompatility and biodegradability, low cost and simplicity of synthesis.[6] There are still some limitations concerning the use of hydrogels obtained from natural polymers, mainly derived from the crosslinking mechanisms used or the characteristics of its constituents *in vivo*. This includes their limited mechanical properties, which may be additionally hard to control (with some exceptions), and problems in terms of reproducibility.[2] In order to maximize the functionality of natural hydrogels and improve their mechanical properties, thus widening the amount of biomedical applications, there exists a necessity to investigate new strategies for the preparation of novel hydrogel architectures.[7] These include the development of interpenetrating polymer networks (IPNs) in which there is a synergistic combination of the properties of both polymers,[8] nanocomposite hydrogels prepared by incorporation of inorganic nanoparticles that provide further functionalities to the hydrogels (*e.g.*, silver nanoparticles for antibacterial materials[9] or iron oxide nanoparticles for controlled drug release and magnetic hyperthermia therapy)[10-12] or development of double-network hydrogels that leads to significant toughening of the resulting hydrogels.[13]

A representative example of an efficient and novel gel architecture are LbL hydrogels. A pioneering work published by Ladet et al.[14], showed that it is possible to induce an onion-like structure from chitosan solutions just by controlling the time of neutralization in basic pH of its chains which, in turn, determines the gelation of chitosan by controlled precipitation of chitosan

chains. A recent study has revealed that the mechanical properties of these materials are dependent on the layer organization.[15] LbL hydrogels can be developed through the layer-by-layer (LbL) method, by the incorporation of successive polymer layers that interact with each other electrostatically, H-bonded or covalently onto a hydrogel core.[16] The LbL method applied to hydrogels provides several advantages, for example, drugs can be loaded in the intermembrane spaces providing sustained release, so that the higher the surface area of such spaces, the greater loading capacity of the LbL gel.[14] They can be built with single-component or multicomponent layers. Single-component hydrogels have been used for augmenting drug release and preventing the initial burst characteristic of commonplace hydrogels.[17] On the other hand, multicomponent LbL hydrogels have been designed for the rapid release of a certain drug and the slow release of a second drug in order to overcome the drug resistance effect.[18] In addition, LbL hydrogels are very interesting for tissue engineering: not only drugs can be loaded into their intermembrane spaces, but also cells. In particular, LbL hydrogels resemble the complexity of complete organs such as intervertebral disk (IVD), and have been used as bioreactors for chondrocytes with potential applications as IVD replacements.[19]

The aim of this chapter is to investigate the assembly of these two natural polymers, gelatin and chondroitin sulfate by dipping LbL, which has not been described in the literature to the best of our knowledge. The main characteristics of both polymers have been described in Chapter 3. The capacity of ChS to enhance the mechanical properties of gelatin gels and its bioactivity, together with the fact that ChS and gelatin are among the most abundant biopolymers in the ECM of mammals, makes the combination of these two polymers highly attractive for both cell encapsulation and drug delivery. Gelatin and ChS hydrogels have been applied in corneal regeneration and encapsulation of chondrocytes for mimicking articular cartilage.[20, 21] In this chapter, the LbL assembly of these polymers will be carried out onto gelatin cores to obtain LbL hydrogels. In addition, a detailed study about their composition along the depth of the multilayer coating will be performed. Due to the fact that these LbL hydrogels are intended to be used for potential biomedical applications, such as tissue engineering and drug delivery, their mechanical properties will be studied by rheological measurements.

8.2. EXPERIMENTAL PART

8.2.1. Materials

Chondroitin sulphate A sodium salt from bovine trachea (C9819), gelatin type A from porcine skin (G1890), poly(ethylenimine) (PEI) with a molecular weight (M_w) of 25000 and acetic acid were supplied by Aldrich and used as received.

8.2.2. Determination of interactions in the multilayer assembly

FTIR spectroscopy

Prior to the fabrication of LbL hydrogels, the assembly of gelatin and chondroitin sulphate over a polystyrene substrate (PS) of 70 μm thickness was followed through FTIR spectra acquired at different steps of the material buildup for concentrations of GL and ChS of 10 mg/mL and 25 mg/mL with pH 3 and 5, respectively. IR transmittance was carried out in a Perkin Elmer Spectrum One FT-IR Spectrometer in the range 450-4000 cm^{-1} with a resolution of 4 cm^{-1}, performing 4 scans per sample.

For that, PS was immersed in the GL solution (10 mg/mL, pH 3) during 15 minutes, then washed in Milli-Q water for 3 minutes, followed by immersion in the ChS solution (25 mg/mL, pH 5) for 15 minutes and a final rinsing in Milli-Q water for 3 minutes. The pH of the washing solutions were identical to the preceding polymer solutions in which the gels were immersed. In order to follow the deposition process, sequential spectra were acquired at different number of deposited layers.

In addition, the FTIR spectra of both polymer solutions in isolation was carried out through the measurement of a gelatin film and a chondroitin sulphate film prepared by film casting of its aqueous solutions at pH 3 and 5, respectively.

XRD diffraction

X-Ray diffraction (XRD) experiments were performed using a X-Ray diffractometer Bruker D8 Advance by using Cu Kα radiation (λ=1.5418 Å) in the range 2θ = 2−50°. Previously, ChS/GL hydrogels were dried at room temperature under the hood.

8.2.3. LbL hydrogels prepared through dipping assembly

Experimental conditions for the design of multilayer gels

A study was performed to determine the optimal concentration and pH conditions for generating interactions between gelatin (GL) and chondroitin sulphate (ChS), which take place by the formation of a precipitate. Both polymers were dissolved separately in water at three different concentrations, 5, 10 and 25 mg/mL. The selected pH values were 3 and 5 and they were adjusted with acetic acid 1M. 250 mL of each polymer solution were mixed in vials and observed after 3 hours in order to determine the presence of a precipitate. A total of 36 combinations of gelatin and ChS were considered.

Preparation of multilayer gels using the LbL method

LbL hydrogels have been prepared through the dipping LbL method by immersing a gelatin hydrogel acting as core (10 %w/v, 6 mm diameter, volume 0.6 mL) in solutions of ChS (10 and 25 mg/mL) and GL (10 mg/mL) at different pH (5, 3 or unaltered, that is, 6.75 for ChS and 5.2 for GL). The process is represented in Scheme 8.1, which shows how the gelatin core is immersed in the ChS solution during 15 minutes, then washed in Milli-Q water for 3 minutes, followed by immersion in the GL solution for 15 minutes and a final washing in water for 3 minutes. The pH of the washing solutions were the same as those corresponding to the polymer solutions. The process was repeated 10 times. Hydrogels were designated as $(ChS10/GL10)_n$ (pH 6.75, 5.2); $(ChS10/GL10)_n$ (pH 5, 3); and $(ChS25/GL10)_n$ (pH 5, 3). $(ChSx/GL10)_n$, where x = 10 and 25 are the different ChS concentrations in mg/mL used for dipping, n stands for the number of bilayers and finally the pH of ChS and GL respectively are indicated.

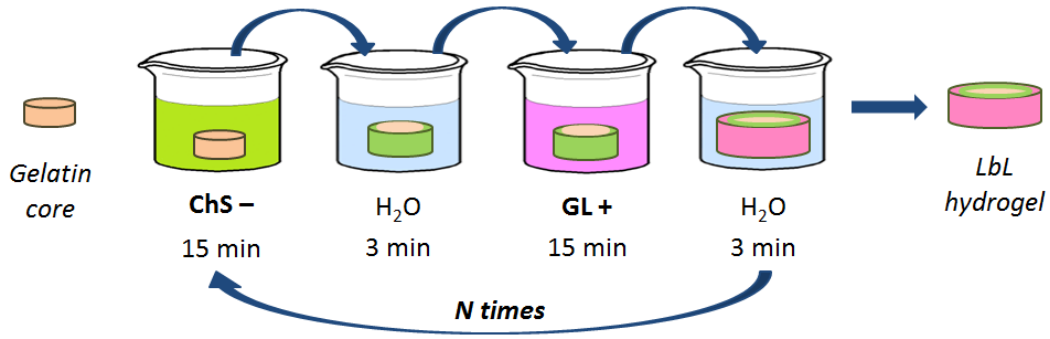

Scheme 8.1. Schematic representation of the dipping procedure to obtain LbL hydrogels $(ChSx/GL)_n$.

8.2.4. Characterization of LbL hydrogels

Chemical characterization

Fourier transform Infra-Red – Attenuated total reflectance (FTIR-ATR) spectroscopy was carried out in a Perkin Elmer spectromether equipped with a diamond cell in the range 4000 - 450 cm^{-1} with a resolution of 4 cm^{-1}, performing 4 scans/sample. Prior to this, LbL hydrogels were left to dry at room temperature under the hood.

Raman spectroscopy was performed in a Renishaw InVia Reflex confocal Raman microscope (Renishaw PLC, UK). An excitation laser of 514 nm was used, and Raman shift was measured in the range 770 - 3200 cm^{-1}. The confocal microscope was then used to obtain a depth profile with 2 μm steps for a single sample. Raman spectra were taken on ChS/GL hydrogels dried at room temperature under the hood. The spectra corresponding to powder gelatin and ChS were also recorded for reference.

Morphological characterization

The surface and internal morphology of the LbL hydrogels were observed by scanning electron microscopy (SEM) using a Hitachi SU 8000 microscope operating at 1.5 kV. Previously, LbL hydrogels were freeze-dried for 24 hours, then frozen in liquid nitrogen and split in half with the aid of tweezers, in order to study their cross section. Then, an ultrathin coating of platinum was deposited on the samples by high-vacuum metallization.

Mechanical properties

The rheological properties of ChS/GL hydrogels were evaluated in an AR-G2 rheometer (TA instruments, USA) using parallel steel plates of 20 mm. A solvent trap was used to prevent solvent evaporation during the course of the experiments. Temperature sweeps were carried out from 20 to 90 ºC at 10 ºC/min and at 1Hz frequency. All experiments were performed at a constant strain in the linear viscoelastic region (LVR) of the gels, determined with the aid of strain sweeps carried out at 1 Hz and 20 ºC. Results were visualized using the Rheology Advantage Data Analysis software (TA instruments, USA).

8.3. RESULTS AND DISCUSSION

8.3.1. Optimization of conditions for the design of LbL hydrogels

Positively charged GL and negatively charged ChS are expected to interact electrostatically at the appropriate pH conditions. Gelatin has an isoelectric point at neutral to basic pH (between 7 and 9),[22] implying that when diluted in deionized water (pH = 5.2) it has a slightly positive character. On the other hand, ChS has carboxylate and O-sulphate groups with pKa of 4.6 and 2.6 respectively,[23] implying that it has a strong negative charge even at low pH (both groups are deprotonated and attain negative charge at pH > pKa).

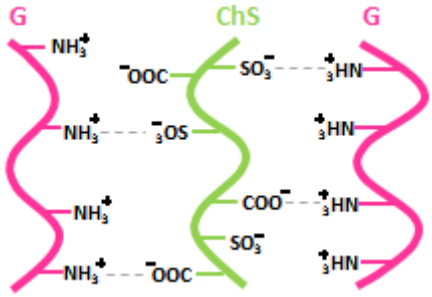

Scheme 8.2. Schematic representation of the electrostatic interactions between gelatin and chrondroitin sulphate.

GL and ChS solutions with pH 3 and 5 in concentrations 5-25 mg/mL were mixed in all possible combinations to observe which conditions gave the greatest amount of precipitate and, therefore, higher degree of electrostatic interactions (Figure 8.1a). Samples with pH 5 in both ChS and GL were transparent after 4 hours, indicating that minimum interactions take place whenever the pH of the solutions is equal and 5. These conditions are similar to the pH of unaltered ChS and GL solutions (5.2 and 6.75 respectively), which did not produce observable interactions (P0) either. A consistent trend involving an increase in polymer-aggregate precipitation was observed in samples with ChS at pH 3; as a general rule, the amount of precipitate increased with the ChS concentration. Samples with high gelatin concentration gelified after 4 hours and, hence, they were not employed for the LbL method (P9, P10, P12, P22, P23, P32-36).

Taking into account these results, the experimental conditions chosen to carry out the LbL experiments were a fixed GL concentration of 10 mg/mL and two different ChS concentrations, 10 and 25 mg/mL. The pH of GL and ChS solutions were maintained at pH 3 and 5, respectively. These conditions were employed in the preparation of samples labelled as P19 and P31 as shown in Figure 8.1a. An additional sample prepared with unaltered pH and 10 mg/ml of ChS and GL

will also be used in LbL experiments as control (P0 in Figure 8.1b), conditions at which no significant electrostatic interactions are expected.

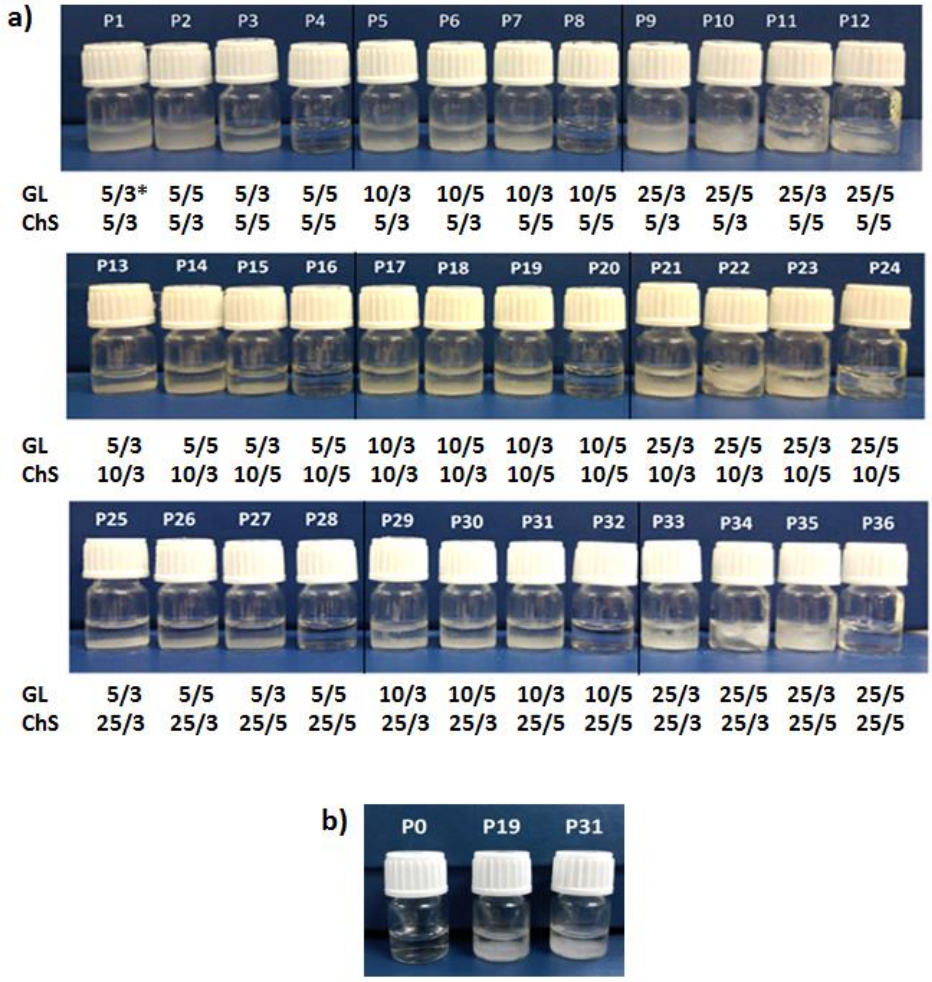

Figure 8.1. a) Experimental conditions used to carry out precipitation tests. *5/3, the first number indicates the concentration in mg/mL and the second refers to pH.* P1 (GL 5/3, ChS 5/3) corresponds to a mixture of gelatin whose concentration is 5 mg/mL and pH 3, with chondroitin sulphate, whose concentration is 5 mg/mL and pH 3 and b) selected mixtures to make LbL ChS/GL hydrogels by dipping LbL.

8.3.2. Study of the interactions of gelatin and chondroitin sulphate in a multilayer assembly

Prior to study the assembly of ChS and GL onto the gelatin cores, the FTIR spectra corresponding to a GL film and a ChS film, prepared by film casting of aqueous solutions at pH 3 and 5 respectively, as well as a $(ChS25/GL10)_{10}$ (pH 5, 3) film, were plotted in the Figure 8.2 in the range 2000 - 800 cm^{-1} with their corresponding assignment of bands.

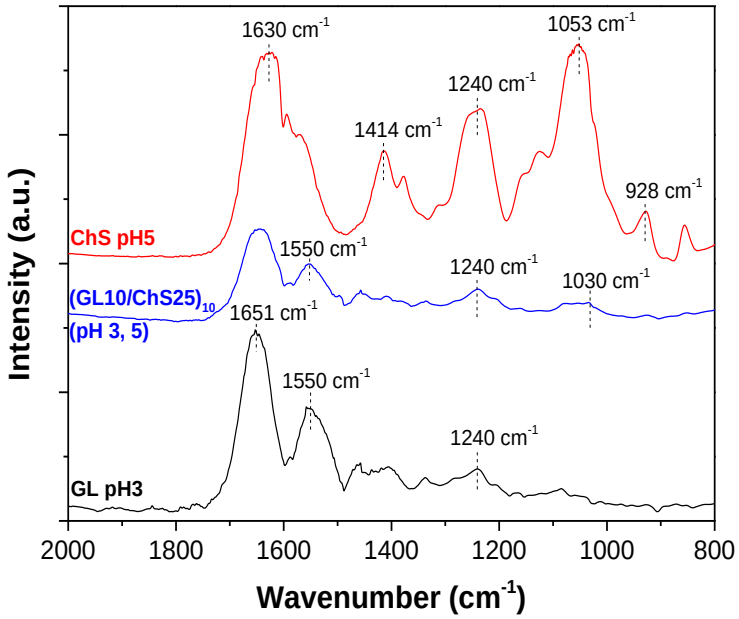

Figure 8.2. FTIR spectra of GL at pH 3, ChS at pH 5 and the sample $(ChS25/GL10)_{10}$ (pH 5, 3).

Gelatin shows a characteristic band at 1651 cm^{-1} assigned to amide I representing C=O stretching/hydrogen bonding coupled with COO^-. The band located at 1550 cm^{-1} is attributed to amide II arises from the bending vibration of N–H groups and stretching vibrations of C–N groups. The band corresponding to amide III is located at 1240 cm^{-1} and it is related to vibrations in the plane of C–N and N–H groups of bound amide or vibrations of CH_2 groups of glycine, one of the amino acids that takes part in the polypeptidic structure of gelatin.[24,25] In the chondroitin sulphate spectrum, bands located at 1630, 1414, and 1053 cm^{-1} are assigned to the bending vibrations of the N–H (*N*-acetylated residues, amide band), C–O–C and C–O stretching, and O–H angular coupling, indicating the existence of free carboxyl groups, respectively. Notice that the band located at 1630 cm^{-1} shows a shoulder at 1570 cm^{-1} which can be attributed to amide II C-N stretch and N-H bend. The absorption band assigned to the S=O stretching related to the sulfate groups on ChS, appeared at 1240 cm^{-1} and the absorption band assigned to the α-(1,4) glycoside bond is observed at 928 cm^{-1}. [26, 27]

In the spectrum corresponding to the sample $(ChS25/GL10)_{10}$ (pH 5, 3), the band at 1550 cm^{-1} is assigned to amide II of gelatin and arises from the bending vibration of N–H groups and stretching vibrations of C–N groups. This band is also present in chondroitin sulphate as a shoulder located at 1570 cm^{-1} and it is assigned to amide II C-N stretch and N-H bend corresponding to *N*-acetylated residues in ChS. The band at 1240 cm^{-1} can be assigned to S=O stretching related to the sulfate groups of ChS overlapped with that corresponding to amide III of

gelatin.[25-27] The band at 1650 cm^{-1} is attributed to COO^- groups of ChS and gelatin and peaks around 1030 cm^{-1} are due to the C-O-C stretching vibration attributed to the saccharide structure of both components.[28-30]

Figure 8.3a shows representative FTIR spectra plotted in the range 2000 to 800 cm^{-1} acquired at different steps of the buildup of the sample $(ChS25/GL10)_n$ (pH 5, 3). During the film buildup, the absorbance increased with the successive depositions of the polyelectrolytes, indicative of film growth and hence of the establishment of interactions between both polymers. This increase in absorbance was mainly verified on the bands located at 1650 cm^{-1}, 1550 cm^{-1} and 1240 cm^{-1}.

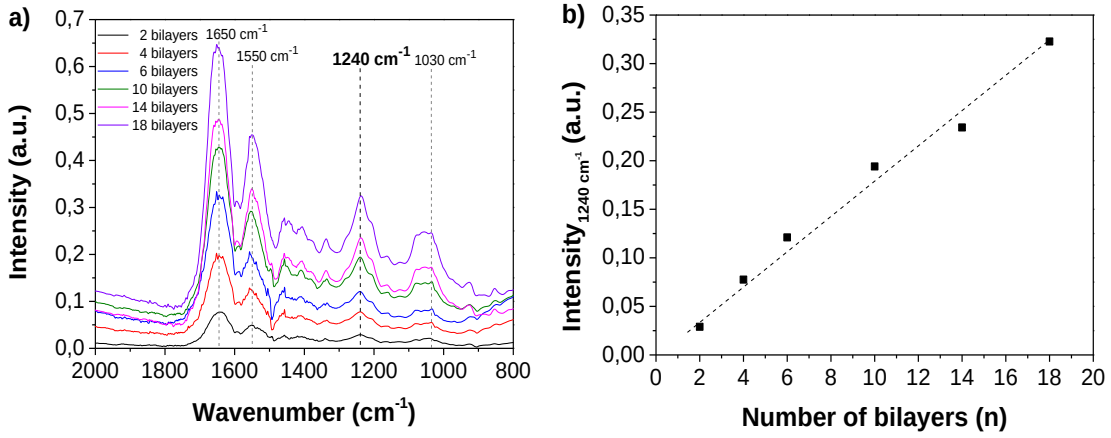

Figure 8.3. a) FTIR spectra of $(ChS25/GL10)_n$ pH (5, 3) films by layers and b) evolution of the absorbance band at 1240 cm^{-1} with the number of bilayers (n) (dashed line is a guide to the eye).

To have more insight about growth during the multilayer process, the absorbance of the band located at 1240 cm^{-1} was plotted against the number of layers and results are shown in Figure 8.3b. The absorbance of this band increases with the number of bilayers confirming the growth of the multilayer system ChS/GL. It is important to note that the extensive overlapping of the main characteristic FTIR bands of both polymers prevents the observation of possible shifting due to the establishment of ionic interactions between both polymers.

The X-ray patterns might provide additional information about the molecular interactions occurring upon the assembly of gelatin and chondroitin sulphate. XRD spectra are shown in Figure 8.4. The diffraction pattern corresponding to gelatin contains an extensive broadening peak in the 2θ range of 5–45°, which is a typical XRD pattern of pure gelatin.[31] Similarly, chondroitin sulphate presents a broad peak centered at 22° with a shoulder at 11.5°. Note the absence of diffraction peaks associated with 3D crystalline order for GL or ChS which shows that both polymers present a backbone with low crystalline profile. Interestingly, the XRD

spectrum corresponding to sample $(ChS25/GL10)_{10}$ (pH 5, 3) besides to a broad peak located at 20° presents a distinct peak at 8.1° which indicates the occurrence of characteristic ordering at higher distances. This might be attributed to the formation of novel ordered regions as a consequence of the electrostatic interaction between the cationic NH_3^+ groups of gelatin and the anionic groups (SO_3^- and COO^-) of ChS in agreement with previous results on polyelectrolyte complexes.[32]

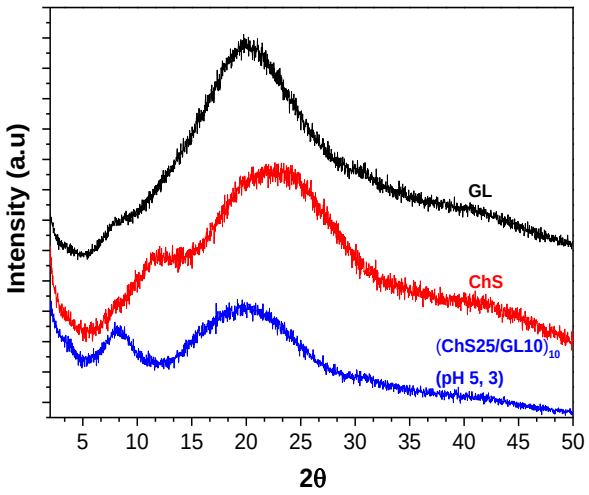

Figure 8.4. X-ray diffractograms of gelatin, chondroitin sulphate and sample $(ChS25/GL10)_{10}$ (pH 5, 3).

8.3.3. Preparation and characterization of LbL hydrogels

In the present chapter an electrostatic assembly of ChS and GL with modulation of pH is attempted. So that, LbL hydrogels were prepared by alternate immersion of gelatin cores (10 %w/v) into ChS and GL solutions. The concentrations and pH of the studied solutions were selected from the optimization of the experimental conditions described above and hydrogels were named as $(ChS10/GL10)_{10}$ (pH 6.75, 5.2), $(ChS10/GL10)_{10}$ (pH 5, 3) and $(ChS25/GL10)_{10}$ (pH 5, 3).

Chemical characterization

To characterize the chemical structure of these three LbL hydrogels and compare them with the spectra of raw polymers, chondroitin sulphate and gelatin, ATR-FTIR spectroscopy was employed. Spectra corresponding to LbL $(ChSx/GL)_n$ hydrogels are plotted in Figure 8.5. The presence of ChS and GL in all samples suggesting that the protocol for depositing layers over a gelatin core is effective. This is confirmed by the presence of a band centered at 1034 cm^{-1} which is characteristic of ChS and can be assigned to polysaccharide C-O stretching and the band at

1630 cm^{-1} attributed to amide I of gelatin. In addition, it is interesting to note that samples denoted as $(ChS10/GL10)_{10}$ (pH 5, 3) and $(ChS25/GL10)_{10}$ (pH 5, 3) presented a higher intensity of the band centered at 1034 cm^{-1} than that observed in the spectrum of the sample $(ChS25/GL10)_{10}$ (pH 6.75, 5.2). This might be related to the existence of a higher number of interactions and hence to an increase of the concentration of ChS deposited.

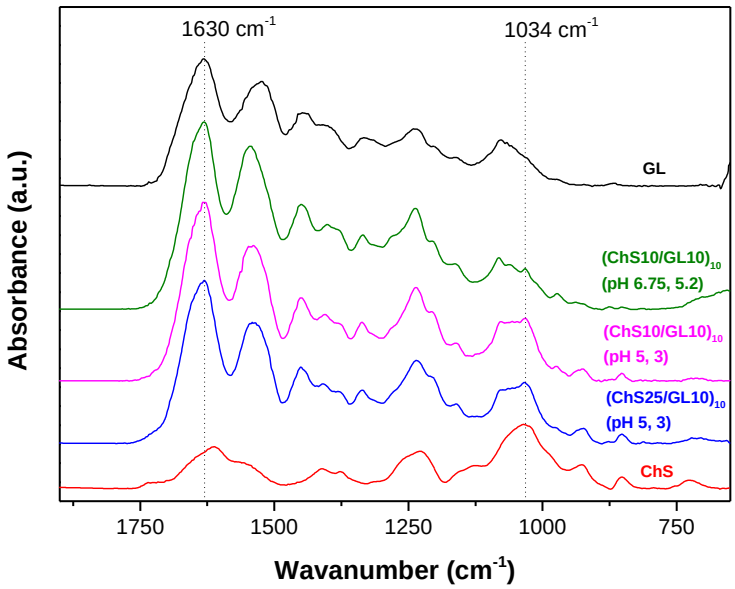

Figure 8.5. FTIR spectra of individual polymers and three different LbL $(ChSx/GL)_n$ hydrogels.

Raman spectroscopy was also employed in order to extend the information about the chemical structure of the three LbL hydrogels under study. The Raman spectra corresponding to all the samples under study and pristine polymers, GL and ChS, were acquired in order to determine the most characteristic bands and they are shown in the Figure 8.6. ChS present bands located at 1340, 1374 and 1411 cm^{-1}, corresponding to CH_2 deformation, symmetric $–CH_3$ and symmetric COO^-, respectively[33] and gelatin has a characteristic band at 1460 cm^{-1} assigned to the CH_2 and CH_3 deformations.[34] A similar result to that obtained through ATR-FTIR (Figure 8.5) can be retrieved by focusing on the band located at 1374 cm^{-1}, characteristic of ChS and not present in pure gelatin. The Raman intensity corresponding to this band is higher in samples ChS10/GL10 (pH 5, 3) and ChS25/GL10 (pH 5, 3) with respect to ChS10/GL10 (pH 6.75, 5.2), which confirms the presence of a higher concentration of ChS adsorbed in these samples and higher as ChS concentration increases.

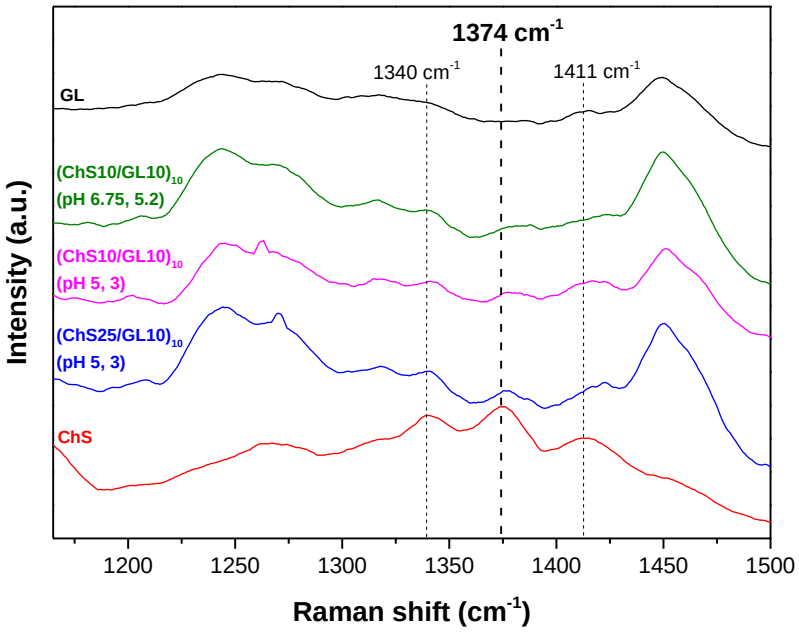

Figure 8.6. Raman spectra of individual polymers and three different LbL (ChS*x*/GL)$_n$ hydrogels.

Morphological characterization

Figure 8.7 illustrates SEM images corresponding to the cross section of a gelatin core (Figure 8.7a) and three different LbL hydrogels, (ChS10/GL10)$_{10}$ (pH 6.75, 5.2) (Figure 8.7b), (ChS10/GL10)$_{10}$ (pH 5, 3) (Figure 8.7c) and (ChS25/GL10)$_{10}$ (pH 5, 3) (Figures 8.7d). LbL hydrogels assembled at pH 5 for ChS and pH 3 for GL showed a bilayer structure with two distinguishable layers surrounding the gelatin core which were not observed neither on the control gelatin gel nor in the sample (ChS10/GL10)$_{10}$ (pH 6.75, 5.2). In the two LbL hydrogels with a bilayer structure, the thickness corresponding to the outer layer increased with the ChS concentration from 9 ± 1 μm for LbL hydrogel (ChS10/GL10)$_{10}$ (pH 5, 3) to 20 ± 3 μm for LbL hydrogel (ChS25/GL10)$_{10}$ (pH 5, 3), as well as the thickness corresponding to the inner layer which increased from 34 ± 8 μm in LbL hydrogel (ChS10/GL10)$_{10}$ (pH 5, 3) to 54 ± 4 μm in LbL hydrogel (ChS25/GL10)$_{10}$ (pH 5, 3). A higher ChS concentration provides more SO_3^- and COO^- groups to interact with the NH_3^+ groups of gelatin, giving rise to a high number of electrostatic interactions increasing the thickness.

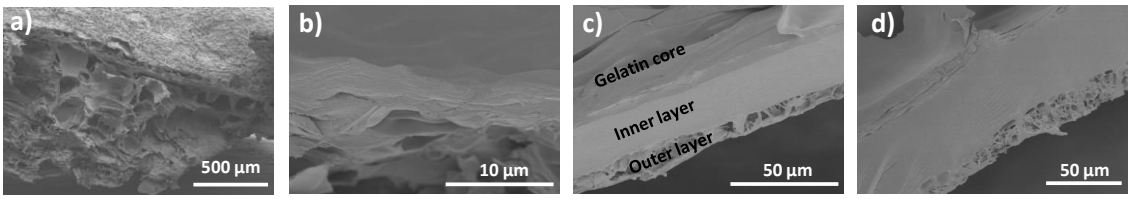

Figure 8.7. SEM images corresponding to the cross-section of a) a gelatin control gel and b) $(ChS10/GL10)_{10}$ (pH 6.75, 5.2), c) $(ChS10/GL10)_{10}$ (pH 5, 3) and d) $(ChS25/GL10)_{10}$ (pH 5, 3) LbL hydrogels.

To partially summarize, the ATR-FTIR and Raman results showed a higher number of interactions when the pH of ChS and GL solution was adjusted to 5 and 3, respectively. In addition, SEM results proved that the bilayer structure is only formed for these pHs as well as a higher thickness of the inner and outer layers with the increase of ChS concentration. Therefore, the assembly of the LbL hydrogel $(ChS25/GL10)_{10}$ (pH 5, 3) is going to be studied in detail to elucidate the chemical composition along the bilayer structure and mechanical properties.

8.3.4. Determination of the compositional structure along the layer distribution of LbL hydrogels

As it was mentioned before, LbL hydrogels $(ChS25/GL10)_{10}$ (pH 5, 3) exhibit a bilayer structure. In order to supply information related to the chemical composition at different depths of this multilayer structure, confocal Raman spectroscopy was used.

Figure 8.8a shows the confocal Raman spectra of a LbL hydrogel $(ChS25/GL10)_{10}$ (pH 5, 3) at different depths. Steps of 10 µm were measured until a total depth of 80 µm into the LbL hydrogel and spectra were normalized with respect to the band at 1460 cm^{-1}, which does not shift in any spectra and it is attributed to the CH_2 deformation of ChS and CH_2 and CH_3 deformations of gelatin.[34] Bands located at 1340, 1374 and 1411 cm^{-1}, corresponding to CH_2 deformation, symmetric $–CH_3$ deformation and symmetric COO-, respectively[33] are characteristic of the ChS.

Through observation of the bands corresponding to CH_2 deformation and symmetric $–CH_3$ deformation of ChS (1340 and 1374 cm^{-1} respectively), it is possible to conclude that the amount of ChS seems to be scarce or almost absent in the surface of the sample, corresponding to incorporation of gelatin during the last LbL cycle. There is also scarce ChS at depths -10 and -20 µm. In addition, the amount of ChS increases with the depth analyzed, considering the higher total intensity of the band at 1340 cm^{-1} until depths of -80 µm. This may correspond to the first layer of ChS assembled on the gelatin core. The analysis of greater depths would have presumably showed the gelatin core, but there was significant light scattering as profundity was

increased. Finally, there are no clear alternating chemical patterns attributable to differentiated layers along the depth; on the contrary, there is coexistence of gelatin and ChS suggesting that there may be interpenetration of both biopolymers as they were assembled on succession.

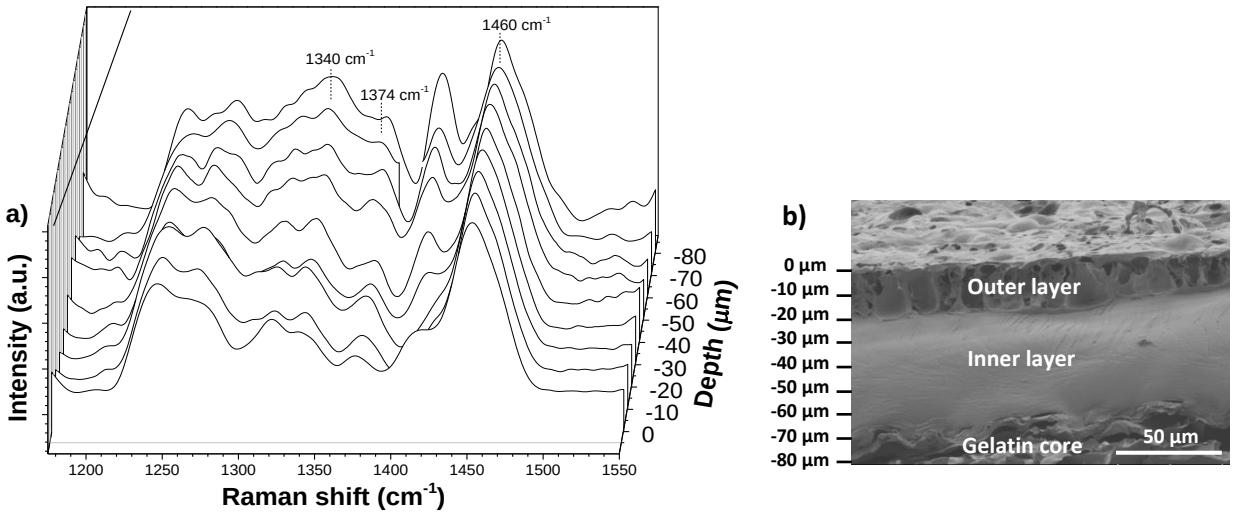

Figure 8.8. a) Depth profile of Raman spectra in the sample $(ChS25/GL10)_{10}$ (pH 5, 3) measured with confocal raman spectrometer. Spectra were normalized with respect to the band at 1460 cm^{-1}. The evolution of ChS bands located at 1340 and 1374 cm^{-1} are studied. b) SEM image of the cross-section of a bilayered LbL hydrogel $(ChS25/GL10)_{10}$ (pH 5, 3) with micrometer vertical scale incorporated for reference.

Figure 8.8b shows a SEM image corresponding to the cross section of this sample, with a micrometer scale incorporated as reference, to relate with Confocal Raman spectroscopy results. It is possible to confirm an extensive degree of interpenetration of both polymers during the LbL assembly which gives rise to a double-membrane morphology. This morphology is characterized by a ~20 μm thickness of the outer layer which is constituted by gelatin and a ~60 μm thickness of the inner layer which corresponds to the interpenetration of both polymers. This might be attributed to the fact that the restructuration of both polyelectrolytes during the LbL assembly progressively hinders the diffusion of gelatin (the outer layer) into the restructured zone (the inner layer). This mechanism of assembly has been explained at a molecular level for other polymer multilayers consisting of at least one polypeptide or a polysaccharide.[35] The model is based on the 'in' and 'out' diffusion of at least one of the polyelectrolytes throughout the whole assembly. The material restructuration occurring in the process of LbL deposition would progressively hinder the diffusion of one of the polyelectrolytes constituting the assembly. This "forbidden zone" would grow with the increasing number of deposition steps so that the outer membrane kept a constant thickness and moved upward as the total thickness increased.

8.3.5. Determination of the mechanical properties

In order to determine the effect of the morphology of hydrogels on their mechanical properties and gel melting temperature, oscillatory rheological experiments were carried out as a function of temperature on a gelatin core (10 %w/v) and a LbL hydrogel $(ChS25/GL10)_{10}$ (pH 5, 3) and results are depicted in Figure 8.9.

In both cases, the elastic modulus (G') is higher than the loss modulus (G''), corroborating that the gel is formed. Focusing on the LbL hydrogel $(ChS25/GL10)_{10}$ (pH 5, 3), a *plateau* in the elastic modulus is observed below its melting temperature, T_m, which is located at 33 ºC. Above T_m, the value of G´ dramatically decreased and ultimately reached a second *plateau*, above which the hydrogel completely melted down. The elastic modulus of the $(ChS25/GL10)_{10}$ (pH 5, 3) hydrogel, G´ = 4775 ± 158 Pa, greatly increased with respect to that corresponding to the gelatin core, G´ = 511 ± 198 Pa. This increase on the mechanical properties is due to the interactions between both polymers that take place all over the sample.[8]

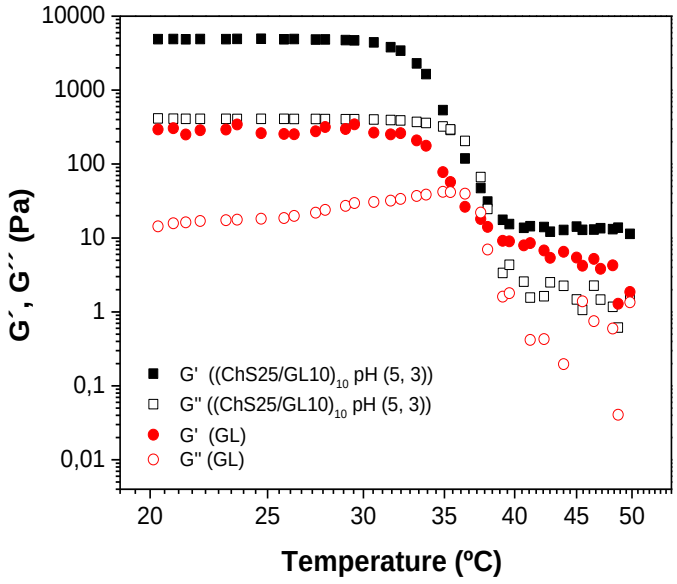

Figure 8.9. Evolution of the elastic modulus G´ and the loss modulus G´´ as a function of temperature for a LbL hydrogel $(ChS25/GL10)_{10}$ (pH 5, 3) (G´ (■) and G´´ (□)) and a gelatin core (10 %w/v) (G´ (●) and G´´ (○)).

It is important to remark that LbL ChS/GL hydrogels reported here are generated just by electrostatic interactions without the employment of any chemical crosslinker. Still the reinforcement is very remarkable taking into account that there exists layer formation that restricts the number of interactions notwithstanding some degree of interpenetration between both polymers as it was demonstrated through Confocal Raman Spectroscopy. Note that the

value of T_m depends on the gelatin concentration and thus it is similar for ChS25/GL10 (pH 5, 3) and the gelatin core (10 %w/v) reaching a value of T_m = 33 ºC.

8.4. CONCLUSIONS

A novel method to prepare hydrogels from gelatin and chondroitin sulphate based on electrostatic layer-by-layer assembly is presented, being this a combination of polymers not studied in literature for LbL hydrogels before.

Concentration and pH conditions were optimized to ensure electrostatic assembly of alternating layers of ChS and GL by dipping LbL in aqueous solutions of the natural polymers.

The assembly of ChS and GL at different steps of the LbL process was studied by FTIR spectroscopy following the absorbance of the band located at 1240 cm^{-1} which increased with the number of deposited bilayers confirming the growth of the multilayer system ChS/GL.

A structure organized in layers was identified in SEM images and compositionally characterized with Raman confocal microscopy, to conclude that a double membrane structure is formed on gelatin cores and there was interpenetration between both polymers along the whole LbL estructure. The thickness of the inner layer could be increased with adequate pH conditions and increasing concentration of ChS.

The coating of gelatin cores with LbL ChS/GL by dipping gave rise to an increase in the elastic modulus without affecting its melting point. The thermal responsiveness together with enhanced mechanical properties might mimic the *in vivo* rheological characteristics of soft tissues organized in layers as, for example, intervertebral discs or employed in drug delivery applications for which their inner structure organized in layers might provide materials for complex drug codelivery.

8.5. REFERENCES

1. Elisseeff, J., Hydrogels: Structure starts to gel. *Nature Materials* **2008,** 7, (4), 271-273.

2. Lee, K. Y.; Mooney, D. J., Hydrogels for Tissue Engineering. *Chemical reviews* **2001,** 101, (7), 1869-1880.

3. Qiu, Y.; Park, K., Environment-sensitive hydrogels for drug delivery. *Advanced Drug Delivery Reviews* **2001,** 53, (3), 321-339.

4. Dong, L.; Agarwal, A. K.; Beebe, D. J.; Jiang, H., Adaptive liquid microlenses activated by stimuli-responsive hydrogels. *Nature* **2006,** 442, (7102), 551-554.

5. Discher, D. E.; Mooney, D. J.; Zandstra, P. W., Growth Factors, Matrices, and Forces Combine and Control Stem Cells. *Science* **2009,** 324, (5935), 1673.

6. Hoffman, A. S., Hydrogels for biomedical applications. *Advanced Drug Delivery Reviews* **2012,** 64, Supplement, 18-23.

7. Costa, A. M. S.; Mano, J. F., Extremely strong and tough hydrogels as prospective candidates for tissue repair – A review. *European Polymer Journal* **2015,** 72, 344-364.

8. Zamora-Mora, V.; Velasco, D.; Hernández, R.; Mijangos, C.; Kumacheva, E., Chitosan/agarose hydrogels: Cooperative properties and microfluidic preparation. *Carbohydrate Polymers* **2014,** 111, (0), 348-355.

9. Rescignano, N.; Hernandez, R.; Lopez, L. D.; Calvillo, I.; Kenny, J. M.; Mijangos, C., Preparation of alginate hydrogels containing silver nanoparticles: a facile approach for antibacterial applications. *Polymer International* **2016,** 65, (8), 921-926.

10. Hernández, R.; Sacristán, J.; Asín, L.; Torres, T. E.; Ibarra, M. R.; Goya, G. F.; Mijangos, C., Magnetic Hydrogels Derived from Polysaccharides with Improved Specific Power Absorption: Potential Devices for Remotely Triggered Drug Delivery. *The Journal of Physical Chemistry B* **2010,** 114, (37), 12002-12007.

11. Zamora-Mora, V.; Fernández-Gutiérrez, M.; Román, J. S.; Goya, G.; Hernández, R.; Mijangos, C., Magnetic core–shell chitosan nanoparticles: Rheological characterization and hyperthermia application. *Carbohydrate Polymers* **2014,** 102, 691-698.

12. Bruvera, I.; Hernández, R.; Mijangos, C.; Goya, G. F., An integrated device for magnetically-driven drug release and in situ quantitative measurements: design, fabrication and testing. *Journal of Magnetism and Magnetic Materials* **2015,** *377*, 446-451.

13. Zhao, Y.; Nakajima, T.; Yang, J. J.; Kurokawa, T.; Liu, J.; Lu, J.; Mizumoto, S.; Sugahara, K.; Kitamura, N.; Yasuda, K.; Daniels, A. U. D.; Gong, J. P., Proteoglycans and Glycosaminoglycans Improve Toughness of Biocompatible Double Network Hydrogels. *Advanced Materials* **2014,** 26, (3), 436-442.

14. Ladet, S.; David, L.; Domard, A., Multi-membrane hydrogels. *Nature* **2008,** 452, (7183), 76-79.

15. Nie, J.; Lu, W.; Ma, J.; Yang, L.; Wang, Z.; Qin, A.; Hu, Q., Orientation in multi-layer chitosan hydrogel: morphology, mechanism, and design principle. *Scientific Reports* **2015,** 5, 7635.

16. Kozlovskaya, V.; Kharlampieva, E.; Erel, I.; Sukhishvili, S. A., Multilayer-derived, ultrathin, stimuli-responsive hydrogels. *Soft Matter* **2009,** 5, (21), 4077-4087.

17. Lynam, D.; Peterson, C.; Maloney, R.; Shahriari, D.; Garrison, A.; Saleh, S.; Mehrotra, S.; Chan, C.; Sakamoto, J., Augmenting protein release from layer-by-layer functionalized agarose hydrogels. *Carbohydrate Polymers* **2014,** 103, 377-384.

18. Lin, N.; Gèze, A.; Wouessidjewe, D.; Huang, J.; Dufresne, A., Biocompatible Double-Membrane Hydrogels from Cationic Cellulose Nanocrystals and Anionic Alginate as Complexing Drugs Codelivery. *ACS Applied Materials & Interfaces* **2016,** 8, (11), 6880-6889.

19. Ladet, S. G.; Tahiri, K.; Montembault, A. S.; Domard, A. J.; Corvol, M. T. M., Multi-membrane chitosan hydrogels as chondrocytic cell bioreactors. *Biomaterials* **2011,** 32, (23), 5354-5364.

20. Lai, J.-Y., Corneal Stromal Cell Growth on Gelatin/Chondroitin Sulfate Scaffolds Modified at Different NHS/EDC Molar Ratios. *International Journal of Molecular Sciences* **2013,** 14, (1), 2036-2055.

21. Zhu, Y.; Gao, C.; He, T.; Liu, X.; Shen, J., Layer-by-Layer Assembly To Modify Poly(l-lactic acid) Surface toward Improving Its Cytocompatibility to Human Endothelial Cells. *Biomacromolecules* **2003,** 4, (2), 446-452.

22. Ahmed, J., Chapter 15 - Rheological Properties of Gelatin and Advances in Measurement. In *Advances in Food Rheology and its Applications*, Woodhead Publishing: 2017; pp 377-404.

23. Umerska, A.; Corrigan, O. I.; Tajber, L., Design of chondroitin sulfate-based polyelectrolyte nanoplexes: Formation of nanocarriers with chitosan and a case study of salmon calcitonin. *Carbohydrate Polymers* **2017,** 156, 276-284.

24. Payne, K. J.; Veis, A., Fourier transform ir spectroscopy of collagen and gelatin solutions: Deconvolution of the amide I band for conformational studies. *Biopolymers* **1988,** 27, (11), 1749-1760.

25. Nur Hanani, Z. A.; Roos, Y. H.; Kerry, J. P., Use of beef, pork and fish gelatin sources in the manufacture of films and assessment of their composition and mechanical properties. *Food Hydrocolloids* **2012,** 29, (1), 144-151.

26. Mader, K. T.; Peeters, M.; Detiger, S. E. L.; Helder, M. N.; Smit, T. H.; Le Maitre, C. L.; Sammon, C., Investigation of intervertebral disc degeneration using multivariate FTIR spectroscopic imaging. *Faraday Discussions* **2016,** 187, (0), 393-414.

27. Fajardo, A. R.; Silva, M. B.; Lopes, L. C.; Piai, J. F.; Rubira, A. F.; Muniz, E. C., Hydrogel based on an alginate-Ca2+/chondroitin sulfate matrix as a potential colon-specific drug delivery system. *RSC Advances* **2012,** 2, (29), 11095-11103.

28. Radev, L.; Mostafa, N. Y.; Michailova, I.; Salvado, I. M.; Fernandes, M. H., In vitro bioactivity of collagen/calcium phosphate silicate composites, cross-linked with chondroitin sulfate. *International Journal of Materials and Chemistry* **2012,** 2, (1), 1-9.

29. Lai, J.-Y.; Li, Y.-T.; Cho, C.-H.; Yu, T.-C., Nanoscale modification of porous gelatin scaffolds with chondroitin sulfate for corneal stromal tissue engineering. *International Journal of Nanomedicine* **2012,** 7, 1101-1114.

30. Pezeshki-Modaress, M.; Mirzadeh, H.; Zandi, M.; Rajabi-Zeleti, S.; Sodeifi, N.; Aghdami, N.; Mofrad, M. R., Gelatin/Chondroitin Sulfate Nanofibrous Scaffolds for Stimulation of Wound Healing: In-Vitro and In-Vivo Study. *Journal of Biomedical Materials Research Part A* **2016**.

31. Karthika, A.; Kavitha, L.; Surendiran, M.; Kannan, S.; Gopi, D., Fabrication of divalent ion substituted hydroxyapatite/gelatin nanocomposite coating on electron beam treated titanium: mechanical, anticorrosive, antibacterial and bioactive evaluations. *RSC Advances* **2015,** 5, (59), 47341-47352.

32. Fajardo, A. R.; Lopes, L. C.; Pereira, A. G. B.; Rubira, A. F.; Muniz, E. C., Polyelectrolyte complexes based on pectin–NH2 and chondroitin sulfate. *Carbohydrate Polymers* **2012,** 87, (3), 1950-1955.

33. Ellis, R.; Green, E.; Winlove, C. P., Structural Analysis of Glycosaminoglycans and Proteoglycans by Means of Raman Microspectrometry. *Connective Tissue Research* **2009,** 50, (1), 29-36.

34. Frushour, B. G.; Koenig, J. L., Raman scattering of collagen, gelatin, and elastin. *Biopolymers* **1975,** 14, (2), 379-391.

35. Borges, J.; Mano, J. F., Molecular Interactions Driving the Layer-by-Layer Assembly of Multilayers. *Chemical Reviews* **2014,** 114, (18), 8883-8942.

CHAPTER 9

General conclusions and perspectives

This PhD work has been focused on "***Layer-by-layer assembly of natural polymers for biomedical applications***". To achieve this objective, different multilayer systems based on natural polymers have been built up using the LbL technique and morphologically and mechanically characterized. An alginate-based magnetic ferrofluid was developed in order to be incorporated into multilayer films for magnetic hyperthermia applications. Finally, the biomedical applications of alginate/chitosan films were tested *in vitro* with neuroblastoma cells (SH-SY5Y) for magnetic hyperthermia therapy and human dermal fibroblasts (HDF) and human caucasian breast adenocarcinoma cells (MCF-7) for sustained drug delivery applications.

Taking into account the experimental results, the following conclusions can be obtained:

a) Different multilayer polymer structures based on natural polymers have been built up through spray LbL and dipping LbL. The main polymer system developed in this thesis formed by alginate and chitosan was assembled by spray LbL because of is a quicker technique which allowed to obtain greater thickness than dipping LbL. The growth of Alg/Chi films by spray assisted LbL, studied by ellipsometry up to 5 bilayers, showed a linear increase of the thickness with the number of deposited bilayers being higher as Alg concentration increased. From 5 bilayers, the growth was followed by SEM illustrating a change of tendency from linear to exponential up to 20 bilayers, point wherein growth slightly increased towards a *plateau* due to the rearrangements of polymer chains during the deposition process. The growth rate of Alg/Chi films assembled by spray was 20 nm/layer, ten-fold higher than by dipping (2 nm/layer).

   The buildup process of hyaluronic acid/poly(allylamine hydrochloride) was carried out by dipping LbL due to the fact that no growth was observed by ellipsometry when both polymers were assembled by spray LbL. The growth of these films was exponential for all concentrations due to the presence of NaCl and the diffusion of PAH within the multilayer film structure and increased with the PAH concentration. A gel-like layer formed by alginate crosslinked with iron II ions was successfully incorporated into the HA/PAH multilayer structure as it was demonstrated by QCM-D experiments.

b) The synthesis and characterization of an alginate-based magnetic ferrofluid was carried out through a coprecipitation method. The obtained ferrofluid was formed by magnetite nanoparticles with an average particle size of ~ 7 nm dispersed in Milli-Q water with

colloidal stability at neutral pH and a hydrodynamic diameter around 100 nm for a magnetite concentration of 8.0 mg/mL.

c) The morphological and mechanical characterization of Alg/Chi films was carried out reaching the following conclusions:

- The mechanical properties of multilayer Alg/Chi films, thermally crosslinked Alg/Chi films and nanocomposite Alg/Chi films built up via spray LbL were determined by (PF-QNM) AFM revealing that: the elastic moduli increased with the number of deposited bilayers until a value of ~12 GPa, thermal crosslinking of Alg/Chi films increased the elastic modulus, being much more significant as alginate concentration increased. Deformation values were almost constant and below 2 nm either in non-crosslinked or crosslinked Alg/Chi films and adhesion force varied between 1 and 4 nN. The incorporation of iron oxide NPs increased the roughness of multilayer Alg/Chi films and induced an increase of their elastic moduli and the deformation values. The presence of NPs on the ending layer of nanocomposite films produced a two-fold increase in the elastic modulus with respect to chitosan ending nanocomposite films, without altering the deformation values.

- The study of the inner structure of nanocomposite films by GISAXS revealed that films assembled by dipping LbL gave rise to a structure in which nanoparticles were dispersed throughout the films, whereas those assembled by spray LbL could form separated NPs layers with some degree of dispersion of NPs along the structure.

d) The biomedical applications of Alg/Chi films and nanocomposite Alg/Chi films were tested *in vitro*.

According to the results obtained from the study carried out to determine the efficiency of nanocomposite Alg/Chi films to act as thermomagnetic films (TMFs) for magnetic hyperthermia on neuroblastoma cells, we concluded that:

- Nanocomposite Alg/Chi films obtained by incorporation of the alginate-based magnetic ferrofluid within Alg/Chi films through spray assisted LbL showed an ordered distribution in layers being the iron the major component with a percentage of 65% as it

was determined by EDX analysis. Nanocomposite Alg/Chi films with different iron contents, modulated by the number of magnetic nanoparticles (NPs) layers, were fabricated in order to examine their magnetic remote heating by application of an alternating magnetic field (AMF). The final magnetite content in every film was determined by UV-Vis transmission spectrophotometry showing a linear increase of magnetite content with the number of NPs layers deposited. The specific power absorption (SPA) of the alginate-based magnetic ferrofluid with different magnetite concentrations, 4.84 and 8.0 mg/mL, was measured at different frequencies (*f*) and magnetic field amplitudes (H) showing an increase of the SPA with the magnetite concentration. The immobilization of NPs in gelatin produced a decrease of SPA (H = 24 kA/m and *f* = 571 kHz) from 868.4 ± 1.9 W/g to 77.2 ± 0.1 W/g due to the block of the Brownian relaxation. Nanocomposite Alg/Chi films could act as TMFs as revealed by the linear temperature increase from 6 to 12 ºC for films with a varying number of NPs layers from 80 to 160 layers when they were subjected to an H = 35 kA/m and *f* = 180 kHz for 5 minutes.

- The employment of these TMFs as patches for magnetic hyperthermia applications was tested *in vitro* with human neuroblastoma cells. TMFs showed good cell adhesion properties and biocompatibility with neuroblastoma cells. *In vitro* experiments by remote heating of TMFs using an AMF (H = 35 kA/m and *f* = 180 kHz) showed different results depending on the number of cycles of MHT and the experimental protocol. MHT applied on TMFs with neuroblastoma cells adhered onto their surface showed a reduction in cell viability up to 67% and 20% for one and three heating cycles, respectively. In addition, in order to mimic *in vivo* applications, other experimental protocol was carried out by application of the MHT on TMFs placed over neuroblastoma cells previously cultured on an ibidi dish, showing a cell viability reduction of 85% after two MHT cycles.

Considering the results obtained from the study carried out to determine the cell adhesion on Alg/Chi films and their efficiency as controlled drug delivery systems, it was concluded that:

- Multilayer Alg/Chi films obtained through spray assisted LbL can be chemically crosslinked using the carbodiimide chemistry and their surface can be easily tuned by spraying a layer of alginate or hyaluronic acid (HA) at the end of the Alg/Chi LbL deposition process. The average roughness (R_a) of films with different number of

bilayers, determined by AFM, showed an increase of R_a with the number of bilayers. Native and crosslinked Alg/Chi films were biocompatible, as it was demonstrated through *in vitro* experiments with human dermal fibroblast (HDF) and human caucasian breast adenocarcinoma (MCF-7) cells. Films ended in HA were more prone to degradation in physiological environment (DMEM at 37ºC) than Alg ending ones after 15 days and this degradation was diminished by the chemical crosslinking.

- Cell adhesion experiments carried out *in vitro* with HDF and MCF-7 cells proved that the number of bilayers did not influenced the cell adhesion of these two kind of cells, the crosslinking process favored the MCF-7 cell adhesion on Alg-ending films where the contact angle remained constant after crosslinking and decreased the MCF-7 cell adhesion on HA-ending films where the contact angle increased after crosslinking. With regards to HDF cell adhesion, non-significant differences were observed with the surface chemistry or the crosslinking.
- The final application of Alg/Chi films as platforms for sustained drug release was tested *in vitro*. For that purpose, tamoxifen, a therapeutic agent against breast cancer, was incorporated in different intermediate positions of the multilayer Alg/Chi films and results showed a more sustained release over time as number of deposited bilayers increased. It was proven that there was not degradation of these films after the drug delivery experiment and the release mechanism was diffusion controlled and could be described by the Ritger-Peppas model. The release of TMX from Alg/Chi films during *in vitro* experiments decreased the cell viability of MCF-7 cells whereas the HDF cell viability remained unaffected.

e) Finally, a new LbL system composed of ChS and GL, which had not been studied in literature before, has been investigated, reaching the following conclusions: the FTIR absorbance intensity increased with the number of ChS/GL deposited bilayers confirming the growth of the multilayer system through dipping LbL assembly. This assembly process carried out over a gelatin core gave rise to a layered organized structure, as it was observed by SEM, where multilayers formed a double membrane structure and there was interpenetration between both polymers along the LbL structure. The thickness of the multilayers could be increased by increasing the ChS concentration at pH 3 for gelatin and pH 5 for ChS. Mechanical properties of LbL hydrogels revealed that the elastic modulus increased with respect to the uncoated gelatin core from 511 ± 198 Pa to 4775 ± 158 Pa

without altering their melting point at 33 ºC, allowing to employ these LbL hydrogels as cell encapsulation and drug delivery systems in the future.

From this PhD work several fruitful national and international collaborations have been established with different groups as, for example, with F. Boulmedais (ICS-CNRS, Strasbourg), T. Ezquerra (CSIC, Spain), J. San Román (CSIC, Spain) and G. Goya (INA, Spain).

Considering the results obtained in the present PhD work, new challenges arise for other PhD and Master projects. Future work is focused on the development of light-responsive nanostratified materials based on combining polymer multilayers in between gel layers to encapsulate drugs for dermal applications, as well as the development of multilayer LbL hydrogels assembled over gelatin cores with drugs incorporated with the objective of developing materials for complex drug delivery.

ANNEXES

ANNEX I. Iron calibration curve

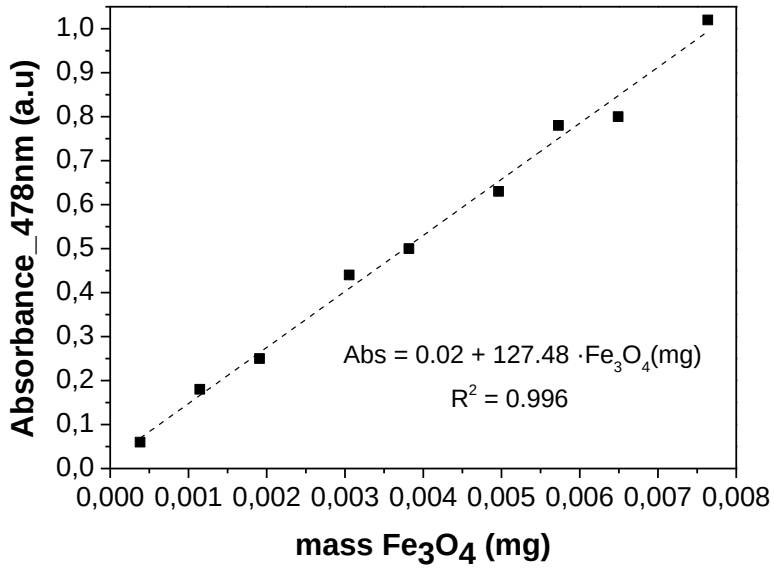

Figure A.I.1. Standard calibration curve for magnetite determination by UV-Vis spectrophotometry at 478 nm. Dashed line represents the linear fit of the data.

ANNEX II. Tamoxifen calibration curve

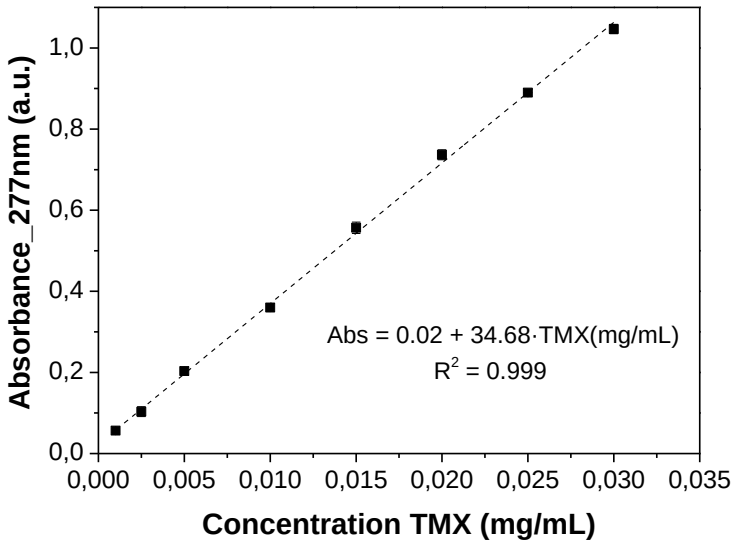

Figure A.II.1. Standard calibration curve of TMX in PBS with 1 %w/v Tween 80 at 277 nm. Dashed line represents the linear fit of the data.

ANNEX III. AFM morphological images of $(Alg/Chi)_nAlg$ and $(Alg/Chi)_nHA$ films

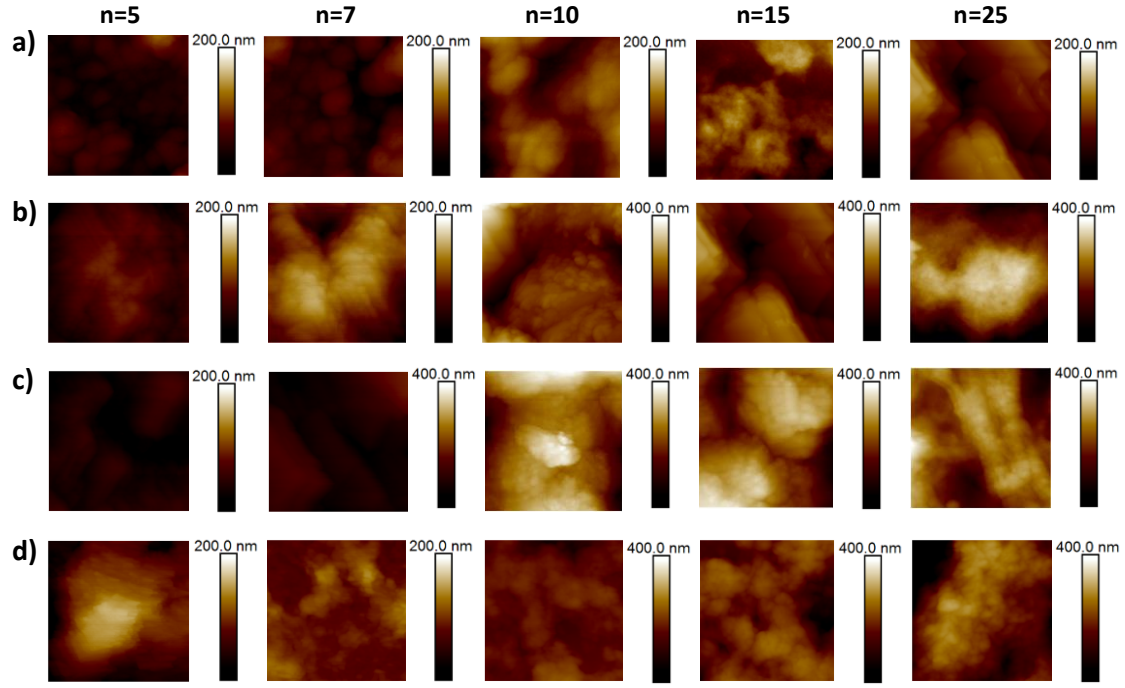

Figure A.III.1. AFM topographic images (2μm × 2μm) corresponding to non-crosslinked films a) $(Alg/Chi)_nAlg$ and b) $(Alg/Chi)_nHA$ and crosslinked films c) $(Alg/Chi)_nAlg$ and d) $(Alg/Chi)_nHA$ with different number of bilayers.

ANNEX IV. Fluorescence microscope images of HDF and MCF-7 cell adhesion on $(Alg/Chi)_nAlg$ and $(Alg/Chi)_nHA$ films

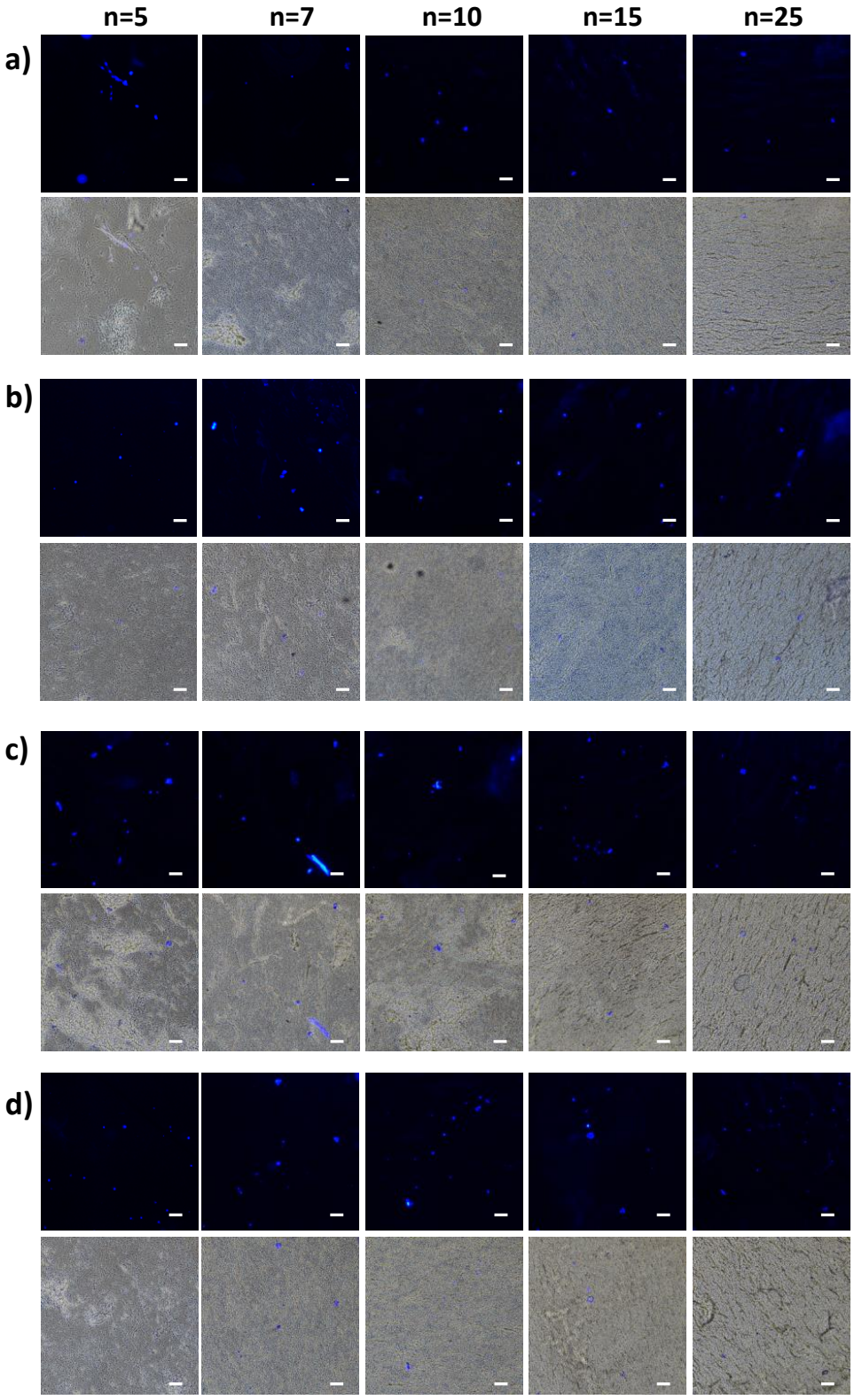

Figure A.IV.1. Fluorescence microscope images of HDF cell adhesion on non-crosslinked films a) $(Alg/Chi)_nAlg$ and b) $(Alg/Chi)_nHA$ and crosslinked films c) $(Alg/Chi)_nAlg$ and d) $(Alg/Chi)_nHA$ with different number of bilayers after 3 days. Scale bars 100 μm.

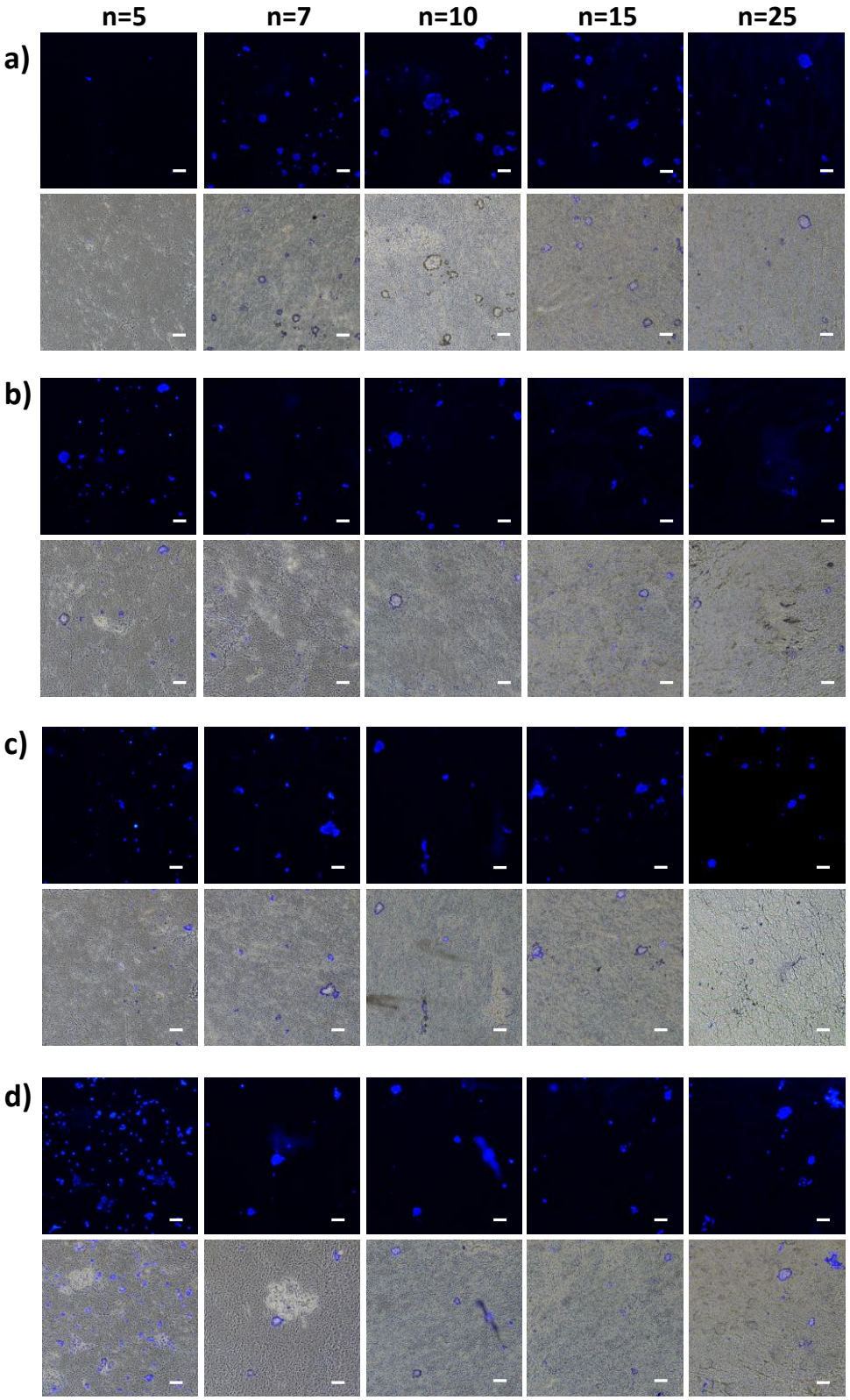

Figure A.IV.2. Fluorescence microscope images of MCF-7 cell adhesion on non-crosslinked films a) $(Alg/Chi)_nAlg$ and b) $(Alg/Chi)_nHA$ and crosslinked films c) $(Alg/Chi)_nAlg$ and d) $(Alg/Chi)_nHA$ with different number of bilayers after 3 days. Scale bars 100 μm.

ABBREVIATIONS

AB	Alamar blue
AFM	Atomic Force Microscopy
AG-NPs	Silver nanoparticles
Alg	Sodium alginate
AMF	Alternating Magnetic Field
APTT	Activated partial thromboplastin time
Au-NPs	Gold nanoparticles
bFGF	Basic fibroblastic factor
CaP	Phosphate precipitates
Chi	Chitosan
ChS	Chondroitin sulphate
CL	Crosslinked
CLSM	Confocal laser microscopy
COL	Collagen
CV	Cell viability
DAPI	4’,6-Diamidino-2-(Phenylindole, Dihydrochloride)
DD	Deacetylation degree
Dex	Dextran
D_{hyd}	Hydrodynamic diameter
DLS	Dynamic Light Scattering
DMA	Dynamic mechanical analysis
DMEM	Dulbecco’s Eagle’s Medium
DMSO	Dimethylsulfoxide
DMT	Derjaguin-Muller-Toporov
DN	Dopamine
DPI	Dual-polarization interferometry
E.coli	Escherichia coli
EBs	Embryoid bodies
EDC	1-Ethyl-3-(3-dimethylaminopropyl)-carbodiimide
EDTA	Ethylendiaminetetraacetic acid
EDX	Energy-dispersive X-ray spectroscopy
EHT	Exogenous hyperthermia

EMC	Extracellular matrix
EthD-1	Ethidium homodimer-1
f	Frequency
FBS	Fetal bovine serum
FEG	Field emission gun
FIB	Focus Ion Beam
FT-IR	Fourier Transform Infra-Red spectroscopy
FTIR-ATR	Fourier Transform Infra-Red spectroscopy – Attenuated total reflectance
FWHM	Full width at half maximum
GISAXS	Grazing-incident small angle X-ray scattering
GIXD	Grazing-incidence X-ray diffraction
GL	Gelatin
^{1}H	Proton
H	Magnetic field amplitude
HA	Hyaluronic acid
HDF	Human dermal fibroblasts
HEP	Heparin
HEPES	4-(2-hydroxylethyl)-1-piperazineethanesulfonic acid
HUAECs	Human umbilical artery endothelial cells
HUVEC	Human umbilical vein endothelial cells
IDG	Intermodular detector gap
IOP	Intraocular pressure
IPNs	Interpenetrating polymer networks
IVD	Intervertebral disk
LB	Langmuir-Blodgett
LbL	Layer-by-layer
LVR	Linear viscoelastic region
Mb	Myoglobin
MCF-7	Human caucasian breast adenocarcinoma
MHT	Magnetic hyperthermia
MSCs	Bone marrow-derive ovine cells
$\overline{M_v}$	Viscosity average molecular weight
M_w	Molecular weight

NCC	Nanocrystalline cellulose
NHS	N-Hydroxysuccinimide
NMR	Nuclear Magnetic Resonance
NPs	Magnetic nanoparticles
OAlg	Oxidized sodium alginate
OWLS	Optical waveguide lightmode spectroscopy
PA	Polyanion
PAA	Poly(acrylic acid)
PAH	Poly(allylamine hydrochloride)
PBS	Phosphate buffered solution
PC	Polycation
PCNs	Polyelectrolyte complex nanoparticles
PDDA	Poly(diallyldimethylammonium chloride)
PDI	Polydispersity index
PEC	Polyelectrolyte complex
PEI	Poly(ethylenimine)
PEMs	Polyelectrolyte multilayer films
PET	Polyethylene terephthalate
PET	Poly(ethylene terephthalate)
PF-QNM	PeakForce Quantitative Nanomechanical Mapping
PGA	Poly(g-glutamic acid)
PLL	Poly(L-lysine)
PLLA	Poly(L-lactic acid)
PS	Polystyrene
PSS	Poly(styrene sulfonate)
PT	Prothrombin time
PU	Polyurethane
PVA	Polyvinyl alcohol
PVP	Poly(vynil pyrrolidone)
Px	Piroxicam
QCM	Quartz Crystal Microbalance
QCM-D	Quartz Crystal Microbalance with dissipation monitoring
R_a	Average roughness

RGD	Arginine-glycine-aspartate
SAR	Scanning angle reflectometry
SAXS	Small angle X-ray scattering
SBS	Specular beam stop
SEM	Scanning Electron Microscopy
SH-SY5Y	Human neuroblastoma cells
SNP	Sodium nitroprusside
SPA	Specific Power Adsorption
SPR	Surface plasmon resonance
TEM	Transmission Electron Microscopy
TGA	Thermogravimetric analysis
THF	Tetrahydrofuran
TMFs	Thermomagnetic films
TMX	Tamoxifen citrate salt
UV-Vis	Ultraviolet-visible spectroscopy
XPS	X-ray photoelectron spectroscopy
XRD	X-Ray Diffraction
α-MSH	Alpha-melanocyte stimulating hormone
ΔT	Temperature increase

LIST OF PUBLICATIONS

Publications directly related to this thesis:

1. **M. Criado**, E. Rebollar, A. Nogales, T. Ezquerra, F. Boulmedais, C. Mijangos, R. Hernández. Quantitative nanomechanical properties of multilayer films made of polysaccharides through spray assisted layer-by-layer assembly. *Biomacromolecules*, **2017**, 18, 169-177.

2. **M. Criado**, B. Sanz, G. F. Goya, C. Mijangos, R. Hernández. Magnetically responsive biopolymeric multilayer films for controlled hyperthermia. *ACS Applied Materials & Interfaces,* submitted **2017**, Manuscript ID am-2017-03852f.

3. **M. Criado**, J. M. Rey, C. Mijangos, R. Hernández. Double-membrane Thermoresponsive Hydrogels from Gelatin and Chondroitin Sulphate with Enhanced Mechanical Properties. *RSC Advances*, **2016**, 6, 105821-105826.

4. **M. Criado**, M. Fernández-Gutiérrez, J. San Román, C. Mijangos, R. Hernández. Multilayer polymer films with tailored structures for sustained drug delivery and cellular adhesion. *Submitted, biomacromolecules*, **2017**.

5. **M. Criado**, C. Mijangos, R. Hernández. Procesos de fabricación y aplicaciones avanzadas de filmes poliméricos nanoestructurados capa a capa (layer-by-Layer). *Revista Plásticos Modernos*, **2015**, 110, 13-17.

6. **M. Criado**, C. Mijangos, R. Hernández. Hidrogeles multimembrana obtenidos a partir de polímeros naturales. *Revista Plásticos Modernos*, en prensa, Mayo, **2017**.

7. **M. Criado**, E. Rebollar, A. Nogales, T. Ezquerra, C. Mijangos, R. Hernandez. Determinación of the inner structure of hybrid multilayer polymer films through grazing incidence X-ray scattering (GISAXS), *in preparation.*

8. **M. Criado,** L. Lerma, F. Boulmedais, C. Mijangos, R. Hernández. Light-responsive nanostratified polymer materials for drug delivery applications, *in preparation.*

Patents:

9. **M. Criado**, C. Mijangos, R. Hernández. Ferrofluidos acuosos de base polimérica con altos coeficientes de absorción específica y procedimiento de obtención, ES, No. 201631442, **2016**.

Other related publications:

10. A. Lejardi, R. Hernández, **M. Criado**, J. I. Santos, A. Etxeberria, J. R. Sarasua, C. Mijangos. Novel hydrogels of chitosan and poly(vinyl alcohol)-g-glycolic acidcopolymer with enhanced rheological properties. *Carbohydrate Polymers*, **2014**, 103, 267-273.

11. R. Hernández, **M. Criado**, A. Nogales, M. Sprung, C. Mijangos, T. Ezquerra. Deswelling of Poly(N-isopropylacrylamide) Derived Hydrogels and Their Nanocomposites with Iron Oxide Nanoparticles As Revealed by X-ray Photon Correlation Spectroscopy. *Macromolecules*, **2015**, 48, 393-399.